HEME-IRON AND HEME/COPPER OXYGEN CHEMISTRY OF METALLOENZYME ACTIVE SITES WITH BIO-INSPIRED SYNTHETIC MODEL SYSTEM

by

Hyun Kim

A dissertation submitted to Johns Hopkins University in conformity with the requirements for the degree of Doctor of Philosophy

Baltimore, Maryland

December 2020

Abstract

The activation and reduction of dioxygen are the most important process in biological respiration and in energy conversion systems such as fuel cells which harness clean and effective electrical power generated from chemical fuels that use O_2 as an electron/cation acceptor. The stepwise reduction of dioxygen to water is highly exothermic transformation which is substantial for aerobic respiration. The metal-bound reduced-O_2 intermediates are formed in the course of reductive O–O bond activation. Establishing redox and thermodynamic relationships between metal-oxy species and its reduced (and protonated) derivatives is critically important for a full understanding of (bio)chemical processes involving metalloenzyme mediated dioxygen processing. Biomimetic synthetic model chemistry is a powerful tool to better understand fundamental elements of metalloprotein electronics, functions, and selectivity/reactivity.

In chapter 1, an overview of reductive dioxygen activation by heme and heme-peroxide-copper based systems is provided. It also includes important intermediates in the catalytic reduction of dioxygen by metalloenzymes.

Chapter 2 presents a new iron-porphyrinate complex, which employs a tridentate ligand that incorporated a histamine moiety appended to the periphery of a fluorinated tetraphenylporphyrin and the reactivity of various reduced heme compounds, toward 2,6-dimethyl-phenyl isocyanide (DIMPI) and nitric oxide (NO). The generated DIMPI-Fe^{II} and NO-Fe^{II} complexes were characterized by UV-vis, IR, NMR, and EPR spectroscopies.

In chapter 3, the dioxygen reactivity of reduced heme, which is an advanced cytochrome *c* oxidase (C*c*O) active site model system as a binucleating ligand, is reported in the absence and the presence of copper ion. This work represents that the process of

oxygenation of the iron complex in the absence and presence of copper ion matches well with proposed C*c*O catalytic cycle, i.e., Cu-independent generation of heme superoxide and subsequent formation of peroxide moiety with copper ion.

Chapter 4 discusses the stepwise reduction and protonation of a ferric heme superoxide complex and the first example of experimentally determined thermodynamics (reduction potential and pK_a). With these measure thermodynamic parameters, the OO–H bond dissociation free energy (BDFE) was calculated employing thermodynamic square scheme and Bordwell equation. The determined BDFE value was confirmed by the oxidizing capability of ferric heme superoxide species via hydrogen atom transfer (HAT).

In chapter 5, thermodynamic comparisons for O_2-derived iron-porphyrinate interrelated ferric superoxide, peroxide and hydroperoxide complexes in the presence and absence of an appended imidazolyl axial base are described. Also, the reactivity results of superoxide species with/without axial ligand with external substrates reveal their oxidizing capability, and these observations corroborate the new thermodynamic results presented here.

Advisor: Dr. Kenneth D. Karlin

Thesis Committee: Dr. David P. Goldberg

Dr. V. Sara Thoi

Acknowledgements

My experience pursuing bioinorganic chemistry during Ph.D. study at Johns Hopkins University has been nothing short of amazing. This would not have been possible without so many people I have met. First and foremost, I would like to sincerely thank my Ph.D. advisor, Prof. Kenneth D. Karlin for his continuous support and tremendous mentorship throughout my time at Johns Hopkins University. His scientific insight and guidance have encouraged me to grow a great deal as a scientist and I appreciate the many lessons I have learned from him.

I would also like to thank Prof. David P. Goldberg and Prof. V. Sara Thoi for serving as my committee members and for their support. I must also give a special thanks to Prof. Alan T. Stone for agreeing to be on my chemistry Graduate Board Organization (GBO) committee and for his support. I am grateful to Prof. Cheal Kim who introduced me to the field of bioinorganic chemistry under his tutelage, mentored me during my master's study, and as well supported me on the way. Finally, I am thankful to my collaborators, Dr. Andrew W. Schaefer in Prof. Edward I. Solomon's laboratory for useful discussions and collecting resonance Raman data.

I would like to extend my gratitude to my lab mates of the Karlin's group. I would specifically like to thank Dr. Savita K. Sharma and Dr. Patrick J. Rogler, for helping me start up in the laboratory, the extensive chemistry discussions and collaborations and Dr. Sunghee Kim, Dr. Jung Yoon Lee, and Dr. Suzanne M. Adam, for providing a supportive and encouraging research environment. I would also like to thank Dr. Daniel Diaz-Romero and Dr. Mayukh Bhadra, for being my good company and lab mate, and maintaining my

sanity by hanging out outside of lab. Also, thanks to present members, Austin E. Herzog, Dr. Pradip K. Hota, and Bohee Kim for making the lab a fun place to work.

In addition, I am grateful to Goldberg's group members for their help whenever I needed it. Special thanks to Vishal Yadav and Jireh Joy D. Sacramento for helpful scientific discussions and for having our dinner meeting. I would also like to thank department of chemistry staff who tirelessly work behind the scenes, Meghan Carter, John Kidwell, Joe Russell, Indira Jones, Jasmine Harris, Dr. Joel Tang, Dr. Maxime A. Siegler, and particularly Boris Steinberg.

Last but not least, I would like to thank the most important people of all, my family, my mother, Myoungsook Sung, and my brother, Wansoo Kim for all their love, sacrifices, endless support, and encouragement. I would not have accomplished this goal without your support. I would further like to thank my friends whom I met in Baltimore for making my life more colorful. Also, many thanks to my friends in Korea.

During the long journey of my Ph.D. study, I have been helped and motivated by many people. It was a great honor for me to have all of this support and an opportunity to work with good faculty and lab mates.

Hyun Kim

Table of Contents

List of Figures and Tables

CHAPTER 1

CHAPTER 2

CHAPTER 3

CHAPTER 4

CHAPTER 5

Chapter 1

Dioxygen Activation of Heme and Heme-Copper Enzymes

1.1 Fundamental properties and activation/reduction of dioxygen

Dioxygen (O_2) is the most abundant and a critical constituent of the earth's atmosphere, which is paramagnetic with a triplet ground state resulting from the presence of two unpaired electrons in degenerate molecular orbitals.[1] Although molecular dioxygen in its triplet ground state is a kinetically inert under ambient conditions, it is a thermodynamically powerful oxidant due to the inherent reactivity of its double bond. However, in order to utilize the high oxidizing power, the O=O double bond needs to be reductively activated.[2] The activation/reduction of dioxygen is the most important process in biological respiration and in energy conversion systems such as fuel cells which harness clean and effective electrical power generated from chemical fuels that use O_2 as an electron/cation acceptor.[3,4] Such processes convert chemical to electrical energies via the oxygen reduction reaction (ORR).[5,6] The first prerequisite for the broad application of fuel cells is catalysts that use H_2/O_2 on the anode and cathode, respectively. At the anode, H_2 is oxidized, releasing protons and at the cathode, the protons/electrons are used to reduce dioxygen.[7]

$$2H_2 \rightarrow 4H^+ + 4e^- \qquad \text{Anode}$$

$$O_2 + 4H^+ + 4e^- \rightarrow 2H_2O \qquad \text{Cathode}$$

This oxygen reduction reaction (ORR) occurs mainly by two pathways: the two-proton/ two-electron ($2H^+/2e^-$) reduction to hydrogen peroxide (H_2O_2) or the four-proton/ four-electron ($4H^+/4e^-$) reduction to water (H_2O) in aqueous solutions.[8–12] The first one electron reduction of O_2 to superoxide ion is thermodynamically unfavorable, as shown in Figure 1.1. However, stepwise one electron reduction from superoxide to peroxide species

and direct the two-electron reduction of dioxygen are thermodynamically favorable reactions (Figure 1.1).

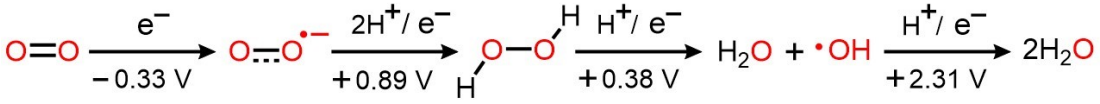

Figure 1.1 Thermodynamics of the stepwise reduction of dioxygen. Reduction potentials shown are versus normal hydrogen electrode (NHE) at 25 °C.

The oxygen reduction reaction (ORR) at the cathode is much slower than the hydrogen oxidation reaction occurring at the anode. In order to speed up the ORR kinetics, nature uses terminal oxidases in the respiratory chain where O_2 is reduced to H_2O in a four-electron process and the energy harvested from this reduction is converted into a proton gradient to drive the synthesis of ATP. Thus, the most common type of ORR is catalyzed by the heme a_3/Cu_B site with an iron porphyrin core structure in cytochrome *c* oxidase (C*c*O) (*vide infra*).[8]

The reactions between triplet state O_2 (S = 1) with organic substrates where most of the organic molecules have spin-paired singlet spin state (S = 0), are spin-forbidden.[13] To overcome this spin-barrier which makes a direct O_2 mediated substrate oxidation kinetically sluggish, nature has utilized metalloenzymes which contain metal ions such as iron, copper, and manganese.[14] These enzyme cofactors can be classified into two types, oxygenases and oxidases based on the role of O_2 in the reaction.[15] Oxygenases incorporate one (monooxygenase) or both (dioxygenase) oxygen atoms into organic substrates (eq 1and eq 2, and Figure 1.2a), whereas oxidases utilize O_2 to oxidize the organic substrates while coupling these processes to the reduction of O_2 to H_2O or H_2O_2 (eq 3 and eq 4, and Figure 1.2b).[16]

Monooxygenases: $R–H + O_2 + 2H^+ + 2e^- \rightarrow R–OH + H_2O$ (1)

Dioxygenases: $R–H + O_2 \rightarrow R(O)OH$ (2)

Oxidases: $O_2 + 4H^+ + 4e^- \rightarrow 2H_2O$ (3)

$O_2 + 2H^+ + 2\ e^- \rightarrow H_2O_2$ (4)

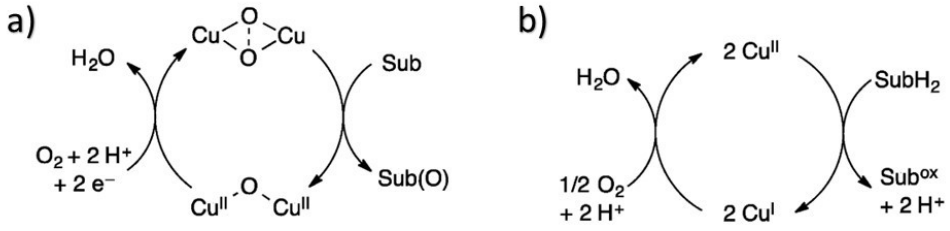

Figure 1.2 Catalytic cycles for copper-based (a) oxygenase (b) oxidase (adapted from ref 16).

1.2 Dioxygen activation/reduction by metalloenzymes

Metalloenzymes activate dioxygen to carry out a variety of biological reactions. These enzymes use diverse active sites, such as heme and nonheme iron, copper and other metal sites. Herein, this chapter focuses on dioxygen activating heme enzymes.

1.2.1 Heme enzymes

Heme-containing proteins are of particular importance for living organisms and the interaction of iron of hemes with dioxygen plays a variety of biological roles such as transport and storage of dioxygen (hemoglobin and myoglobin: Figure 1.3), electron transfer (cytochromes), one-electron oxidation (peroxidases) and monooxygenation of foreign substrates (cytochrome P450s), dismutation of H_2O_2 (catalases), NO synthesis

(NOS) and four-electron reduction of O_2 (oxidases). In this regard, myoglobin (Mb) and hemoglobin (Hb) are biological dioxygen carriers and are responsible for the storage and transport of O_2 in most aerobic organisms. Myoglobin contains one heme prosthetic group, while hemoglobin which transports O_2 is a tetramer where four O_2 molecules bind cooperatively (Figure 1.3).[17,18]

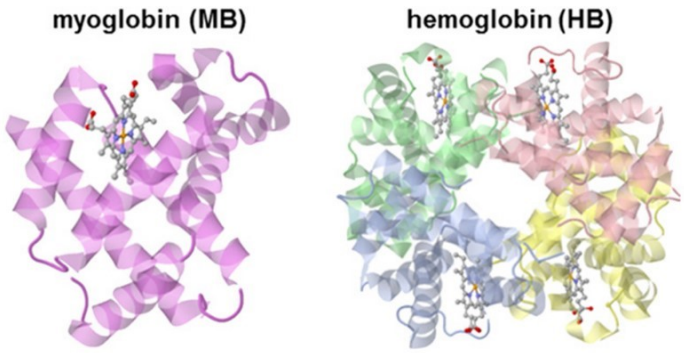

Figure 1.3 Crystal structures of human myoglobin (Left, PDB: 2DN2) and hemoglobin (Right, PDB: 3RGK) (adapted from ref 19).

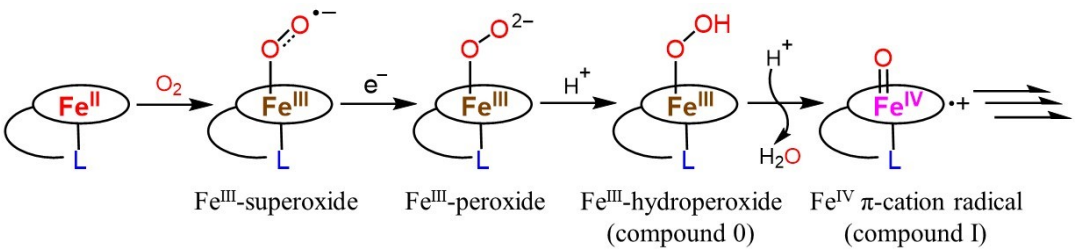

Figure 1.4 Schematic drawing of the interaction of dioxygen with heme enzymes. L is an axial ligand.

The reduction sequence of dioxygen activation by metalloenzymes proceeds by electron and proton transfer reactions as shown in Figure 1.4. In all of the above systems the common mechanistic process is the stepwise oxidation of Fe^{II} or Fe^{III} and then on to the Fe^{IV} oxidation state. The initial reduction step of O_2 activation mechanism is the

binding of dioxygen to the heme iron, forming a low-spin ferric superoxide (oxy ferrous) intermediate. The subsequent reduction of the oxygenated species, [(P)Fe^{III}–($O_2^{\cdot-}$)] or [(P)Fe^{II}–(O_2)], forms a ferric peroxide complex, [(P)Fe^{II}–(O_2^{2-})], which is followed by protonation at the distal oxygen to generate a ferric hydroperoxide, [(P)Fe^{III}-(OOH)], also known as compound 0 (Cmpd 0). A second protonation on the distal oxygen of hydroperoxide species causes heterolytic O−O bond cleavage to produce a highly reactive high-valent ferryl-oxo π-cation porphyrinate radical ((P$^{\bullet+}$)Fe^{IV}=O, compound I, Cmpd I), releasing a molecule of water.[20]

Cmpd I, which is an oxidation state two-electron equiv higher than the resting state, was first discovered in horseradish peroxidase (HRP)[21] and is formed by O–O bond activation of O_2 or H_2O_2 depending on the class of enzymes. This species is identified as key reactive intermediates in the catalytic cycles of heme-containing peroxidases, catalases, and cytochrome P450s (CYP450s). The radical of Cmpd I resides generally on the porphyrin or the axial ligand. The electronic structure is described as S = $^3/_2$ due to the ferromagnetic coupling between S =1 ferryl species and S = ½ porphyrin π cation radical, as in most peroxidases and catalases, while for chloroperoxidase (CPO) and CYP450s, strong antiferromagnetic coupling is observed, resulting in an overall S = ½ state.[14,22] The reactivity of Cmpd I differs from enzyme to enzyme. In peroxidases, the high-valent oxo iron porphyrin oxidizes amines, phenols, and other aromatic substrates, whereas the species oxidizes hydrogen peroxide to oxygen molecule in catalases.[23] For CYP450s the high-valent species transfers a single oxygen atom directly to a variety of substrates.

1.2.1.1 Cytochrome P450s

Cytochrome P450s (CYP450s) were discovered in the early 1960s,[24] and they are thiolate-ligated heme-containing monooxygenases (Figure 1.5), present in almost every aerobic species and play a key role in a wide variety of oxidative reactions in biology, including hydroxylation, epoxidation, heteroatom oxidation, and heteroatom dealkylation.[25–34] They are primarily responsible for oxygen transfer from dioxygen into biological substrates, with the second oxygen atom being reduced by two electrons provided by nicotinamide adenine dinucleotide phosphate, NAD(P)H via a reductase protein to a water molecule (Scheme 1.1). These processes are of essential importance in biosystems, where the enzyme participates in detoxification and biosynthesis of steroids, terpenoids, alkaloids, antibiotics, pigments, antioxidants, etc.[35]

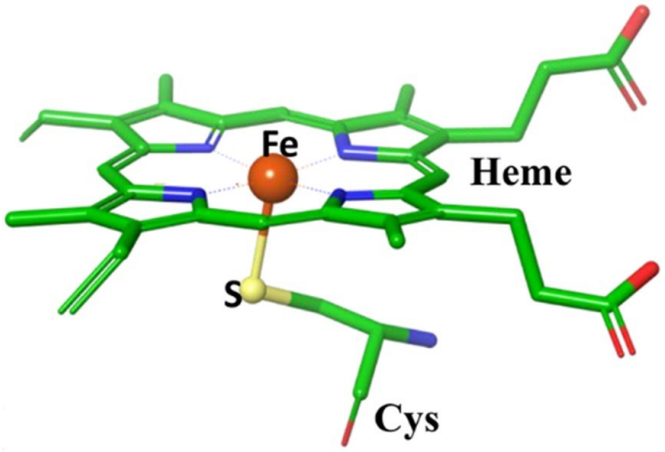

Figure 1.5 The active site of cytochrome P450 (adapted from ref 36) containing a prosthetic heme IX complex coordinated by a thiolate ligand from a cysteine residue.

Scheme 1.1 Overall oxygenation reaction catalyzed by cytochrome P450

In hydroxylation reactions catalyzed by cytochrome P450s, the hydrogen abstraction oxygen "rebound" mechanism shown in Figure 1.6 (see below in Chapter 4 for more details) was proposed by Groves et al.[37] In this pathway, the high-valent ferryl-oxo π-cation porphyrinate radical species (Cmpd I) abstracts a hydrogen atom from the substrate (R–H) to form a carbon radical (R•) with the iron(IV) hydroxide complex. The incipient radical then reacts with the Fe^{IV}–OH species (compound II, Cmpd II) i.e., "oxygen rebound step", to produce the alcohol product and the ferric resting state.[15]

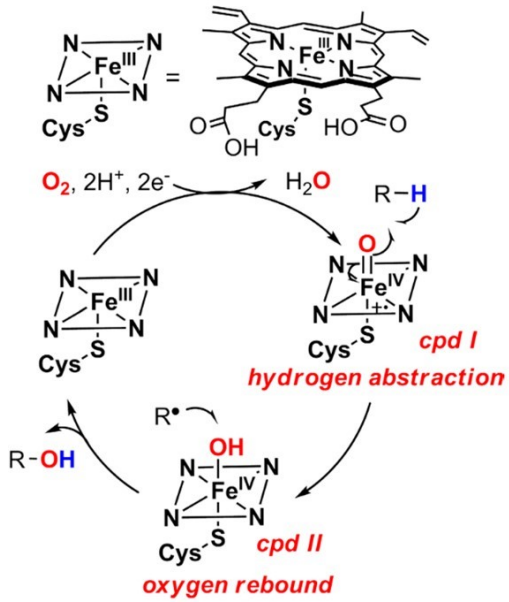

Figure 1.6 The hydrogen abstraction/oxygen "rebound" mechanism for cytochrome P450 (adapted from ref 15).

1.2.1.2 Peroxidases and catalases

Peroxidases and catalases which contain protoporphyrin IX as the heme prosthetic group are ubiquitous oxidoreductase heme enzymes. The heme structure is similar to CYP450s (Figure 1.5), and the difference is that peroxidases have a proximal axially

coordinated histidine residue while catalases accommodate a tyrosinate residue as an axial ligand (Figure 1.7).[38,39] Also, the structural differences between peroxidases and catalases are the distal side residues, in peroxidases His/Arg (H42/R38) and in catalases His/Asn (H56/N129) (Figure 1.7).[40]

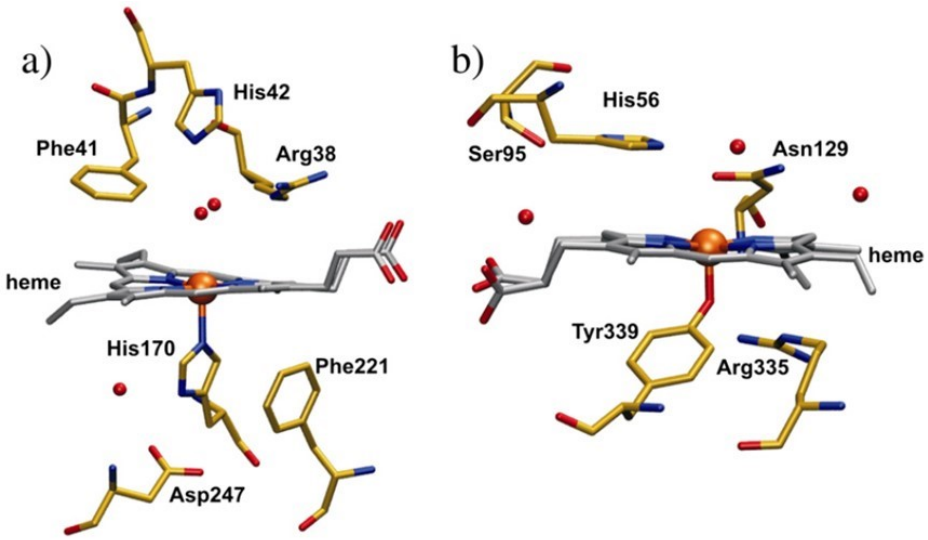

Figure 1.7 (a) Active site of peroxidases (PDB entry: 1ATJ). (b) active site of catalases (PDB entry: 2IQF) (adapted from ref 40).

Peroxidases and catalases catalyze the removal of hydrogen peroxide (H_2O_2) which is deleterious intermediate from the cells. Their catalysis reaction is initiated by the reduction of H_2O_2 to H_2O by heterolytic cleavage of the peroxide (HO–OH) bond, forming a $(P^{\bullet+})Fe^{IV}$=O, Cmpd I species (eq 5).[41] The main difference between peroxidases and catalases about catalytic reaction is the reactivity of Cmpd I. In peroxidases Cmpd I oxidizes one electron donating substrates forming high-valent iron(IV)-oxo ($(P)Fe^{IV}$–OH, compound II, Cmpd II) (eq 6). Subsequent reduction of Cmpd II by one electron reforms

$(P)Fe^{III}$ resting state enzyme giving water (eq 7). Catalases use Cmpd I to oxidize a second molecule of H_2O_2, forming dioxygen and water (eq 8). In other words, Cmpd I in peroxidases mediates substrate dehydrogenative oxidations, while for the catalases a second equiv of H_2O_2 is oxidized to dioxygen via disproportionation.

$$(P)Fe^{III} + H_2O_2 \longrightarrow (P^{\bullet+})Fe^{IV}{=}O + H_2O \quad (5)$$

$$(P^{\bullet+})Fe^{IV}{=}O + H^+ + e^- \longrightarrow (P)Fe^{IV}{-}OH \quad (6)$$

$$(P)Fe^{IV}{-}OH + H^+ + e^- \longrightarrow (P)Fe^{III} + H_2O \quad (7)$$

$$(P^{\bullet+})Fe^{IV}{=}O + H_2O_2 \longrightarrow (P)Fe^{III} + H_2O + O_2 \quad (8)$$

1.2.2 Heme-copper oxidases

More than 90% of O_2 consumption by living organisms is processed by heme-copper oxidases (HCOs) which are a large superfamily of integral membrane proteins that exist in eukaryotic mitochondria and some bacteria.[42] One subset of the HCOs superfamily includes Cytochrome *c* oxidase (C*c*O), which serves as a trans-membrane enzyme involved as the terminal oxidase of cell respiration.[18,43,44] C*c*O catalyzes the reduction of O_2 to H_2O (eq 9) in the respiratory chain of aerobic organisms using reduced cytochrome *c* as an electron donor. As shown in eq 9, a single molecule of dioxygen interacts with eight protons, four of which are taken up from the inner side of the membrane to form two water molecules, while the remaining four protons are diffused to the outer side of the membrane (Figure 1.8). The exergonic electron transfers are coupled to endergonic proton translocation processes across the membrane, thus creating an electrochemical proton gradient that drives ATP generation.[45–49]

$$8H^{+}_{in} + 4e^{-} + O_2 \rightarrow 4H^{+}_{out} + 2H_2O \quad (9)$$

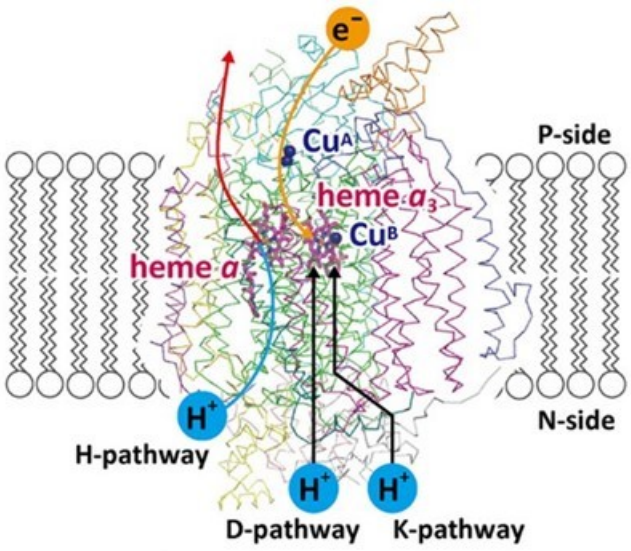

Figure 1.8 Proton and electron transport pathways of cytochrome *c* oxidase (adapted from ref 50).

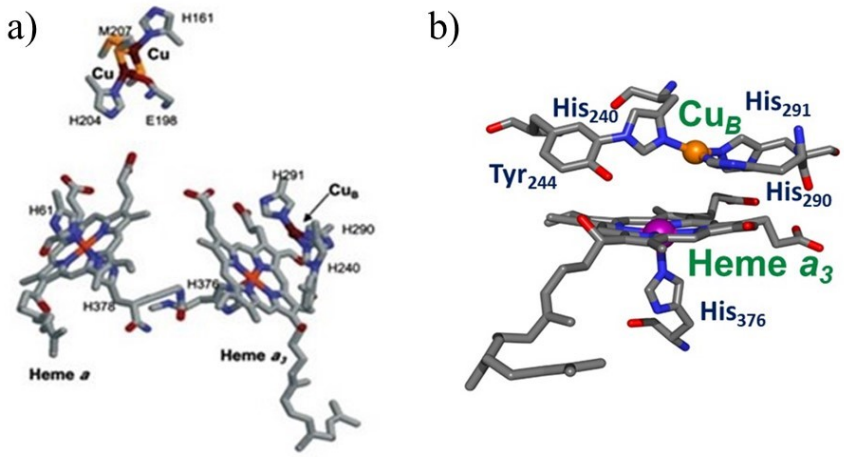

Figure 1.9 (a) X-ray structures of the redox-active metal sites of bovine heart cytochrome *c* oxidase.[51] (b) active site of cytochrome *c* oxidase from bovine heart in the reduced state (adapted from ref 49).

As shown in Figure 1.9a, cytochrome *c* oxidase has four redox centers; Cu_A, heme *a* and heme a_3/Cu_B. In subunit II Cu_A which is a homodinuclear Cu dimer, acts as a one-electron redox center at the membrane surface. This center transfers electrons supplied from cytochrome *c* to heme *a* which is a low-spin bis-imidazole-ligated heme of subunit I. The six-coordinate heme *a* then passes the electrons to the high-spin heme a_3 center axially ligated by a proximal histidine. The two hemes (heme *a* and heme a_3) are linked through their axial histidine ligands: His(Fe_a)–Phe–His(Fe_{a3}). Heme a_3 is magnetically coupled to the Cu_B center, thus comprising of a binuclear active site where O_2 binds and is subsequently reduced. In the highest resolution crystal structure to-date,[50] the distance between the heme a_3 and Cu_B is 4.8 Å. The Cu_B ion is coordinated by three histidine residues (His-291, His-290, and His-240) one of which (His-240) is covalently cross-linked to a tyrosine residue (Tyr-244), likely a result of a post-translational modification (Figure 1.9b).[52–56]

During or subsequent to the process of synthesis, proteins undergo a variety of post-translational modifications (PTMs), which may involve covalent modification between amino acid side chains at protein active sites.[57] For example, a well-known and widely prevalent side chain cross-link is disulfide bond formation giving Cystine which is the oxidized dimer form of the amino acid. As such, the unique post-translationally modified covalent cross-link between nitrogen atom (N_ε) of a nearby histidine residue and carbon atom (C_β) of a tyrosine residue in C*c*O has been revealed by crystallographic studies of the active site. The crystal structure (Figure 1.9b) shows that one of the Cu_B ligands, His-240, is cross-linked to Tyr-244 and that cross-linked tyrosyl is optimally positioned to participate in dioxygen activation. During O_2 reduction catalysis, three of the electrons are

clearly provided by heme a_3/Cu_B binuclear center (BNC), where one additional electron must originate from elsewhere. In peroxidases and catalases, the source of a similar electron is often the heme macrocycle, but in C*c*O neither optical nor resonance Raman spectroscopy support the formation of porphyrin π-cation radical resulting from heme iron oxidation.[58] Thus, the most likely possibility of this additional electron source is an amino acid residue. On the basis of the proximity of the cross-linked tyrosine, it has been speculated that this residue could be the source of the fourth electron required for O–O bond cleavage. This post-translational linkage is postulated to play a critical functional role during the reduction of the heme-copper center. It is believed that the cross-link His-Tyr unit results in decreased pK_a value of the tyrosine–OH, facilitating the proton delivery and tyrosyl radical formation and increase the redox potential, based on model studies.[59–62] Also, it is proposed that the tyrosine-histidine cross-link stabilizes the precise geometry of the binuclear active site. In other words, in the absence of the His-Tyr cross-link, one of the histidines that is bound to Cu_B coordinates to the heme a_3, leaving the binuclear center severely disrupted, and rendering the enzyme inactive. Recently, it is proposed that Tyr is the source for both the proton and the electron to cleave O–O bond during the catalytic cycle of O_2 reduction. Despite these advances, the exact role of the His-Tyr cross-link still remains unclear.

1.3 References

(1) Borden, W. T.; Hoffmann, R.; Stuyver, T.; Chen, B. Dioxygen: What Makes This Triplet Diradical Kinetically Persistent? *J. Am. Chem. Soc.* **2017**, *139*, 9010–9018.

(2) Warren, J. J.; Tronic, T. A.; Mayer, J. M. Thermochemistry of Proton-Coupled Electron

Transfer Reagents and Its Implications. *Chem. Rev.* **2010**, *110*, 6961–7001.

(3) Kulkarni, A.; Siahrostami, S.; Patel, A.; Nørskov, J. K. Understanding Catalytic Activity Trends in the Oxygen Reduction Reaction. *Chem. Rev.* **2018**, *118*, 2302–2312.

(4) Pegis, M. L.; Wise, C. F.; Martin, D. J.; Mayer, J. M. Oxygen Reduction by Homogeneous Molecular Catalysts and Electrocatalysts. *Chem. Rev.* **2018**, *118*, 2340–2391.

(5) Savéant, J. M. Molecular Catalysis of Electrochemical Reactions. Mechanistic Aspects. *Chem. Rev.* **2008**, *108*, 2348–2378.

(6) Mittra, K.; Chatterjee, S.; Samanta, S.; Dey, A. Selective $4e^{-}/4H^{+}$ O_2 Reduction by an Iron(Tetraferrocenyl)Porphyrin Complex: From Proton Transfer Followed by Electron Transfer in Organic Solvent to Proton Coupled Electron Transfer in Aqueous Medium. *Inorg. Chem.* **2013**, *52*, 14317–14325.

(7) Gewirth, A. A.; Varnell, J. A.; Diascro, A. M. Nonprecious Metal Catalysts for Oxygen Reduction in Heterogeneous Aqueous Systems. *Chem. Rev.* **2018**, *118*, 2313–2339.

(8) Su, D. S.; Sun, G. Nonprecious-Metal Catalysts for Low-Cost Fuel Cells. *Angew. Chem. Int. Ed.* **2011**, *50*, 11570–11572.

(9) Zhang, W.; Lai, W.; Cao, R. Energy-Related Small Molecule Activation Reactions: Oxygen Reduction and Hydrogen and Oxygen Evolution Reactions Catalyzed by Porphyrin- and Corrole-Based Systems. *Chem. Rev.* **2017**, *117*, 3717–3797.

(10) Shao, M.; Chang, Q.; Dodelet, J. P.; Chenitz, R. Recent Advances in Electrocatalysts for Oxygen Reduction Reaction. *Chem. Rev.* **2016**, *116*, 3594–3657.

(11) Cracknell, J. A.; Vincent, K. A.; Armstrong, F. A. Enzymes as Working or Inspirational Electrocatalysts for Fuel Cells and Electrolysis. *Chem. Rev.* **2008**, *108*, 2439–

2461.

(12) Mano, N.; De Poulpiquet, A. O_2 Reduction in Enzymatic Biofuel Cells. *Chem. Rev.* **2018**, *118*, 2392–2468.

(13) Pau, M. Y. M.; Lipscomb, J. D.; Solomon, E. I. Substrate Activation for O_2 Reactions by Oxidized Metal Centers in Biology. *Proc. Natl. Acad. Sci. U. S. A.* **2007**, *104*, 18355–18362.

(14) Huang, X.; Groves, J. T. Oxygen Activation and Radical Transformations in Heme Proteins and Metalloporphyrins. *Chem. Rev.* **2018**, *118*, 2491–2553.

(15) Huang, X.; Groves, J. T. Beyond Ferryl-Mediated Hydroxylation: 40 Years of the Rebound Mechanism and C–H Activation. *J. Biol. Inorg. Chem.* **2017**, *22*, 185–207.

(16) McCann, S. D.; Stahl, S. S. Copper-Catalyzed Aerobic Oxidations of Organic Molecules: Pathways for Two-Electron Oxidation with a Four-Electron Oxidant and a One-Electron Redox-Active Catalyst. *Acc. Chem. Res.* **2015**, *48*, 1756–1766.

(17) Collman, J. P.; Fu, L. Synthetic Models for Hemoglobin and Myoglobin. *Acc. Chem. Res.* **1999**, *32*, 455–463.

(18) Collman, J. P.; Boulatov, R.; Sunderland, C. J.; Fu, L. Functional Analogues of Cytochrome *c* Oxidase, Myoglobin, and Hemoglobin. *Chem. Rev.* **2004**, *104*, 561–588.

(19) Schuth, N.; Mebs, S.; Huwald, D.; Wrzolek, P.; Schwalbe, M.; Hemschemeier, A.; Haumann, M. Effective Intermediate-Spin Iron in O_2-Transporting Heme Proteins. *Proc. Natl. Acad. Sci. U. S. A.* **2017**, *114*, 8556–8561.

(20) Ohta, T.; Liu, J. G.; Naruta, Y. Resonance Raman Characterization of Mononuclear Heme-Peroxo Intermediate Models. *Coord. Chem. Rev.* **2013**, *257*, 407–413.

(21) Moody, P. C. E.; Raven, E. L. The Nature and Reactivity of Ferryl Heme in

Compounds I and II. *Acc. Chem. Res.* **2018**, *51*, 427–435.

(22) Dey, A.; Ghosh, A. "True" Iron(V) and Iron(VI) Porphyrins: A First Theoretical Exploration. *J. Am. Chem. Soc.* **2002**, *124*, 3206–3207.

(23) Fujii, H. Electronic Structure and Reactivity of High-Valent Oxo Iron Porphyrins. *Coord. Chem. Rev.* **2002**, *226*, 51–60.

(24) Omura, T.; Sato, R. Liver Microsomes Spermidine in the Extraction of the Deoxyribosyl-Synthesizing System from Escherichia. *J. Biol. Chem.* **1962**, *237*, 1375–1376.

(25) Denisov, I. G.; Makris, T. M.; Sligar, S. G.; Schlichting, I. Structure and Chemistry of Cytochrome P450. *Chem. Rev.* **2005**, *105*, 2253–2277.

(26) Shaik, S.; Hirao, H.; Kumar, D. Reactivity Patterns of Cytochrome P450 Enzymes : Multifunctionality of the Active Species , and the Two States – Two Oxidants Conundrum. *Nat. Prod. Rep.* **2007**, *24*, 533–552.

(27) Song, W. J.; Ryu, Y. O.; Song, R.; Nam, W. Oxoiron (IV) Porphyrin π-Cation Radical Complexes with a Chameleon Behavior in Cytochrome P450 Model Reactions. *J. Biol. Inorg. Chem.* **2005**, *10*, 294–304.

(28) Sono, M.; Roach, M. P.; Coulter, E. D.; Dawson, J. H. Heme-Containing Oxygenases. *Chem. Rev.* **1996**, *96*, 2841–2887.

(29) Meunier, B.; de Visser, S. P.; Shaik, S. Mechanism of Oxidation Reactions Catalyzed by Cytochrome P450 Enzymes. *Chem. Rev.* **2004**, *104*, 3947–3980.

(30) Shaik, S.; Kumar, D.; de Visser, S. P.; Altun, A.; Thiel, W. Theoretical Perspective on the Structure and Mechanism of Cytochrome P450 Enzymes. *Chem. Rev.* **2005**, *105*, 2279–2328.

(31) Ortiz de Montellano, P. R. Hydrocarbon Hydroxylation by Cytochrome P450 Enzymes. *Chem. Rev.* **2010**, *110*, 932–948.

(32) Shaik, S.; Cohen, S.; Wang, Y.; Chen, H.; Kumar, D.; Thiel, W. P450 Enzymes: Their Structure, Reactivity, and Selectivity-Modeled by QM/MM Calculations. *Chem. Rev.* **2010**, *110*, 949–1017.

(33) Poulos, T. L. Heme Enzyme Structure and Function. *Chem. Rev.* **2014**, *114*, 3919–3962.

(34) McQuarters, A. B.; Wolf, M. W.; Hunt, A. P.; Lehnert, N. 1958–2014: After 56 Years of Research, Cytochrome P450 Reactivity Is Finally Explained. *Angew. Chem., Int. Ed.* **2014**, *53*, 4750–4752.

(35) Krest, C. M.; Onderko, E. L.; Yosca, T. H.; Calixto, J. C.; Karp, R. F.; Livada, J.; Rittle, J.; Green, M. T. Reactive Intermediates in Cytochrome P450 Catalysis. *J. Biol. Chem.* **2013**, *288*, 17074–17081.

(36) Dubey, K. D.; Shaik, S. Cytochrome P450-The Wonderful Nanomachine Revealed through Dynamic Simulations of the Catalytic Cycle. *Acc. Chem. Res.* **2019**, *52*, 389–399.

(37) Groves, J. T.; McClusky, G. A.; White, R. E.; Coon, M. J. Aliphatic Hydroxylation by Highly Purified Liver Microsomal Cytochrome P-450. Evidence for a Carbon Radical Intermediate. *Biochem. Biophys. Res. Commun.* **1978**, *81*, 154–160.

(38) Adam, S. M.; Wijeratne, G. B.; Rogler, P. J.; Diaz, D. E.; Quist, D. A.; Liu, J. J.; Karlin, K. D. Synthetic Fe/Cu Complexes: Toward Understanding Heme-Copper Oxidase Structure and Function. *Chem. Rev.* **2018**, *118*, 10840–11022.

(39) Roth, J. P.; Cramer, C. J. Direct Examination of H_2O_2 Activation by a Heme Peroxidase. *J. Am. Chem. Soc.* **2008**, *130*, 7802–7803.

(40) Vidossich, P.; Alfonso-Prieto, M.; Rovira, C. Catalases versus Peroxidases: DFT Investigation of H_2O_2 Oxidation in Models Systems and Implications for Heme Protein Engineering. *J. Inorg. Biochem.* **2012**, *117*, 292–297.

(41) Alfonso-Prieto, M.; Biarnés, X.; Vidossich, P.; Rovira, C. The Molecular Mechanism of the Catalase Reaction. *J. Am. Chem. Soc.* **2009**, *131*, 11751–11761.

(42) Wikström, M.; Krab, K.; Sharma, V. Oxygen Activation and Energy Conservation by Cytochrome *c* Oxidase. *Chem. Rev.* **2018**, *118*, 2469–2490.

(43) Yoshikawa, S.; Shimada, A. Reaction Mechanism of Cytochrome *c* Oxidase. *Chem. Rev.* **2015**, *115*, 1936–1989.

(44) Kaila, V. R. I.; Verkhovsky, M. I.; Wikstro, M. Proton-Coupled Electron Transfer in Cytochrome Oxidase. *Chem. Rev.* **2010**, *110*, 7062–7081.

(45) Marten K. F. Wikstrom. Proton Pump Coupled to Cytochrome *c* Oxidase in Mitochondria. *Nature* **1977**, *266*, 271–273.

(46) Ferguson-Miller, S.; Babcock, G. T. Heme / Copper Terminal Oxidases. *Chem. Rev.* **1996**, *96*, 2889−2907.

(47) Babcock, G. T. How Oxygen Is Activated and Reduced in Respiration. *Proc. Natl. Acad. Sci. U. S. A.* **1999**, *96*, 12971–12973.

(48) Solomon, E. I.; Heppner, D. E.; Johnston, E. M.; Ginsbach, J. W.; Cirera, J.; Qayyum, M.; Kieber-Emmons, M. T.; Kjaergaard, C. H.; Hadt, R. G.; Tian, L. Copper Active Sites in Biology. *Chem. Rev.* **2014**, *114*, 3659–3853.

(49) Quist, D. A.; Diaz, D. E.; Liu, J. J.; Karlin, K. D. Activation of Dioxygen by Copper Metalloproteins and Insights from Model Complexes. *J. Biol. Inorg. Chem.* **2017**, *22*, 253–288.

(50) Shimada, A.; Etoh, Y.; Kitoh-Fujisawa, R.; Sasaki, A.; Shinzawa-Itoh, K.; Hiromoto, T.; Yamashita, E.; Muramoto, K.; Tsukihara, T.; Yoshikawa, S. X-Ray Structures of Catalytic Intermediates of Cytochrome *c* Oxidase Provide Insights into Its O_2 Activation and Unidirectional Proton-Pump Mechanisms. *J. Biol. Chem.* **2020**, *295*, 5818–5833.

(51) Kim, E.; Chufa, E. E.; Kamaraj, K.; Karlin, K. D. Synthetic Models for Heme − Copper Oxidases. *Chem. Rev.* **2004**, *104*, 1077–1133.

(52) Das, T. K.; Pecoraro, C.; Tomson, F. L.; Gennis, R. B.; Rousseau, D. L. The Post-Translational Modification in Cytochrome *c* Oxidase Is Required to Establish a Functional Environment of the Catalytic Site. *Biochemistry* **1998**, *37*, 14471–14476.

(53) Liu, X.; Yu, Y.; Hu, C.; Zhang, W.; Lu, Y.; Wang, J. Significant Increase of Oxidase Activity through the Genetic Incorporation of a Tyrosine-Histidine Cross-Link in a Myoglobin Model of Heme-Copper Oxidase. *Angew. Chem. Int. Ed.* **2012**, *51*, 4312–4316.

(54) Ravikiran, B.; Mahalakshmi, R. Unusual Post-Translational Protein Modifications: The Benefits of Sophistication. *RSC Adv.* **2014**, *4*, 33958–33974.

(55) Davidson, V. L. Protein-Derived Cofactors Revisited: Empowering Amino Acid Residues with New Functions. *Biochemistry* **2018**, *57*, 3115–3125.

(56) Lin, Y. W. Structure and Function of Heme Proteins Regulated by Diverse Post-Translational Modifications. *Arch. Biochem. Biophys.* **2018**, *641*, 1–30.

(57) Uchida, T.; Mogi, T.; Nakamura, H.; Kitagawa, T. Role of Tyr-288 at the Dioxygen Reduction Site of Cytochrome Bo Studied by Stable Isotope Labeling and Resonance Raman Spectroscopy. *J. Biol. Chem.* **2004**, *279*, 53613–53620.

(58) Cappuccio, J. A.; Ayala, I.; Elliott, G. I.; Szundi, I.; Lewis, J.; Konopelski, J. P.; Barry, B. A.; Einarsdóttir, Ó. Modeling the Active Site of Cytochrome Oxidase: Synthesis and

Characterization of a Cross-Linked Histidine-Phenol. *J. Am. Chem. Soc.* **2002**, *124*, 1750–1760.

(59) Aki, M.; Ogura, T.; Naruta, Y.; Le, T. H.; Sato, T.; Kitagawa, T. UV Resonance Raman Characterization of Model Compounds of Tyr244 of Bovine Cytochrome *c* Oxidase in Its Neutral, Deprotonated Anionic, and Deprotonated Neutral Radical Forms: Effects of Covalent Binding between Tyrosine and Histidine. *J. Phys. Chem. A* **2002**, *106*, 3436–3444.

(60) Gorbikova, E. A.; Belevich, I.; Wikström, M.; Verkhovsky, M. I. The Proton Donor for O–O Bond Scission by Cytochrome *c* Oxidase. *Proc. Natl. Acad. Sci. U. S. A.* **2008**, *105*, 10733–10737.

(61) McCauley, K. M.; Vrtis, J. M.; Dupont, J.; Van Der Donk, W. A. Insights into the Functional Role of the Tyrosine-Histidine Linkage in Cytochrome *c* Oxidase. *J. Am. Chem. Soc.* **2000**, *122*, 2403–2404.

(62) Pratt, D. A.; Pesavento, R. P.; Van Der Donk, W. A. Model Studies of the Histidine-Tyrosine Cross-Link in Cytochrome *c* Oxidase Reveal the Flexible Substituent Effect of the Imidazole Moiety. *Org. Lett.* **2005**, *7*, 2735–2738.

Chapter 2

Isocyanide or Nitrosyl Complexation to Hemes with Varying Tethered Axial Base Ligand Donors: Synthesis and Characterization

---

This work was co-authored with the following authors and is published under the following citation:

Savita K. Sharma[1], Hyun Kim[1], Patrick J. Rogler[1], Maxime Siegler[1], Kenneth D. Karlin[1]

[1]Department of Chemistry, The Johns Hopkins University, Baltimore, MD 21218, USA

J. Biol. Inorg. Chem. **2016**, *21*, 729–743

2.1 Introduction

Heme proteins participate in critical and diverse biological functions which include electron-transfer, catalysis and signaling. For the latter two subjects, small molecule diatomic gases are often involved, such as O_2, NO and CO.[1,2] There exist classes of proteins which serve to discriminate between these molecules for purposes including detection, signaling and/or function.[3,4] For molecular oxygen, roles include storage-transfer, or activation of O_2 for substrate oxidation or oxygenation chemistries.[5] Nitric oxide (nitrogen monoxide) is a signaling molecule[6] such as in its interaction with the heme center in guanylate cyclase, wherein binding leads to a signaling cascade resulting in smooth muscle relaxation.[7–14] Carbon monoxide is also a diatomic gas which is biosynthesized through heme O_2-activation chemistry (i.e., in heme oxygenases);[15–17] CO can also act in biological signaling via heme protein binding.[18]

In the history of the study of O_2 interactions with hemoproteins, the investigation of the binding of diatomic surrogate ligands, mainly CO and NO, has received considerable attention. These have been utilized as structural models, but also are useful in the study of ligand binding dynamics and electronic structure of the ligated reduced hemes.[19–23] For example, CO bound hemes are amenable to vibrational spectroscopic analyses, along with CO-photoejection and CO re-binding study.[21–24] As well, reduced hemes with NO bound are active for EPR spectroscopic interrogation. The replacement of CO with isocyanide (RNC:) ligands has also been found to be a useful probe to investigate vibrational spectroscopy and binding kinetics or heme-ligand photodissociation and time resolved rebinding. The strong isocyanide N–C triple-bond stretching vibration can be monitored, whereas variation in the size or nature of the isocyanide R-group, e.g., R = aryl vs –Me or

–*t*Bu, provides insights concerning steric effects or issues of small ligand binding to iron relative to the size or shape of a protein active-site pocket.[25–30]

One of our research group's major foci has been and continues to be the study of dioxygen binding and reduction at heme-copper heterobinuclear metal ion centers.[31] We seek to determine how neighboring copper-ligand moieties influence the binding of O_2 to hemes, and in a complementary manner see how hemes affect O_2 binding to copper ion in varying ligand environments. Then, as such synthetic heme-O_2-Cu assemblies can be compared and related to the active-site chemistry of heme-copper oxidases which bind and reduce O_2 to two water molecules (while also translocating protons through a mitochondrial membrane which downstream facilitates ATP biosynthesis), we are interested in elucidating detailed insights into the O–O reductive cleavage process, as a function of the exact nature (structure and electronics/bonding behavior) of the heme, the copper-ligand and the source of electrons ($E°$ value) and protons (pK_a). Additional factors include heme or copper-ligand electron-donating ability (and thus the Fe^{III}/Fe^{II} and/or Cu^{II}/Cu^{I} $E°$ value), nature of porphyrinate peripheral groups and/or copper-ligand denticity and their possible steric influences or affects upon the entire heme-O_2-Cu(ligand) structure, for example the Fe···Cu distance in the heme-O_2-Cu assembly.[31–35]

A specific example of such a synthetic construct is shown in Figure 2.1, where also an added heme axial 'base', dicyclohexylimidazole (DCHIm), is present.[35,36] As anticipated, the structural, spectroscopic properties and reactivity of this and other such assemblies significantly depend on the detailed nature of the heme, the copper ligand, the axial base, etc., as mentioned above.[31,36]

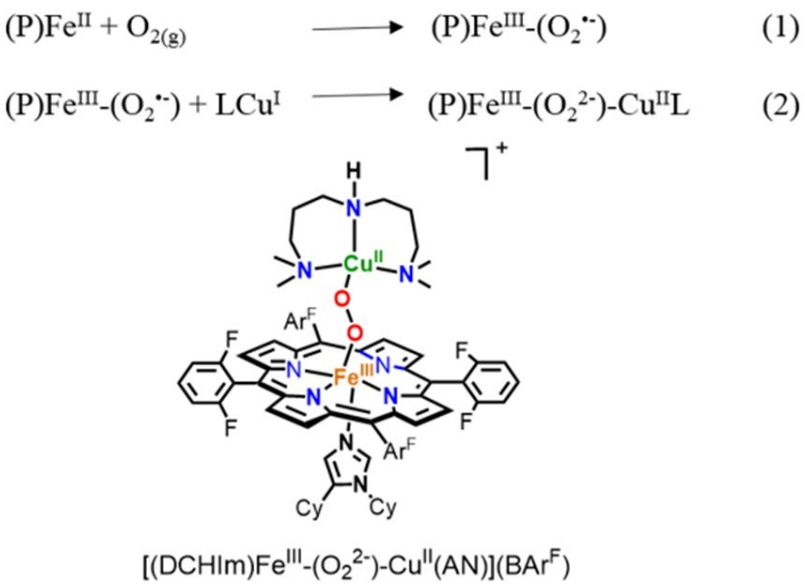

Figure 2.1 Synthetic steps involved in generation of a low-spin heme-peroxo-copper complex.

As such, it is critical that complementary investigations be carried out on surrogate ligand binding to the various components of our assemblies. One such aspect is the investigation of O_2, CO, NO and/or RNC binding to varying designed porphyrinoids, wherein the axial base ligand is varied between a weak O-donor (as solvent) such as tetrahydrofuran (THF), or N-donor ligands such as DCHIm (Figure 2.2) or a covalently linked imidazolyl or pyridyl ligand. To better our understanding of the chemistry of full heme-O_2-Cu assemblies, it is very useful to understand the structural aspects, physical properties and reactivity patterns of just these heme-containing moieties with varying axial ligand base, with O_2, CO, NO and RNC's. In fact, some of this information has been obtained and previously published, in particular for heme-O_2 (Fe^{III}-superoxide) complexes, for four of the five species shown in Figure 2.2.[37,38] Also, some of the related (heme)Fe^{II}-CO and (heme)Fe^{II}-NO compounds have also been described.[37] Here, we report on advances made from the study of new (heme)Fe^{II} derived adducts with 2,6-dimethylphe-

nyl isocyanide (DIMPI) along with nitric oxide, using the F_8, P^{Im}, P^{Py} and a brand new heme P^{ImH} possessing a covalently linked histamine moiety, see Figure 2.2 and equations 3 & 4. New insights have been obtained based on the X-ray structures and physical properties which are described and also compared with corresponding adducts using F_8, which does not incorporate a tethered axial ligand.

$$(P)Fe^{II} + DIMPI \longrightarrow (P)Fe^{II}\text{-}DIMPI \qquad (3)$$

$$(P)Fe^{II} + {\bullet}NO_{(g)} \longrightarrow (P)Fe^{II}\text{-}NO \qquad (4)$$

$$(P) = F_8,\ P^{Py},\ P^{Im},\ P^{ImH}$$

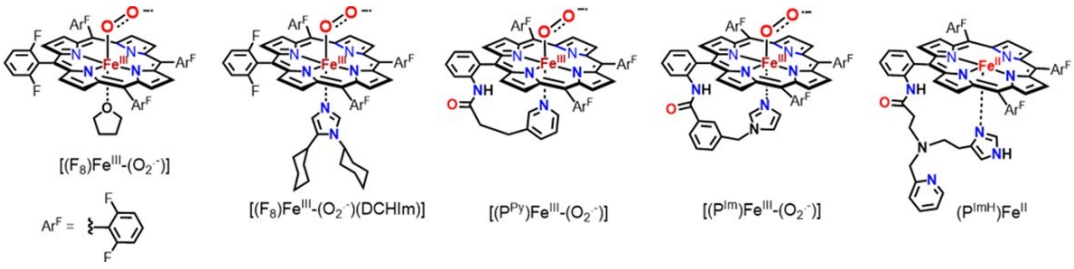

Figure 2.2 Ferric heme-superoxide complexes previously characterized and a new five-coordinate ferrous species.

2.2 Results and discussion

2.2.1 Stable heme-isocyanide complex formation

DIMPI reacts immediately with the reduced synthetic ferrous-heme complexes, $[(F_8)Fe^{II}]$, $[(P^{Py})Fe^{II}]$, $[(P^{Im})Fe^{II}]$ and $[(P^{ImH})Fe^{II}]$ (Scheme 2.1) to yield six-coordinate low-spin ferrous heme isonitrile species, as shown in Schemes 2.2 and 2.3.

Scheme 2.1 Steps involved in the synthesis of the (P^{ImH})Fe^{II} (**4**) complex

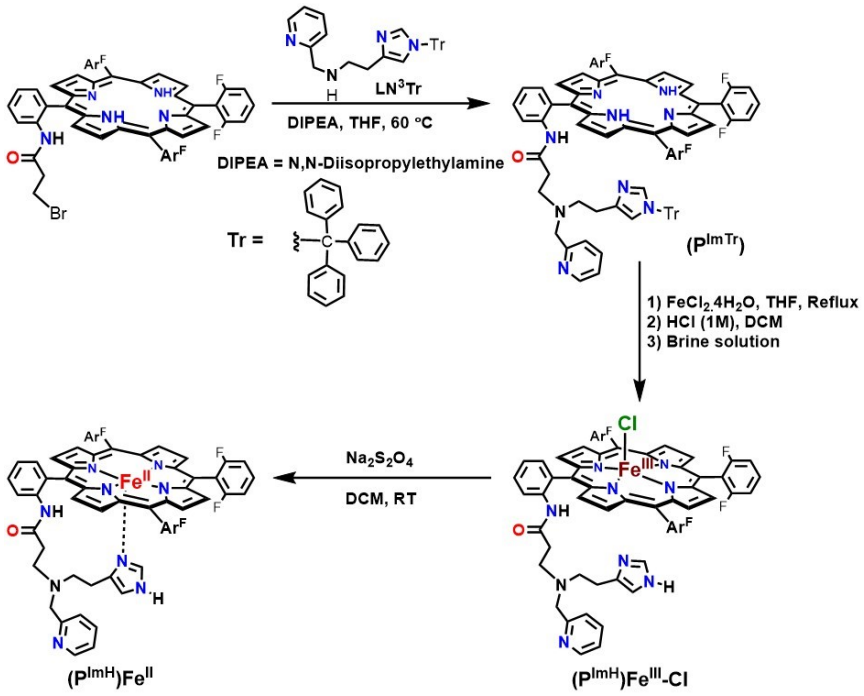

Scheme 2.2 Generation of bis-isocyanide ferrous heme complex, (**1**)-DIMPI at room temperature

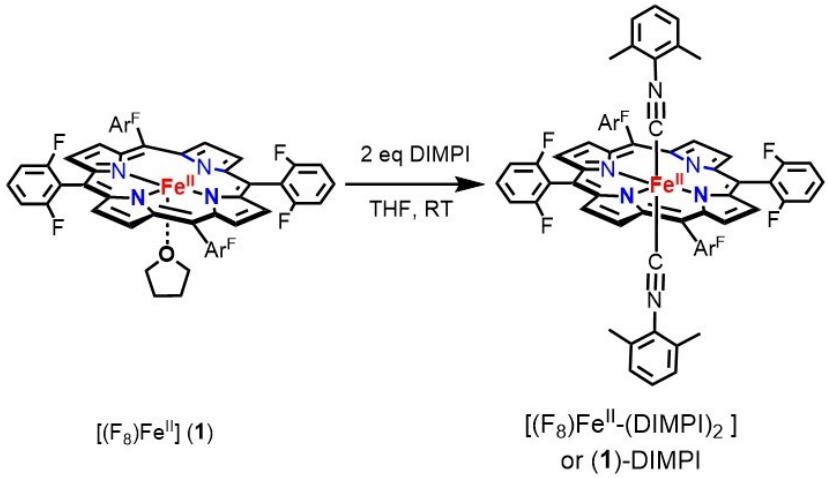

Scheme 2.3 Generation of six-coordinate ferrous heme isocyanide complexes; (**2**), (**3**) and (**4**)-DIMPI

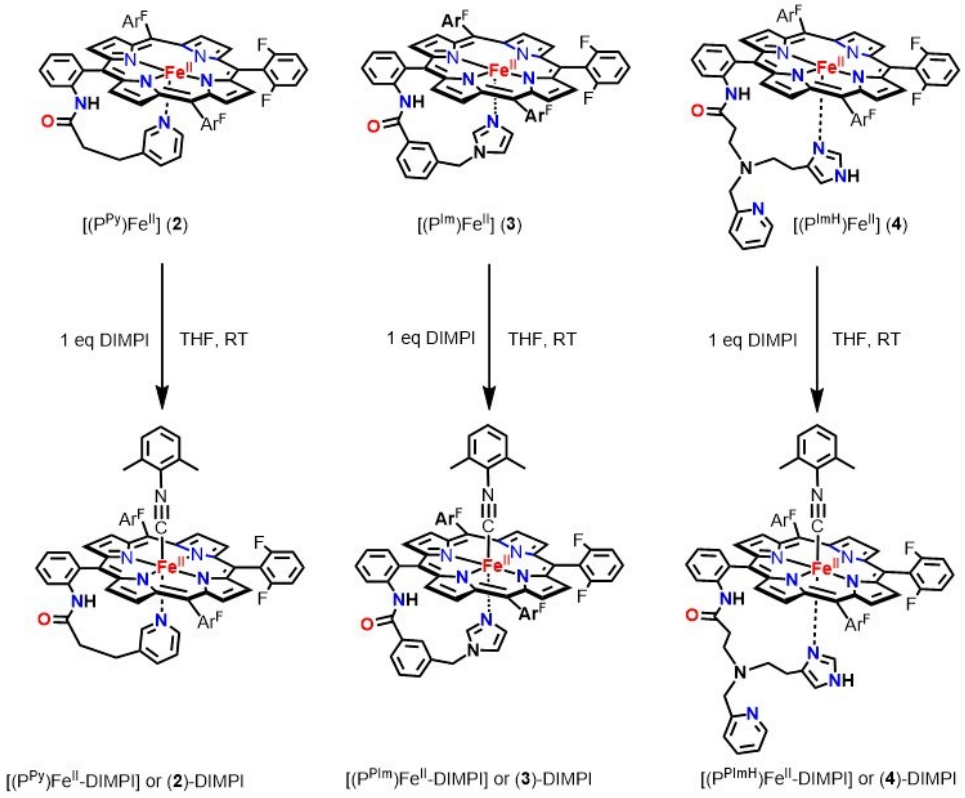

2.2.1.1 Generation of bis-isocyanide-porphyrin complex [$(F_8)Fe^{II}$-$(DIMPI)_2$]

When one equivalent DIMPI is added to a THF solution of [$(F_8)Fe^{II}$] at room temperature, a new UV-Vis peak at 430 nm is observed, but the absorption at 422 nm characteristic of the starting complex still remains. However, addition of another equivalent of DIMPI leads to the full formation of the 430 nm peak in the Soret region (Figure 2.3 and Scheme 2.2). Additional DIMPI added to the solution does not change the UV-Vis spectral features. Based on these observations, we postulate that two DIMPI molecules are bound to the Fe^{II} center, as also confirmed by integration of peaks in the ^{1}H-NMR spectrum of [$(F_8)Fe^{II}$-$(DIMPI)_2$]. Similar UV-Vis spectral features were observed for a structurally characterized bis-isocyanide iron(II) complex with tetraphenylporphyrin (TPP),

[(TPP)Fe^{II}-(*t*BuNC)$_2$].[39] The reactivity of DIMPI with reduced synthetic hemes is similar to that in general and previously observed for carbon monoxide (CO) as the heme ligand.[37,40] Complex (**1**)-DIMPI was further characterized by FT-IR spectroscopy where a single $\nu_{(C\equiv N)}$ stretch is observed at 2124 cm^{-1} (*vide infra*, Figure 2.4, Table 2.1), as would be expected for this highly symmetric compound, even with the presence of two DIMPI ligands per molecule. Also, the ^{19}F-NMR spectrum of (**1**)-DIMPI shows one sharp absorbance at –109.0 ppm for the *o*-difluoro substituted phenyl rings of the F_8 porphyrin.[41]

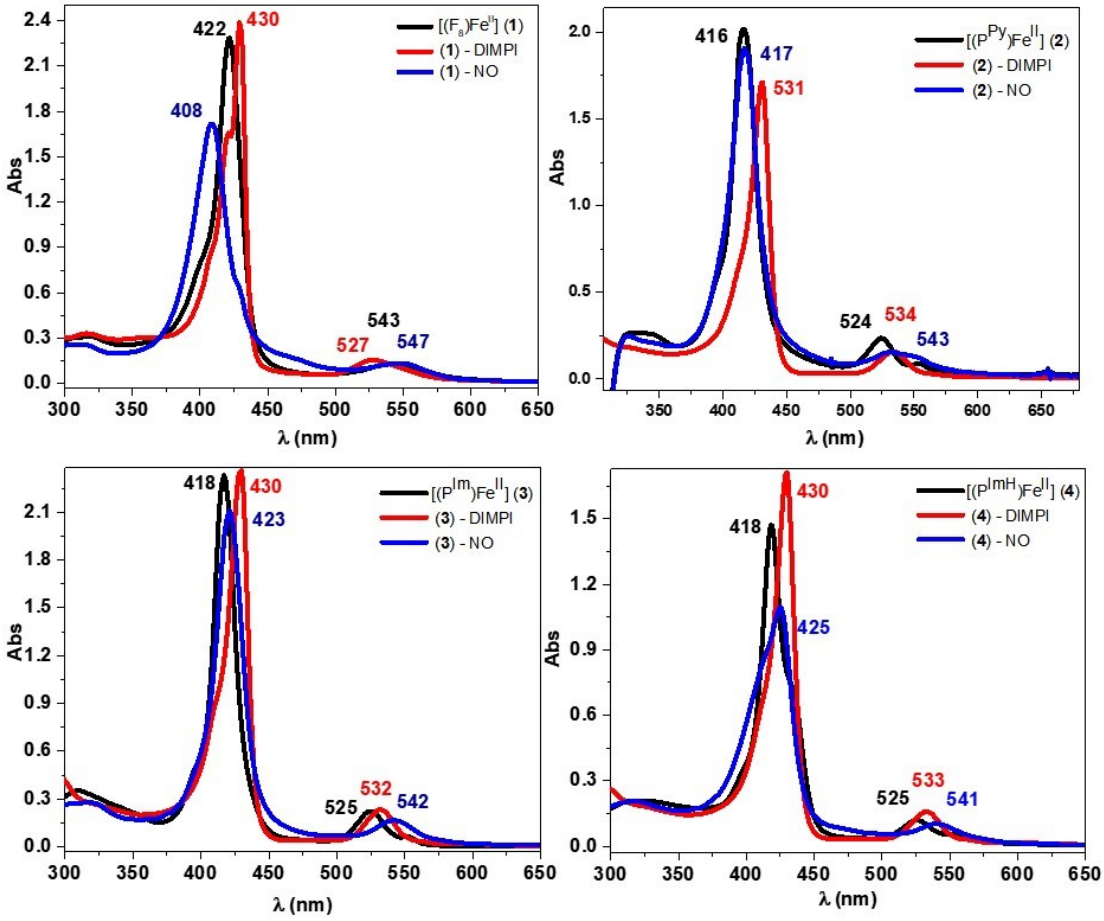

Figure 2.3 UV-Vis spectroscopic data for the ferrous DIMPI and NO complexes of (**1**), (**2**), (**3**), and (**4**) in THF at room temperature. **Black**-reduced Fe^{II} species; **Red**-Fe^{II}-DIMPI and **Blue**-Fe^{II}-NO complexes.

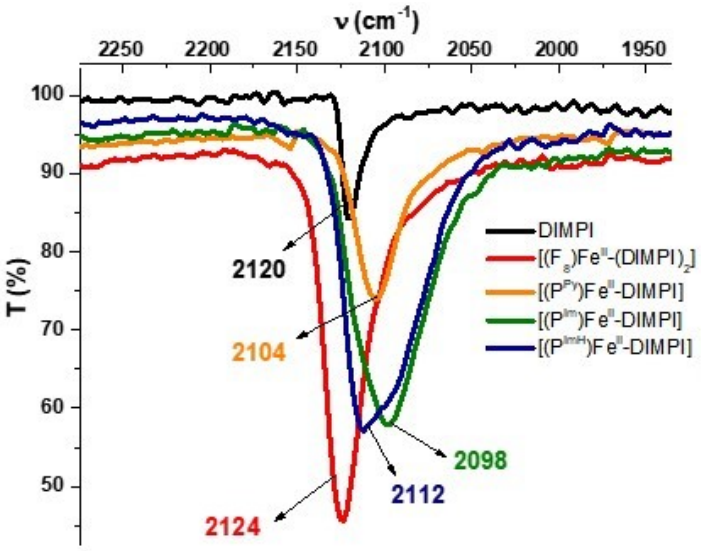

Figure 2.4 Solid state FT-IR spectra for Fe^{II}-DIMPI complexes of (**1**), (**2**), (**3**), and (**4**).

Table 2.1 Properties of ferrous heme-DIMPI and ferrous heme-NO model complexes

Compound	UV-Vis (nm)	IR (cm^{-1}) ν(C≡N) / ν(N–O)	EPR (*g* values)
$[(F_8)Fe^{II}\text{-}(DIMPI)_2]$	430	2124	Silent
$[(P^{Py})Fe^{II}\text{-}(DIMPI)]$	430	2104	Silent
$[(P^{Im})Fe^{II}\text{-}(DIMPI)]$	430	2098	Silent
$[(P^{ImH})Fe^{II}\text{-}(DIMPI)]$	430	2112	Silent
$[(F_8)Fe^{II}\text{-}NO]$	408	1688	2.09/2.01/1.99
$[(P^{Py})Fe^{II}\text{-}NO]$	417	1648	2.08/2.00/1.97
$[(P^{Im})Fe^{II}\text{-}NO]$	423	1650	2.07/2.00/1.97
$[(P^{ImH})Fe^{II}\text{-}NO]$	425	1650	2.07/1.99/1.95

2.2.1.2 Generation of six-coordinate (P^{Py}/P^{Im}/P^{ImH}) iron(II)-DIMPI complexes

$[(P^{Py})Fe^{II}]$ and $[(P^{Im})Fe^{II}]$ in THF solution at RT exhibit different structures in this solvent, as previously deduced by observation of the positions of NMR spectroscopic pyrrole resonances. $[(P^{Py})Fe^{II}]$ and $[(P^{Im})Fe^{II}]$ are both five-coordinate high-spin, the former at all temperatures between RT and –90 °C. However, at low temperature $[(P^{Im})Fe^{II}]$

is six-coordinate low-spin (S = 0), with the pyrrole resonances appearing in the diamagnetic region, indicating that both the imidazolyl group and a THF solvent molecule act as axial ligands.[37] The new complex [(P^{ImH})Fe^{II}] behaves similarly, at room temperature it is 5-coordinate high spin where the tethered imidazolyl is axially bound to the Fe^{II} center. This results in an asymmetry and four different pyrrole resonances appear in a ratio of 4 (δ_{ppm} 57.0) :2 (δ_{ppm} 49.0) :1 (δ_{ppm} 19.0, 15.7):1 (δ_{ppm} 8.30), see Figure 2.5. By contrast, at lower temperatures [(P^{ImH})Fe^{II}] forms a six-coordinate low spin (S = 0) species, again postulated to have both a THF and imidazole bound to the Fe^{II} center, as $\delta_{pyrrole}$ = 9.80 ppm, Figure 2.5.

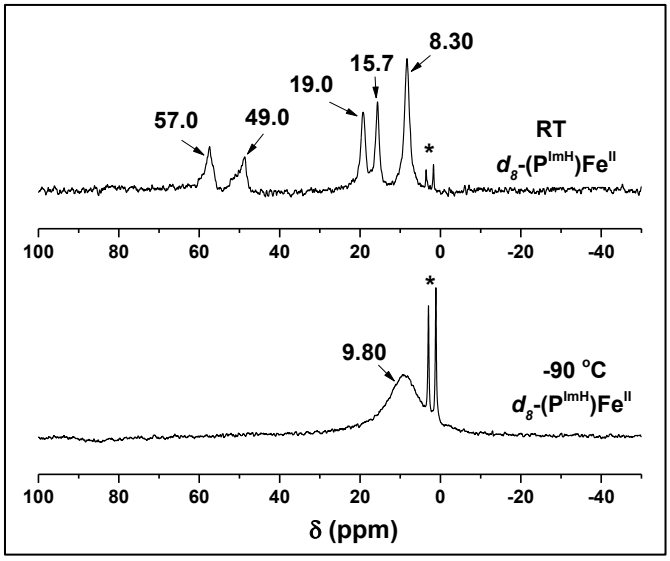

Figure 2.5 (top) ^{2}H-NMR spectra of heme Fe^{II} complex d_8-[(P^{ImH})Fe^{II}] in THF ($\delta_{pyrrole}$ = 57.0, 49.0, 19.0, 15.7, 8.30 ppm) at 293 K, (ratio of pyrrole-H is 1:1:2:4). (bottom) ^{2}H-NMR spectra of heme iron(II) complex d_8-[(P^{ImH})Fe^{II}] in THF ($\delta_{pyrrole}$ = 9.80 ppm) at 183 K. See main text for detail. (*) corresponds to solvent molecule THF.

Addition of one equivalent of DIMPI solution to each of the reduced Fe^{II} porphyrinates ([$(P^{Py})Fe^{II}$], [$(P^{Im})Fe^{II}$] and [$(P^{ImH})Fe^{II}$]) in THF at room temperature leads to a substantial change in the UV-Vis Soret region, with the formation of a band at 430 nm in all three cases. Additional equivalents of DIMPI do not yield any change in the UV-Vis spectra (Figure 2.3, Scheme 2.3). This may indicate that only one DIMPI molecule is bound to the iron(II) center axially while the covalently linked axial base imidazole/pyridine is coordinated to the Fe^{II} center giving an overall six-coordinate low-spin ferrous-DIMPI complex. These conclusions are borne out by the X-ray structures determined for complexes (**3**)-DIMPI and (**4**)-DIMPI (see below, Figure 2.6).

We have also carried out experiments to determine binding constants of DIMPI with the ferrous hemes with covalently attached axial ligand bases. Titrations with DIMPI were performed using $(P^{Py})Fe^{II}$ (**2**), $(P^{Im})Fe^{II}$ (**3**) and $(P^{ImH})Fe^{II}$ (**4**), and isosbestic behavior was seen for all the titrations (Figure 2.7). A plot of the absorbance at 430 nm versus [DIMPI] (Figure 2.7) reaches a maximum at ∼1 equiv of DIMPI, and no further spectral changes are observed with the addition of more DIMPI. Assuming that DIMPI reversibly binds to the ferrous heme complexes $(P^{Py})Fe^{II}$ (**2**), $(P^{Im})Fe^{II}$ (**3**) and $(P^{ImH})Fe^{II}$ (**4**) under equilibrium conditions, a good fit of the data can be obtained with a model for a one-to-one binding isotherm. This fit gives association constants (K_a) of $2.29 \times 10^7\ M^{-1}$, $1.19 \times 10^7\ M^{-1}$, and $1.29 \times 10^7\ M^{-1}$, for (**2**), (**3**), and (**4**), respectively. These values are comparable to those measured for DIMPI binding to hemoglobin (Hb) and myoglobin (Mb) [$K_a = 1.0 \times 10^8\ M^{-1}$]. The binding constant for complex (**2**)-DIMPI is 2-fold greater than (**3**)-DIMPI and (**4**)-DIMPI, which is consistent with a less strong binding of the pyridine axial base in (**2**)-DIMPI when compared to the imidazole and histamine containing complexes.

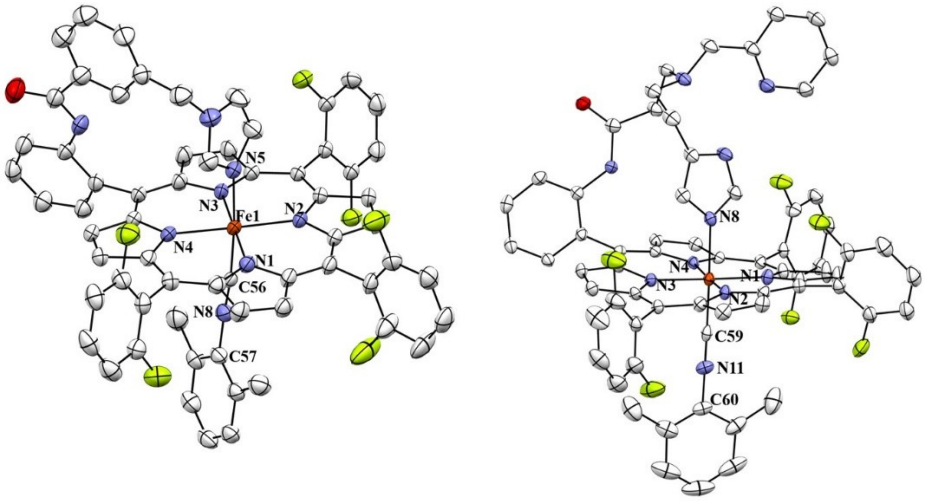

Figure 2.6 Displacement ellipsoid plots (50% probability level) of [(P^{Im})Fe^{II}-(DIMPI)] (left; **3**-DIMPI) and [(P^{ImH})Fe^{II}-(DIMPI)] (right; **4**-DIMPI), in both cases showing the imidazolyl and 2,6-dimethylphenyl isocyanide ligands bound to Fe(II) center. Lattice solvent molecules and H atoms have been omitted for the sake of clarity. Selected bond lengths and bond angles are reported in Table 2.3.

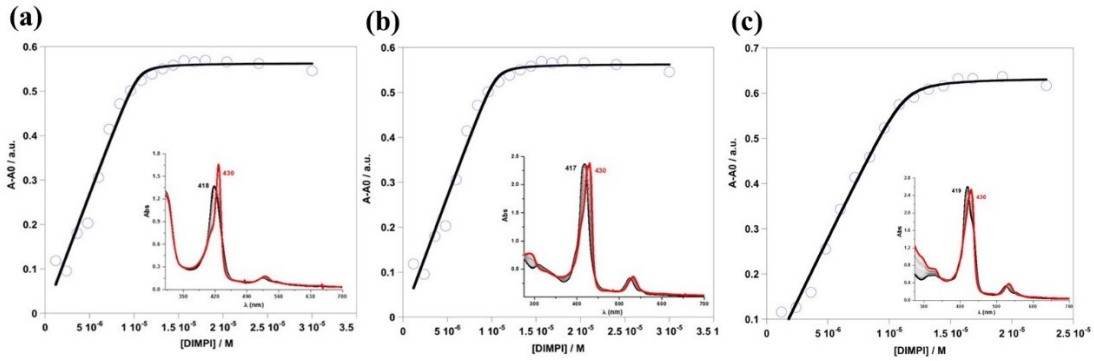

Figure 2.7 Binding isotherm at 430 nm resulting from the reaction of (a) (P^{Py})Fe^{II} (12 μM in 2.5 mL Tetrahydrofuran, THF, black) and DIMPI (red, (P^{Py})Fe^{II}-DIMPI). K_a = 2.29 x 10^7 M^{-1}; (b) (P^{Im})Fe^{II} (12 μM in 2.5 mL Tetrahydrofuran, THF, black) and DIMPI (red, (P^{Im})Fe^{II}-DIMPI). K_a = 1.19 x 10^7 M^{-1}; (c) (P^{ImH})Fe^{II} (12 μM in 2.5 mL Tetrahydrofuran, THF, black) and DIMPI (red, (P^{ImH})Fe^{II}-DIMPI). K_a = 1.29 x 10^7 M^{-1}. See main text for detailed discussion.

UV-vis Spectral Titrations for (P)Fe^{II} + DIMPI. To a solution of (P)Fe^{II} (12 μM, THF; P = P^{Py}, P^{Im}, P^{ImH}) was added 0.1 – 2.5 equiv of DIMPI in 0.1 equiv increments from a stock solution in THF. UV-vis spectrum was taken after each addition of DIMPI, showing isosbestic conversion of (P)Fe^{II} to (P)Fe^{II}-DIMPI. The reaction mixture was allowed to equilibrate fully until no further spectral change was observed prior to the next equivalent of DIMPI. A plot of the change in absorbance at 430 nm vs DIMPI resulted in the binding curve shown in Fig. S9 – S11 and could be well fit by a 1:1 binding model, eq 1–4. Using this equation, the best fit of the plot for P^{Py}, P^{Im} and P^{ImH} system gives K_a = 2.29 x 10^7 M^{-1}, 1.19 x 10^7 M^{-1} and 1.29 x 10^7 M^{-1}.

$$(P)Fe^{II} + DIMPI \rightleftharpoons (P)Fe^{II}\text{-}DIMPI \qquad (P) = P^{Py}, P^{Im}, P^{ImH} \tag{1}$$

$$K_a = \frac{[(P)Fe^{II}\text{-}DIMPI]}{[(P)Fe^{II}][DIMPI]} \tag{2}$$

$$\frac{(A - A_0)}{(\varepsilon_{FeII\text{-}DIMPI} - \varepsilon_{FeII})} = [(P)Fe^{II}\text{-}DIMPI] \tag{3}$$

$$[(P)Fe^{II}\text{-}DIMPI] = \frac{1}{2}\left[\left\{[DIMPI] + [(P)Fe^{II}]_i + \left(\frac{1}{Ka}\right)\right\} - \sqrt{\left([DIMPI] + [(P)Fe^{II}]_i + \left(\frac{1}{Ka}\right)\right)^2 - 4\,[DIMPI][(P)Fe^{II}]_i}\right] \tag{4}$$

2.2.2 Crystal structure of Isocyanide Complexes

In order to understand the similarities and differences in the coordination geometry of these Fe^{II}-DIMPI complexes, crystal structures of (**3**)-DIMPI and (**4**)-DIMPI were determined. The structures are depicted in Figure 2.6 and important structural parameters are listed in Tables 2.2 and 2.3. In both structures, the geometry around the iron is octahedral, where the 5th ligand is the covalently linked imidazole (or pyridine), while the 6th ligand is the isocyanide (DIMPI). The metal center lies in the porphyrinate plane. The observed bond distances and angles for both indicate very little strain within the linker arm. A slight perturbation from the expected linear Fe–C–N bond angle is seen for complex (**3**)-DIMPI, with a ∠Fe–C–N value of 173.8(4)°. This is notably less linear when compared with (**4**)-DIMPI where, ∠Fe–C–N, 179.3(3)° is nearly linear. This difference could arise due to crystal packing effects. The Fe–C(DIMPI) bond distances are *ca.* 1.82 Å for both **(3**)-DIMPI, and **(4**)-DIMPI. The Fe–N(imidazole) bond distances are *ca.* 2.02 Å, while the average Fe–N(porphyrin) bond distances are 1.99 Å, similar to our previously reported [$(F_8)Fe^{II}$]•2THF complex.[42] Both structures are well ordered except the difluorophenyl group and toluene solvent molecule in complex (**4**)-DIMPI, see Materials and Methods. These appear to be disordered over two orientations and can rotate slightly from perpendicularity with respect to the porphyrin plane. Lehnert and co-workers have previously published on a crystal structure of the Zn^{II} analogue, a five-coordinate complex with the P^{Im} ligand.[43]

Table 2.2 Crystallographic data for complex [(P^{Im})Fe^{II}-(DIMPI)] and [(P^{ImH})Fe^{II}-(DIMPI)]

Compounds	(**3**)-DIMPI	(**4**)-DIMPI • Toluene
FormulaWeight (g/mol)	1106.89	1271.13
T (K)	110(2)	110(2)
Crystal shape	small dark red plate ($0.11 \times 0.05 \times 0.02$ mm^3)	dark red plate ($0.15 \times 0.08 \times 0.03$ mm^3)
Space group	triclinic, *P*-1 (no. 2)	monoclinic, $P2_1/c$ (no. 14)
a (Å)	12.3852(6)	12.4643(2)
b (Å)	12.5816(6)	12.3010(2)
c (Å)	19.3657(12)	39.9319(8)
α (^{0})	104.424(5)	90
β (^{0})	95.293(4)	93.9552(18)
γ (^{0})	111.823(5)	90
V ($Å^3$)	2655.1(3)	6107.91(19)
Z	2	4
D_x (g cm^{-3})	1.385	1.382
μ (mm^{-1})	2.897	2.601
Absorption correction range	0.797–0.947	0.759–0.940
$(\sin \theta/\lambda)_{max}$ ($Å^{-1}$)	0.60	0.60
Total, Unique, and Observed Reflections	24276, 9448, 6441	40278, 11998, 8909
R_{int}	0.0467	0.0597
GOF	1.041	1.021
$R1/wR2$ [$I > 2\sigma(I)$]	0.0703/0.1902	0.0501/0.1089
$R1/wR2$	0.1038/0.2151	0.0760/0.1220
$\Delta\rho_{max}$, $\Delta\rho_{min}$, rms	1.126, –0.478, 0.083	0.644, –0.483, 0.054

Table 2.3 Selected bond lengths (Å) and bond angles (°) for (**3**)-DIMPI and (**4**)-DIMPI. Proposed H-bonds are also listed

Compound	(**3**)-DIMPI Bond length (Å)	Compound	(**4**)-DIMPI•Toluene Bond length (Å)
Fe – N1	1.998 (4)	Fe – N1	1.994 (2)
Fe – N2	2.000 (3)	Fe – N2	1.991 (2)
Fe – N3	1.990 (4)	Fe – N3	1.995 (2)
Fe – N4	2.001 (3)	Fe – N4	1.985 (2)
Fe – N5	2.034 (4)	Fe – N8	2.024 (2)
Fe – C56	1.824 (4)	Fe – C59	1.835 (3)
N8 – C56	1.163 (6)	N11 – C59	1.166 (3)
Compound	(**3**)-DIMPI Bond angle (^{0})	Compound	(**4**)-DIMPI•Toluene Bond angle (^{0})
N1 – Fe – N5	91.38 (15)	N1 – Fe – N8	85.99 (8)
N2 – Fe – N5	89.77 (15)	N2 – Fe – N8	89.90 (9)
N3 – Fe – N5	88.85 (15)	N3 – Fe – N8	91.10 (8)
N4 – Fe – N5	88.58 (14)	N4 – Fe – N8	89.03 (9)
N5 – Fe – C56	176.03 (16)	N8 – Fe – C59	177.61 (9)
Fe – C56 – N8	173.8 (4)	Fe – C59 – N11	179.3 (3)
Weak C–H···F interaction:	Bond Length(Å)/ Bond Angles (^{0})	Weak C–H···F interaction:	Bond Length(Å)/ Bond Angles (^{0})
F1···H64$_{methyl}$ (C64)	2.731/ (133.93)	F1···H35$_{py}$ (C35)	3.089/ (129.88)
F2···H7$_{pyrrole}$ (C7)	3.490 / (95.04)	F1···H40$_{imid}$ (C40)	2.914 / (135.45)
F3···H8$_{pyrrole}$ (C8)	2.966 / (95.57)	F2···H67$_{methyl}$ (C67)	3.148 / (146.75)
F4···H39$_{imid}$ (C39)	3.117 / (153.44)	F3···H12$_{pyrrole}$ (C12)	3.163 / (91.25)
F5···H2$_{pyrrole}$ (C2)	2.926 / (100.23)	F4···H8$_{pyrrole}$ (C8)	2.883 / (101.78)
F6···H41$_{imid}$ (C41)	2.991/ (166.53)	F5···H17$_{pyrrole}$ (C17)	2.903 / (100.89)
		F6···H66$_{methyl}$(C66)	2.539 / (176.34)
		N9H···N7$_{pyridine}$	1.986/ (173.74)

Other potentially important (from a structural perspective) observations obtained from the crystal structures of both complexes are that weak but noticeable intramolecular CH···F interactions occur, as shown in Figure 2.8 and listed in Table 2.3. The observed range of C–H···F interactions for our new structures lie between 2.73–3.08 Å, which is greater than the sum of reported Van der Waals radii for hydrogen and fluorine (approximately 2.3–2.5 Å). Based on reported structural observations and DFT calculations,[44] the very strong H-bonding ability of fluorine gives rise to such C–H···F

interactions which vary between ~ 2.7 to 3.1 Å , similar to what is observed for (**3**)-DIMPI, and (**4**)-DIMPI. Such literature examples of organic compounds with longer distance H···F interactions occur even where the CH···F angle lies in the range between 130° and 145° and even in some cases it is close to 100°.[44] Further comparisons may be made to examples of non-bonded CH···O contacts made between an O-atom in an Fe^{IV}-oxo complex with surrounding ligand methyl group H-atoms; there, short CH···O distances are observed (2.3 to 2.7 Å) while very acute CH···O angles are present (~ 100 – 109°).[45,46]

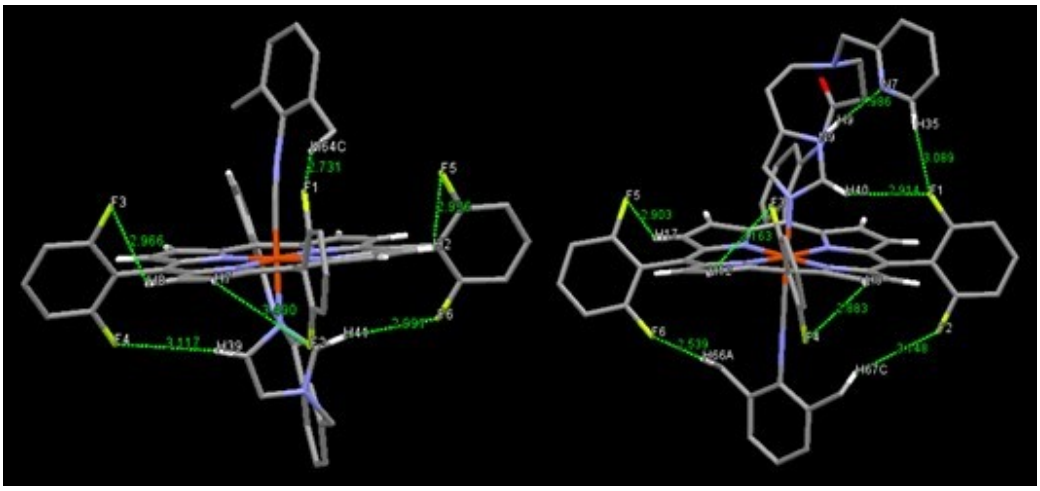

Figure 2.8 Crystal structures showing weak intramolecular CH···F interaction identified from the green lines shown. (Left) (**3**)-DIMPI and (Right) (**4**)-DIMPI. See text for further discussion.

With these precedents in mind, we postulate that in the solid state structure of (**3**)-DIMPI, a CH···F interaction occurs between the methyl group on the DIMPI ligand (H64C) and F1 from the proximate *o*-F aryl porphyrinate substituent, see the green line in the middle top of the (**3**)-DIMPI structure in Figure 2.8-left, and Figure 2.9(a); here the CH···F distance and angle are 2.73 Å and 134°, respectively (Table 2.3). A far closer to linear interaction occurs between F6 and H41 from the ligated imidazolyl group with a bond distance and angle of 2.99 Å and 167°, respectively (Table 2.3 and Figure 2.8, bottom right). Notice F6 and F5, on the same porphyrinate aryl group both H-bond, the latter to the pyrrole hydrogen atom (H2), this F5···H2C interaction is likely synergistic with F6···H41 interaction. Envisioning the iron atom as a kind-of pseudo center of symmetry, the F3 and F4 atoms on the left-hand *o*-F_2-phenyl ring forms two H-bonds, between F3···$H8_{pyrrole}$ (C8) and F4···$H39_{imid}$ (C39) (Table 2.3). The overall result is that the H-bonding interactions formed by the four F-atoms just described fixes the orientation of the imidazolyl axial ligand, which is already close to perpendicular to the porphyrinate plane, to be nearly coplanar with both of the aryl rings containing these F3, F4, F5 and F6 atoms {Notice how in viewing the structure of (**3**)-DIMPI (Figure 2.8, Left) that these two aryl rings and the imidazolyl ring seem to lie in the plane of the sheet.} This imidazole orientation could also lead to a close interaction of F2···$H7_{pyrrole}$ (C7) in the solution state (see ^{19}F-NMR spectroscopy, below), whereas in solid state structure this distance seems too long for this interaction to occur (Table 2.3).

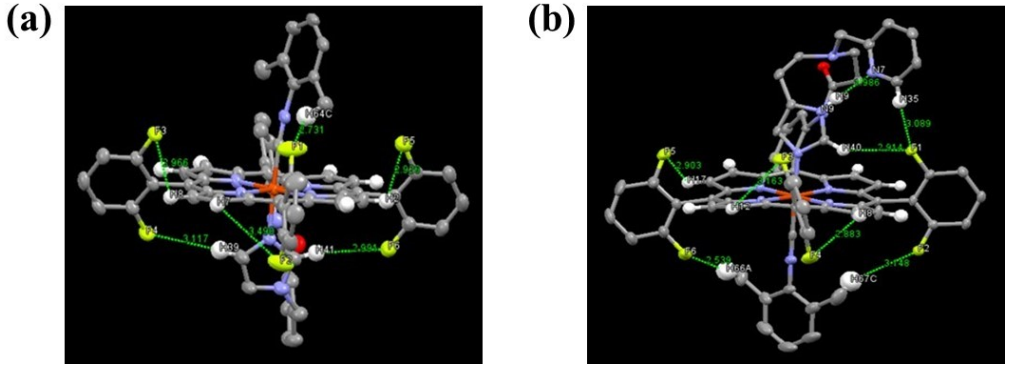

Figure 2.9 Crystal structure of (a) (**3**)-DIMPI and (b) (**4**)-DIMPI showing weak intramolecular CH…F interactions identified by the dotted green lines. See main text for detailed discussion.

Similarly, for (**4**)-DIMPI we observe close to linear CH…F interaction between a methyl group H-atom on the DIMPI ligand (H66) and F6 from the *o*-F porphyrinate aryl substituent, shown by the green dotted line on the lower left side of Figure 2.8-Right; here the CH···F distance and angle are 2.54 Å and 176°, respectively (Table 2.3 and Figure 2.8-right, also see Figure 2.9(b). The other methyl group on the DIMPI ligand likewise forms an H-bond, with the F2 atom on the aryl group to the lower right side of (**4**)-DIMPI, as shown in Figure 2.8, Right. To the left side (Figure 2.8, Right), the F5 atom, that on the same ring as F6, is involved in H-bonding to a pyrrole H-atom (H17) (Table 2.3). For F1, on the right hand aryl group, we postulate that multiple H…F interactions occur, to H40 from the ligated imidazolyl group as well as H35 from the dangling free pyridyl group, see the green lines to the upper right of the (**4**)-DIMPI structure in Figure 2.8-Right; here the CH···F distances and angles are 2.91 Å and 135° (F1···H40), and 3.08 Å and 130° (F1···H35), respectively. Tilting of the *o*-F_2-aryl group containing F3 and F4, allows for two H-bonds to form to pyrrole H-atoms (Table 2.3). Thus, all six fluorine atoms in (**4**)-DIMPI may participate in H-bonding. In part, we postulate that these solid-state interactions persist in

solution, as indicated by ^{19}F-NMR spectroscopy where almost all of the fluorine resonances exist as doublets due to H-atom coupling, as described below.

Another H-bond observed in this X-ray structure of (**4**)-DIMPI is a very strong one, between the H-atom on the uncoordinated N-atom of the imidazolyl group, to the N-atom of the dangling pyridine (Figure 2.8-Right). Here, the N9H···N7$_{pyridine}$ angle is near linear (173.7 °) with a N9H···N7 distance of 1.986 Å (and where N9···N7 = 2.863 Å) (Table 2.3).

Complexes (**2**)-DIMPI, (**3**)-DIMPI and (**4**)-DIMPI were also characterized by FT-IR spectroscopy (Figure 2.4, Table 2.1). The IR spectrum for (**1**)-DIMPI shows a single sharp $\nu_{(C\equiv N)}$ band (2124 cm^{-1}), corresponding to the absorption for both isonitrile ligands in [$(F_8)Fe^{II}$-$(DIMPI)_2$], which is shifted 4 cm^{-1} higher in energy relative to the stretching frequency of the uncomplexed ligand. The shift to higher energy is relatively small and could be attributed to a ligand (σ_{NC}) to metal (d_σ) interaction, consistent with the expected behavior for an isonitrile ligand acting as a σ-donor to a metal center. [(TPP)Fe^{II}-(*t*BuNC)$_2$],[39] as mentioned above, was structurally characterized but no IR data were given.

On the other hand, for all three porphyrin Fe^{II}-DIMPI complexes with covalently attached axial bases (pyridine/imidazole/histamine moieties), we observe a shift in the C≡N bond stretch of the isonitrile ligand to lower energy with respect to the uncomplexed ligand. The $\nu_{(C\equiv N)}$ band for (**2**)-DIMPI is 2104 cm^{-1}, 16 cm^{-1} lower in energy compared to that of free DIMPI, and also 20 cm^{-1} lower in energy with respect to (**1**)-DIMPI. For (**3**)-DIMPI, the value of $\nu_{(C\equiv N)}$ is 2098 cm^{-1}, which is 23 cm^{-1} lower in energy with free ligand. In (**4**)-DIMPI [$\nu_{(C\equiv N)}$ band (2112 cm^{-1})], we again observe a lower energy C≡N bond stretch compared to free DIMPI, but only by a small amount ($\Delta\nu_{(C\equiv N)} = -8$ cm^{-1}). The shift to lower energy in all these cases could be due to the presence of a more strongly donating axial

base *trans* to the isonitrile ligand. This will most likely decrease the σ-donation to the Fe^{II} from the isocyanide ligand, while increasing backbonding to the ligand C≡N π* orbitals from the Fe^{II} dπ orbitals.

Diamagnetic ^{1}H-NMR spectra were observed for all Fe^{II}-DIMPI (S=0, d^6) complexes. The pyrrole hydrogens of the Fe^{II}-DIMPI porphyrinates resonate between 8.5–9.5 ppm compared with the starting reduced high-spin five-coordinated paramagnetic Fe^{II} (d^6) species ranging in $\delta_{pyrrole}$ = 12 to 58 ppm.[37] We also observed a singlet δ 2.65 ppm for the DIMPI *o*-methyl protons and a multiplet for the aromatic protons of bound DIMPI at δ 7.2–7.5 ppm, both sets of peaks are slightly shifted downfield from what is observed for free DIMPI.

In the ^{19}F-NMR for bis-isocyanide complex, [$(F_8)Fe^{II}$-$(DIMPI)_2$] / (**1**)-DIMPI, we observe one sharp singlet peak at –109.0 ppm, as shown in Figure 2.10. Therefore, unlike what we have suggested (and described above) for what is observed in the X-ray crystal structures for the supers-structured hemes ((**3**)-DIMPI, and (**4**)-DIMPI), there are no observed F-atom interactions or coupling to porphyrin or isocyanide H atoms.

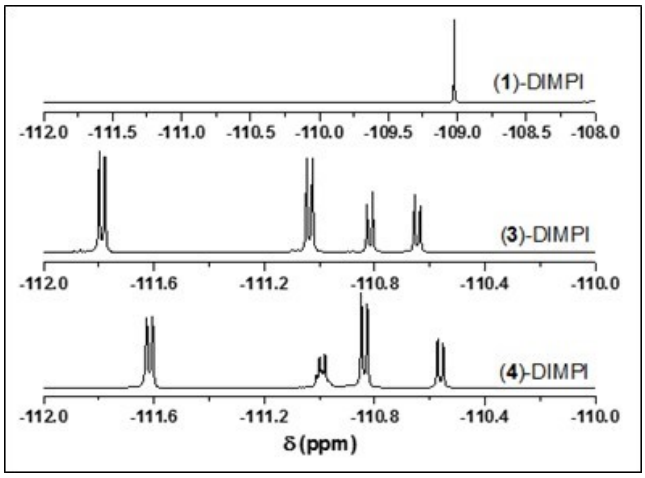

Figure 2.10 ^{19}F-NMR of (**1**)-DIMPI (top), (**3**)-DIMPI (middle) and (**4**)-DIMPI (bottom) complexes in THF at room temperature.

On the other hand, we observed CH…F coupling for, (**3**)-DIMPI and (**4**)-DIMPI, (Figure 2.10) with peaks for the *ortho* F-atom resonances on the porphyrinate aryl groups occurring between –110 to –112 ppm.[41] In the case of (**3**)-DIMPI, doublet peaks, proposed to be due to ^{19}F resonances coupled to a S = ½ H-atom, are observed at –111.7 and –111.0 ppm and both of these appear to integrate to two F-atoms. Our suggested assignments are as follows: (a) One of the two upfield (more negative delta value) doublets corresponds to F4 and F6 coupling to imidazole H-atoms H39 and H41, which spatially line up rather well, see Table 2.3, Figure 2.8. (b) The other upfield doublet represents 2 *o*-fluorine H-bonds with pyrrole H-atoms, possibly F3 and F5 with pyrrole H-atoms H8 and H2, and these also seem to be in very closely matching chemical environments. (c) One of the two absorptions, –110.8 or –110.6 corresponds to a single *o*-fluorine atom (F2) also coupling to a pyrrole CH7 atom, but by symmetry this is in a different chemical environment then for the interactions discussed just above for F5 and F3. (d) Then, the other upfield absorption is a unique interaction of F1 with the DIMPI methyl group H-atoms (CH64···F1).

Similarly, for (**4**)-DIMPI we observe four *ortho* F-atom resonances, three doublets and one multiplet in ^{19}F-NMR spectroscopy, Figure 2.10. The peaks at –111.6 and –110.8 ppm both integrate to two fluorine atoms, which we propose are due to (a) fluorine atom F6 and F2 coupling with the DIMPI methyl H-atoms H66A and H67C, see Table 2.3, Figure 2.8, (b) while the other generally upfield doublet represents two fluorine atom being in same chemical environments due to the coupling of F-atoms F3 and F4 from the same porphyrinate phenyl ring, forming H-bonds with the pyrrole H atoms H8 and H12. If (or probably when) the aryl ring with F3 and F4 tilts the other way, then symmetry related switching of H-bonding to pyrrole H-atoms may (or probably does) occur, but the result is

the same type of CH…F H-bonding. Further, the doublet resonance at –110.5 ppm should correspond to F5 coupling to the pyrrole H-atom H17. This leaves the multiplet peak at –110.9 ppm which likely arises due to the H-bonding interaction and magnetic coupling of F1 to two H-atoms, the imidazole H-atom H40 and the dangling pyridine H-atom H35, see Table 2.3 and Figure 2.8. During the dynamic behavior expected in solution, the dangling pyridyl ring may break its H35…F1 interaction, and twist over to the other side (to the left in Figure 2.8-Right), as the imidazole bound to Fe also twists in order to maintain the very strong imidazole N-H to pyridine nitrogen hydrogen bond); the pyridyl H35 would now H-bond to F5 (instead of F1); further, F5 may then gain an H-bond to H40. All of these motions would leave the ^{19}F-NMR shifts and couplings unchanged.

As mentioned, for (**1**)-DIMPI, we do not observe any DIMPI ligand H-atom coupling to F-atoms of the F_8 heme. Also, we do not observe any such couplings for the compound (THF)(F_8)Fe^{II}-CO (unpublished observation). We suggest that when there is a tethered axial ligand such as in P^{Im} or P^{ImH}, there are constraints in the movement or rotation of the axial ligand, which thereby allow for these weaker imidazole-H…F interactions to be observed. Further studies may be warranted.

2.2.3 Stable Heme–Fe–Nitrosyl formation

In this study, we have also investigated the reactivity of [(F_8)Fe^{II}], [(P^{Py})Fe^{II}], [(P^{Im})Fe^{II}], and the newly synthesized [(P^{ImH})Fe^{II}] towards nitric oxide (NO). All iron (II) complexes form a NO-adduct at room temperature by bubbling $NO_{(g)}$ through the solution of each of the reduced iron complexes, as shown in Scheme 2.4. We have systematically characterized Fe^{II}–NO complexes by using UV-Vis, FT-IR, ^{1}H-NMR, ^{19}F-NMR

spectroscopy and low temperature EPR spectroscopy, to access the binding properties of our covalently tethered N-donor ligands.

In-depth studies have been done by Lehnert and coworkers[8,43] using synthetic heme porphyrins with tethered N-donor ligands which indicate a direct correlation between the coordination geometry of the iron center and the observed spectroscopic properties obtained from UV-Vis, IR, and EPR. For five-coordinate (5C) heme nitrosyls, the Soret band (UV-Vis) is typically about 405 nm, whereas in six-coordinate (6C) porphyrinoids, where the proximal ligand (N-donor) is bound to the Fe center, the Soret λmax shifts to ~426 nm. Similarly, in IR spectroscopy, 5C and 6C ferrous-heme mononitrosyl species have distinct N–O stretching modes. For 5C complexes, the N–O stretch typically lies between 1675 and 1700 cm^{-1}, whereas for 6C complexes, the N–O stretch occurs at ~1630 cm^{-1}. Low temperature EPR spectroscopy studies conducted by several authors reveal interesting differences between the 5C and 6C iron(II) porphyrin NO adducts.[47] Hyperfine lines resulting from the bound nitrogen of NO are observed at the lowest *g* value (g min) in 5C ferrous-heme nitrosyls. The coordination of the proximal nitrogen atom in 6C ferrous-heme nitrosyls causes a broadening in the EPR spectrum at g-mid resulting from the hyperfine lines of the bound NO and the *trans*-N donor ligand. Based on spectroscopic data available from the literature, our [$(F_8)Fe^{II}$-NO] complex forms a typical 5C ferrous-heme mono-nitrosyl complex with a Soret band λ_{max} at 408 nm in the UV-vis region at room temperature (Figure 2.3), along with a characteristic N–O stretching band ν(N–O) at 1680 cm^{-1} in its IR spectrum.[48,49] Additional evidence for the 5C nitrosyl complex can be seen in its EPR spectrum, which displays *g* values at 2.09, 2.02, and 1.99, with three

hyperfine splittings at g(min) (Figure 2.11).[48,49] In the ^{19}F-NMR, a broad *o*-phenyl fluorine signal is observed at −106.0 ppm.

Scheme 2.4 Six coordinate ferrous heme mono nitrosyl complexes of $(P^{Py})Fe^{II}$, $(P^{Im})Fe^{II}$ and $(P^{ImH})Fe^{II}$

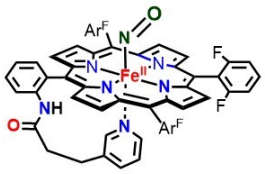

$[(P^{Py})Fe^{II}\text{-NO}]$ or (**2**)-NO

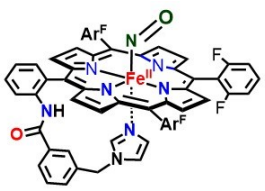

$[(P^{Pim})Fe^{II}\text{-NO}]$ or (**3**)-NO

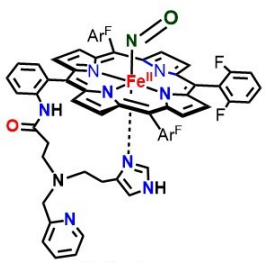

$[(P^{PImH})Fe^{II}\text{-NO}]$ or (**4**)-NO

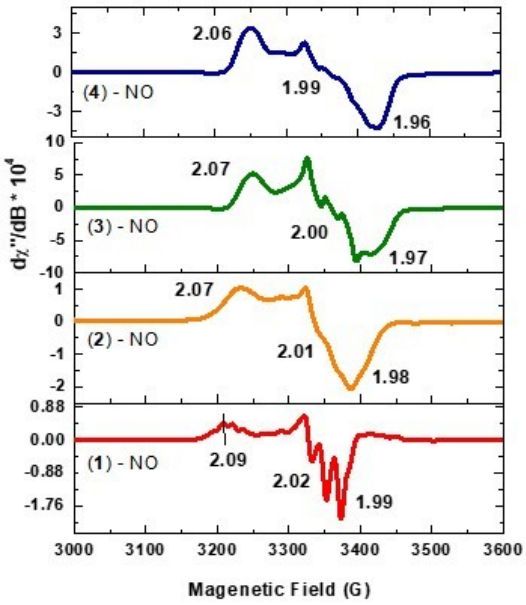

Figure 2.11 X-band EPR at 8 K in THF for ferrous heme-NO complexes. $[(F_8)Fe^{II}\text{-NO}]$ (**Red**, 5C species), while (**2**), (**3**), and (**4**) form 6C species. $[(P^{Py})Fe^{II}\text{-NO}]$ (**Orange**, 6C), $[(P^{Im})Fe^{II}\text{-NO}]$ (**Green**, 6C) and $[(P^{ImH})Fe^{II}\text{-NO}]$ (**Blue**, 6C). These spectra were analyzed further using an EPR simulation computer program, and the results of those fits, giving g-values and hyperfine coupling constants, are given in the Figure 2.12.

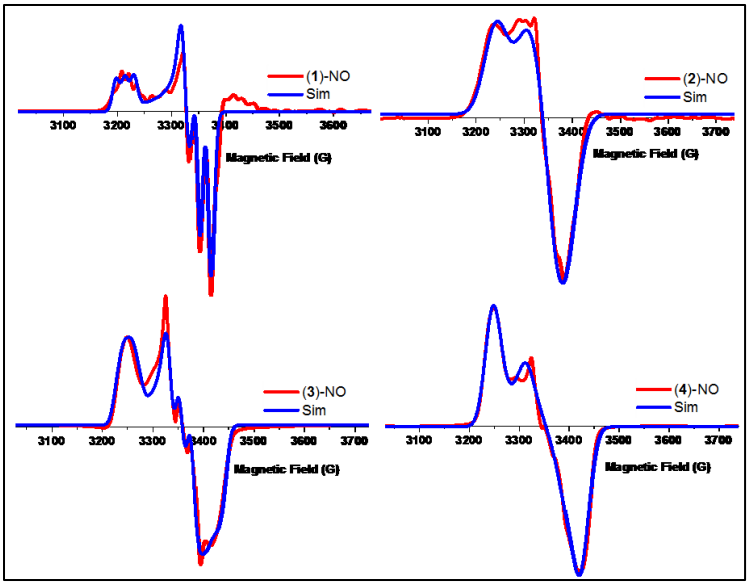

Figure 2.12 X-band EPR spectroscopy of ferrous heme-NO complexes recorded at 8K in frozen THF (**red**) and fit of the spectrum using the program Easy Spin (**blue**). Fit parameters:
(a) (**1**)–NO (g_1 = 2.0918, g_2 = 2.0074, g_3 = 2.0052; N hyperfine: $^{NO}A_1$ = 48.78, $^{NO}A_2$ = 67.63, $^{NO}A_3$ = 35.68)
(b) (**2**)–NO (g_1 = 2.0746, g_2 = 2.0081, g_3 = 1.9904; N hyperfine: $^{NO}A_1$ = 4.0, $^{NO}A_2$ = 60.4, $^{NO}A_3$ = 35.8; $^{Py}A_1$ = 18.1, $^{Py}A_2$ = 20.1, $^{Py}A_3$ = 19.1)
(c) (**3**)–NO (g_1 = 2.0686, g_2 = 2.002, g_3 = 1.9662; N hyperfine: $^{NO}A_1$ = 44.10, $^{NO}A_2$ = 63.18, $^{NO}A_3$ = 47.45; $^{Im}A_1$ = 22.94, $^{Im}A_2$ = 1.29, $^{Im}A_3$ = 16.84)
(d) (**4**)–NO (g_1 = 2.0690, g_2 = 2.0050, g_3 = 1.9643; N hyperfine: $^{NO}A_1$ = 14.68, $^{NO}A_2$ = 23.97, $^{NO}A_3$ = 71.75; $^{ImH}A_1$ = 2.0, $^{ImH}A_2$ = 4.3, $^{ImH}A_3$ = 10.2)

In the case of [(P^{Py})Fe^{II}-NO], the Soret band absorption is observed at 417 nm (Figure 2.3), which lies in between that known for 5C and 6C iron-nitrosyl complexes. This indicates that in solution at room temperature, the proximal pyridine is weakly bound to the iron center to give 6C species. Further evidence comes from the low temperature EPR spectrum of [(P^{Py})Fe^{II}-NO], shown in Figure 2.11, Figure 2.12 and Table 2.1, which clearly resembles the spectra of other 6C low-spin heme-Fe(II)-nitrosyl complexes;[43] lowering the temperature allows for stronger binding of the pyridyl group, as would be expected. The spectrum shows small, unresolved hyperfine splitting at g(mid) due to the presence of the

proximal pyridine ligand (g = 2.07, 2.01, 1.98). The lack of UV-Vis spectral features at 400, and 470 nm, as well as EPR data for [(P^{Py})Fe^{II}-NO] confirms that in solution it forms a 6C species, but where the pyridyl group is weakly bound to the iron center at room temperature.

On the other hand complexes [(P^{Im})Fe^{II}-NO] and [(P^{ImH})Fe^{II}-NO] form very stable 6C iron(II) nitrosyl species. In the UV-vis region, the observed Soret bands shift to 423 nm for (**3**)-NO, and 425 nm for (**4**)-NO (Figure 2.3) which match very well with reported 6C iron(II) nitrosyl complexes.[43] To further investigate the strength of the proximal (imidazole) ligand binding to the iron center in (**3**)-NO and (**4**)-NO, the EPR spectra of both complexes were recorded. The observed *g* values are 2.07, 2.00, and 1.97 for (**3**)-NO and 2.06, 1.99 and 1.96 for (**4**)-NO (Figure 2.11, Figure 2.12, Table 2.1). For both species, the hyperfine pattern is on g(mid) and the hyperfine lines are not well resolved. Also, the stretching frequency, $\nu_{(N-O)}$ for complexes (**3**)-NO and (**4**)-NO are the same, at 1650 cm^{-1}. This lower stretching frequency is due to the binding of the N-donor ligand (Imidazole) *trans* to the NO, which weakens the Fe–NO σ-bond.[50] Interestingly, these frequencies are higher in energy compared to a similar ferrous heme nitrosyl with a free axial base, [Fe(T*o*-F_2PP)(MI)(NO)] (MI = methylimidazole; $\nu_{(N-O)}$ = 1624 cm^{-1}). The trend observed is in line with a previous study by Scheidt,[14] further suggesting that the tethered axial ligand bases bind to the heme more weakly that would or does a freely added (or present) base. The IR data matches closely with reported work by Lehnert and co-workers[43] and indicates that the benzyl-imidazole linker and the histamine linker impede the binding of the proximal N-donor ligand when compared to the free base, but still allow for the formation of very stable 6C complexes at room temperature.

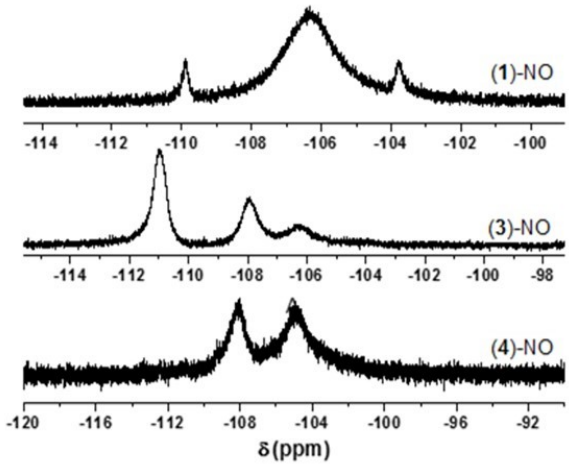

Figure 2.13 ^{19}F-NMR of (**1**)-NO (top), (**3**)-NO (middle) and (**4**)-NO (bottom) complexes in THF at room temperature.

In ^{1}H-NMR, the pyrrole hydrogen atoms resonate at 8.8 and 9.65 ppm for (**3**)-NO and (**4**)-NO, respectively. While in ^{19}F-NMR, the *o*-fluorine atoms resonate at –106, –107, –110 ppm for (**3**)-NO, and –105, –108 ppm, for (**4**)-NO, as seen in Figure 2.13. Here peaks are very broad compared with all the Fe^{II}-DIMPI complexes, where peaks were very sharp, and displayed visible H–F coupling interactions.

2.3 Conclusions

we have described the synthesis of a new porphyrin with a covalently tethered histamine type ligand, which binds to the iron center. These new ferric [(P^{ImH})Fe^{III}-Cl] and ferrous [(P^{ImH})Fe^{II}] hemes have been thoroughly characterized by various spectroscopic methods. Using this newly designed heme and a family of other covalently tethered axial ligands (pyridine/imidazole) synthesized in our lab, we have explored their reactivity towards 2,6-dimethylphenyl isocyanide (DIMPI), and nitric oxide (NO). Towards this aim, we have generated and characterized the six coordinate ferrous heme complexes; [(P^{Py})Fe^{II}(DIMPI)], [(P^{Im})Fe^{II}(DIMPI)] and [(P^{ImH})Fe^{II}(DIMPI)], which have UV-Vis, IR,

and EPR properties that are clearly distinguishable from those of [$(F_8)Fe^{II}(DIMPI)_2$]. The X-ray structures reveal a significant contribution from H-bonding between porphyrinate meso-phenyl ortho-fluorine atoms, and these have been described. These are emphasized in large part because ^{19}F-NMR spectroscopy clearly indicates that most if not all of these interactions are maintained in solution. We have also characterized several ferrous heme mono-nitrosyl complexes by multinuclear NMR, UV-Vis, EPR and solid FT-IR spectroscopy. At room temperature, [$(P^{Im})Fe^{II}$] and [$(P^{ImH})Fe^{II}$] form very stable six-coordinate ferrous iron-NO complexes. [$(F_8)Fe^{II}$] forms a five-coordinate ferrous heme nitrosyl complex, while [$(P^{Py})Fe^{II}$] appears to be somewhere between 5-coordinate, and 6-coordinate due to its weakly binding axial pyridyl ligand.

As mentioned, the impetus for synthesizing ferrous heme porphyrinates using the (P^{Py}), (P^{Im}) and (P^{ImH}) ligand systems is to utilize these porphyrins in our ongoing research into modeling the active site chemistry of cytochrome *c* oxidase. An understanding of the nature of reactions and structures, i.e., coordination numbers, ligation preferences (e.g., pyridyl vs imidazolyl vs solvent THF), and other bonding or structural aspects can help to better understand the types of structures obtained in heme-O_2-copper chemistry, and also inform the design of hemes utilized for such studies.

2.4 Experimental section

2.4.1 Materials and methods

All chemicals and solvents were purchased as commercially available analytical grade unless otherwise specified. Tetrahydrofuran (THF, inhibitor free) was dried over sodium/benzophenone ketyl, and purified by distillation under argon. Pentane was dried

by distillation over calcium hydride. Toluene was used after passing through a 60 cm long column of activated alumina (Innovative Technologies), under argon. 2,6-Dimethylphenyl isocyanide (DIMPI) was purchased from Sigma Aldrich. •NO gas was obtained from Matheson Gases and purified following methods previously described in the literature.[51] A three-way syringe was used for the addition of •NO gas to all metal complex solutions. Preparation and handling of air-sensitive compounds were performed under an argon atmosphere using standard Schlenk techniques or in an MBraun Labmaster 130 inert atmosphere (less than 1 ppm O_2, less than 1 ppm H_2O) drybox filled with nitrogen. Deoxygenation of all solvents was accomplished by either repeated freeze/pump/thaw cycles or bubbling with argon for 45–60 min.

Instrumentation: Benchtop UV-Vis measurements were carried out by using a Hewlett Packard 8453 diode array spectrophotometer equipped with HP Chemstation software and a Unisoku thermostated cell holder for low temperature experiments. A 10 mm path length quartz cell cuvette modified with an extended glass neck with a female 14/19 joint, and stopcock was used to perform all UV-Vis experiments. ESI-MS were acquired using a Finnigan LCQ Duo ion-trap mass spectrometer equipped with an electrospray ionization source (Thermo Finnigan, San Jose, CA). The heated capillary temperature was 250 ºC and the spray voltage was 5 keV. Spectra were recorded continuously after injection. Infrared (IR) spectra were obtained on solid samples using a Thermo Scientific Nicolet Nexus 670 Fourier transform IR (FT-IR) spectrophotometer with ATR attachment. ^{1}H-NMR and ^{19}F-NMR spectra were acquired using a Bruker 300-MHz NMR spectrometer. Chemical shifts were reported as δ (ppm) values relative to an internal standard (tetramethylsilane) and the residual solvent proton peak. Electron

paramagnetic resonance (EPR) spectra were recorded with a Bruker EMX spectrometer equipped with a Bruker ER 041 X G microwave bridge and a continuous-flow liquid helium cryostat (ESR900) coupled to an Oxford Instruments TC503 temperature controller. Spectra were obtained at 8 K under nonsaturating microwave power conditions (ν = 9.428 GHz, microwave power = 0.201 mW, modulation amplitude = 10 G, microwave frequency = 100 kHz, receiver gain = 5.02×10^3). EPR spectra were simulated by using the Easy Spin (see Figure 2.12). The compounds $(F_8)Fe^{II}$ (**1**),[35,52,53] $(P^{Py})Fe^{II}$ (**2**)[37,38] and $(P^{Im})Fe^{II}$ (**3**)[37,54] were synthesized as previously described.

2.4.2 Synthesis of $(P^{ImH})Fe^{II}$ (4)

The synthesis of complex $(P^{ImH})Fe^{II}$ (**4**) involves multiple steps as shown in Scheme 2.1, where $F_6(NHCOCH_2CH_2Br)TPPH_2$[55] and LN^3Tr[56] were synthesized as previously described.

2.4.2.1 Synthesis of P^{ImTr} ligand

To a 50 mL round bottom flask containing 1.8 g (2.0 mmol) of $F_6(NHC(O)CH_2CH_2Br)TPPH_2$ and 0.7 mL of diisopropylethyl amine was added to 1.7 g (4 mmol) of LN^3Tr in 15 mL of THF. The resulting mixture was heated to reflux overnight. After cooling to room temperature, the solvent was removed under vacuum. The solid residue was re-dissolved in dichloromethane and washed several times with distilled water, from which the organic layer was dried over anhydrous sodium sulfate. Column chromatography of the crude material on alumina (ethyl acetate : hexane = 97:3, $R_f = 0.4$) yielded 2.3 g (1.9 mmol, 65 %) of the desired product as a purple solid. ESI-MS (m/z):

1236.11 $(M + H)^+$ (Figure 2.14); ^{1}H-NMR (CD_3CN, 300 MHz; δ, ppm, RT): 8.88-8.78 (m, 8H, pyrrole-H), 8.73 (s, 1H, pyridine-H), 8.29 (d, 1H, pyridine-H), 8.02 (d, 1H, pyridine-H), 7.91-7.73 (m, 4H, Ar-H, pyridine-H), 7.47-7.19 (m, 20H, Ar-H, Tr-H), 6.94-6.92 (m, 6H, Ar-H), 6.87 (s, 1H, Imidazole-H), 6.04 (s, 1H, Imidazole-H), 1.68 (t, 2H, ($-CH_2-$)), 1.49 (t, 2H, ($-CH_2-$)), 1.32 (t, 2H, ($-CH_2-$)), 1.20 (t, 2H, ($-CH_2-$)), 1.04 (s, 2H, $(-CH_2-)_{py}$), -2.87 (s, 2H, $NH_{pyrrole}$) (Figure 2.15).

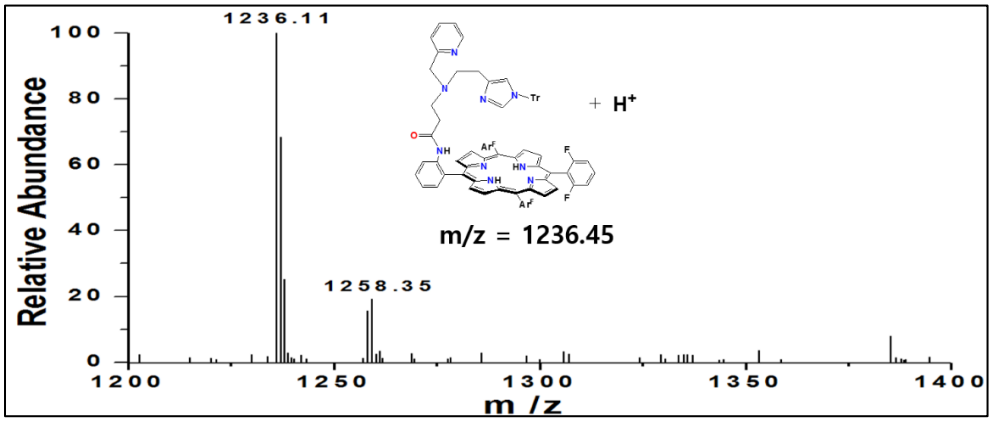

Figure 2.14 ESI-MS of the porphyrin ligand P^{ImTr}, corresponding to $M+H^+$ and $M+Na^+$ (1258.35) in CH_2Cl_2 at 293 K.

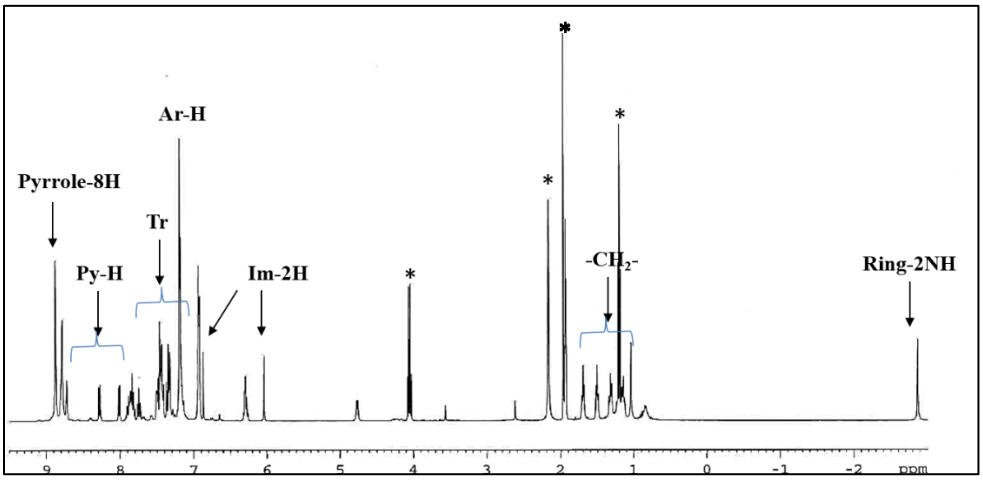

Figure 2.15 ^{1}H-NMR spectra of covalently linked histamine containing porphyrin P^{ImTr} in CD_3CN at 293 K. (*) corresponds to solvent molecules, residual NMR solvent CH_3CN and ethyl acetate (used as an eluent for column chromatography.

2.4.2.2 Synthesis of P^{ImTr}-d_8 ligand

The pyrrole deuterated porphyrin ligand P^{ImTr}-d_8 was prepared using a procedure identical to that described above for P^{ImTr}, but employing the pyrrole deuterated porphyrin $F_6(NH_2)$-d_8[36] instead of $F_6(NH_2)$.

2.4.2.3 Synthesis of [(P^{ImH})Fe^{III}-Cl]

The ligand P^{ImTr} (1.3 g, 1.05 mmol) was dissolved in 20 mL THF under an argon atmosphere. Fe^{II} chloride tetrahydrate (7 g, 55.2 mmol) was added and the solution was heated to reflux at 60 ºC under argon for 3 h. After cooling to room temperature, the solution was exposed to air and stirred for 3 h. The solvent was removed by rotary evaporation and the residue obtained was re-dissolved in 100 mL CH_2Cl_2 followed by filtering the insoluble solid present. The solution was stirred with HCl (1 M, 100 mL) for 3 h and then neutralized using solid $NaHCO_3$. The organic layer was washed with 100 mL saturated $NaHCO_3$ then brine solution and dried over anhydrous $MgSO_4$. The desired product was purified by column chromatography (silica, CH_2Cl_2: MeOH = 95:5, R_f = 0.4). Yield: 0.8 g, 72%. UV-Vis spectrum [λ_{max}, nm] in THF: 419, 527, 553 (Figure 2.16). ESI-MS (m/z): 1047.01 $(M–Cl^–)^+$ (Figure 2.17) ^{1}H-NMR (300 MHz, THF, δ, ppm, RT): 82 (s, br, pyrrole-H). EPR spectra (X-band spectrometer, ν = 9.428 GHz): g = 6.0, 1.98 in THF at 7 K.

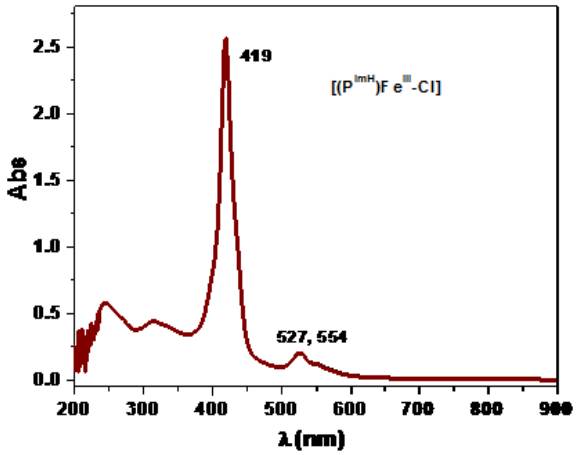

Figure 2.16 UV-Vis spectra of heme iron(III) porphyrin, [(P^{ImH})Fe^{III}-Cl] complex in CH_2Cl_2 at 293 K.

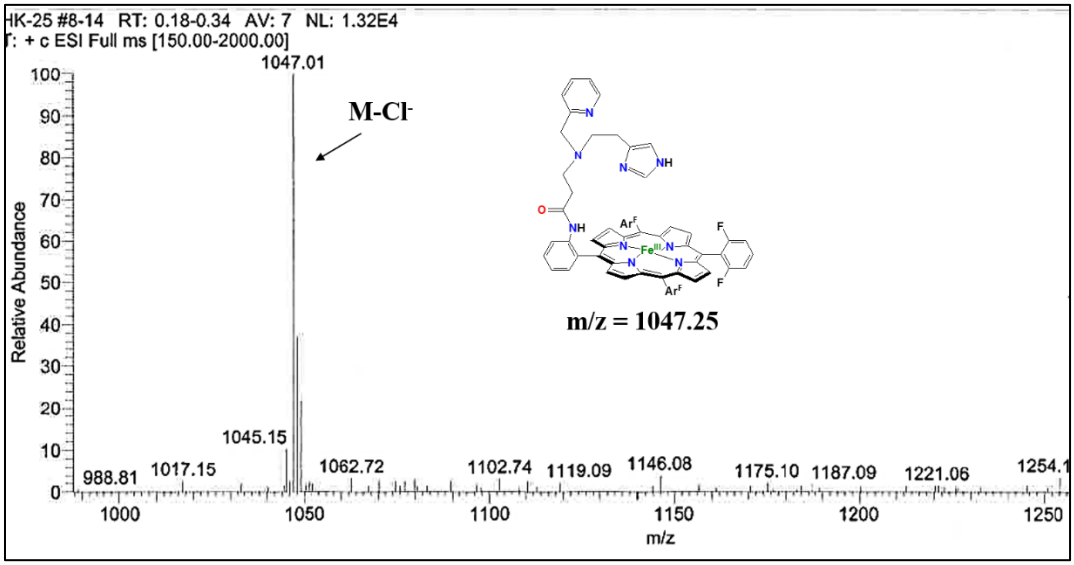

Figure 2.17 ESI-MS of [(P^{ImH})Fe^{III}-Cl] in CH_2Cl_2 at 293 K; the peak at 1047.01 corresponds to M-Cl^-.

2.4.2.4 Synthesis of [(P^{ImH})Fe^{III}-Cl]-*d*$_8$

The pyrrole deuterated heme–Fe^{III} [(P^{ImH})Fe^{III}-Cl]-*d*$_8$ was prepared using an identical procedure to that described above for [(P^{ImH})Fe^{III}-Cl], but employing pyrrole

deuterated porphyrin P^{ImTr}-d_8 instead of P^{ImTr}. ^{2}H NMR (THF, 300 MHz, δ, ppm, RT): 82 (s, br, pyrrole-D) and (δ, ppm, –90 ºC): 126.0 (s, br, pyrrole-D), shown in Figure 2.18.

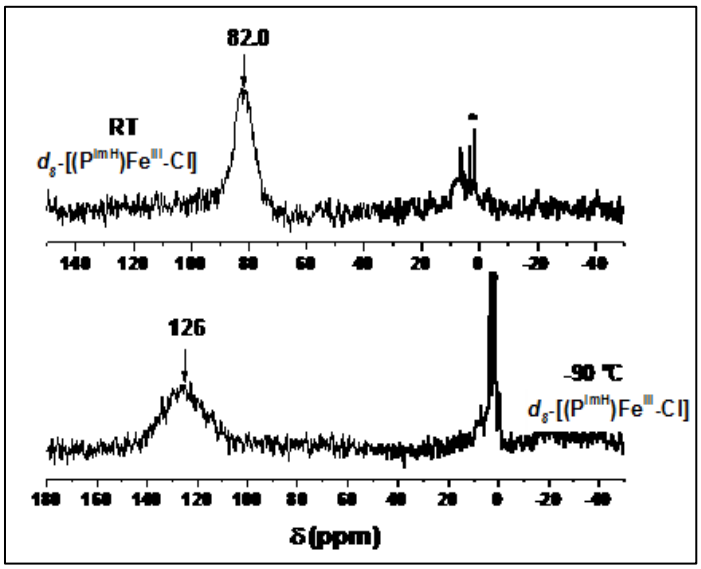

Figure 2.18 (top) ^{2}H-NMR spectra of heme iron(III) complex d_8-[(P^{ImH})Fe^{III}-Cl] in THF ($\delta_{pyrrole}$ = 82.0 ppm) at 293 K. (bottom) ^{2}H-NMR spectra of heme iron(III) complex d_8-[(P^{ImH})Fe^{III}-Cl] in THF ($\delta_{pyrrole}$ = 126 ppm) at 183 K. (*) corresponds to solvent molecule THF.

2.4.2.5 Synthesis of (P^{ImH})Fe^{II}

The degassed solution of [(P^{ImH})Fe^{III}-Cl] (500 mg, 0.5 mmol) in 120 mL CH_2Cl_2 was added to a degassed 50 mL saturated $Na_2S_2O_4$ (aq) solution under an argon atmosphere. The two solutions were mixed using argon bubbling for 30 min in an additional funnel. The reaction mixture was allowed to sit for 20 min until the two layers separated. The organic layer was separated and passed through anhydrous Na_2SO_4 powder loaded in a filter tube (one end connecting to the additional funnel and the other end connecting to a Schlenk flask) under an argon atmosphere. Then the solvent was removed and dried in vacuo for 3 h. The resulting solid was kept in glove box. Yield: 437.1 mg, 93%. UV–Vis

spectrum [$\lambda_{max,}$ nm] in THF: 419, 525, 552. ^{19}F-NMR (THF-d_8, 282 MHz; δ, ppm): –109.7, –110.3, –111.0, –111.6, –112.4.

2.4.2.6 Synthesis of (P^{ImH})Fe^{II}-d_8

The pyrrole deuterated heme–Fe^{II} (P^{ImH})Fe^{II}-d_8 was prepared using an identical procedure to that described above for (P^{ImH})Fe^{II}, but employing pyrrole deuterated porphyrin [(P^{ImH})Fe^{III}-Cl]-d_8 instead of [(P^{ImH})Fe^{III}-Cl]. ^{2}H NMR (300 MHz, THF): δ 57.0 (s, 1H, pyrrole-D), 49.0 (s, 1H, pyrrole-D), 19.0 (s, 1H, pyrrole-D), 15.7 (s, 1H, pyrrole-D), 8.3 (s, 4H, (pyrrole-D**)**. ^{2}H-NMR (THF, 300 MHz; δ, ppm, –90ºC): 9.80 (Figure 2.5).

2.4.3 Synthesis of DIMPI complex

2.4.3.1 Synthesis of [(F_8)Fe^{II}-(DIMPI)$_2$], (1)-DIMPI

In the drybox, to a solution of (F_8)Fe^{II} (**1**) (10.0 mg, 0.024 mmol) in THF (5 mL) was added 2,6-dimethylphenyl isocyanide (6.3 mg, 0.048 mmol). After stirring the reaction mixture for 30 min, the solvent was removed under vacuum to yield a red solid. The crude solid obtained was further dissolved in THF and layered with pentane to obtain a very fine crystalline material. UV-Vis spectrum [$\lambda_{max,}$ nm] in THF: 430, 527. ^{1}H-NMR (THF-d_8, 300 MHz; δ, ppm): 10.45 (pyrrole-H), 2.43 (s, -CH_3 (DIMPI)), 7.2 (m, ArH (DIMPI)); ^{19}F-NMR (THF-d_8, 282 MHz; δ, ppm): –109 (d). FT-IR spectrum (solid): ν_{CN} = 2124 cm^{-1}.

2.4.3.2 Synthesis of [(P^{Py})Fe^{II}-(DIMPI)], (2)-DIMPI

[(P^{Py})Fe^{II}-(DIMPI)], (**2**)-DIMPI: In the dry box, to the THF solution of (P^{Py})Fe^{II}, (**2**) (10.0 mg, 0.011 mmol) in a 10 mL Schlenk flask, we added one equivalent of DIMPI (1.5

mg, 0.012 mmol) and the reaction mixture was stirred for half an hour. The solvent was removed under vacuum to yield a deep red colored solid, which was further recrystallized by dissolving in a minimal amount of THF and layering it with pentane to obtain the fine crystalline material. UV-Vis spectrum [$\lambda_{max,}$ nm] in THF: 430, 534. FT-IR spectrum (solid): ν_{CN} = 2104 cm^{-1}.

2.4.3.3 Synthesis of [(P^{Im})Fe^{II}-(DIMPI)], (3)-DIMPI

This complex was synthesized in a similar manner to complex (**2**)-DIMPI. X-ray quality crystals were obtained from the solution of MeTHF/pentane. UV-Vis spectrum [λ_{max}, nm] in THF: 430, 532. ^{1}H-NMR (THF-d_8, 300 MHz; δ, ppm): 9.1 (pyrrole-H), 7.2 (m, ArH (DIMPI)), 2.43 (s, -CH_3 (DIMPI)); ^{19}F-NMR (THF-d_8, 282 MHz; δ, ppm): –110.6 (d), –110.8 (d), –111.0 (d), –111.7 (d). FT-IR spectrum (solid): ν_{CN} = 2098 cm^{-1}.

2.4.3.4 Synthesis of [(P^{ImH})Fe^{II}-(DIMPI)], (4)-DIMPI

This complex was also synthesized in a similar manner as the afore-mentioned complexes, (**2**)-DIMPI and (**3**)-DIMPI. X-ray quality crystals were obtained from a solution of Toluene/pentane. UV-Vis spectrum [$\lambda_{max,}$ nm] in THF: 430, 533. ^{1}H-NMR (THF-d_8, 300 MHz; δ, ppm): 9.78 (pyrrole-H), 7.2 (m, ArH (DIMPI)), 2.27 (m, -CH_3 (DIMPI)); ^{19}F-NMR (THF-d_8, 282 MHz; δ, ppm): –110.55 (d), –110.8 (d), –110.9 (m), –111.6 (d). FT-IR spectrum (solid): ν_{CN} = 2112 cm^{-1}.

2.4.4 Synthesis of NO complex

2.4.4.1 Synthesis of [(F_8)Fe^{II}-NO], (1)-NO[48]

The ferrous mono-nitrosyl complex (**1**)-NO was generated by bubbling excess NO gas through the THF solution of (F_8)Fe^{II} (**1**) (2 mM) under argon atmosphere at room temperature. After the reaction mixture stirred for 2 hours, the solvent was removed under vacuum to obtain a dark red solid. A highly pure material was obtained by dissolving red solid in the minimum amount of THF and layering it with pentane inside the dry box. UV-Vis spectrum [λ_{max}, nm] in THF: 408, 547. ^{1}H-NMR (THF-d_8, 300 MHz; δ, ppm): 6.9 (br, pyrrole-H); ^{19}F-NMR (THF-d_8, 282 MHz; δ, ppm): –106 (br). FT-IR spectrum (solid): ν_{NO} = 1688 cm^{-1}. EPR spectra (X-band spectrometer, v = 9.428 GHz): g = 2.09, 2.02, 1.99 (hyperfine) in THF at 7 K.

2.4.4.2 Synthesis of [(P^{Py})Fe^{II}-NO], (2)-NO[46]

A method similar to that used to synthesize complex (**1**)-NO was used to make complex (**2**)-NO. Excess of NO gas was bubbled through the 2 mM THF solution of (P^{Py})Fe^{II} (**2**). UV-Vis spectrum [λ_{max}, nm] in THF: 417, 543. ^{1}H-NMR (THF-d_8, 300 MHz; δ, ppm): 8.0 (pyrrole-H). FT-IR spectrum (solid): ν_{NO} = 1648 cm^{-1}. EPR spectra (X-band spectrometer, v = 9.428 GHz): g = 2.07, 2.01 (br-hyperfine), 1.98 in THF at 7 K.

2.4.4.3 Synthesis of [(P^{Im})Fe^{II}-NO], (3)-NO[46]

This complex was prepared in the same manner as complexes (**1**)-NO and (**2**)-NO. UV-Vis spectrum [λ_{max}, nm] in THF: 423, 542. ^{1}H-NMR (THF-d_8, 300 MHz; δ, ppm): 8.8 (pyrrole-H); ^{19}F-NMR (THF-d_8, 282 MHz; δ, ppm): –106.2 (br), –107.9 (br), –110.9 (br).

FT-IR spectrum (solid): ν_{NO} = 1650 cm^{-1}. EPR spectra (X-band spectrometer, ν = 9.428 GHz): g = 2.07, 2.00 (hyperfine), 1.97 in THF at 7 K.

2.4.4.4 Synthesis of [(P^{ImH})Fe^{II}-NO], (4)-NO

Synthesis of this complex was accomplished as mentioned above for the preparation of (**1**)-NO. UV-Vis spectrum [λ_{max}, nm] in THF: 425, 541. ^{1}H-NMR (THF-d_8, 300 MHz; δ, ppm): 9.65 (pyrrole-H); ^{19}F-NMR (THF-d_8, 282 MHz; δ, ppm): –104.9 (br), –108.1 (br). FT-IR spectrum (solid): ν_{NO} = 1650 cm^{-1}. EPR spectra (X-band spectrometer, ν = 9.428 GHz): g = 2.06, 1.99 (hyperfine), 1.96 in THF at 7 K.

2.4.5 X-Ray Structure Determination

X-ray structure determination of (**3**)-DIMPI and (**4**)-DIMPI was performed at the X-ray diffraction facility at Johns Hopkins University. CIF files have been deposited with the Cambridge Crystallographic Data Centre (CCDC). CCDC 1455862 and 1455863 contain the supplementary crystallographic data for this article. These data can be obtained free of charge from the CCDC via http://www.ccdc.cam.ac.uk/data_request/cif. All reflection intensities were measured at 110(2) K using a SuperNova diffractometer (equipped with Atlas detector) with Cu *K*α radiation (λ = 1.54178 Å) under the program CrysAlisPro (Version 1.171.36.32 Agilent Technologies, 2013). The program CrysAlisPro (Version 1.171.36.32 Agilent Technologies, 2013) was used to refine the cell dimensions and for data reduction. The structures were solved with the program SHELXS-2013 (Sheldrick, 2013) and was refined on F^2 with SHELXL-2013 (Sheldrick, 2013). Analytical numeric absorption correction based on a multifaceted crystal model was applied using

CrysAlisPro (Version 1.171.36.32 Agilent Technologies, 2013). The temperature of the data collection was controlled using the system Cryojet (manufactured by Oxford Instruments). The H atoms were placed at calculated positions using the instructions AFIX 23, AFIX 43 or AFIX 137 with isotropic displacement parameters having values 1.2 or 1.5 times *U*eq of the attached C or N atoms.

Crystals of (**3**)-DIMPI were obtained from a MeTHF solution of complex and layered with pentane, while crystals of (**4**)-DIMPI were obtained from saturated solution of toluene. The structure of (**3**)-DIMPI is partly disordered. Some unresolved electron density – *i.e.*, a very disordered lattice methyl THF solvent molecule – has been taken out in the final refinement (SQUEEZE details are provided in the CIF file, Spek, 2009). In addition, the imidazole / amide arm may be slightly disordered, but the disorder is not significant enough to model it in the final refinement. The structure (**4**)-DIMPI is partly disordered. One difluorophenyl group and the lattice toluene solvent molecule are found to be disordered over two orientations, and the occupancy factors of the major components of the disorder refine to 0.561(16) and 0.722(4), respectively; see the Electronic Supplementary Material, i.e., the appropriate CIF file.

2.5 References

(1) Nam, W. Dioxygen Activation by Metalloenzymes and Models. *Acc. Chem. Res.* **2007**, *40*, 465.

(2) Zhu, Y.; Silverman, R. B. Revisiting Heme Mechanisms. A Perspective on the Mechanisms of Nitric Oxide Synthase (NOS), Heme Oxygenase (HO), and Cytochrome P450s (CYP450s). *Biochemistry* **2008**, *47*, 2231–2243.

(3) Aono, S. Metal-Containing Sensor Proteins Sensing Diatomic Gas Molecules. *Dalt. Trans.* **2008**, *9226*, 3137–3146.

(4) Ohta, T.; Kitagawa, T. Resonance Raman Investigation of the Specific Sensing Mechanism of a Target Molecule by Gas Sensory Proteins. *Inorg. Chem.* **2005**, *44*, 758–769.

(5) Williams, P. A.; Cosme, J.; Sridhar, V.; Johnson, E. F.; McRee, D. E. Mammalian Microsomal Cytochrome P450 Monooxygenase: Structural Adaptations for Membrane Binding and Functional Diversity. *Mol. Cell* **2000**, *5*, 121–131.

(6) Walker, F. A. Nitric Oxide Interaction with Insect Nitrophorins and Thoughts on the Electron Configuration of the $\{FeNO\}^6$ complex. *J. Inorg. Biochem.* **2005**, *99*, 216–236.

(7) Tennyson, A. G.; Lippard, S. J. Generation, Translocation, and Action of Nitric Oxide in Living Systems. *Chem. Biol.* **2011**, *18*, 1211–1220.

(8) Hunt, A. P.; Lehnert, N. Heme-Nitrosyls: Electronic Structure Implications for Function in Biology. *Acc. Chem. Res.* **2015**, *48*, 2117–2125.

(9) Traylor, T. G.; Sharma, V. S. Why NO? *Biochemistry* **1992**, *31*, 2847–2849.

(10) Schopfer, M. P.; Wang, J.; Karlin, K. D. Bioinspired Heme, Heme/Nonheme Diiron, Heme/Copper, and Inorganic NOx Chemistry: •NO (g) Oxidation, Peroxynitrite-Metal Chemistry, and $\bullet NO_{(g)}$ Reductive Coupling. *Inorg. Chem.* **2010**, *49*, 6267–6282.

(11) Toledo, J. C.; Augusto, O. Connecting the Chemical and Biological Properties of Nitric Oxide. *Chem. Res. Toxicol.* **2012**, *25*, 975–989.

(12) Poulos, T. L. Soluble Guanylate Cyclase. *Curr. Opin. Struct. Biol.* **2006**, *16*, 736–743.

(13) Zhao, Y.; Brandish, P. E.; Ballou, D. P.; Marletta, M. A. A Molecular Basis for Nitric Oxide Sensing by Soluble Guanylate Cyclase. *Proc. Natl. Acad. Sci. U. S. A.* **1999**, *96*,

14753–14758.

(14) Scheidt, W. R.; Brinegar, A. C.; Ferro, E. B.; Kirner, J. F. Nitrosylmetalloporphyrins. 4. Molecular Stereochemistry of Two Crystalline Forms of Nitrosyl-α,β,γ,δ-Tetraphenylporphinato(4-Methylpiperidine)-Iron(II). A Structural Correlation with *v*(NO). *J. Am. Chem. Soc.* **1977**, *99*, 7315–7322.

(15) Matsui, T.; Unno, M.; Ikeda-saito, M. Heme Oxygenase Reveals Its Strategy For. *Acc. Chem. Res.* **2010**, *43*, 240–247.

(16) Wilks, A.; Ikeda-Saito, M. Heme Utilization by Pathogenic Bacteria: Not All Pathways Lead to Biliverdin. *Acc. Chem. Res.* **2014**, *47*, 2291–2298.

(17) Schuller, D. J.; Wilks, A.; Ortiz De Montellano, P. R.; Poulos, T. L. Crystal Structure of Human Heme Oxygenase-1. *Nat. Struct. Biol.* **1999**, *6*, 860–867.

(18) Watkins, C. C.; Boehning, D.; Kaplin, A. I.; Rao, M.; Ferris, C. D.; Snyder, S. H. Carbon Monoxide Mediates Vasoactive Intestinal Polypeptide-Associated Nonadrenergic/Noncholinergic Neurotransmission. *Proc. Natl. Acad. Sci. U. S. A.* **2004**, *101*, 2631–2635.

(19) Larsen, R. W.; Mikšovská, J. Time Resolved Thermodynamics of Ligand Binding to Heme Proteins. *Coord. Chem. Rev.* **2007**, *251*, 1101–1127.

(20) Vos, M. H. Ultrafast Dynamics of Ligands within Heme Proteins. *Biochim. Biophys. Acta - Bioenerg.* **2008**, *1777*, 15–31.

(21) Spiro, T. G.; Soldatova, A. V.; Balakrishnan, G. CO, NO and O_2 as Vibrational Probes of Heme Protein Interactions. *Coord. Chem. Rev.* **2013**, *257*, 511–527.

(22) Vos, M. H.; Liebl, U. Time-Resolved Infrared Spectroscopic Studies of Ligand Dynamics in the Active Site from Cytochrome *c* Oxidase. *Biochim. Biophys. Acta* **2015**,

1847, 79–85.

(23) Liebl, U.; Lambry, J. C.; Vos, M. H. Primary Processes in Heme-Based Sensor Proteins. *Biochim. Biophys. Acta* **2013**, *1834*, 1684–1692.

(24) Spiro, T. G.; Wasbotten, I. H. CO as a Vibrational Probe of Heme Protein Active Sites. *J. Inorg. Biochem.* **2005**, *99*, 34–44.

(25) Bandyopadhyay, D.; Walda, K. N.; Grogan, T. M.; Magde, D.; Traylor, T. G.; Sharma, V. S. Evidence for a Slow Tertiary Relaxation in the Reaction of Tert-Butyl Isocyanide with Horseradish Peroxidase. *Biochemistry* **1996**, *35*, 1500–1505.

(26) Derbyshire, E. R.; Marletta, M. A. Butyl Isocyanide as a Probe of the Activation Mechanism of Soluble Guanylate Cyclase: Investigating the Role of Non-Heme Nitric Oxide. *J. Biol. Chem.* **2007**, *282*, 35741–35748.

(27) Evans, J. P.; Kandel, S.; Ortiz De Montellano, P. R. Isocyanides Inhibit Human Heme Oxygenases at the Verdoheme Stage. *Biochemistry* **2009**, *48*, 8920–8928.

(28) Lucas, H. R.; Karlin, K. D. *Copper-Carbon Bonds in Mechanistic and Structural Probing of Proteins as Well as in Situations Where Copper Is a Catalytic or Receptor Site.* **2009**, *6*, 295–361.

(29) Blouin, G. C.; Schweers, R. L.; Olson, J. S. Alkyl Isocyanides Serve as Transition State Analogues for Ligand Entry and Exit in Myoglobin. *Biochemistry* **2010**, *49*, 4987–4997.

(30) Blouin, G. C.; Olson, J. S. The Stretching Frequencies of Bound Alkyl Isocyanides Indicate Two Distinct Ligand Orientations within the Distal Pocket of Myoglobin. *Biochemistry* **2010**, *49*, 4968–4976.

(31) Hematian, S.; Garcia-Bosch, I.; Karlin, K. D. Synthetic Heme/Copper Assemblies:

Toward an Understanding of Cytochrome *c* Oxidase Interactions with Dioxygen and Nitrogen Oxides. *Acc. Chem. Res.* **2015**, *48*, 2462–2474.

(32) Kim, E.; Helton, M. E.; Wasser, I. M.; Karlin, K. D.; Lu, S.; Huang, H-w.; Moënne-Loccoz, P.; Incarvito, C. D.; Rheingold, A. L.; Honecker, M.; Kaderli, S.; Zuberbühler, A. D. Superoxo, μ-Peroxo, and μ-Oxo Complexes from Heme/O_2 and Heme-Cu/O_2 Reactivity: Copper Ligand Influences in Cytochrome *c* Oxidase Models. *Proc. Natl. Acad. Sci. U. S. A.* **2003**, *100*, 3623–3628.

(33) Halime, Z.; Kieber-Emmons, M. T.; Qayyum, M. F.; Mondal, B.; Gandhi, T.; Puiu, S. C.; Chufán, E. E.; Sarjeant, A. A. N.; Hodgson, K. O.; Hedman, B.; Solomon, E. I.; Karlin, K. D. Heme-Copper-Dioxygen Complexes: Toward Understanding Ligand-Environmental Effects on the Coordination Geometry, Electronic Structure, and Reactivity. *Inorg. Chem.* **2010**, *49*, 3629–3645.

(34) Halime, Z.; Kotani, H.; Li, Y.; Fukuzumi, S.; Karlin, K. D. Homogeneous Catalytic O_2 Reduction to Water by a Cytochrome *c* Oxidase Model with Trapping of Intermediates and Mechanistic Insights. *Proc. Natl. Acad. Sci. U. S. A.* **2011**, *108*, 13990–13994.

(35) Kieber-Emmons, M. T.; Qayyum, M. F.; Li, Y.; Halime, Z.; Hodgson, K. O.; Hedman, B.; Karlin, K. D.; Solomon, E. I. Spectroscopic Elucidation of a New Heme/Copper Dioxygen Structure Type: Implications for O···O Bond Rupture in Cytochrome *c* Oxidase. *Angew. Chem. Int. Ed.* **2012**, *51*, 168–172.

(36) Garcia-Bosch, I.; Adam, S. M.; Schaefer, A. W.; Sharma, S. K.; Peterson, R. L.; Solomon, E. I.; Karlin, K. D. A "Naked" Fe^{III}-(O_2^{2-})-Cu^{II} Species Allows for Structural and Spectroscopic Tuning of Low-Spin Heme-Peroxo-Cu Complexes. *J. Am. Chem. Soc.* **2015**, *137*, 1032–1035.

(37) Li, Y.; Sharma, S. K.; Karlin, K. D. New Heme-Dioxygen and Carbon Monoxide Adducts Using Pyridyl or Imidazolyl Tailed Porphyrins. *Polyhedron* **2013**, *58*, 190–196.

(38) Sharma, S. K.; Rogler, P. J.; Karlin, K. D. Reactions of a Heme-Superoxo Complex toward a Cuprous Chelate and •NO (g) : C*c*O and NOD Chemistry. *J. Porphyr. Phthalocyanines* **2015**, *19*, 352–360.

(39) Jameson, G. B.; Ibers, J. A. Structure of Bis(Tert-Butyl Isocyanide)(Meso-Tetraphenylporphyrinato)Iron(II)-Bis(Toluene). *Inorg. Chem.* **1979**, *18*, 1200–1208.

(40) Kretzer, R. M.; Ghiladi, R. A.; Lebeau, E. L.; Liang, H. C.; Karlin, K. D. Synthesis and Characterization of Reduced Heme and Heme/Copper Carbonmonoxy Species. *Inorg. Chem.* **2003**, *42*, 3016–3025.

(41) Song, B.; Yu, B. S. Fluorine-^{19}NMR Spectroscopic Studies of Phenyl-Fluorinated Iron Tetraarylporphyrin Complexes. *Bull. Korean Chem. Soc.* **2003**, *24*, 981–985.

(42) Thompson, D. W.; Kretzer, R. M.; Lebeau, E. L.; Scaltrito, D. V.; Ghiladi, R. A.; Lam, K. C.; Rheingold, A. L.; Karlin, K. D.; Meyer, G. J. Synthesis, Characterization, and Laser Flash Photolysis Reactivity of a Carbonmonoxy Heme Complex. *Inorg. Chem.* **2003**, *42*, 5211–5218.

(43) Berto, T. C.; Praneeth, V. K. K.; Goodrich, L. E.; Lehnert, N. Iron-Porphyrin NO Complexes with Covalently Attached N-Donor Ligands: Formation of a Stable Six-Coordinate Species in Solution. *J. Am. Chem. Soc.* **2009**, *131*, 17116–17126.

(44) Kryachko, E.; Scheiner, S. CH···F Hydrogen Bonds. Dimers of Fluoromethanes. *J. Phys. Chem. A* **2004**, *108*, 2527–2535.

(45) Rohde, J.-U.; In, J.-H.; Lim, M. H.; Brennessel, W. W.; Bukowski, M. R.; Stubna, A.; Münck, E.; Nam, W.; Que, L. Crystallographic and Spectroscopic Characterization of a

Nonheme Fe(IV)=O Complex. *Science* **2003**, *299*, 1037–1039.

(46) England, J.; Guo, Y.; Farquhar, E. R.; Young, V. G.; Münck, E.; Que, L. The Crystal Structure of a High-Spin Oxoiron(IV) Complex and Characterization of Its Self-Decay Pathway. *J. Am. Chem. Soc.* **2010**, *132*, 8635–8644.

(47) Hayes, R. G.; Ellison, M. K.; Scheidt, W. R. Definitive Assignment of the g Tensor of [Fe(OEP)(NO)] by Single-Crystal EPR. *Inorg. Chem.* **2000**, *39*, 3665–3668.

(48) Wang, J.; Schopfer, M. P.; Puiu, S. C.; Sarjeant, A. A. N.; Karlin, K. D. Reductive Coupling of Nitrogen Monoxide (•NO) Facilitated by Heme/Copper Complexes. *Inorg. Chem.* **2010**, *49*, 1404–1419.

(49) Wasser, I. M.; Huang, H. W.; Moe, P.; Karlin, K. D. Heme / Non-Heme Diiron(II) Complexes and O_2 , CO , and NO Adducts as Reduced and Substrate-Bound Models for the Active Site of Bacterial Nitric Oxide Reductase. *J. Am. Chem. Soc.* **2005**, *127*, 3310–3320.

(50) Praneeth, V. K. K.; Neese, F.; Lehnert, N. Spin Density Distribution in Five- and Six-Coordinate Iron(II)-Porphyrin NO Complexes Evidenced by Magnetic Circular Dichroism Spectroscopy. *Inorg. Chem.* **2005**, *44*, 2570–2572.

(51) Schopfer, M. P.; Mondal, B.; Lee, D. H.; Sarjeant, A. A. N.; Karlin, K. D. Heme/O_2/•NO Nitric Oxide Dioxygenase (NOD) Reactivity: Phenolic Nitration via a Putative Heme-Peroxynitrite Intermediate. *J. Am. Chem. Soc.* **2009**, *131*, 11304–11305.

(52) Chufán, E. E.; Puiu, S. C.; Karlin, K. D. Heme-Copper/Dioxygen Adduct Formation, Properties, and Reactivity. *Acc. Chem. Res.* **2007**, *40*, 563–572.

(53) Ghiladi, R. A.; Kretzer, R. M.; Guzei, I.; Rheingold, A. L.; Neuhold, Y.-M.; Hatwell, K. R.; Zuberbühler, A. D.; Karlin, K. D. (F_8TPP)Fe^{II}/O_2 Reactivity Studies {F_8TPP =

Tetrakis(2,6-Difluorophenyl)Porphyrinate(2−)}: Spectroscopic (UV−Visible and NMR) and Kinetic Study of Solvent-Dependent (Fe/O_2 = 1:1 or 2:1) Reversible O_2-Reduction and Ferryl Formation. *Inorg. Chem.* **2001**, *40*, 5754–5767.

(54) Garcia-Bosch, I.; Sharma, S. K.; Karlin, K. D. A Selective Stepwise Heme Oxygenase Model System: An Iron(IV)-Oxo Porphyrin π-Cation Radical Leads to a Verdoheme-Type Compound via an Isoporphyrin Intermediate. *J. Am. Chem. Soc.* **2013**, *135*, 16248–16251.

(55) Kim, E.; Shearer, J.; Lu, S.; Moeenne-Loccoz, P.; Helton, M. E.;Kaderli, S.; Zuberbuehler, A. D.; Karlin, K. D. Heme/Cu/O_2 Reactivity: Change in Fe^{III}-(O_2^{2-})-Cu^{II} Unit Peroxo Binding Geometry Effected by Tridentate Copper Chelation. *J. Am. Chem. Soc.* **2004**, *126*, 12716–12717.

(56) Kamaraj, K.; Kim, E.; Galliker, B.; Zakharov, L. N.; Rheingold, A. L.; Zuberbu, A. D.; Karlin, K. D. Copper(I) and Copper(II) Complexes Possessing Cross-Linked Imidazole-Phenol Ligands : Structures and Dioxygen Reactivity. *J. Am. Chem. Soc.* **2003**, *125*, 6028–6029.

Chapter 3

Heme-Cu Binucleating Ligand Supports Heme/O_2 and Fe^{II}–Cu^{I}/O_2 Reactivity Providing High- and Low-Spin Fe^{III}-Peroxo-Cu^{II} Complexes

---

This work was co-authored with the following authors and is published under the following citation:

Hyun Kim,[†] Savita K. Sharma,[†] Andrew W. Schaefer,[‡] Edward I. Solomon,*[,‡] and Kenneth D. Karlin*[,†]

[†]Department of Chemistry, Johns Hopkins University, Baltimore, Maryland 21218, USA

[‡]Department of Chemistry, Stanford University, Stanford, California 94305, USA

Inorg. Chem. **2019**, *58*, 15423–15432

3.1 Introduction

Heme-copper oxidases (HCOs), the terminal enzyme of the respiratory chain in the mitochondrial inner membrane from mammalian and bacterial sources, reduces dioxygen to water, coupling the redox energy to membrane proton translocation utilized for ATP synthesis.[1–10] The enzyme possesses five key redox-active metal ion centers, dicopper complex Cu_A, which is a binuclear electron-transfer center, a low-spin heme *a* (cytochrome *a*), and the heterobinuclear (Fe_{a3}/Cu_B) active site, where dioxygen binding and reduction occurs.[1–10] The latter (Scheme 3.1) consists of a high-spin heme and a neighboring (~ 4.5–5.0 Å) copper ion possessing three histidine imidazole nitrogen ligands, one of which is cross-linked to a tyrosine (Tyr) residue biosynthesized via a post-translational modification.[11–16] With a focus on the heme/Cu active site in varying redox or ligation states, structural aspects and the O_2-reduction mechanism have been studied extensively, utilizing many spectroscopic methods,[1–10] X-ray crystallography[17,18] and computational approaches.[19]

The current state of our understanding of early stages in the C*c*O O_2-binding and reduction are given in Scheme 3.1. Molecular oxygen reacts with a fully reduced $Fe^{II}\cdots Cu^{I}$ binuclear active site, initially forming a detectable, transient, Fe–O_2 ("oxy-heme") adduct, formally a Fe^{III}–($O_2^{\cdot -}$) (A) species possessing end-on superoxide binding. This assignment is consistent with resonance Raman (rR) spectroscopic properties, as being similar to those found in oxy-hemoglobin (ν_{Fe-O} = 567 cm^{-1}) and oxy-myoglobin (ν_{Fe-O} = 570 cm^{-1}).[20,21]

Intermediate **A** rapidly undergoes O–O cleavage to yield $\mathbf{P_M}$.[22] A total of four electrons are required to fully reductively cleave the O–O bond of dioxygen. Three electrons are provided by the binuclear site (two from iron ($Fe^{II} \rightarrow Fe^{IV}$) and one from Cu_B

($Cu^{I} \rightarrow Cu^{II}$)). It is now accepted that the fourth electron derives from the phenol residue of the nearby His-Tyr cross-link. This phenol residue serves as an overall hydrogen atom donor (H•), leaving $\mathbf{P_M}$ formulated as a Fe^{IV}=O/Cu^{II}–OH/Tyr$^{\bullet}$ moiety, i.e., thus with a ferryl-oxo (Fe_{a3}^{IV}=O; ν(Fe–O) = 804 cm^{-1}), cupric-hydroxide (Cu_B^{II}–OH) and a tyrosyl radical (Scheme 3.1).[6,8,10] Also, evidence suggests that the His-Tyr cross-link enables enzyme Cu_B incorporation and stabilizes the precise geometry of the binuclear active site.[11,16]

On the basis of biochemical experiments,[23] computational studies[24–27] and synthetic modeling,[5,10] a peroxo-bridged heterobinuclear Fe^{III}–(O_2^{2-})–Cu^{II} ($\mathbf{I_P}$) has been predicted as an intermediate species occurring on the pathway from **A** to $\mathbf{P_M}$. This peroxo moiety critically precedes O–O bond cleavage via initial H-bonding or protonation,[19] possibly through a water molecule bridge, as shown in Scheme 3.1.

Scheme 3.1 Proposed O–O Reductive Cleavage Mechanism by Heme-Copper Oxidases for Cytochrome *c* Oxidase

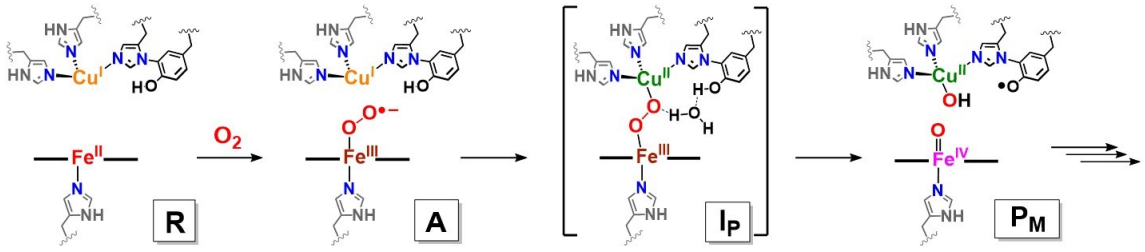

Design and construction of heme/copper synthetic models provide critical information about structure, spectroscopy and reactivity relevant to C*c*O enzyme mechanism, in the usual manner that models contribute to scientific advances, allowing a

breakdown and attention to particular aspects of the protein structure/function. With respect to dioxygen reactivity, reduced heme-copper assemblies (or components) have been shown to generate heme-Fe^{III}-superoxide entities (like intermediate **A**, Scheme 3.1), see complexes from Collman[28] and Naruta[29] and their co-workers, Figure 3.1. Other studies from Naruta[30] and our laboratories[31,32] have revealed that peroxo-bridged heme-Fe^{III}–(O_2^{2-})–Cu^{II}(ligand) complexes can be generated possessing three structural types[10] (high-spin (HS) μ-η^2:η^1-peroxo (C, D),[30,31,33] HS μ-η^2:η^2-peroxo (E)[31,32] and low-spin (LS) μ-1,2-peroxo (F))[10,34] (Figure 3.1). Collman's investigations involving elegant binucleating (for Fe and Cu) ligands, demonstrated efficient electrocatalytic four-electron four-proton O_2-reduction to water (ORR),[35] and stoichiometric studies where a phenol H-atom donor could reductively cleave the O–O bond of a heme-O_2-Cu construct.[36] We have developed similar model systems with simpler compounds, i.e., complex **D**, (Figure 3.1) which effect efficient electrocatalytic ORR chemistry.[37,38]

In stoichiometric reactivity studies, detailed synthetic and theoretical/computation insights have been obtained concerning elements critical for reductive cleavage of heme-Cu bound O_2 (as peroxide) intermediate. However, many details and fundamental aspects have not been elucidated or fully understood. These include the exact structural requirements for the Fe–O–O–Cu moiety, tridentate versus tetradentate Cu-chelation, factors such as H-bonding to a peroxide O-atoms (which one?) versus actual protonation, the origin and pK_a of the proton-donor, the timing of electron versus proton injection, and so on. Thus far, for heme-Cu–O_2 constructs, very small changes in the local (ligand) environment may lead to absolutely varying chemistry, and there is a need to understand these effects in obtaining fundamental insights. For example, **LS-3DCHIm** (F) and **LS-**

4DCHIm (G) (Figure 3.1), which differ by only one DCHIm Cu-ligand, behave completely differently toward proton-electron sources. The former is completely unreactive, while the latter, in the presence of an H-bonding phenol, undergoes clean peroxide O–O reductive cleavage to give water.[10,19,34,39]

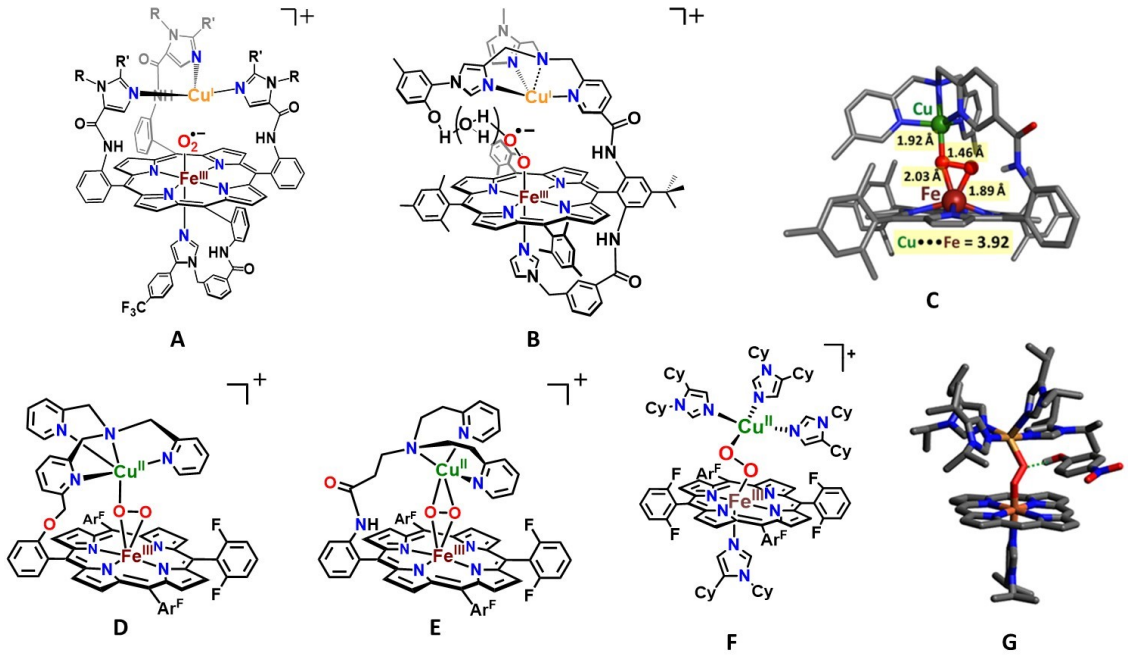

Figure 3.1 Various complexes of heme/copper synthetic models: superoxide heme-Fe^{III}–($O_2^{\bullet-}$)···Cu^{I}(ligand) complexes, (**A**, Collman's group; **B**, Naruta's group). Heme-Fe^{III}–(O_2^{2-})–Cu^{II}(ligand) complexes: X-ray crystal structure of Naruta's HS μ-η^2:η^1-peroxo-bridged complex (**C**: adapted from ref 26); Karlin group analog (**D**); μ-η^2:η^2-peroxo compound (**E**); LS heme peroxo adducts with a μ-1,2-peroxo structure type, **LS-3DCHIm** (**F**); DFT-calculated structure for [**LS- 4DCHIm**(ArOH)] (**G**: adapted from ref 30), a phenol adduct.

From these perspectives, considerable further studies and advancements are needed. These include a continued effort to define the dioxygen reactivity of reduced heme-copper assemblies, while also if possible, elucidating the heme only and (ligand)-Cu O_2-chemistry.

For further elaborated/new heme-O_2–Cu species, subsequent defining of O–O reductive cleavage chemistry is a longer-term goal, in the contexts mentioned above.

In the present study, we report on an advanced C*c*O active site model system with binucleating ligand P^{ImH}; this employs a new tridentate ligand which includes a histamine moiety appended to the periphery of a fluorinated tetraphenylporphyrin. The Fe^{II}-porphyrinate complex $(P^{ImH})Fe^{II}$ (**1**), is shown in Chart 3.1.[40] Herein, we report the oxygenation chemistry of **1**, whose chemistry mimics the initial O_2 binding in C*c*O, as well as (of course) formation of oxy-hemoglobin and -myoglobin. The generation of a heme-copper derivative of **1** has been accomplished and oxygenation of the reduced Fe^{II}–Cu^{I} form gives a high-spin heme-peroxo-copper product. Lastly, addition of DCHIm as a heme axial ligand to the high-spin solution leads to low-spin complex. All complexes have been spectroscopically characterized by UV-vis, ^{2}H-NMR and EPR spectroscopies; for the O_2 derived complexes, vibrational data has been obtained using rR.

Chart 3.1 C*c*O active site model system

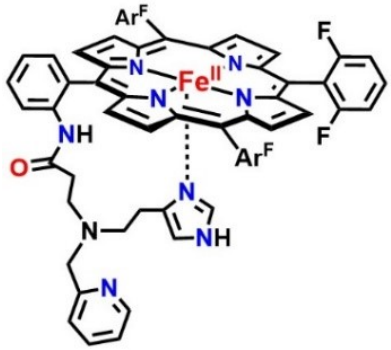

$(P^{ImH})Fe^{II}$ (**1**)

3.2 Results and discussion

3.2.1 Dioxygen reactivity of (P^{ImH})Fe^{II} (1)

Complex **1** reacted with dioxygen to form a low-temperature stable superoxide level intermediate, which was characterized by UV-vis, ^{2}H NMR, rR and EPR spectroscopies. Bubbling dry O_2 through a solution of (P^{ImH})Fe^{II} (**1**) {λ_{max} = 419, 526 and 552(sh) nm} in THF at –80 °C led to new features at 424 and 541 nm which were ascribed to a (P^{ImH})Fe^{III}–($O_2^{\bullet-}$) (**2**), Figure 3.2. Further characterization of the **1**/O_2 reaction product comes from low temperature ^{2}H-NMR spectroscopic investigation, employing a deuterated (β-pyrrolic hydrogens) analog of **2** (**2**-d_8) in THF solvent (Figure 3.3). It confirms the proposed formation of a myoglobin-like Fe^{III}-superoxide complex. Complex **2** gives rise to a diamagnetic spectrum (δ = 9.12 ppm), consistent with the formation of (P^{ImH})Fe^{III}–($O_2^{\bullet-}$) (**2**-d_8) and suggesting a low-spin (S = 0) six-coordinate iron.[41] As expected for a diamagnetic species, complex **2** is EPR silent. The literature on hemoglobin and model compounds has generally proposed that the unpaired electron of the low-spin Fe^{III} ion is antiferromagnetically coupled with the unpaired electron of the superoxide radical anion, making the complex diamagnetic.[41] It should be noted, however, that recent X-ray spectroscopic data have shown the electronic structure to more closely resemble Fe^{II}–(O_2) in a similar model system, while oxy-hemoglobin has more Fe^{III}–($O_2^{\bullet-}$) character (although not fully to the low-spin ferric level).[42] Nevertheless, the latter notation is used here for clarity.

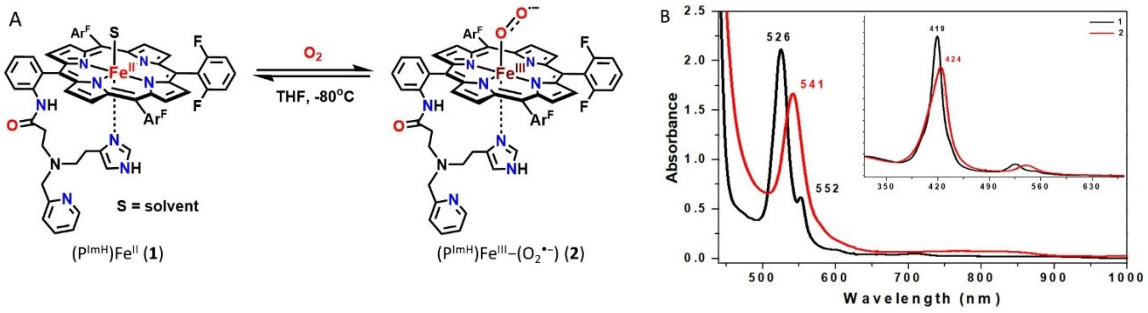

Figure 3.2 (A) Reaction scheme showing reversible ferric heme superoxide (**2**) formation by bubbling $O_{2(g)}$ into a solution of fully reduced complex **1**. (B) UV-vis spectra (THF at –80 °C) of the deoxygenation reaction of **1**. Shown are spectra of complex **1** (black) and **2** (red).

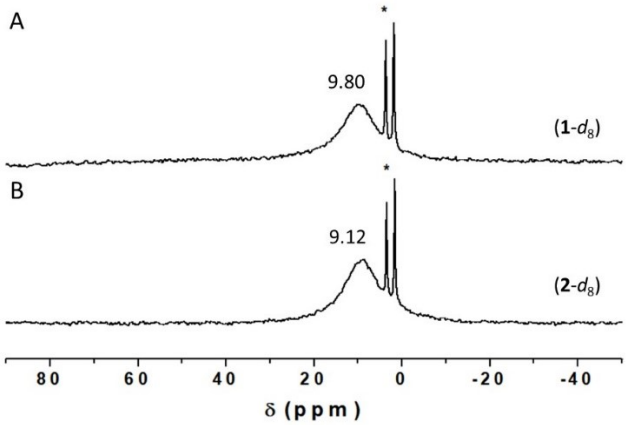

Figure 3.3 ^{2}H NMR spectra of (A) d_8-(P^{ImH})Fe^{II} (**1**-d_8) and (B) d_8-(THF)(P^{ImH})Fe^{III}–($O_2^{\bullet-}$) (**2**-d_8) in THF at –80 °C. The sharp peaks at δ 3.58 and 1.73 ppm correspond to solvent THF.

We postulate that the sixth axial ligand present in **2** is the imidazolyl group of the tridentate tether in P^{ImH} (see Chart 3.1). We base this conclusion on our previous X-ray crystallographic finding that in a six-coordinate iron(II) complex with P^{ImH}, also containing a strong isocyanide donor ligand DIMPI (2,6-dimethylphenyl isocyanide), [(P^{ImH})Fe^{II}–DIMPI], the free imidazole group binds strongly (Fe-N_{Im} = 2.024 Å) as the axial ligand trans to DIMPI (see diagram below).[40]

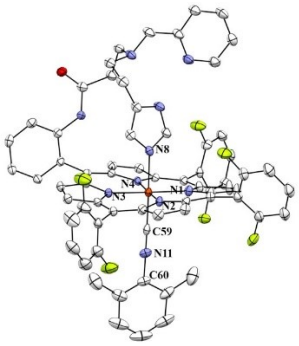

The O_2-binding to **1** was reversible, as we have found for some other heme-Fe(II) O_2-adducts with porphyrinates possessing electron-withdrawing fluorine-substituents,[43] where warming a solution of **2** to room temperature in a closed system allows for release of dioxygen and regeneration of $(P^{ImH})Fe^{II}$ (**1**), to the extent of ~ 80%. Cooling of this solution (without further addition of O_2) to –80 °C leads to close to full regeneration of $(P^{ImH})Fe^{III}–(O_2^{\bullet-})$ (**2**). Dioxygen binding cycling in this manner illustrated in the Figure 3.4. Several cycles of the reversible O_2-binding process could be monitored by UV-vis spectroscopy.

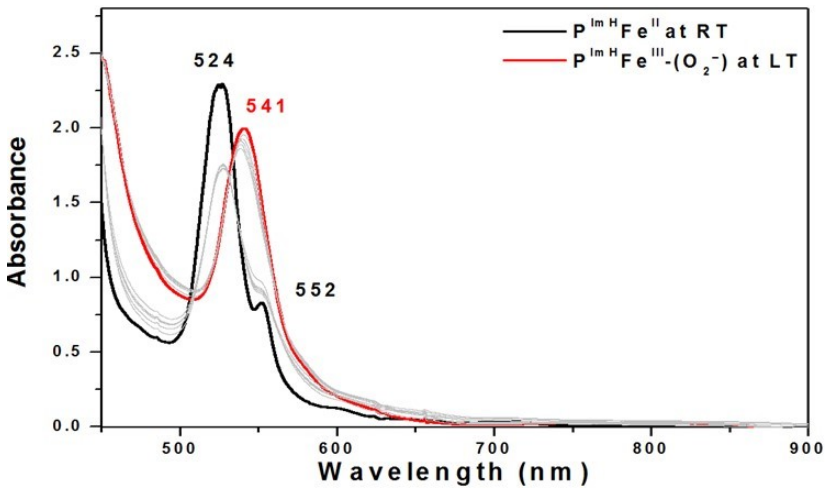

Figure 3.4 Reversible dioxygen binding to $(P^{ImH})Fe^{II}$ (**1**) (black) yielding $(P^{ImH})Fe^{III}–(O_2^{\bullet-})$ (**2**) (red) in THF. Spectra shown in grey are generated during the transformation. It was repeated five times.

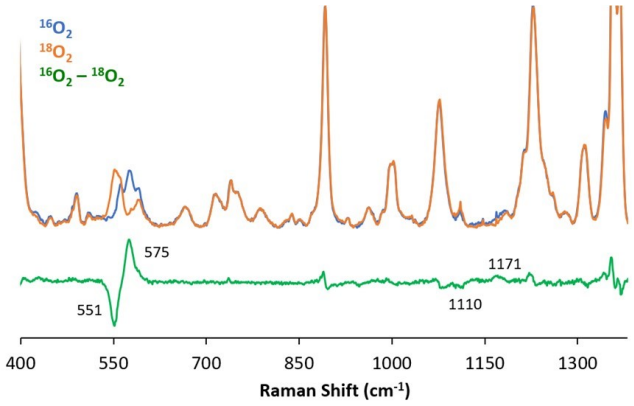

Figure 3.5 Resonance Raman spectra of ferric superoxide complex (P^{ImH})Fe^{III}–($O_2^{\bullet-}$) (**2**) in frozen THF obtained at 77 K with 413 nm excitation: Fe–O and O–O stretching frequencies for the complex generated with $^{16}O_2$ (blue) or $^{18}O_2$ (orange). The $^{16}O_2$–$^{18}O_2$ difference spectrum is shown in green.

Complex (P^{ImH})Fe^{III}–($O_2^{\bullet-}$) (**2**) was further characterized by rR spectroscopy (Figure 3.5). In the lower-frequency region, a ν_{Fe-O} stretch is detected at 575 cm^{-1} which is similar to that of other known "oxy-heme" Fe^{III}–($O_2^{\bullet-}$) synthetic models with a nitrogen axial ligand.[10,41,44] This Fe–O stretch shifts down by 24 cm^{-1} upon $^{18}O_2$ substitution. An oxygen isotope-sensitive feature corresponding to the O–O stretch was detected at ν_{O-O} = 1171 cm^{-1}, which shifted to 1110 cm^{-1} with $^{18}O_2$. With the hemes that our research group has utilized, having 3 or 4 of the meso-aryl groups possessing 2,6-difluoro substituents, we have observed O–O stretches at similar frequencies (Table 3.1). Also consistent with the assignments is our finding that the ν_{Fe-O} and ν_{O-O} of $^{16}O/^{18}O$ isotope shifts (vide supra) closely match those calculated using the harmonic oscillator model: $\Delta_{calcd\ Fe-O}$ ($^{16}O_2/^{18}O_2$) = –26 cm^{-1}, $\Delta_{calcd\ O-O}$ ($^{16}O_2/^{18}O_2$) = –67 cm^{-1}. However, it is quite common that this vibrational mode of dioxygen-bound heme complexes is not observable.[10,28,45] Table 3.1 lists examples from our own investigations, along with several protein and synthetic oxy-

heme (Fe^{III}-superoxide) complexes, where ν_{O-O} is observed. A more complete listing can be found elsewhere.[10]

Table 3.1 rR stretching frequencies (cm^{-1}) of heme-Fe^{III}-superoxide complexes

complex[a]	ν_{O-O} ($\Delta^{18}O_2$)	ν_{Fe-O} ($\Delta^{18}O_2$)	ref
Mb WT	1103	578 (−29)	46
Cyt P450 WT	1139 (−66)	546 (−31)	47
Cyt P450 D251N	1136 (−66)	537 (−30)	48
$(THF)(F_8)Fe^{III}–(O_2^{\bullet-})$	1178 (−64)	568 (−24)	49
$(^6L)Fe^{III}–(O_2^{\bullet-})$	1176 (−64)	572 (−24)	33
$(P^{Im})Fe^{III}–(O_2^{\bullet-})$	1180 (−56)	575 (−23)	50
$(P^{ImH})Fe^{III}–(O_2^{\bullet-})$ (**2**)	1171 (−61)	575 (−24)	this work
$[(\alpha_4Fe(CO_2Me)_4)O_2^{\bullet-}]$	1004(−53) 967 (−56)	581 (−22)	51
$[(Fe^{III}(OPhP))–O_2^{\bullet-}]$	1147 (−59)	570 (−22)	44

[a]Mb WT, wild-type myoglobin; Cyt P450 WT, wild-type cytochrome P-450 monooxygenase (P450); P450 Asp-251 mutated to Asn. See Figure 3.6 for diagrams of the other synthetic $Fe^{III}–(O_2^{\bullet-})$ complexes.

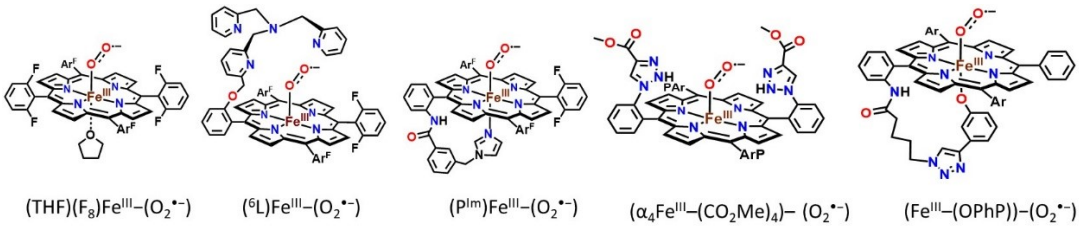

Figure 3.6 Diagrams of heme-Fe^{III}-superoxide synthetic model systems.[33,44,49–51]

3.2.2 Generation of a reduced Heme–Cu complex using P^{ImH}

Addition of 1 equiv of $[Cu^I(CH_3CN)_4](B(C_6F_5)_4)$ to the reduced complex $(P^{ImH})Fe^{II}$ (**1**) led to the desired reduced heterobinuclear Fe^{II}/Cu^I compound $[(P^{ImH})Fe^{II}Cu^I]^+$ (**3**), which had prominent UV-vis absorptions at 423 and 542 nm at low temperature (Figure 3.7). An asymmetry in pyrrole resonances of reduced complex **1** is observed in ^{1}H-NMR spectroscopy, where different chemical shifts for inequivalent porphyrin phenyl substituents leads to observation of two peaks (at δ 50 and 59 ppm) (Figure 3.8). Addition

of the copper(I) ion leads to disappearance of upfield shifted resonances (< 0 ppm) which we assign as being derived from methylene hydrogen atoms of the tethered histamine group. Since the copper ion takes up (i.e., binds to) the tridentate chelate from this complex, the imidazolyl group of the histamine arm is no longer bound to the iron center. The pyrrolic protons in ^{2}H-NMR spectroscopy at –80 °C resonate at δ 89.4 and 102.8 ppm, typical of a five-coordinate high-spin ferrous heme (Figure 3.9A). Complex **3** is EPR silent.

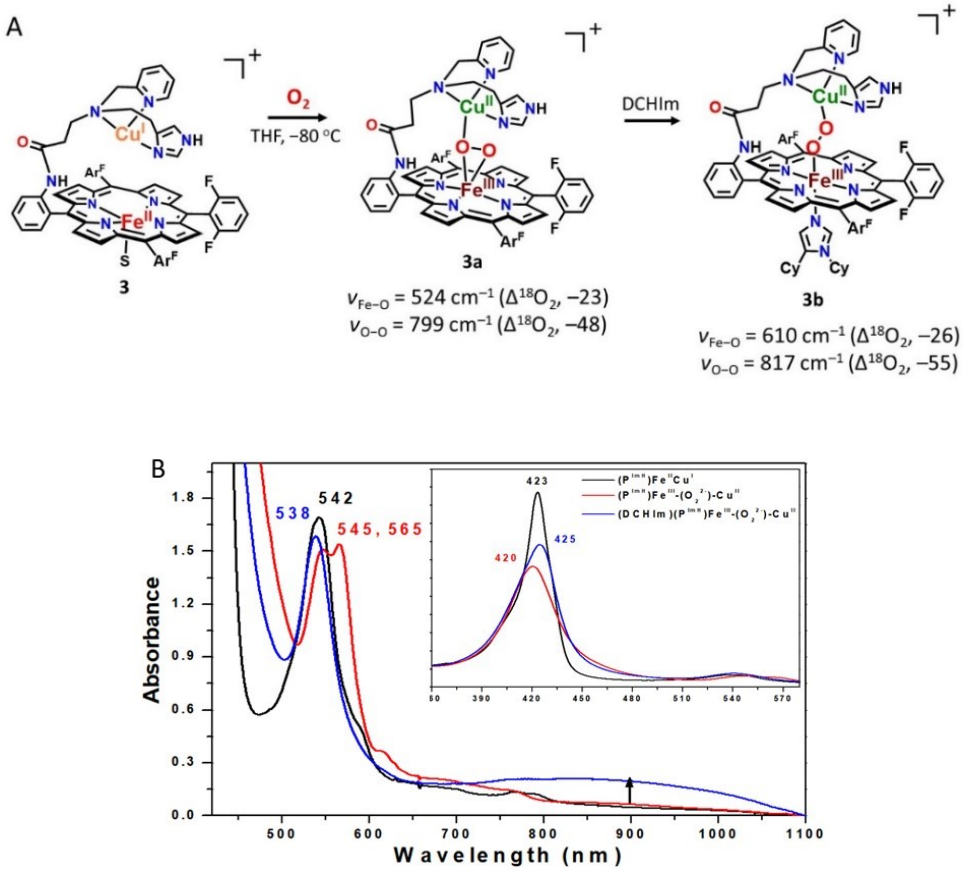

Figure 3.7 (A) Overall scheme for reactivity of $[(P^{ImH})Fe^{II}Cu^{I}]^{+}$ (**3**) toward $O_{2(g)}$ at –80 °C in THF to yield a HS peroxo species $[(P^{ImH})Fe^{III}–(O_2^{2–})–Cu^{II}]^{+}$ (**3a**) and LS peroxo complex $[(DCHIm)(P^{ImH})Fe^{III}–(O_2^{2–})–Cu^{II}]^{+}$ (**3b**) following addition of DCHIm. (B) UV-vis spectra (–80 °C) for in situ generated HS **3a** (red) and LS **3b** (blue) starting following oxygenation of **3** (black).

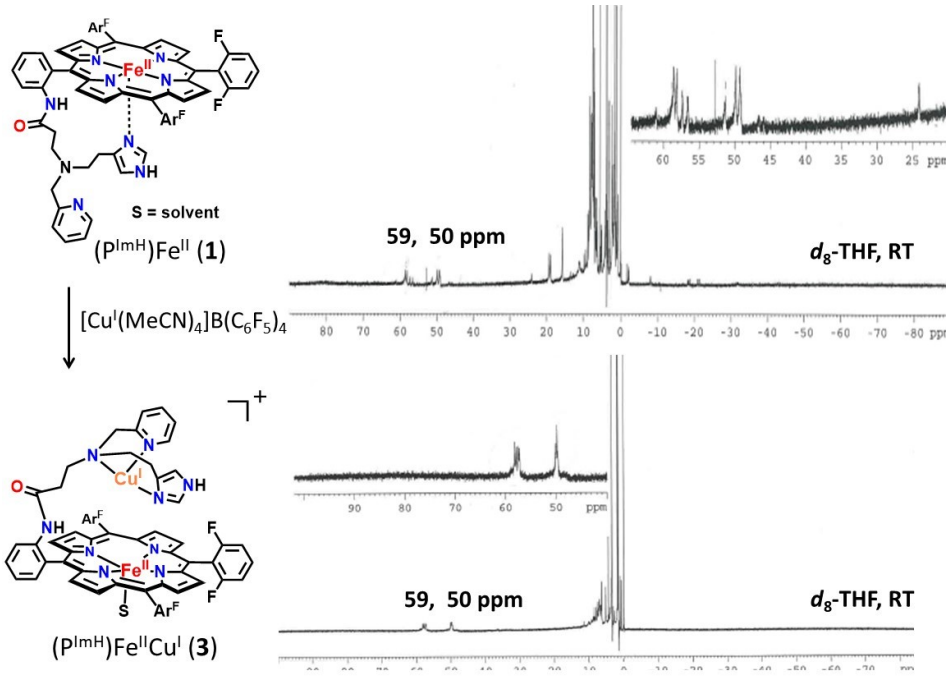

Figure 3.8 ^{1}H-NMR spectrum of (top) complex (P^{ImH})Fe^{II} (**1**) and (bottom) (P^{ImH})$Fe^{II}Cu^{I}$ (**3**) at room temperature.

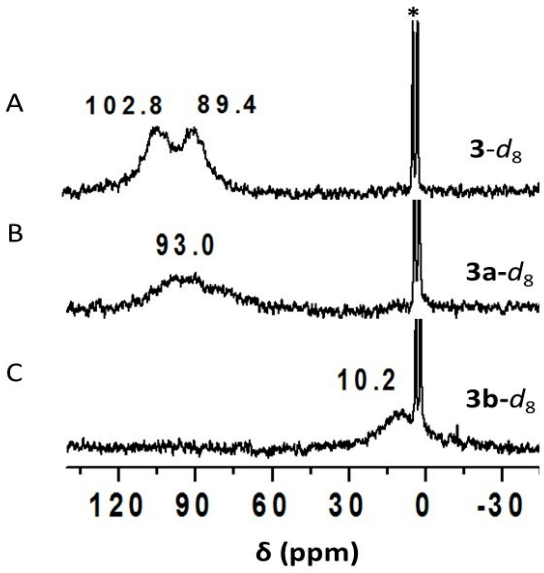

Figure 3.9 ^{2}H-NMR spectra of (A) in situ generation of d_8-[(P^{ImH})$Fe^{II}Cu^{I}$]$^{+}$ (**3**-d_8); (B) d_8-[(P^{ImH})Fe^{III}–(O_2^{2-})–Cu^{II}]$^{+}$ (**3a**-d_8) generated by bubbling O_2; (C) d_8-[(DCHIm)(P^{ImH})Fe^{III}–(O_2^{2-})–Cu^{II}]$^{+}$ (**3b**-d_8) generated by the reaction of **3a**-d_8 with DCHIm. The strong sharp peaks at δ 1.73 and 3.58 ppm correspond to solvent THF.

3.2.3 Generation of the high-spin heme–peroxo–Cu complex

Addition of dry $O_{2(g)}$ to the THF solution of fully reduced heterobinuclear heme-copper complex $[(P^{ImH})Fe^{II}Cu^{I}]^{+}$ (**3**) at low-temperature resulted in the formation of new species $[(P^{ImH})Fe^{III}–(O_2^{2–})–Cu^{II}]^{+}$ (**3a**) with UV-vis spectral features at 420, 545 and 565 nm (Figure 3.7B), notably with two Q-band features. These characteristics are the same as those known for other previously well-characterized high-spin heme–peroxo–Cu complexes also with tridentate ligands on the copper ion. (Figure 3.7A).[10,31,32,49,52,53]

To provide more detail concerning the structure of $[(P^{ImH})Fe^{III}–(O_2^{2–})–Cu^{II}]^{+}$ (**3a**), we carried out rR spectroscopy (Figure 3.10) and found that the peroxo ligand $\nu_{O–O}$ vibration is observed at 799 $cm^{–1}$; this shifts to 751 $cm^{–1}$ upon $^{18}O_2$ substitution. In addition, a band at 524 $cm^{–1}$ ($\Delta^{18}O_2 = –23$ $cm^{–1}$) is assigned to $\nu_{Fe–O}$ for this peroxide complex. Again, as discussed above for $(P^{ImH})Fe^{III}–(O_2^{\bullet–})$ (**2**), observed isotope frequency shifts when using $^{18}O_2$ match well with values calculated using the harmonic oscillator model ($\Delta_{calcd\ O–O}$ ($^{16}O_2/^{18}O_2$) = –46 $cm^{–1}$, $\Delta_{calcd\ Fe–O}$ ($^{16}O_2/^{18}O_2$) = –23 $cm^{–1}$), corroborating our assignments. While the UV-vis features for **3a** are most like high-spin heme-peroxo complexes with tridentate chelates bound to copper(II) (vide supra), we note that the $\nu_{O–O}$ value observed for **3a** (799 $cm^{–1}$) is much higher in energy than that found for the three other examples we have previously studied, which have tridentate ligands on the Cu(II) ion and where side-on μ-η^2:η^2–$O_2^{2–}$ binding to both Fe(III) and Cu(II) occurs, $\nu_{O–O}$ = 747–767 $cm^{–1}$.[31,32,49,54] In copper-dioxygen coordination chemistry, ligand denticity induces different O_2 (as peroxide, $O_2^{2–}$) binding modes;[55–57] Cu^{I}-chelates with tridentate ligands prefer a side-on binding mode with a resulting peroxide ligand, giving $[(L)Cu^{II}–(\mu$-η^2:η^2-$O_2^{2–})–Cu^{II}(L)]^{2+}$ binuclear

complexes whereas with tetradentate ligands (L)Cu^{I} complexes react with O_2 to give end-on binding, i.e., [(L)Cu^{II}–(μ-1,2-O_2^{2-})–Cu^{II}(L)]$^{2+}$ species.

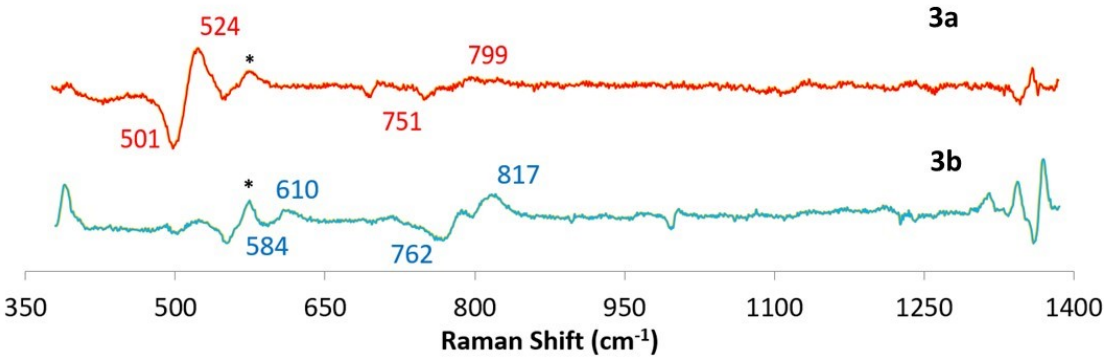

Figure 3.10 rRaman data ($^{16}O_2$–$^{18}O_2$ difference) collected at 413 nm excitation and 77 K for HS **3a** and LS **3b**. Complex **2** is present as an impurity, observed as a set of $^{16}O_2$/$^{18}O_2$ peaks at 575/550 cm^{-1} (marked with an asterisk).

Chart 3.2 HS/LS-TMPA heme-peroxo-copper complexes

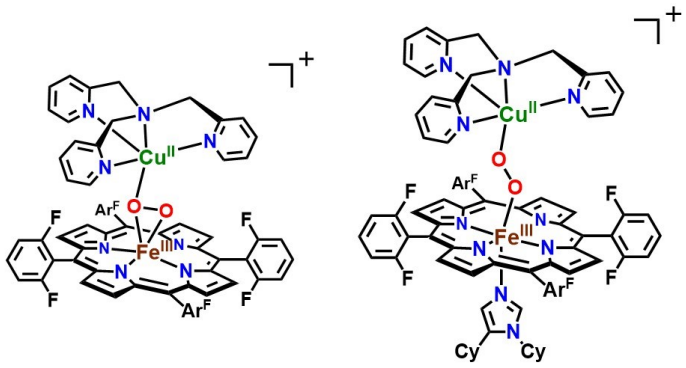

ν_{Fe-O} = 538 cm^{-1} ($\Delta^{18}O_2$, −22)
ν_{O-O} = 804 cm^{-1} ($\Delta^{18}O_2$, −43)

ν_{Fe-O} = 623 cm^{-1} ($\Delta^{18}O_2$, −27)
ν_{O-O} = 812 cm^{-1} ($\Delta^{18}O_2$, −50)

However, these **3a** vibrations (ν_{Fe-O} = 524 cm^{-1}; ν_{O-O} = 799 cm^{-1}; Figure 3.9) are very close to those previously reported for the **HS-TMPA** heme-peroxo-copper complex (Chart 3.2). For this complex with tetradentate chelate bound to copper, ν_{O-O} = 804 cm^{-1}, and the peroxo unit is bound side-on to the high-spin Fe^{III}, but end-on to the Cu^{II}, for an

overall μ-η^2:η^1 coordination mode that has been supported by EXAFS spectroscopy and DFT calculations.[39,58] We posit that the P^{ImH} tridentate chelate induces considerable geometric distortion in the Cu(II) coordination sphere, which results in the peroxo binding to Cu in an essentially η^1 fashion. Thus, we postulate that **3a** possesses a μ-η^2:η^1-peroxo coordination, formulated as $[(P^{ImH})Fe^{III}–(\mu\text{-}\eta^2\text{:}\eta^1\text{-}O_2^{2–})–Cu^{II}]^+$, as shown in Figure 3.7A.

On the basis of past extensive NMR spectroscopic studies on $[(F_8)Fe^{III}–X–Cu^{II}(TMPA)]^+$ (X = $O^{2–}$, $OH^–$; TMPA = tris(2-pyridyl)methylamine),[59] the peroxo analog (X = $O_2^{2–}$),[58,60] and $[(^2L)Fe^{III}–(\mu\text{-}\eta^2\text{:}\eta^2\text{-}O_2^{2–})–Cu^{II}]^+$ [32,61] (shown as **E**, Figure 3.1), the further analog with tridentate chelates for Cu ion, [49,59,61,62] $[(P^{ImH})Fe^{III}–(O_2^{2–})–Cu^{II}]^+$ (**3a**) has an overall electronic structure where S = 2, derived from antiferromagnetic coupling of high-spin Fe^{III} (S = 5/2) and Cu^{II} (S = 1/2) centers. This assignment is further supported by its EPR silent behavior (12 K, in THF frozen solution). Further supporting the S = 2 electronic structure assignment, **3a** displays a pyrrole signal in the paramagnetic region at 93.0 ppm (−80 °C, THF; see Figure 3.9B), very similar to that observed for other HS complexes which are listed in Table 3.2. The 93.0 ppm pyrrole resonance is in the range expected for HS ferric iron.

Table 3.2 ^{2}H-NMR data and pyrrole chemical shifts of heme/copper dioxygen adducts or heme-peroxo-copper complexes[a]

complex	$\delta_{pyrrole}$	solvent	temp(K)	ref
D	92	acetone	193	63
$(F_8)Fe^{III}O_2Cu^{II}(L^{Me2N})$	105	CH_2Cl_2/6% EtCN	178	49
E	106	THF	183	61
$(F_8)Fe^{III}O_2Cu^{II}(L^{N4}OH)$	83	THF	213	64
HS-TMPA	68	MeCN	233	65
HS-AN	95	acetone	193	53
3a	93	THF	193	this work

[a]See the Figure 3.11 for figures of $(F_8)Fe^{III}O_2Cu^{II}(LMe_2N)$, $(F_8)Fe^{III}O_2Cu^{II}(LN_4–OH)$, and HS-AN and Chart 3.2 for HS-TMPA

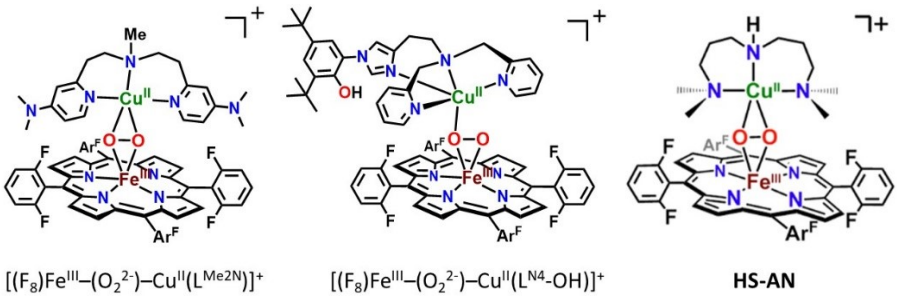

Figure 3.11 Figures of high-spin heme-peroxo-copper synthetic model systems.[49,53,64]

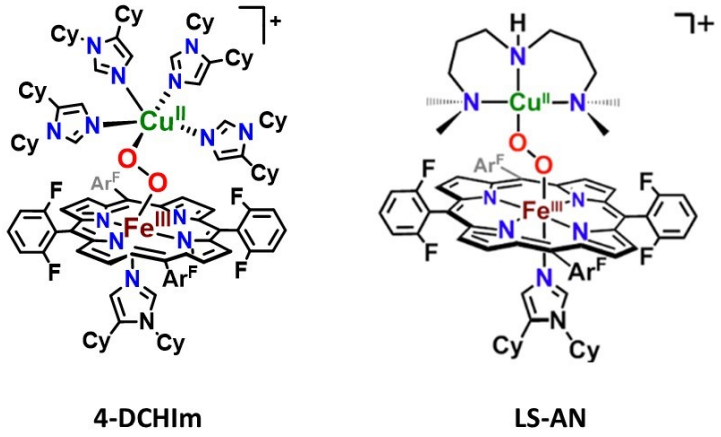

Figure 3.12 Diagrams of low-spin μ-1,2-peroxo configuration complexes.[34,39,66]

3.2.4 Generation of a low-spin heme–peroxo–Cu complex with P^{ImH}

A low-spin analog to $[(P^{ImH})Fe^{III}–(O_2^{2–})–Cu^{II}]^+$ (**3a**) was generated by the addition of axial base DCHIm in THF at −80 °C (Figure 3.7A). This resulted in a drastic change in the UV-vis features (Figure 3.7B). Relatively intense low-energy features observed at ~ 800-900 nm (assigned as peroxo-to-Fe LMCT bands) are characteristic of LS μ-1,2-peroxo species, as previously demonstrated for **F** and **G** (Figure 3.1) and in a number of other cases (see Figure 3.12 for **4-DCHIm** and **LS-AN**, and Chart 3.2 for **LS-TMPA**).[34,39,66] The addition of DCHIm resulted in clear Soret and Q-band shifts (from those observed in **3a**)

to 425 and 538 nm, respectively (Figure 3.7B). ^{2}H-NMR spectroscopy confirms the spin state change from high-spin **3a** (pyrrole signal at 93.0 ppm) to low-spin **3b** (pyrrole signal at 10.2 ppm, i.e., in the diamagnetic region; see Figure 3.9). This behavior suggests that in **3b**, there exists antiferromagnetic coupling between the low-spin (S = 1/2) six-coordinate Fe^{III} and the d^9 Cu^{II} (also S = 1/2) centers, through the peroxo bridge. Complex **3b** is EPR silent (12K, THF), also consistent with antiferromagnetic coupling and a resulting S = 0 electronic structure formulation.

Resonance Raman spectroscopic interrogation of LS compound $[(DCHIm)(P^{ImH})Fe^{III}–(O_2^{2–})–Cu^{II}]^+$ (**3b**) reveals the expected differences in $\nu_{Fe–O}$ and $\nu_{O–O}$ stretching vibrations in comparison to HS complex $[(P^{ImH})Fe^{III}–(O_2^{2–})–Cu^{II}]^+$ (**3a**) (Figure 3.10). Coordination of DCHIm to generate **3b** produced two isotope-sensitive peaks, an O−O vibration at 817 cm^{-1} ($\Delta^{18}O_2$ = –55 cm^{-1}) and an Fe−O stretch at 610 cm^{-1} ($\Delta^{18}O_2$ = –26 cm^{-1}). This observed $\nu_{Fe–O}$ ($^{16}O_2/^{18}O_2$) shift is close to expected value ($\Delta_{calcd\ Fe–O}$ ($^{16}O_2/^{18}O_2$) = –27 cm^{-1}) in the harmonic oscillator approximation. The magnitude of the isotope shift for $\nu_{O–O}$ (= –55 cm^{-1}) is a bit larger than the calculated value ($\Delta_{calcd\ O–O}$ ($^{16}O_2/^{18}O_2$) = –47 cm^{-1}), however it is still consistent with the assignment of this stretch to that of a peroxide ligand. Changing from HS (**3a**) to LS (**3b**) dramatically increases $\nu_{Fe–O}$ by 86 cm^{-1} (Figure 3.7A), while a smaller increase (18 cm^{-1}) is observed for $\nu_{O–O}$. Similar effects have been observed recently[39,67] for DCHIm binding and indicate a change in Fe spin state and Fe-peroxo coordination geometry. The relatively high $\nu_{O–O}$ stretch for the peroxo group in **3b** (compared to that of **3a**) indicates a LS μ-1,2-peroxo coordination mode in the former. Thus, **3b** is formulated as $[(DCHIm)(P^{ImH})Fe^{III}–(\mu\text{-}1,2\text{-peroxo–}O_2^{2–})–Cu^{II}]^+$ (shown in Figure 3.7A), based on our previous investigation and resulting

established structure of **LS-TMPA** (Chart 3.2), that has been supported by DFT calculations.[39]

3.3 Conclusions

we investigated the dioxygen reactivity of reduced heme (P^{ImH})Fe^{II} (**1**) in the absence and the presence of copper ion. Reaction of **1** and O_2 results in O_2-bound ferrous heme compound, (P^{ImH})Fe^{III}–($O_2^{\bullet-}$) (**2**), such as that found in oxygenated myoglobin and hemoglobin. ^{2}H-NMR suggests that **2** is low-spin six-coordinate iron. The evidence points to the imidazolyl group of the appended tridentate chelate as serving as an axial ligand base. Addition of Cu(I) ion leads to a new reduced heme-copper complex (P^{ImH})$Fe^{II}Cu^{I}$ (**3**), an advanced C*c*O active site model system due to (i) its tridentate ligand Cu^{I}-binding and (ii) the imidazolyl ligand has a free N–H group (see below). At low temperature, dioxygen reaction with **3** gives a high-spin species [(P^{ImH})Fe^{III}–(μ-η^2:η^1-O_2^{2-})–Cu^{II}]$^+$ (**3a**) and addition of DCHIm as an axial ligand changes the peroxo coordination to end-on, resulting in formation of LS species with end-on peroxo coordination, [(DCHIm)(P^{ImH})Fe^{III}–(μ-1,2-O_2^{2-})–Cu^{II}]$^+$ (**3b**).

This oxygenation chemistry with (P^{ImH})Fe^{II} (**1**) lays the groundwork for a better understanding of $Fe^{II}/Cu^{I}/O_2$ reactions chemistry. Our ongoing studies are focused on investigating the reductive O–O cleavage relevant to C*c*O enzyme active site chemistry of heme-(O_2^{2-})-Cu complexes by employing systematically varied H^+/e^- sources. Also, since P^{ImH} has a built-in imidazole and tridentate system in copper chelation as occurs in C*c*O, another goal of our research is to mimic the post-translational modification which occurs

in C*c*O, that being formation of a histidine-tyrosine cross-link which is functionally critical[16] (see the Introduction).

3.4 Experimental section

3.4.1 Materials and methods

All reagents and solvents purchased and used were of commercially available quality except as noted. Inhibitor-free tetrahydrofuran (THF) was distilled over Na/benzophenone under argon and deoxygenated with argon before use. The preparation and handling of air-sensitive compounds were performed under a MBraun Labmaster 130 inert atmosphere (< 1 ppm of O_2 and < 1 ppm of H_2O) glovebox filled with nitrogen. Dioxygen gas purchased from Airgas and dried by passing it through Drierite. $^{18}O_2$ gas was purchased from ICON, Summit, NJ, and $^{16}O_2$ gas was purchased from BOC gases, Murray Hill, NJ.

All UV−vis measurements were carried out using a Hewlett-Packard 8453 diode array spectrophotometer with HP Chemstation software and a Unisoku thermostated cell holder for low-temperature experiments. A 10 mm path length quartz cell cuvette modified with an extended glass neck with a female 14/19 joint, and stopcock was used to perform all UV–vis experiments, as previously described.[33,50,68] ^{1}H and ^{2}H-NMR spectra were measured on a Bruker 300-MHz NMR spectrometer at ambient or low temperatures. Chemical shifts were reported as δ (ppm) values relative to an internal standard (tetramethylsilane) and the residual solvent proton peaks. Electron paramagnetic resonance (EPR) spectra were recorded with a Bruker EMX spectrometer equipped with a Bruker ER 041 × G microwave bridge and a continuous flow liquid helium cryostat (ESR900) coupled

to an Oxford Instruments TC503 temperature controller. Spectra were obtained at 8 K under non-saturating microwave power conditions (ν = 9.428 GHz, microwave power = 0.201 mW, modulation amplitude = 10 G, microwave frequency = 100 kHz, and receiver gain = 5.02×10^3). The compounds $(P^{ImH})Fe^{II}$,[30] the pyrrole deuterated derivative d_8-$(P^{ImH})Fe^{II}$,[30] and $Cu^{I}(CH_3CN)_4(B(C_6F_5)_4)$[35] were synthesized as previously described.

3.4.2 UV-vis spectroscopy

3.4.2.1 UV-vis spectroscopy of $[(P^{ImH})Fe^{III}–(O_2^{\bullet-})]$ (2)

Complex $[(P^{ImH})Fe^{III}–(O_2^{\bullet-})]$ (**2**) was generated in THF solution, by preparing 0.01 mM (for Soret band monitoring) or 0.1 mM solutions of $(P^{ImH})Fe^{II}$ (**1**) in a 10 mm path length quartz Schlenk cuvette, which was sealed with a rubber septum in the glovebox. The cuvette was then cooled to –80 °C, and the solution was bubbled with O_2 to generate the superoxide compound **2**. UV-vis: λ_{max} = 424, 541 nm.

3.4.2.2 UV-vis spectroscopy of $[(P^{ImH})Fe^{II}Cu^{I}]^+$ (3), $[(P^{ImH})Fe^{III}–(O_2^{2-})–Cu^{II}]^+$ (3a), and $[(DCHIm)(P^{ImH})Fe^{III}–(O_2^{2-})–Cu^{II}]^+$ (3b)

In a similar manner, in the glovebox, 1 equiv of $[Cu^{I}(CH_3CN)_4](B(C_6F_5)_4)$ (from a 2 mM stock solution (THF)) was added to the 10 mm path length quartz Schlenk cuvette containing the reduced complex $(P^{ImH})Fe^{II}$ (**1**) (125 μL of a 2 mM solution) to generate complex $[(P^{ImH})Fe^{II}Cu^{I}]^+$ (**3**); the cuvette was then filled with THF up to a total volume of 2.5 mL. This cuvette was then cooled to –80 °C, and the solution was bubbled with O_2 to generate the complex $[(P^{ImH})Fe^{III}–(O_2^{2-})–Cu^{II}]^+$ (**3a**). Subsequently, addition of 1.5 equiv of DCHIm to the same cuvette results in LS complex $[(DCHIm)(P^{ImH})Fe^{III}–(O_2^{2-})–Cu^{II}]^+$

(**3b**). UV-vis: $[(P^{ImH})Fe^{II}Cu^{I}]^{+}$ (**3**) λ_{max} = 423, 542 nm; $[(P^{ImH})Fe^{III}–(O_2^{2–})–Cu^{II}]^{+}$ (**3a**) λ_{max} = 420, 545, 565 nm; $[(DCHIm)(P^{ImH})Fe^{III}–(O_2^{2–})–Cu^{II}]^{+}$ (**3b**) λ_{max} = 425, 538 nm.

3.4.3 EPR spectroscopy

3.4.3.1 EPR spectroscopy of $(P^{ImH})Fe^{II}$ (1) and $[(P^{ImH})Fe^{III}–(O_2^{\bullet–})]$ (2)

In a glovebox, 1.0 mg of $(P^{ImH})Fe^{II}$ (**1**) was dissolved in 0.5 mL of deoxygenated THF in an EPR tube. Outside the glovebox, the solution was cooled to –80 °C (acetone-dry ice bath) and bubbled with O_2 to generate the superoxide compound **2**. Then, the EPR spectrum was recorded at 12 K. Both **1** and **2** were found to be EPR silent.

3.4.3.2 EPR spectroscopy of $[(P^{ImH})Fe^{II}Cu^{I}]^{+}$ (3), $[(P^{ImH})Fe^{III}–(O_2^{2–})–Cu^{II}]^{+}$ (3a) and $[(DCHIm)(P^{ImH})Fe^{III}–(O_2^{2–})–Cu^{II}]^{+}$ (3b)

In a glovebox, 1.0 mg of $(P^{ImH})Fe^{II}$ and 0.9 mg of $Cu^{I}(CH_3CN)_4(B(C_6F_5)_4)$ were dissolved in 0.5 mL of deoxygenated THF in an EPR tube and sealed properly. Outside the glovebox, the solution was cooled to –80 °C (acetone-dry ice bath) and dioxygen was bubbled into the solution using a syringe to generate the Heme–Peroxo–Cu complex, $[(P^{ImH})Fe^{III}–(O_2^{2–})–Cu^{II}]^{+}$ (**3a**). A total of 1.5 equiv of DCHIm (3.5 mg of DCHIm in 0.5 mL of THF) was added to the reaction mixture. Then, the EPR spectrum was recorded at 12 K. Both **3a** and **3b** were found to be EPR silent.

3.4.4 ^{2}H-NMR spectroscopy

3.4.4.1 ^{2}H-NMR spectroscopy of [d_8-(P^{ImH})Fe^{III}–($O_2^{\bullet-}$)] (2-d_8)

In the glovebox, 2.6 mg of d_8-(P^{ImH})Fe^{II} (**1**-d_8) was dissolved in 0.5 mL of deoxygenated THF in a NMR tube. To the cold THF solution (at –80 °C, acetone-dry ice bath) of **1**-d_8 was bubbled with O_2. ^{2}H-NMR (300 MHz, THF) **2**-d_8: δ_{pyrr} 9.12 ppm.

3.4.4.2 ^{2}H-NMR spectroscopy of [d_8-(P^{ImH})$Fe^{II}Cu^{I}$]$^{+}$ (3-d_8), [d_8-(P^{ImH})Fe^{III}–(O_2^{2-})–Cu^{II}]$^{+}$ (3a-d_8) and [d_8-(DCHIm)(P^{ImH})Fe^{III}–(O_2^{2-})–Cu^{II}]$^{+}$ (3b-d_8)

In the glove box, a 1:1 mixture of 2.6 mg of d_8-(P^{ImH})Fe^{II} (**1**-d_8) and 2.3 mg of [$Cu^{I}(CH_3CN)_4$]($B(C_6F_5)_4$) was dissolved in 0.5 mL of deoxygenated THF in a NMR tube to generate complex [d_8-(P^{ImH})$Fe^{II}Cu^{I}$]$^{+}$ (**3**-d_8). To the cold THF solution (at –80 °C, acetone-dry ice bath) of **3**-d_8 was bubbled with O_2. In the same NMR tube 1.5 equiv of DCHIm was added 1.5 equiv to generate LS peroxo [d_8-(DCHIm)(P^{ImH})Fe^{III}–(O_2^{2-})–Cu^{II}]$^{+}$ (**3b**-d_8). ^{2}H-NMR (300 MHz, THF): Complex **3**-d_8, δ_{pyrr} 89.4, 102.8 ppm; **3a**-d_8, 93.0 ppm; **3b**-d_8, 10.2 ppm.

3.4.5 resonance Raman (rR) spectroscopy

3.4.5.1 rR spectroscopy of [(P^{ImH})Fe^{III}–($O_2^{\bullet-}$)] (2)

In the glovebox, 2 mM solutions of an (P^{ImH})Fe^{II} in THF were prepared and transferred to rR tube and capped with tightfitting septa. The sample tubes were placed in a cold bath (dry ice/acetone) and oxygenated using $^{16}O_2$ or $^{18}O_2$ gases. The oxygenated samples were set in a cold bath for 10 min, after which the sample tubes were frozen in liquid N_2 and sealed by flame. Resonance Raman samples were excited at 413 nm, using

either a Coherent I90C-K Kr+ ion laser while the sample was immersed in a liquid nitrogen cooled (77 K) EPR finger Dewar (Wilmad). Power was ~2 mW at the sample, which was continuously rotated to minimize photodecomposition. The spectra were recorded using a Spex 1877 CP triple monochromator, and detected by an Andor Newton CCD cooled to –80 °C. rRaman [Fe^{III}–($O_2^{\bullet-}$)] (**2**): ν_{O-O}, 1171 cm^{-1} ($\Delta^{18}O_2$, –61 cm^{-1}); ν_{Fe-O}, 575 cm^{-1} ($\Delta^{18}O_2$, –24 cm^{-1}).

3.4.5.2 rR spectroscopy of $[(P^{ImH})Fe^{II}Cu^{I}]^+$ (3), $[(P^{ImH})Fe^{III}–(O_2^{2-})–Cu^{II}]^+$ (3a) and $[(DCHIm)(P^{ImH})Fe^{III}–(O_2^{2-})–Cu^{II}]^+$ (3b)

In the glovebox, 5 mM solutions of an equimolar mixture of $(P^{ImH})Fe^{II}$ and $[Cu^{I}(CH_3CN)_4](B(C_6F_5)_4)$ in THF were prepared and transferred to rR tube and capped with tightfitting septa. The sample tubes were placed in a cold bath (dry ice/acetone) and oxygenated using $^{16}O_2$ and $^{18}O_2$. The labeled gases were cooled in dry ice for 5 min and injected through the solution by using a Hamilton gastight syringe. The oxygenated samples were set in a cold bath for 10 min, after which the sample tubes were frozen in liquid N_2 and sealed by flame. To the cold THF solution (at –80 °C, acetone-dry ice bath) of **3a** was added 1.5 equiv (3.5 mg of DCHIm in 0.5 mL of THF) of DCHIm for complex **3b**. rRaman $[(P^{ImH})Fe^{III}–(O_2^{2-})–Cu^{II}]^+$ (**3a**): ν_{O-O}, 799 cm^{-1} ($\Delta^{18}O_2$, –48 cm^{-1}); ν_{Fe-O}, 524 cm^{-1} ($\Delta^{18}O_2$, –23 cm^{-1}), $[(DCHIm)(P^{ImH})Fe^{III}–(O_2^{2-})–Cu^{II}]^+$ (**3b**): ν_{O-O}, 817 cm^{-1} ($\Delta^{18}O_2$, –55 cm^{-1}); ν_{Fe-O}, 610 cm^{-1} ($\Delta^{18}O_2$, –26 cm^{-1}).

3.5 References

(1) Wikström, M. K. F. Proton Pump Coupled to Cytochrome *c* Oxidase in Mitochondria. *Nature* **1977**, *266*, 271−273.

(2) Ferguson-Miller, S.; Babcock, G. T. Heme/Copper Terminal Oxidases. *Chem. Rev*. **1996**, *96*, 2889−2907.

(3) Babcock, G. T. How Oxygen Is Activated and Reduced in Respiration. *Proc. Natl. Acad. Sci. U. S. A*. **1999**, *96*, 12971−12973.

(4) Peterson, R. L.; Kim, S.; Karlin, K. D. *Comprehensive Inorganic Chemistry II*, 2nd ed.; Elsevier: Amsterdam, 2013; pp 149−177.

(5) Solomon, E. I.; Heppner, D. E.; Johnston, E. M.; Ginsbach, J. W.; Cirera, J.; Qayyum, M.; Kieber-Emmons, M. T.; Kjaergaard, C. H.; Hadt, R. G.; Tian, L. Copper Active Sites in Biology. *Chem. Rev*. **2014**, *114*, 3659−3853.

(6) Yoshikawa, S.; Shimada, A. Reaction Mechanism of Cytochrome *c* Oxidase. *Chem. Rev*. **2015**, *115*, 1936−1989.

(7) Quist, D. A.; Diaz, D. E.; Liu, J. J.; Karlin, K. D. Activation of Dioxygen by Copper Metalloproteins and Insights from Model Complexes. *JBIC, J. Biol. Inorg. Chem*. **2017**, *22*, 253−288.

(8) Wikström, M.; Krab, K.; Sharma, V. Oxygen Activation and Energy Conservation by Cytochrome *c* Oxidase. *Chem. Rev*. **2018**, *118*, 2469−2490.

(9) Huang, X.; Groves, J. T. Oxygen Activation and Radical Transformations in Heme Proteins and Metalloporphyrins. *Chem. Rev*. **2018**, *118*, 2491−2553.

(10) Adam, S. M.; Wijeratne, G. B.; Rogler, P. J.; Diaz, D. E.; Quist, D. A.; Liu, J. J.; Karlin, K. D. Synthetic Fe/Cu Complexes: Toward Understanding Heme-Copper Oxidase Structure and Function. *Chem. Rev*. **2018**, *118*, 10840−11022.

(11) Das, T. K.; Pecoraro, C.; Tomson, F. L.; Gennis, R. B.; Rousseau, D. L. The Post-Translational Modification in Cytochrome *c* Oxidase Is Required to Establish a Functional Environment of the Catalytic Site. *Biochemistry* **1998**, *37*, 14471−14476.

(12) Liu, X.; Yu, Y.; Hu, C.; Zhang, W.; Lu, Y.; Wang, J. Significant Increase of Oxidase Activity through the Genetic Incorporation of a Tyrosine-Histidine Cross-Link in a Myoglobin Model of Heme-Copper Oxidase. *Angew. Chem., Int. Ed*. **2012**, *51*, 4312−4316.

(13) Ravikiran, B.; Mahalakshmi, R. Unusual Post-Translational Protein Modifications: The Benefits of Sophistication. *RSC Adv*. **2014**, *4*, 33958−33974.

(14) Davidson, V. L. Protein-Derived Cofactors Revisited: Empowering Amino Acid Residues with New Functions. *Biochemistry* **2018**, *57*, 3115−3125.

(15) Lin, Y. W. Structure and Function of Heme Proteins Regulated by Diverse Post-Translational Modifications. *Arch. Biochem. Biophys*. **2018**, *641*, 1−30.

(16) Ehudin, M. A.; Senft, L.; Franke, A.; Ivanović-Burmazović, I.; Karlin, K. D. Formation and Reactivity of New Isoporphyrins: Implications for Understanding the Tyr-His Cross-Link Cofactor Biogenesis in Cytochrome *c* Oxidase. *J. Am. Chem. Soc*. **2019**, *141*, 10632−10643.

(17) Iwata, S.; Ostermeier, C.; Ludwig, B.; Michel, H. Structure at 2.8 Å Resolution of Cytochrome *c* Oxidase from *Paracoccus Denitrificans*. *Nature* **1995**, *376*, 660−669.

(18) Yoshikawa, S. Redox-Coupled Crystal Structural Changes in Bovine Heart Cytochrome *c* Oxidase. *Science* **1998**, *280*, 1723−1729.

(19) Schaefer, A. W.; Kieber-Emmons, M. T.; Adam, S. M.; Karlin, K. D.; Solomon, E. I. Phenol-Induced O-O Bond Cleavage in a Low-Spin Heme-Peroxo-Copper Complex: Implications for O_2 Reduction in Heme-Copper Oxidases. *J. Am. Chem. Soc*. **2017**, *139*, 7958−7973.

(20) Brunner, H. Identification of the Iron-Ligand Vibration of Oxyhemoglobin. *Naturwissenschaften* **1974**, *61*, 129.

(21) Van Wart, H. E.; Zimmer, J. Resonance Raman Evidence for the Activation of Dioxygen in Horseradish Oxyperoxidase. *J. Biol. Chem*. **1985**, *260*, 8372−8377.

(22) Intermediate PM derives from an enzyme form where only the binuclear heme−Cu center is reduced, i.e., (Fe_{a3}^{II}/Cu_B^{I}). Many C*c*O biochemical/biophysical studies employ also PR, where four electrons are available for reactivity, i.e., where additional electrons are available also from Cu_A or cytochrome a_3.

(23) Poiana, F.; von Ballmoos, C.; Gonska, N.; Blomberg, M. R. A. A.; Ädelroth, P.; Brzezinski, P. Splitting of the O–O Bond at the Heme-Copper Catalytic Site of Respiratory Oxidases. *Sci. Adv*. **2017**, *3*, e1700279.

(24) Han Du, W.-G.; Noodleman, L. Density Functional Study for the Bridged Dinuclear Center Based on a High-Resolution X-Ray Crystal Structure of ba_3 Cytochrome *c* Oxidase from Thermus Thermophilus. *Inorg. Chem*. **2013**, *52*, 14072−14088.

(25) Noodleman, L.; Han Du, W.-G.; Fee, J. A.; Götz, A. W.; Walker, R. C. Linking Chemical Electron-Proton Transfer to Proton Pumping in Cytochrome *c* Oxidase: Broken-Symmetry DFT Exploration of Intermediates along the Catalytic Reaction Pathway of the Iron-Copper Dinuclear Complex. *Inorg. Chem*. **2014**, *53*, 6458−6472.

(26) Han Du, W.-G.; Götz, A. W.; Yang, L.; Walker, R. C.; Noodleman, L. A Broken-Symmetry Density Functional Study of Structures, Energies, and Protonation States along the Catalytic O-O Bond Cleavage Pathway in ba_3 Cytochrome *c* Oxidase from Thermus Thermophilus. *Phys. Chem. Chem. Phys*. **2016**, *18*, 21162−21171.

(27) Schaefer, A. W.; Roveda, A. C.; Jose, A.; Solomon, E. I. Geometric and Electronic Structure Contributions to O-O Cleavage and the Resultant Intermediate Generated in Heme-Copper Oxidases. *J. Am. Chem. Soc*. **2019**, *141*, 10068−10081.

(28) Collman, J. P.; Sunderland, C. J.; Berg, K. E.; Vance, M. A.; Solomon, E. I. Spectroscopic Evidence for a Heme-Superoxide/Cu(I) Intermediate in a Functional Model of Cytochrome *c* Oxidase. *J. Am. Chem. Soc*. **2003**, *125*, 6648−6649.

(29) Liu, J. G.; Naruta, Y.; Tani, F. A Functional Model of the Cytochrome *c* Oxidase Active Site: Unique Conversion of a Heme-μ-Peroxo-Cu^{II} Intermediate into Heme-Superoxo/Cu^{I}. *Angew. Chem., Int. Ed*. **2005**, *44*, 1836−1840.

(30) Chishiro, T.; Shimazaki, Y.; Tani, F.; Tachi, Y.; Naruta, Y.; Karasawa, S.; Hayami, S.; Maeda, Y. Isolation and Crystal Structure of a Peroxo-Bridged Heme-Copper Complex. *Angew. Chem*. **2003**, *115*, 2894−2897.

(31) Chufán, E. E.; Puiu, S. C.; Karlin, K. D. Heme-Copper/Dioxygen Adduct Formation, Properties, and Reactivity. *Acc. Chem. Res*. **2007**, *40*, 563−572.

(32) Kim, E.; Shearer, J.; Lu, S.; Moënne-Loccoz, P.; Helton, M. E.; Kaderli, S.; Zuberbuehler, A. D.; Karlin, K. D. Heme/Cu/O_2 Reactivity: Change in Fe^{III}-(O_2^{2-})-Cu^{II} Unit Peroxo Binding Geometry Effected by Tridentate Copper Chelation. *J. Am. Chem. Soc*. **2004**, *126*, 12716−12717.

(33) Wasser, I. M.; Huang, H. W.; Moënne-Loccoz, P.; Karlin, K. D. Heme/Non-Heme Diiron(II) Complexes and O_2, CO and NO Adducts as Reduced and Substrate-Bound Models for the Active Site of Bacterial Nitric Oxide Reductase. *J. Am. Chem. Soc*. **2005**, *127*, 3310−3320.

(34) Adam, S. M.; Garcia-Bosch, I.; Schaefer, A. W.; Sharma, S. K.; Siegler, M. A.; Solomon, E. I.; Karlin, K. D. Critical Aspects of Heme-Peroxo-Cu Complex Structure and Nature of Proton Source Dictate Metal-O Peroxo Breakage versus Reductive O-O Cleavage Chemistry. *J. Am. Chem. Soc*. **2017**, *139*, 472−481.

(35) Collman, J. P.; Devaraj, N. K.; Decréau, R. A.; Yang, Y.; Yan, Y.; Ebina, W.; Eberspacher, T. A.; Chidsey, C. E. D. A Cytochrome *c* Oxidase Model Under Rate-Limiting Electron Flux. *Science* **2007**, *315*, 1565−1568.

(36) Collman, J. P.; Decréau, R. A. Functional Biomimetic Models for the Active Site in the Respiratory Enzyme Cytochrome *c* Oxidase. *Chem. Commun*. **2008**, *356*, 5065−5076.

(37) Shin, H.; Lee, D. H.; Kang, C.; Karlin, K. D. Electrocatalytic Four-Electron Reductions of O_2 to H_2O with Cytochrome *c* Oxidase Model Compounds. *Electrochim. Acta* **2003**, *48*, 4077−4082.

(38) Chatterjee, S.; Sengupta, K.; Hematian, S.; Karlin, K. D.; Dey, A. Electrocatalytic O_2-Reduction by Synthetic Cytochrome *c* Oxidase Mimics: Identification of a "Bridging Peroxo" Intermediate Involved in Facile $4e^-/4H^+$ O_2^- Reduction. *J. Am. Chem. Soc*. **2015**, *137*, 12897−12905.

(39) Garcia-Bosch, I.; Adam, S. M.; Schaefer, A. W.; Sharma, S. K.; Peterson, R. L.; Solomon, E. I.; Karlin, K. D. A "Naked" Fe^{III}-(O_2^{2-})-Cu^{II} Species Allows for Structural

and Spectroscopic Tuning of Low-Spin Heme-Peroxo-Cu Complexes. *J. Am. Chem. Soc*. **2015**, *137*, 1032−1035.

(40) Sharma, S. K.; Kim, H.; Rogler, P. J.; Siegler, M. A.; Karlin, K. D. Isocyanide or Nitrosyl Complexation to Hemes with Varying Tethered Axial Base Ligand Donors: Synthesis and Characterization. *JBIC, J. Biol. Inorg. Chem*. **2016**, *21*, 729−743.

(41) Momenteau, M.; Reed, C. A. Synthetic Heme Dioxygen Complexes. *Chem. Rev*. **1994**, *94*, 659−698.

(42) Yan, J. J.; Kroll, T.; Baker, M. L.; Wilson, S. A.; Decréau, R.; Lundberg, M.; Sokaras, D.; Glatzel, P.; Hedman, B.; Hodgson, K. O.; Solomon, E. I. Resonant Inelastic X-Ray Scattering Determination of the Electronic Structure of Oxyhemoglobin and Its Model Complex. *Proc. Natl. Acad. Sci. U. S. A*. **2019**, *116*, 2854−2859.

(43) Kopf, M.-A.; Karlin, K. D. Dioxygen Reactivity of Reduced Heme and Heme-Copper Complexes Utilizing Tetraarylporphyrinates Tethered with Both a Pyridyl Axial Ligand and N,N-Bis[2-(2-Pyridyl)Ethyl]Amine Chelate. *Inorg. Chem*. **1999**, *38*, 4922−4923.

(44) Das, P. K.; Mittra, K.; Dey, A. Spectroscopic Characterization of a Phenolate Bound Fe^{II}-O_2 Adduct: Gauging the Relative "Push" Effect of a Phenolate Axial Ligand. *Chem. Commun*. **2014**, *50*, 5218−5220.

(45) Singha, A.; Dey, A. Hydrogen Atom Abstraction by Synthetic Heme Ferric Superoxide and Hydroperoxide Species. *Chem. Commun*. **2019**, *55*, 5591−5594.

(46) Tsubaki, M.; Nagai, K.; Kitagawa, T. Resonance Raman Spectra of Myoglobins Reconstituted with Spirographis and Isospirographis Hemes and Iron 2,4-Diformylprotoporphyrin IX. Effect of Formyl Substitution at the Heme Periphery. *Biochemistry* **1980**, *19*, 379−385.

(47) Mak, P. J.; Denisov, I. G.; Victoria, D.; Makris, T. M.; Deng, T.; Sligar, S. G.; Kincaid, J. R. Resonance Raman Detection of the Hydroperoxo Intermediate in the Cytochrome P450 Enzymatic Cycle. *J. Am. Chem. Soc*. **2007**, *129*, 6382−6383.

(48) Denisov, I. G.; Mak, P. J.; Makris, T. M.; Sligar, S. G.; Kincaid, J. R. Resonance Raman Characterization of the Peroxo and Hydroperoxo Intermediates in Cytochrome P450. *J. Phys. Chem. A* **2008**, *112*, 13172−13179.

(49) Kim, E.; Helton, M. E.; Wasser, I. M.; Karlin, K. D.; Lu, S.; Huang, H.; Moënne-Loccoz, P.; Incarvito, C. D.; Rheingold, A. L.; Honecker, M.; Kaderli, S.; Zuberbuhler, A. D. Superoxo, μ-Peroxo, and μ-Oxo Complexes from Heme/O_2 and Heme-Cu/O_2 Reactivity: Copper Ligand Influences in Cytochrome *c* Oxidase Models. *Proc. Natl. Acad. Sci. U. S. A*. **2003**, *100*, 3623−3628.

(50) Sharma, S. K.; Schaefer, A. W.; Lim, H.; Matsumura, H.; Moënne-Loccoz, P.; Hedman, B.; Hodgson, K. O.; Solomon, E. I.; Karlin, K. D. A Six-Coordinate Peroxynitrite Low-Spin Iron(III) Porphyrinate Complex - The Product of the Reaction of Nitrogen Monoxide (·NO(g)) with a Ferric-Superoxide Species. *J. Am. Chem. Soc*. **2017**, *139*, 17421−17430.

(51) Mittra, K.; Chatterjee, S.; Samanta, S.; Sengupta, K.; Bhattacharjee, H.; Dey, A. A Hydrogen Bond Scaffold Supported Synthetic Heme Fe^{III}-O_2-Adduct. *Chem. Commun*. **2012**, *48*, 10535−10537.

(52) Kim, E.; Chufan, E. E.; Kamaraj, K.; Karlin, K. D. Synthetic Models for Heme-Copper Oxidases. *Chem. Rev*. **2004**, *104*, 1077−1133.

(53) Halime, Z.; Kieber-Emmons, M. T.; Qayyum, M. F.; Mondal, B.; Gandhi, T.; Puiu, S. C.; Chufán, E. E.; Sarjeant, A. A. N.; Hodgson, K. O.; Hedman, B.; Solomon, E. I.; Karlin, K. D. Heme-Copper-Dioxygen Complexes: Toward Understanding Ligand-Environmental Effects on the Coordination Geometry, Electronic Structure, and Reactivity. *Inorg. Chem*. **2010**, *49*, 3629−3645.

(54) Chufán, E. E.; Mondal, B.; Gandhi, T.; Kim, E.; Rubie, N. D.; Moënne-Loccoz, P.; Karlin, K. D. Reactivity Studies on Fe^{III}-(O_2^{2-})-Cu^{II} Compounds: Influence of the Ligand Architecture and Copper Ligand Denticity. *Inorg. Chem*. **2007**, *46*, 6382−6394.

(55) Que, L., Jr.; Tolman, W. B. Bis(μ-Oxo)Dimetal "Diamond" Cores in Copper and Iron Complexes Relevant to Biocatalysis. *Angew. Chem., Int. Ed*. **2002**, *41*, 1114−1137.

(56) Mirica, L. M.; Ottenwaelder, X.; Stack, T. D. P. Structure and Spectroscopy of Copper-Dioxygen Complexes. *Chem. Rev*. **2004**, *104*, 1013−1046.

(57) Hatcher, Q. L.; Karlin, K. D. Ligand Influences in Copper-Dioxygen Complex-Formation and Substrate Oxidations. *Adv. Inorg. Chem*. **2006**, *58*, 131−184.

(58) del Río, D.; Sarangi, R.; Chufan, E. E.; Karlin, K. D.; Hedman, B.; Hodgson, K. O.; Solomon, E. I. Geometric and Electronic Structure of the Heme-Peroxo-Copper Complex [(F_8TPP)Fe^{III}-(O_2^{2-})-Cu^{II}(TMPA)](ClO_4). *J. Am. Chem. Soc*. **2005**, *127*, 11969−11978.

(59) Nanthakumar, A.; Fox, S.; Murthy, N. N.; Karlin, K. D. Inferences from the 1H-NMR Spectroscopic Study of an Antiferromagnetically Coupled Heterobinuclear Fe(III)-(X)-Cu(II) S = 2 Spin System (X = O^{2-}, OH^-). *J. Am. Chem. Soc*. **1997**, *119*, 3898−3906.

(60) Ghiladi, R. A.; Kretzer, R. M.; Guzei, I.; Rheingold, A. L.; Neuhold, Y. M.; Hatwell, K. R.; Zuberbühler, A. D.; Karlin, K. D. (F_8TPP)Fe^{II}/O_2 Reactivity Studies {F_8TPP = Tetrakis(2,6-Difluorophenyl)Porphyrinate(2-)}: Spectroscopic (UV-Visible and NMR)

and Kinetic Study of Solvent-Dependent (Fe/O_2 = 1:1 or 2:1) Reversible O_2-Reduction and Ferryl Formation. *Inorg. Chem*. **2001**, *40*, 5754−5767.

(61) Kim, E.; Helton, M. E.; Lu, S.; Moënne-Loccoz, P.; Incarvito, C. D.; Rheingold, A. L.; Kaderli, S.; Zuberbühler, A. D.; Karlin, K. D. Tridentate Copper Ligand Influences on Heme-Peroxo-Copper Formation and Properties: Reduced, Superoxo, and μ-Peroxo Iron/ Copper Complexes. *Inorg. Chem*. **2005**, *44*, 7014−7029.

(62) Kopf, M.-A.; Neuhold, Y.-M.; Zuberbühler, A. D.; Karlin, K. D. Oxo- and Hydroxo-Bridged Heme-Copper Assemblies Formed from Acid-Base or Metal-Dioxygen Chemistry. *Inorg. Chem*. **1999**, *38*, 3093−3102.

(63) Ghiladi, R. A.; Ju, T. D.; Lee, D. H.; Moënne-Loccoz, P.; Kaderli, S.; Neuhold, Y. M.; Zuberbühler, A. D.; Woods, A. S.; Cotter, R. J.; Karlin, K. D. Formation and Characterization of a High-Spin Heme-Copper Dioxygen (Peroxo) Complex. *J. Am. Chem. Soc*. **1999**, *121*, 9885−9886.

(64) Kim, E.; Kamaraj, K.; Galliker, B.; Rubie, N. D.; Moënne-Loccoz, P.; Kaderli, S.; Zuberbühler, A. D.; Karlin, K. D. Dioxygen Reactivity of Copper and Heme-Copper Complexes Possessing an Imidazole-Phenol Cross-Link. *Inorg. Chem*. **2005**, *44*, 1238−1247.

(65) Ghiladi, R. A.; Chufan, E. E.; del Río, D.; Solomon, E. I.; Krebs, C.; Huynh, B. H.; Huang, H.-w.; Moënne-Loccoz, P.; Kaderli, S.; Honecker, M.; Zuberbühler, A. D.; Marzilli, L.; Cotter, R. J.; Karlin, K. D. Further Insights into the Spectroscopic Properties, Electronic Structure, and Kinetics of Formation of the Heme-Peroxo-Copper Complex $[(F_8TPP)Fe^{III}\text{-}(O_2^{2-})\text{-}Cu^{II}(TMPA)]^+$. *Inorg. Chem*. **2007**, *46*, 3889−3902.

(66) Kieber-Emmons, M. T.; Qayyum, M. F.; Li, Y.; Halime, Z.; Hodgson, K. O.; Hedman, B.; Karlin, K. D.; Solomon, E. I. Spectroscopic Elucidation of a New Heme/Copper Dioxygen Structure Type: Implications for O-O Bond Rupture in Cytochrome *c* Oxidase. *Angew. Chem., Int. Ed*. **2012**, *51*, 168−172.

(67) Ehudin, M. A.; Schaefer, A. W.; Adam, S. M.; Quist, D. A.; Diaz, D. E.; Tang, J. A.; Solomon, E. I.; Karlin, K. D. Influence of Intramolecular Secondary Sphere Hydrogen-Bonding Interactions on Cytochrome *c* Oxidase Inspired Low-Spin Heme-Peroxo-Copper Complexes. *Chem. Sci*. **2019**, *10*, 2893−2905.

(68) Ghiladi, R. A.; Huang, H.; Moënne-Loccoz, P.; Stasser, J.; Blackburn, N. J.; Woods, A. S.; Cotter, R. J.; Incarvito, C. D.; Rheingold, A. L.; Karlin, K. D. Heme-Copper/Dioxygen Adduct Formation Relevant to Cytochrome *c* Oxidase: Spectroscopic Characterization of $[(^{6}L)Fe^{III}\text{-}(O_2^{2-})\text{-}Cu^{II}]^{+}$. *JBIC, J. Biol. Inorg. Chem*. **2005**, *10*, 63−77.

Chapter 4

Heme-Fe^{III} Superoxide, Peroxide and Hydroperoxide Thermodynamic Relationships: Fe^{III}-$O_2^{\bullet-}$ Complex H-Atom Abstraction Reactivity

---

This work was co-authored with the following authors and is published under the following citation:

Hyun Kim,[†] Patrick J. Rogler,[†] Savita K. Sharma,[†] Andrew W. Schaefer,[‡] Edward I. Solomon,*[,‡] and Kenneth D. Karlin*[,†]

[†]Department of Chemistry, Johns Hopkins University, Baltimore, Maryland 21218, USA

[‡]Department of Chemistry, Stanford University, Stanford, California 94305, USA

J. Am. Chem. Soc. **2020**, *142*, 3104–3116

4.1 Introduction

Cytochrome P450 monooxygenases (CYP450s) catalyze the incorporation of one atom of molecular oxygen into biological substrates, i.e., they hydroxylate nonactivated C–H bonds in hydrocarbon and various other compounds.[1–10] CYP450s are involved in critical biological processes, including the biosynthesis of steroid hormones, degradation of pharmaceutically derived drugs and detoxification of xenobiotics including carcinogens.[11–14] Many excellent review articles concerning CYP450s exist, covering the relevant biochemistry, summarizing available protein X-ray structures[15,16] and detailing aspects of the nature of intermediates and reaction mechanism. Theoretical/computational investigations and analyses have been part of the research efforts.[1,3,5,10,17–21]

The CYP450 catalytic mechanism as currently accepted is depicted in Scheme 4.1. When the substrate (R–H) approaches the heme active-site, it displaces the distally bound axial water molecule from the six-coordinate low-spin ferric ion, converting it to a five-coordinate, high-spin ferric-porphyrinate. The loss of the H_2O causes an increase of the redox potential of the heme iron by approximately 300 mV,[4] which enables electrons transfer from the biological reductase producing a five-coordinate ferrous porphyrinate. Note that in the resting state, the Fe^{III}/Fe^{II} reduction potential ranges between –400 and –170 mV, and thus is inactive to reduction.[2] The ferrous heme binds dioxygen, giving rise to the initial ferric superoxide intermediate, often referred to as the oxy-heme or oxy ferrous intermediate. The addition of a second electron converts superoxide to a ferric peroxide intermediate, and this step is overall rate-determining in the CYP450 catalytic cycle.[17,22] Subsequently, the peroxide is protonated to form a low-spin ferric hydroperoxide intermediate, Fe^{III}–OOH, which is known as Compound 0. A second protonation on the

distal oxygen of hydroperoxide species causes heterolytic O–O bond cleavage to produce a highly reactive high-valent ferryl–oxo π-cation porphyrinate radical (Cmpd I), releasing a molecule of water. Cmpd I is accepted as the active substrate oxidant for the normal CYP450 cycle.[9,23] This species abstracts a hydrogen atom from the substrate to give a radical (R•) and the "OH" from the resulting iron(IV)-OH (Cmpd II) undergoes 'rebound'[24] to the substrate radical, giving products R–OH plus the original (in the cycle) ferric heme.

Scheme 4.1 Catalytic cycle of cytochrome P450 monooxygenases (where R–H is the substrate)[8]

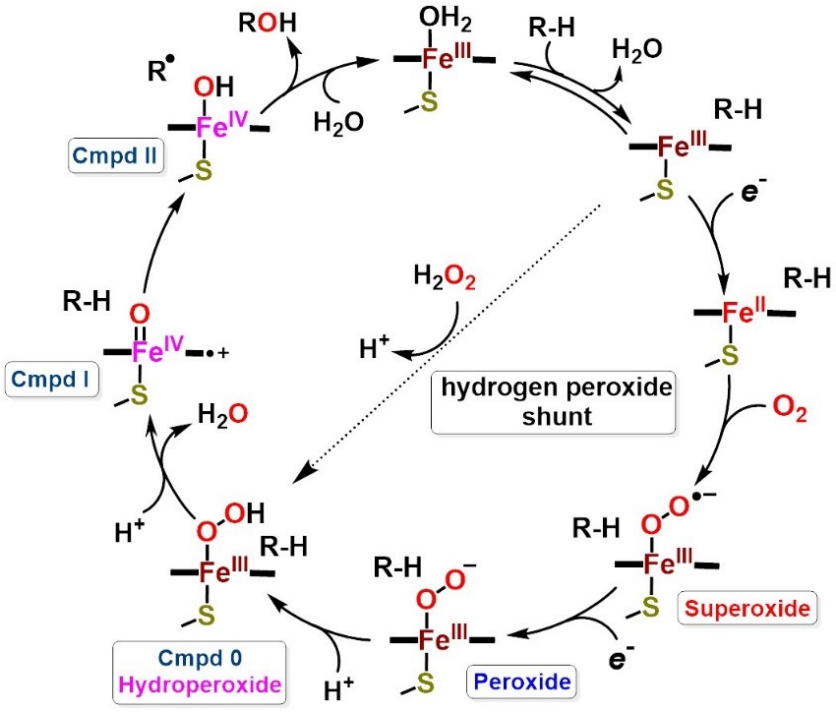

As shown in Scheme 4.1, superoxide/peroxide/hydroperoxide intermediates are involved in catalytic cycle of CYP450. These species also have been observed as intermediates in biological processes involving other O_2 or H_2O_2 activating heme

enzymes.[6] These include heme oxygenase (HO; oxidatively breaking down hemes while also effecting release of iron and CO (or other metabolite): superoxide (Fe^{II}-O_2) and hydroperoxide),[25–27] nitric oxide synthase (NOS; two-step reaction where hydroxylation of L-arginine to N-hydroxy-L-arginine (L-NHA) is followed by oxidation of L-NHA to citrulline and $NO_{(g)}$: superoxide, peroxide, and hydroperoxide),[28,29] steroid hormone multifunctional CYPs (hydroxylation and lyase activities: superoxide, peroxide, and hydroperoxide),[30–32] horseradish peroxidase (HRP; H_2O_2 mediated substrate oxidation: hydroperoxide),[6,9,33,34] chloroperoxidase (CPO; H_2O_2 mediated substrate halogenation: hydroperoxide),[9,35] aromatic peroxygenase (APO; oxygenation of aliphatic and aromatic hydrocarbons: hydroperoxide),[9,36] and tryptophan 2,3-dioxygenase (TDO; transformation to formylkynurenine: superoxide).[6,37] Any and all aspects of CYP or other O_2/H_2O_2 activating heme enzymes (vide supra) reaction mechanisms have been or are being investigated, including what key protonation events take place and how, and what the structures of all intermediates are such as atom-connectivity along with bonding (electronic structure). The initial oxy-heme, the O_2-adduct with ferrous ion (i.e., the ferric superoxide),[38] the subsequently reduced intermediate peroxide and protonated hydroperoxide (Cmpd 0) have not been detected in normal enzyme turnover. However, comprehensive radiolytic cryoreduction studies[25,39–42] have provided many details concerning their structures and physical properties. Theoretical/computational investigations have also provided insights into the structures and thermodynamic inter-relationships for intermediates in the CYP450 catalytic cycle (Scheme 4.1).[5]

However, over the years and continuing on, generation of synthetic analogs of all the intermediates relevant to the CYP450 catalytic cycle has been of great interest (and

importance). In this regard, there are many known heme Fe^{III}-superoxide synthetic compounds,[8,43–52] O_2-adducts of reduced ferrous hemes, including hemoglobin/myoglobin mimics such as the "Picket-Fence" porphyrin O_2-adduct.[43] However, these do not possess thiolate axial ligation as in CYP450s. Ferric heme peroxide and ferric heme hydroperoxide complexes are relatively rare (and see discussions below) even though researchers have suggested that hydroperoxide species may serve as alternative oxidant, since it is a common intermediate in the catalytic cycles of monooxygenases.[19,53–55]

Reviews emphasizing synthesis and reactivity of M^{n+}-($O_2^{\bullet-}$) complexes are now available.[56,57] Many M^{n+}-($O_2^{\bullet-}$) complexes of the first row transition metals, for example Mn, Fe, Co, Ni, Cu and Zn have been synthesized via metal-complex + O_2 or metal-complex + superoxide reactions and their substrate reactivity investigated. Iron-superoxide species are considered to form in the first step of dioxygen activation as the reactive intermediates in heme (vide supra) and non-heme metalloenzymes (e.g., Myo-inositol oxygenase (MIOX) and isopenicillin-N-synthase (IPNS)).[57]

In this report, we describe new synthetic analogues of those intermediates early in the cycle, prior to O–O cleavage, namely the ferric heme superoxide, peroxide and hydroperoxide species (***S***, ***P*** and ***HP***, respectively (Figure 4.1)). We note that in CYP450, the superoxide, peroxide and hydroperoxide intermediates are thought to have an end-on structure,[9,10,58] only binding to iron with one oxygen atom (the proximal O-atom), as depicted in Scheme 4.1. Utilizing the F_8 (F_8 = tetrakis(2,6-difluorophenyl)porphyrinate) heme framework, we have spectroscopically characterized corresponding ***S***, ***P*** and ***HP*** complexes, with UV-vis, electron paramagnetic resonance (EPR) and resonance Raman

(rR) spectroscopies, and further chemically confirmed that ***P*** and ***HP*** are peroxidic (vide infra).

More importantly, and the primary advance described in this report, is that we have experimentally established the thermodynamic relationships between these complexes: (1) The reduction of ferric superoxide compound ***S*** is reversible, using chemical reagents, and a reduction potential $E°'$ has been determined, (2) the ferric peroxo complex ***P***, possessing an intermediate spin and side-on bound peroxide dianion ligand, can be reversibly protonated to give the low-spin ferric hydroperoxide ***HP***. Thus, a pK_a value for ***HP*** has been established. Further, another finding is that the ferric heme superoxide complex ***S*** can effect a hydrogen atom abstraction reaction, and directly produce ferric heme hydroperoxide complex ***HP*** (Figure 4.1). Only recently, Dey and co-workers[45] demonstrated for the first time that a ferric heme superoxide complex could effect a HAT reaction; removal of a hydrogen atom from a porphyrinate appended catechol, thus an intra-molecular process, converted the superoxide complex to the hydroperoxide analog. Such a transformation represents the diagonal part of a thermodynamic square scheme, relating ***S***, ***P*** and ***HP*** complexes (Figure 4.1). Now, with our measured reduction potential ($E°'$) and pK_a values (as mentioned above), the O–H bond dissociation free energy (BDFE) of ferric heme hydroperoxide complex ***HP*** could be determined using the Bordwell relationship (eq. 1) where $C_{G,solv}$ represents the $H^+/H^\bullet$ standard reduction potential in a particular solvent (also see below).[59]

$$BDFE = 1.37(pK_a) + 23.06E^o + C_{G,solv} \qquad (\mathbf{1})$$

Further, the calculated BDFE of complex ***HP***, in fact is shown to be in-line (consistent) with the actual experimental reactivity of ***S*** toward a substrate with O–H bond (vide infra). To the best of our knowledge, the present study reports the first example showing thermodynamics (reduction potential and pK_a) involved and the generation of the ferric heme hydroperoxide species by ferric heme superoxide complex via HAT of an exogenously added substrate.

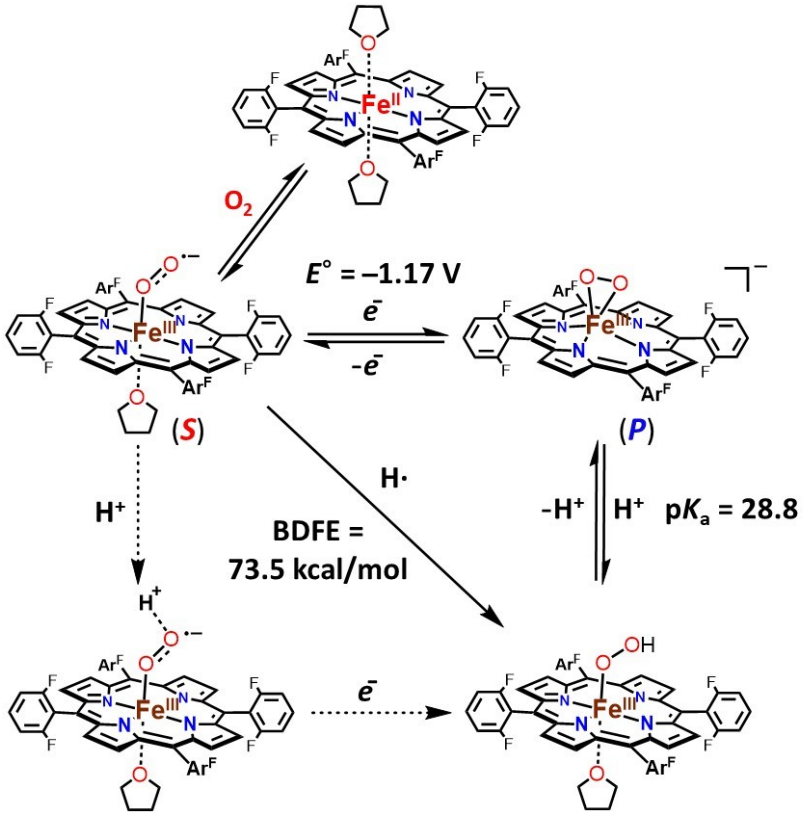

Figure 4.1 Sequential preparation of superoxide/peroxide/hydroperoxide heme analogs and thermodynamic square scheme of reduction ($E°$ as determined vs $Fc^{+/0}$) and protonation of a F_8 ferric heme superoxide analog and O–H BDFE of ferric heme hydroperoxide (Ar^F = 2,6-difluorophenyl group).

4.2 Results and discussion

4.2.1 Generation and characterization of a ferric peroxide, $[(F_8)Fe^{III}\text{-}(O_2^{2-})]^-$ (*P*)

As reported in previous work,[60] addition of the outer sphere strong reductant $CoCp_2$ to the previously well-characterized ferric superoxide complex $[(F_8)Fe^{III}\text{-}(O_2^{\bullet-})]$ (***S***) (λ_{max} = 416 and 535 nm; rRaman, ν_{O-O}, 1178 cm^{-1} ($\Delta^{18}O_2$, –64 cm^{-1}); ν_{Fe-O}, 568 cm^{-1} ($\Delta^{18}O_2$, –24 cm^{-1}))[61,62] at –80 °C in THF yields side-on ferric heme-peroxide complex $[(F_8)Fe^{III}\text{-}(O_2^{2-})]^-$ (***P***) with UV-vis spectral features at 434, 541 and 561 nm (Figure 4.2A). These electronic absorption spectra are the same as those known for other previously well-characterized side-on ferric porphyrin peroxide complexes which have low energy Soret band and two peaks between 500 and 600 nm at α, β-region.[11,49,63,64] Valentine and co-workers[63] originally discovered and characterized such species and synthesized them by the reaction of potassium superoxide solubilized with 18-crown-6 ether, where the first superoxide anion reduced a porphyrinate-$Fe^{III}Cl$ (porphyrinate-H_2 = TPP, OEP)[65] to the Fe^{II} form which then reacted with another equiv of superoxide anion to give the $[(porphyrinate)Fe^{III}(O_2^{2-})]^-$ species with side-on bound peroxide ligand (see diagram below). These species do not possess an additional axial ligand, as deduced previously,[11,49,63,64] and supported by the X-ray structure of a manganese analog $[(TPP)Mn(\eta^2\text{-}O_2^{2-})]^-$; here the Mn^{III} ion lies well above the porphyrinate plane toward the peroxo ligand.[66,67]

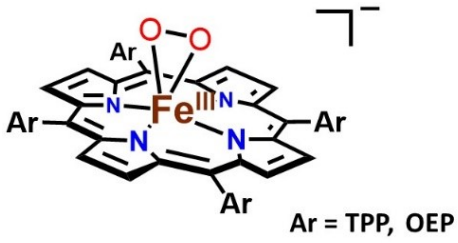

Previously, our complex ***P*** was characterized by UV-vis, EPR (g = 4.2 (S = 3/2); see Figure 4.3) and ^{1}H NMR spectroscopies.[60] Further characterization of ***P*** was carried out and ^{2}H NMR and rR spectroscopies are presented here. The pyrrolic proton in ^{2}H NMR spectroscopy at –80 °C resonates at δ 92.7 ppm (Figure 4.4), and this feature is consistent with the previously reported ^{1}H NMR spectroscopic signature (90 ppm).[60] Resonance Raman experiments confirmed peroxide formulation for ***P***, with the observation of ν_{O-O} vibration (806 cm^{-1}, $\Delta^{18}O_2$ = –46 cm^{-1}) and ν_{Fe-O} stretch (466 cm^{-1}, $\Delta^{18}O_2$ = –19 cm^{-1}) as shown in Figure 4.2B. These observed stretching frequency values match those calculated using the harmonic oscillator model: $\Delta_{O-O,calc}$ ($^{16}O_2/^{18}O_2$) = –47 cm^{-1}, $\Delta_{Fe-O,calc}$ ($^{16}O_2/^{18}O_2$) = –21 cm^{-1}. The relatively low Fe–O stretching frequency, which results from the symmetric stretching vibration of a side-on bound peroxide ligand, is similar to that in two other similarly structured heme peroxo compounds (vide infra, Table 4.1)[49] as well as nonheme[68–70] side-on peroxide complexes. It is notable that ν_{Fe-O} in these compounds is considerably reduced compared to what is observed for oxy-heme (i.e., Fe^{II}-(O_2)) species like oxy-myoglobin (ν_{Fe-O} = 570 cm^{-1}),[71] which we are referring to as ferric superoxide complexes. When strong acid, triflic acid (HOTf), is utilized to protonate peroxide species ***P***, H_2O_2 is released as expected and a yield of 95.5% is obtained (see Figure 4.5 and Experimental Section). If no hydrogen peroxide had been released with the acidification, it would have likely meant that reductive O–O cleavage (to give water) had somehow occurred.[72,73]

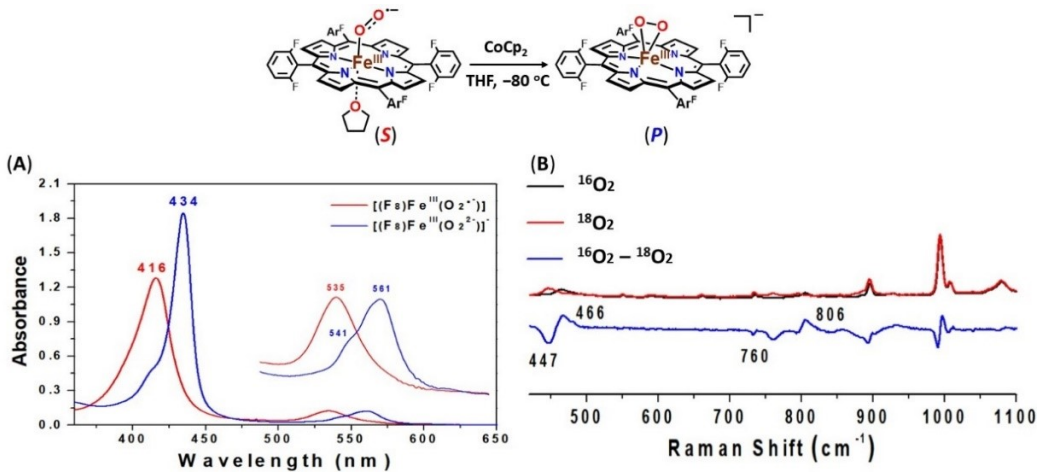

Figure 4.2 (A) UV-vis spectra of $[(F_8)Fe^{III}\text{-}(O_2^{\bullet-})]$ (***S***) (red) to $[(F_8)Fe^{III}\text{-}(O_2^{2-})]^-$ (***P***) (blue) in THF at –80 °C. (B) Resonance Raman spectra of ferric peroxide complex ***P*** in frozen THF obtained at 77 K with 413 nm excitation: Fe–O and O–O stretching frequencies for the complex generated with $^{16}O_2$ (black) or $^{18}O_2$ (red). The $^{16}O_2$–$^{18}O_2$ difference spectrum is shown in blue. The bands at 900 and 1000 cm^{-1} are vibrations within the porphyrin ring, which are generally observed for hemes and minimally impacted by O_2 isotope substitution (i.e. the modes contain minimal O_2 motion).

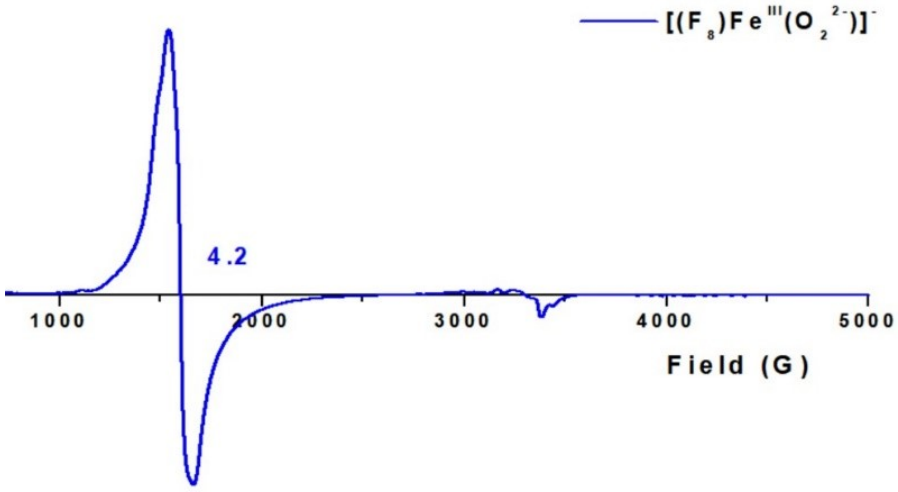

Figure 4.3 Frozen THF solution EPR (10K) spectrum of the side-on bound ferric heme peroxide complex $[(F_8)Fe^{III}\text{-}(O_2^{2-})]^-$ (***P***), identical to that previously determined.[60]

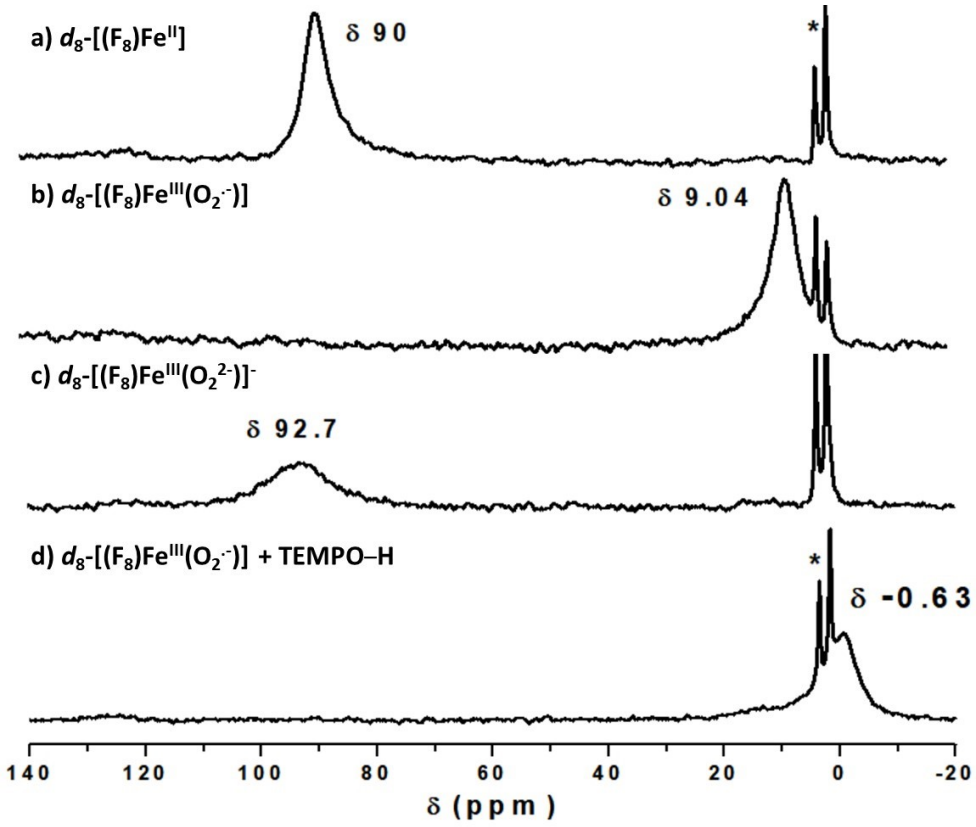

Figure 4.4 ^{2}H-NMR spectra of (a) d_8-$(F_8)Fe^{II}$, (b) d_8-[$(F_8)Fe^{III}$-$(O_2^{\bullet-})$] and (c) d_8-[$(F_8)Fe^{III}$-$(O_2^{2-})]^-$ (d) the reaction of superoxide d_8-[$(F_8)Fe^{III}$-$(O_2^{\bullet-})$] with TEMPO–H in THF at –80 °C, indicating that a low-spin ferric-heme is formed (and see the text). The sharp peaks at δ 3.58 and 1.73 ppm correspond to solvent THF.

Table 4.1 Resonance Raman stretching frequencies (cm^{-1}) of side-on ferric peroxide and end-on ferric hydroperoxide complexes

complex	**ν_{O-O} ($\Delta^{18}O_2$)**	**ν_{Fe-O} ($\Delta^{18}O_2$)**	**ref**
$[(TMPIm)Fe^{III}\text{-}(O_2^{2-})]^-$	807 (–49)	475 (–20)	48
$[(TMP)Fe^{III}\text{-}(O_2^{2-})]^-$	809 (–45)	470 (–19)	48
$[(F_8)Fe^{III}\text{-}(O_2^{2-})]^-$ (***P***)	806 (–46)	466 (–19)	this work
Mb WT	–	617 (–15)	79
Cyt P450 WT	799 (–40)	559 (–27)	81
Cyt P450 D251N	774 (–37)	564 (–28)	82
LPO	–	604 (–24)	117
$[(TMPIm)Fe^{III}\text{-}(O_2H)]$	810 (–47)	570 (–26)	48
$[(TMPIm^{XOMe})Fe^{III}\text{-}(O_2H)]$	807 (–41)	575 (–25)	49
$[(TMPIm^{OH})Fe^{III}\text{-}(O_2H)]$	807 (–40)	579 (–28)	51
$[(TMPIm^{OEt})Fe^{III}\text{-}(O_2H)]$	811 (–42)	576 (–27)	51
$[(\alpha_4\text{-}FeEs_4)\text{-}O_2H]$	830 (–47)	631 (–37)	80
$[Fe^{III}\text{-}O_2H(SQ)]$	783 (–35)	531 (–20)	44
$[(F_8)Fe^{III}\text{-}(OOH)]$ (***HP***)	806 (–46)	576 (–25)	this work

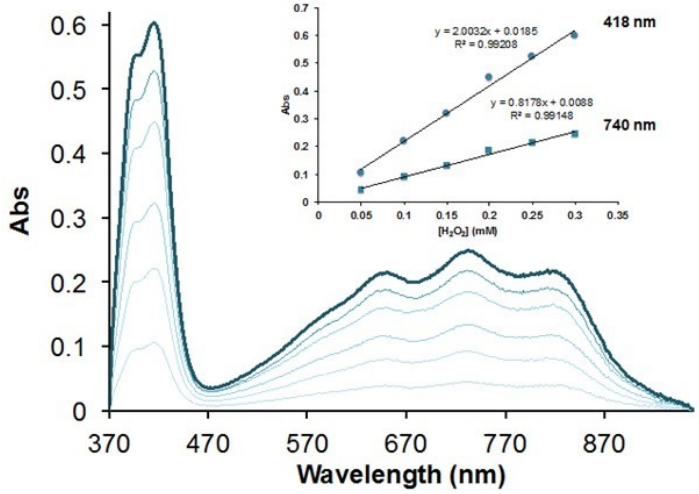

Figure 4.5 Calibration curve used for H_2O_2 quantification by the horseradish peroxidase (HRP) test. See experimental section for details.

4.2.2 Generation and characterization of [(F_8)Fe^{III}-(OOH)] (*HP*)

The addition of one equiv 2,6-lutidinium triflate [($LutH^+$)](OTf) or [(H)DMF](OTf)[74] to the solution of [(F_8)Fe^{III}-(O_2^{2-})]$^-$ (***P***) at –80 °C in THF leads to protonation of this side-on ferric heme peroxide complex to form a corresponding ferric heme hydroperoxide species, [(F_8)Fe^{III}-(OOH)] (***HP***). UV-vis spectra of ***HP*** exhibit absorptions at 418, 536 and 558 nm (Figure 4.6), while an EPR spectrum indicates distinctive changes from the side-on peroxide g = 4.2 signal observed in ***P***, to a low-spin ferric hydroperoxide species characterized by g = 2.23, 2.14 and 1.96 signals (Figure 4.7A), very similar to published values for other ferric end-on hydroperoxide synthetically derived complexes,[45,49,50,52,75–77] as well as for ferric heme hydroperoxides generated within hemoglobin and myoglobin.[78,79] Consistent with our complex formulation as [(F_8)Fe^{III}-(OOH)] (***HP***), a high yield (93.3%) of H_2O_2 was detected when we acidified the complex solution with triflic acid (HOTf) and applied the a quantitative horseradish peroxidase assay (see Figure 4.5 and experimental section).[72,73]

The characterization of [(F_8)Fe^{III}-(OOH)] (***HP***) was further corroborated by rR spectroscopy. The rR spectra of ***HP*** are indicative of a clear change in the ν_{Fe-O} vibrational stretch mode on protonation, shifting from 466 cm^{-1} ($\Delta^{18}O_2$ = –19 cm^{-1}) in side-on ferric peroxide species ***P*** to 576 cm^{-1} ($\Delta^{18}O_2$ = –25 cm^{-1}) in hydroperoxide complex ***HP***, whereas the ν_{O-O} vibrational frequency remains the same, appearing at 806 cm^{-1} ($\Delta^{18}O_2$ = –46 cm^{-1}) as shown in Figure 4.7B. These ν_{Fe-O} and ν_{O-O} vibrational stretching frequency downshifts when using $^{18}O_2$ match well with values calculated using the harmonic oscillator model: $\Delta_{Fe-O,calc}$ ($^{16}O_2/^{18}O_2$) = –26 cm^{-1}, $\Delta_{O-O,calc}$ ($^{16}O_2/^{18}O_2$) = –47 cm^{-1}. Also, these observed ν_{Fe-O} and ν_{O-O} vibrational values are quite similar to those obtained in other

low-spin end-on ferric heme hydroperoxide model complexes (Table 4.1), those from the groups of Naruta[49,50,52] and Dey[80] and their co-workers. This also well matches data obtained from cryogenically ferric hydroperoxide species generated in CYP450's,[81,82] even though the latter have axial cysteinate ligands which makes the coordination environment very different as compared to those for the synthetic analogues (Table 4.1). The combined spectroscopic data (UV-vis, EPR and rRaman) support the formulation of ***HP*** as a low-spin end-on (η^1) ferric hydroperoxide species. We postulate that ***HP*** most likely possesses a solvent THF molecule (Figure 4.6), as we know this can confer low-spin character to six-coordinate ferric hemes with F_8;[61,62,83] there exists the possibility the axial ligand is 2,6-lutidine or DMF, in exchange with THF.

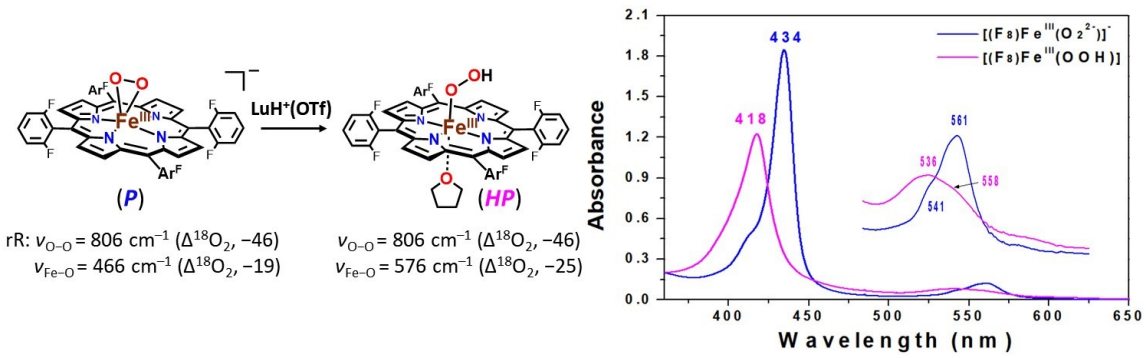

Figure 4.6 UV-vis spectra of illustrating the conversion of $[(F_8)Fe^{III}\text{-}(O_2^{2-})]^-$ (***P***) (blue) to form $[(F_8)Fe^{III}\text{-}(OOH)]$ (***HP***) (pink) by addition of $[(LutH^+)](OTf)$ in THF at –80 °C.

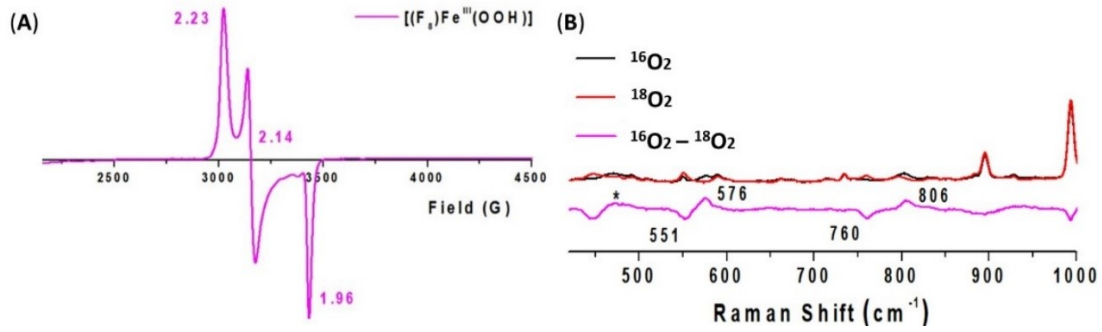

Figure 4.7 (A) Frozen THF solution EPR (10K) spectrum of ***HP***. (B) Resonance Raman spectra of ferric hydroperoxide complex ***HP*** in frozen THF obtained at 77 K with 413 nm excitation: Fe–O and O–O stretching frequencies for the complex generated with $^{16}O_2$ (black) or $^{18}O_2$ (red). The $^{16}O_2$–$^{18}O_2$ difference spectrum is shown in pink. Note that complex ***P*** is present as an impurity, observed as a set of $^{16}O_2$/$^{18}O_2$ peaks at 466/447 cm^{-1} (marked with an asterisk).

4.2.3 Comparison of this work with previously reported hydroperoxide ferric hemes

It has been generally difficult to cleanly synthesize ferric heme hydroperoxide compounds. Tajima and co-workers[75,77,84] reported low-spin ferric hydroperoxide complexes which are in accord with a Fe^{III}-heme(-OH)(-OOH) formulation, based on UV-vis and EPR spectroscopies. Significant advances were made by Naruta and co-workers[49] who extensively characterized an end-on ferric hydroperoxide complex, that shown in Figure 4.8B.[14,20] It was generated by protonation of the seven-coordinated side-on peroxide species [(TMPIm)Fe^{III}-(O_2^{2-})] (Figure 4.8A) with ligated axial imidazole ligand from the covalently attached tether, wherein a spin state change from S = 3/2 (ν_{Fe-O} = 470 cm^{-1} ($\Delta^{18}O_2$ = –19 cm^{-1}); ν_{O-O} = 809 cm^{-1} ($\Delta^{18}O_2$ = –45 cm^{-1})) to low-spin (ν_{Fe-O} = 570 cm^{-1} ($\Delta^{18}O_2$ = –26 cm^{-1}); ν_{O-O} = 810 cm^{-1} ($\Delta^{18}O_2$ = –47 cm^{-1})) occurred (Table 4.1).[49] Therein, a covalently appended axial imidazole ligand was critical to give a stable 6-coordinate ferric heme hydroperoxide complex. In the absence of the imidazolyl axial ligand (Figure

4.8), only decomposition occurred upon protonation. In other case, Anxolabéhère-Mallart and co-workers[76] generated a ferric heme hydroperoxide complex in the presence of 1-methylimidazole as sixth ligand by protonation of its side-on ferric peroxide precursor which is formed from the electrochemical reduction of an in situ formed ferric superoxide species. A significant difference in synthetic protocols occurs with our case (vide supra); while Naruta and co-workers postulated that methanol was the proton source converting peroxide to hydroperoxide complex, a stronger acid ([(LutH$^+$)](OTf) or [(H)DMF](OTf)) was required in our case, but a strong axial base ligand was not necessary.

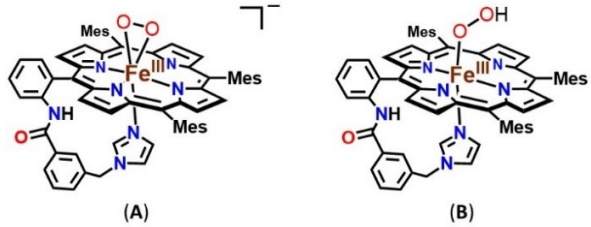

Figure 4.8 Naruta group's synthetic complexes; (A) [(TMPIm)Fe^{III}–(O_2^{2-})], (B) [(TMPIm)Fe^{III}–(OOH)].[49]

4.2.4 Reduction potential of the [(F_8)Fe^{III}-($O_2^{\bullet-}$)] (***S***)/ [(F_8)Fe^{III}-(O_2^{2-})]$^-$ (***P***)

When we set out this study, one of the main goals was to see if we could determine a reduction potential for a superoxide [(F_8)Fe^{III}-($O_2^{\bullet-}$)] (***S***) conversion to side-on peroxide complex [(F_8)Fe^{III}-(O_2^{2-})]$^-$ (***P***). In order to do this accurately it needed to be shown that reduction of ***S*** to ***P*** is a reversible reaction. In fact, we find this to be the case; [(F_8)Fe^{III}-($O_2^{\bullet-}$)] (***S***) and peroxide [(F_8)Fe^{III}-(O_2^{2-})]$^-$ (***P***) are interconvertible using redox reagents. Addition of the strong oxidant, [(4-BrC_6H_4)$_3$N](SbCl_6) (Tris(4-bromophenyl)ammoniumyl cation, known as Magic Blue because of its intense royal blue color; $E_{1/2}$ = 0.67 V vs. Fc$^{+/0}$ in MeCN)[85] to the solution of ***P*** results in complete oxidative conversion of the peroxide to superoxide species (Figure 4.9).

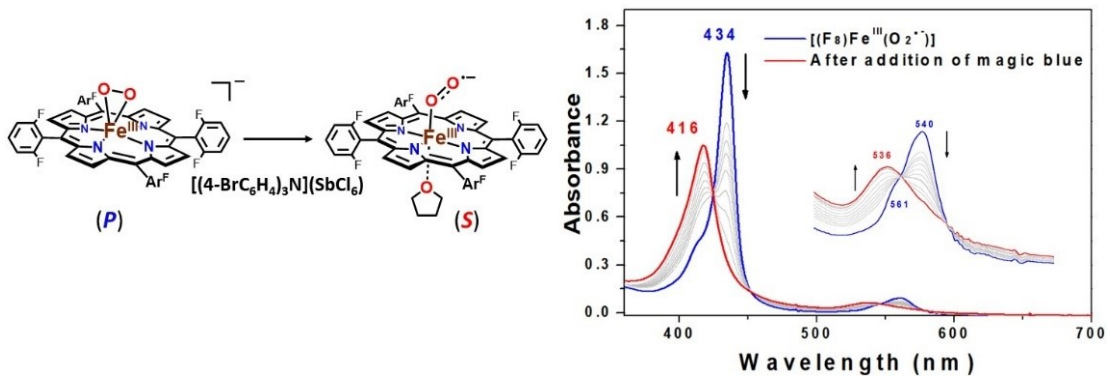

Figure 4.9 UV-vis spectra demonstrating the oxidation of $[(F_8)Fe^{III}\text{-}(O_2^{2-})]^-$ (***P***) (blue) to form $[(F_8)Fe^{III}\text{-}(O_2^{\bullet-})]$ (***S***) (red) in THF at –80 °C. A spectrum (gray lines) was recorded every ~2 min; the reaction goes to completion in ~ 20 min. Also, see the text.

Observations supporting this conclusion are that the product solution containing $[(F_8)Fe^{III}\text{-}(O_2^{\bullet-})]$ (***S***) is EPR silent (10 K, THF) as expected; the low-spin Fe^{III} ion is antiferromagnetically coupled with the unpaired electron of the directly coordinated superoxide radical anion. Interestingly, the addition of the weaker reductant, $Cr(\eta\text{-}C_6H_6)_2$ ($E_{1/2}$ = –1.15 V vs. $Fc^{+/0}$ in CH_2Cl_2),[85] to the solution of ***S*** leads to the formation of an equilibrium mixture of superoxide ***S*** and peroxide ***P***, allowing the determination of the reduction potential for the superoxide (***S***)/peroxide (***P***) couple. A titration of superoxide ***S*** with varying amounts of $Cr(\eta\text{-}C_6H_6)_2$ in THF at –80 °C was monitored by UV-vis spectroscopy (Figure 4.10), allowing the determination of an equilibrium constant value in each instance of added bis-benzene chromium(0) titrant (Table 4.2); the UV-vis absorptions for ***S*** and ***P*** gave direct determination of their concentrations, thus defining the amount/concentration of $Cr(\eta\text{-}C_6H_6)_2$ reacted and of $[Cr(\eta\text{-}C_6H_6)_2]^+$ formed. From the collection of calculated equilibrium constants, corresponding reduction potentials were determined by using the Nernst equation ($E = E°' - (RT/nF)\ln(Q)$). Thus, the reduction potential ($E°'$) for $[(F_8)Fe^{III}\text{-}(O_2^{\bullet-})]$ (***S***)/$[(F_8)Fe^{III}\text{-}(O_2^{2-})]^-$ (***P***) couple was calculated to be –1.17 ± 0.01 V vs. $Fc^{+/0}$ (for which $E°'$ = –0.39 V vs. SHE in THF). See Table 4.2 for further

details. A further demonstration of the reversibility of the reduction and oxidation of complex ***S***/***P*** was established; Peroxide species ***P*** generated by $Cr(\eta\text{-}C_6H_6)_2$ could be fully oxidized back to superoxide ***S*** using Magic Blue and again, this resulting solution could be reduced to peroxide ***P*** with 5 equiv $Cr(\eta\text{-}C_6H_6)_2$, to the extent of ~85% (Figure 4.11).

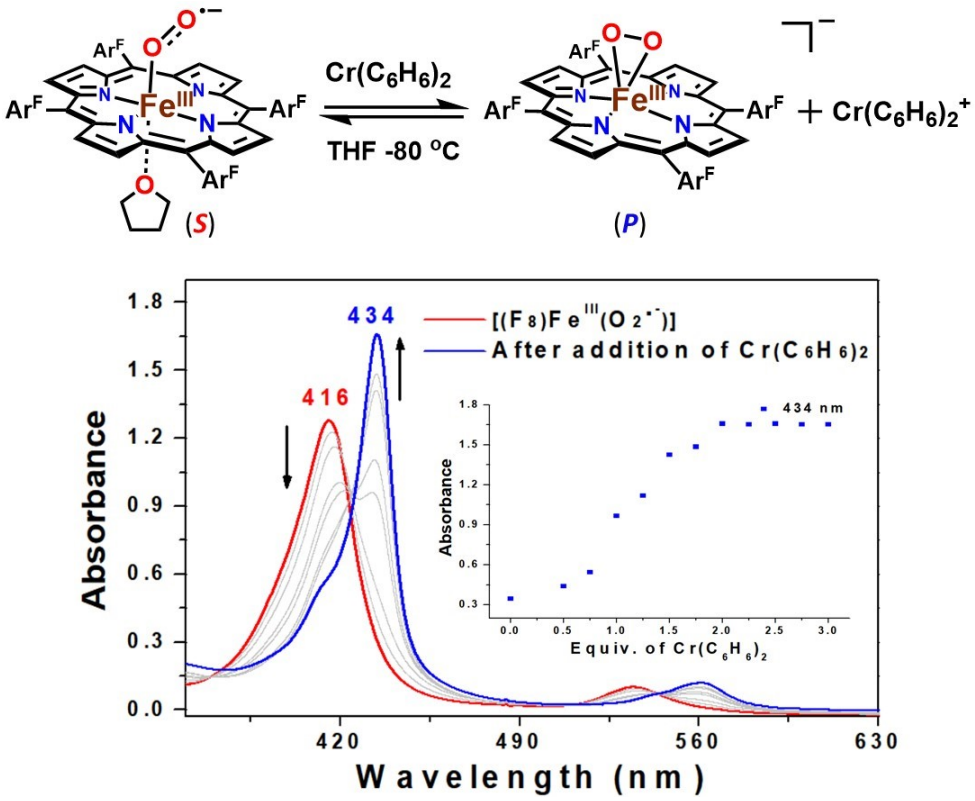

Figure 4.10 Conversion of $[(F_8)Fe^{III}\text{-}(O_2^{\bullet-})]$ (***S***) (red) to $[(F_8)Fe^{III}\text{-}(O_2^{2-})]^-$ (***P***) (blue) upon addition of $Cr(\eta\text{-}C_6H_6)_2$ in THF at –80 °C, resulting in the generation of equilibrium mixtures which allowed the determination of the reduction potential (–1.17 V vs. $Fc^{+/0}$) of the ***S***/***P*** redox couple. Inset: monitoring the absorbance at 434 nm upon addition of various amounts of $Cr(\eta\text{-}C_6H_6)_2$. See Table 4.2 for details.

Table 4.2 Equilibrium concentrations and calculated *E*s values for the titration of Cr(η-$C_6H_6)_2$ into a solution of [$(F_8)Fe^{III}$-$(O_2^{\bullet-})$] (***S***) in THF at –80 °C

$[Cr(C_6H_6)_2]_{added}$	$[Cr(C_6H_6)_2]_{eq}$	$[Peroxide]_{eq}$	$[Superoxide]_{eq}$	$[Cr(C_6H_6)_2]^+_{eq}$	K_{eq}
1.00 x 10^{-5}	1.44 x 10^{-6}	8.56 x 10^{-6}	3.14 x 10^{-5}	8.56 x 10^{-6}	6.18 x 10^{-1}
3.91 x 10^{-5}	1.64 x 10^{-5}	2.33 x 10^{-5}	1.67 x 10^{-5}	2.33 x 10^{-5}	5.01 x 10^{-1}
4.95 x 10^{-5}	2.25 x 10^{-5}	2.70 x 10^{-5}	1.30 x 10^{-5}	2.70 x 10^{-5}	4.03 x 10^{-1}
5.92 x 10^{-5}	2.49 x 10^{-5}	3.44 x 10^{-5}	5.62 x 10^{-6}	3.44 x 10^{-5}	1.18 x 10^{-1}
6.90 x 10^{-5}	3.32 x 10^{-5}	3.58 x 10^{-5}	4.19 x 10^{-6}	3.58 x 10^{-5}	1.08 x 10^{-1}

K_{eq}	*E*s (mV)
6.18 x 10^{-1}	–1.16
5.01 x 10^{-1}	–1.16
4.03 x 10^{-1}	–1.17
1.18 x 10^{-1}	–1.19
1.08 x 10^{-1}	–1.19

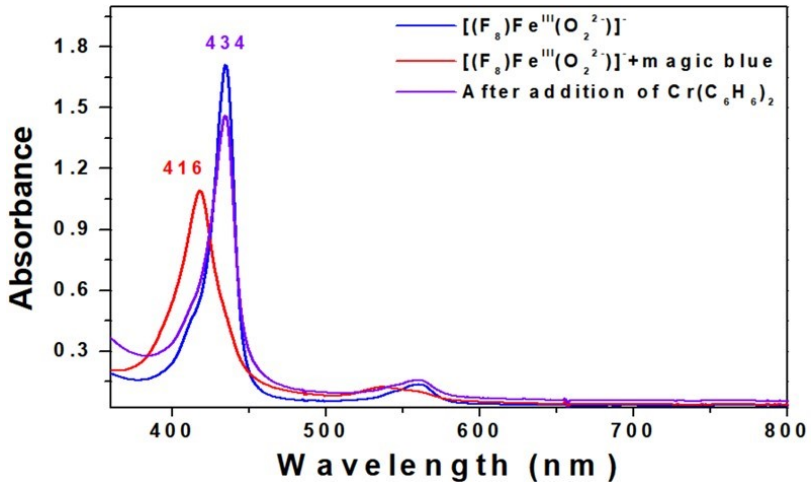

Figure 4.11 Addition of 1 equiv of magic blue to $[(F_8)Fe^{III}$-$(O_2^{2-})]^-$ (***P***) (blue) generated by Cr(η-$C_6H_6)_2$ from $[(F_8)Fe^{III}$-$(O_2^{\bullet-})]$ (***S***), regenerates the formation of ***S*** (red) and again, upon addition of 5 equiv of Cr(η-$C_6H_6)_2$, to this resulting solution, $[(F_8)Fe^{III}$-$(O_2^{2-})]^-$ (***P***) (purple) is formed to the extent of ~85%.

Recently, Naruta and co-workers[52] reported the reduction potential (–0.67 V and –1.1 V vs. SHE) of various ferric heme superoxide synthetic compounds, not experimentally but by employing density functional theory (DFT) calculations. Thus, these values are much more negative than what was found by us for the $[(F_8)Fe^{III}\text{-}(O_2^{\bullet-})]$ (***S***)/$[(F_8)Fe^{III}\text{-}(O_2^{2-})]^-$ (***P***) redox couple, E°' = –0.39 V vs. SHE in THF at –80 °C. Anxolabéhère-Mallart, Fave and co-workers[76] recently reported on the electrochemical generation of the side-on peroxide species $[Fe^{III}(F_{20}TPP)(O_2)]^-$ (EPR; $g = 4.2$) by applying a cathodic potential (E_{app} = –0.60 V vs. SCE; –0.36 V vs. SHE) to the corresponding superoxide precursor in dimethylformamide at –30 °C. The electrochemical reduction was found to be irreversible, nevertheless the finding of ferric heme superoxide complex reduction at $E°' = –0.60$ V vs. SCE (–0.36 V vs. SHE) is most interesting since it lies very close to our own result (vide supra). For Anxolabéhère-Mallart, Fave and co-workers, the superoxide and peroxide complexes employed the highly electron-withdrawing heme ($F_{20}TPP$) with 20 aryl fluorine substituents; no axial base ligand was utilized. Roughly, the comparison of reduction potential of –0.36 V for the $F_{20}TPP$ containing ferric heme superoxide, as well as the –0.39 V value for reversible reduction of $[(F_8)Fe^{III}\text{-}(O_2^{\bullet-})]$ with the far more negative potentials (vide supra) observed for the various $[(P)Fe^{III}\text{-}(O_2^{2-})]$ complexes from Naruta and co-workers, possessing a more electron-rich porphyrinate with axial imidazole ($TMPIm^{OH,OEt}$; Figure 4.12), may make sense. (See Table 4.3 for comparison of reduction potential values.)[86] Interestingly, computational chemists have estimated the reduction potential for the ferric heme superoxide species in CYP450 (Scheme 4.1); depending on "chosen model, QM region, and protonation state", the values obtained range from –2.28 to –1.04 V vs.

SHE.[5] Perhaps this is most reasonable, as the axial cysteinate ligand in CYP450's is a strong anionic donor known for its ability to "push".[9,23]

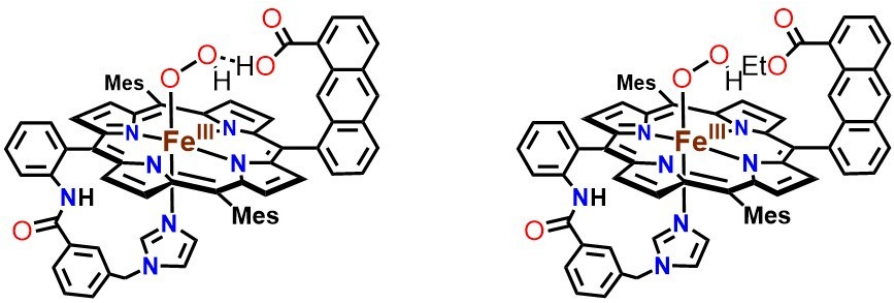

Figure 4.12 Diagrams of hydroperoxide complexes from Naruta and coworkers, not shown in the main text.[51]

Table 4.3 Thermodynamic information (reduction potential and pK_a) and OO–H bond dissociation free energy (BDFE)s (kcal/mol)

complex	***E*°' (V) vs. $Fc^{+/0}$ (Fe^{III}-$O_2^{\bullet-}$)/ (Fe^{III}-O_2^{2-})**	**pK_a (Fe^{III}-OOH)**	**OO–H BDFE (calcd)**	**OO–H BDFE (exptl)**	**ref**
$(TMPIm^{OH})Fe^{III}$	–1.32[a]	25.1[a]	—	—	51
$(TMPIm^{OEt})Fe^{III}$	–1.75[a]	32.3[a]	—	—	51
$(F_{20}TPP)Fe^{III}$	–1.09[b]	—	—	—	76
(por)(Im)Fe^{III}	—	—	66.2[c]	—	91
(por)(SH)Fe^{III}	—	—	63.9[c]	—	91
$(F_8)Fe^{III}$	–1.17	28.8	—	73.5[d]	this work

[a]Calculated in EtCN using DFT
[b]Measured in DMF by CV
[c]Calculated in MeCN using DFT, BDE not BDFE
[d]Measured in THF

4.2.5 Determination of the pK_a Value of [$(F_8)Fe^{III}$-(OOH)] (***HP***)

As mentioned in the Introduction, for the thermodynamic square scheme, the pK_a value of hydroperoxide [$(F_8)Fe^{III}$-(OOH)] (***HP***) has been determined in THF at –80 °C. It was evaluated by spectral titration using the derivatized phosphazene base EtP_2(dma) (pK_a = 28.1 in THF, for the conjugate acid at room temperature, see diagram below).[87]

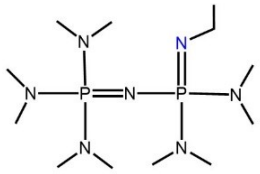

EtP_2(dma)
pK_a (N-H^+ in THF) = 28.1

As shown by a titration followed by UV-vis spectroscopy (Figure 4.13), the absorption band at 418 nm of ***HP*** decreased with increasing concentration of added EtP_2(dma), and the absorption band shifted to 434 nm, with observation of an isosbestic point at 426 nm. Such additions gave rise to an equilibrium mixture of hydroperoxide ***HP*** and the side-on peroxide complex $[(F_8)Fe^{III}\text{-}(O_2^{2-})]^-$ (***P***) (see Table 4.4). From this data, an equilibrium constant for this reaction was calculated in each instance and using the known pK_a value of EtP_2(dma), a pK_a value for deprotonation of ***HP*** was determined to be 28.8 ± 0.5 (THF, –80 °C). Following addition of excess base EtP_2(dma), only the deprotonated complex ***P*** remained. As suggested by the data, the acid-base reaction interconversion of ***HP*** and ***P*** is reversible. This was further shown by adding [($LutH^+$)](OTf) to the solution generated in this titration (Figure 4.13), this gives the fully regenerated hydroperoxide complex ***HP*** (see Figure 4.14 for details). In order to corroborate the [$(F_8)Fe^{III}$-(OOH)] (***HP***) pK_a value determined experimentally, a complementary experiment was conducted employing the conjugate acid of EtP_2(dma), i.e., as expected, based on relative pK_a values,

the addition of $EtP_2(dma)H^+$ (pK_a = 28.1) to peroxide $[(F_8)Fe^{III}\text{-}(O_2^{2-})]^-$ (***P***) results in the ready protonation and formation of ***HP*** (see Figure 4.15).

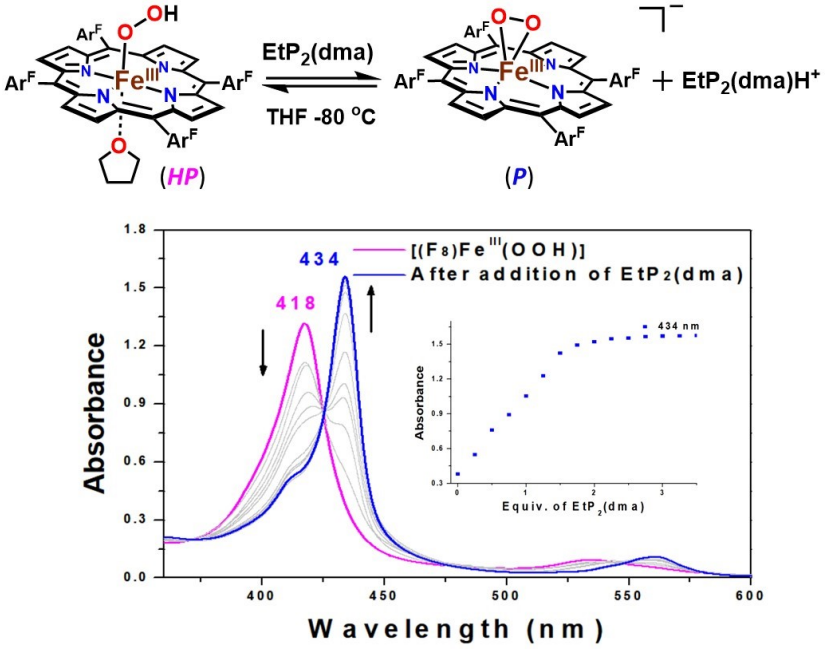

Figure 4.13 UV-vis spectroscopic monitoring of the incremental addition of $EtP_2(dma)$ to a solution of $[(F_8)Fe^{III}\text{-}(OOH)]$ (***HP***) (pink) resulting in the formation of equilibrium mixtures of ***HP***, $EtP_2(dma)$, $[(F_8)Fe^{III}\text{-}(O_2^{2-})]^-$ (***P***) (blue) and protonated base $EtP_2(dma)H^+$ which allowed the determination of the pK_a value (28.8) of ***HP***. Inset: monitoring of the absorbance at 434 nm (blue).

Table 4.4 Equilibrium concentrations and calculated pK_a values for the titration of $EtP_2(dma)$ into a solution of $[(F_8)Fe^{III}(OOH)]$ (***HP***) in THF at –80 °C

$[EtP_2(dma)]_{added}$	$[Peroxide]_{eq}$	$[EtP_2(dma)]_{eq}$	$[Hydroperoxide]_{eq}$	$[EtP_2(dma)H^+]_{eq}$	K_{eq}
2.93×10^{-5}	2.16×10^{-5}	7.71×10^{-6}	1.63×10^{-5}	2.16×10^{-5}	3.68
3.88×10^{-5}	2.54×10^{-5}	1.34×10^{-5}	1.24×10^{-5}	2.54×10^{-5}	3.87
4.83×10^{-5}	2.96×10^{-5}	1.86×10^{-5}	8.30×10^{-6}	2.96×10^{-5}	5.64
5.77×10^{-5}	3.44×10^{-5}	2.33×10^{-5}	3.52×10^{-6}	3.44×10^{-5}	14.3
7.62×10^{-5}	3.68×10^{-5}	3.94×10^{-5}	1.14×10^{-6}	3.68×10^{-5}	29.8

K_{eq}	pK_{eq}	pK_a
3.68	–0.56	28.6
3.87	–0.58	28.6
5.64	–0.75	28.8
14.3	–1.15	29.2
29.8	–1.47	29.5

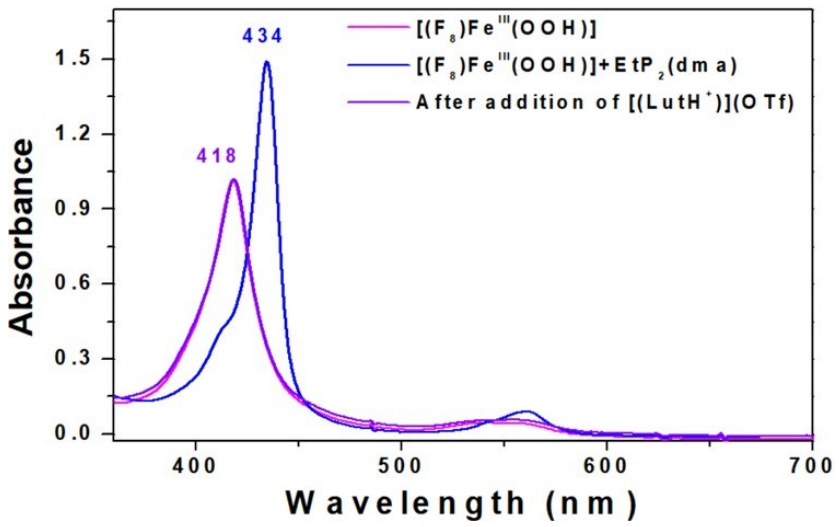

Figure 4.14 Addition of EtP_2(dma) to the solution of [$(F_8)Fe^{III}$-(OOH)] (***HP***) (pink), obtained via the protonation of [$(F_8)Fe^{III}$-(O_2^{2-})]$^-$ (***P***) using [$(LutH^+)$](OTf), regenerates complex ***P*** (blue). This resulting solution can (again) be protonated to give full formation of ***HP*** (purple) by adding 3 equiv of [$(LutH^+)$](OTf); the small excess of acid was required to neutralize the excess base (EtP_2(dma)) present in solution.

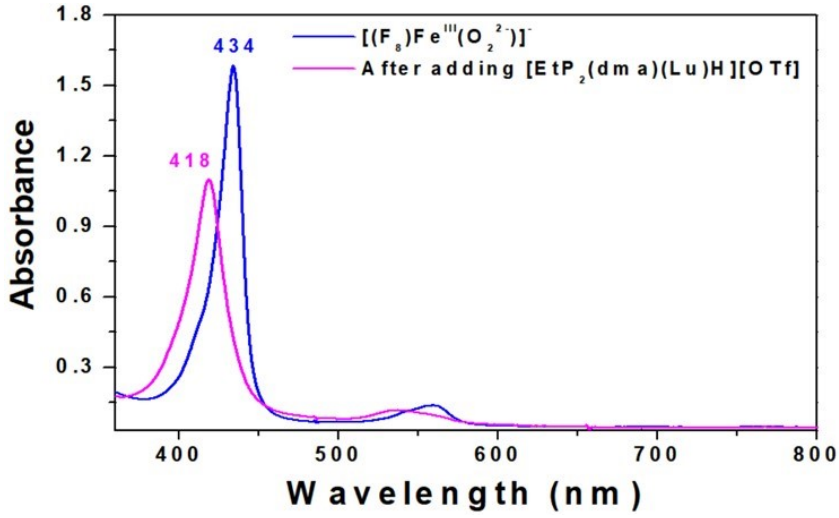

Figure 4.15 Addition of 10 equiv. of [EtP_2(dma)(Lu)H](OTf) (generated *in situ* from addition of 1equiv. of [$(LutH^+)$](OTf) to EtP_2(dma) in THF) to [$(F_8)Fe^{III}$-(O_2^{2-})]$^-$ (***P***) (blue) leads to the formation of [$(F_8)Fe^{III}$-(OOH)] (***HP***) (pink).

As discussed above, Naruta and co-workers[52] synthetically generated several ferric heme hydroperoxide complexes. They did address the question of pK_a values, but only computationally. For two ferric hydroperoxide complexes they described, possessing modified superstructured synthetic hemes (see Figure 4.12), their DFT determined pK_a values were 25.1 or 32.3 in EtCN as a solvent. In reality, these values are not so different from that of our own experimentally determined pK_a value (= 28.8, vide supra) for [$(F_8)Fe^{III}$-(OOH)] (***HP***).

4.2.6 Determination of the OO–H BDFE of [$(F_8)Fe^{III}$-(OOH)] (*HP*)

The bond dissociation free energy (BDFE) is the thermodynamic parameter used to compare the energy, i.e., bond strength, for homolytic bond cleavage of a two atom-centered unit. In order to determine the BDFE, we utilized the Bordwell equation (eq. 1)[88] which uses Hess' law with the redox potential and acidity based on a thermodynamic cycle. Thus, using the measured thermodynamic parameters, $E°'$ (–1.17 V vs. $Fc^{+/0}$, vide supra) and pK_a (28.8, vide supra), a thermodynamic square scheme is completed as shown in Figure 4.1 and this leads to a BDFE of 73.5 ± 0.9 kcal/mol for the OO–H bond in hydroperoxide [$(F_8)Fe^{III}$-(OOH)] (***HP***) according to eq. 2 where C_G is 61 kcal/mol in THF.[89]

$$\mathbf{BDFE}_{O–H} = 1.37(28.8) + 23.06(–1.17) + 61 = \mathbf{73.5\ kcal/mol} \qquad (\mathbf{2})$$

As mentioned, this is to our knowledge the first case where a BDFE value has been reported using experimentally derived thermodynamics (reduction potential and pK_a) for a

heme system, those involving O_2 or its reduced derivatives.[90] Morokuma and co-workers[91] computationally evaluated aspects of other heme-superoxide (as well as other metal-superoxide) species, and their findings are also in accord with the present results, i.e., that for [$(F_8)Fe^{III}$-(OOH)], BDFE = 73.5 kcal/mol. For heme ferric superoxide complexes modeling protein active sites (e.g., hemoglobin, CYP450) where a proximal ligand is either an imidazole or an -SH group (the latter as a computational model for the cysteinate proximal ligand in CYP450's), i.e., (B)(porphyrinate)Fe^{III}-$O_2^{\bullet-}$ (B = imidazole, SH) the ferric heme hydroperoxide complex OO–H BDE's are calculated to be in the range 64–66 kcal/mol. Lai and Shaik[18] also computationally found that a CYP450 ferric heme superoxide is a "sluggish oxidant".

Corresponding OO–H BDFE (or BDE) values for a few product non-heme iron-hydroperoxide complexes are known, but these tetramethylcyclam (TMC) ligand derived complex results come only through computational evaluation.[91,92] These have recently been compared to experimental results on cobalt and other heavier metal-superoxide complexes.[93] Dicopper(II)-μ-hydroperoxide complex OO–H BDFE's have recently been determined.[89,94] In one case, the BDFE is 72 kcal/mol, while in another example, the binucleating ligand utilized results in a hydroperoxide OO–H BDFE of 81 kcal/mol. Thus, the corresponding dicopper(II)-μ-superoxide complex is a quite strong oxidant for HAT reactivity. Experimentation and compilation of O–H bond thermodynamic parameters (i.e., BDE's or BDFE's) of dioxygen-derived species (M-OH, M-OOH or M-oxo species formed from O_2-reduction/protonation) bound to metal complexes, is of considerable general significance and importance.[95]

4.2.7 Reactivity Studies of [$(F_8)Fe^{III}$-$(O_2^{\bullet-})$] (***S***) with O–H, C–H and N–H substrates

One of the utilities of BDFE data is to determine or estimate the oxidative reactivity in this case of the ferric heme superoxide complex. Hydrogen atom transfer oxidation of substrates for [$(F_8)Fe^{III}$-$(O_2^{\bullet-})$] (***S***) would afford the corresponding hydroperoxide analog, [$(F_8)Fe^{III}$-(OOH)] (***HP***). With an ***HP*** BDFE experimentally determined to be 73.5 kcal/mol, we can expect that ***S*** would only be capable of HAT reactions with substrates such as C–H, N–H or O–H BDFE's below or near this value.[96] So, we have probed these possibilities. Addition of an excess of higher BDFE substrates than 73.5 kcal/mol (i.e., *p*-methoxyphenol, BDFE = 83.1 kcal/mol in THF; fluorene, 76.8 kcal/mol in THF; 9,10-dihydroanthracene, 76 kcal/mol in DMSO; *p*-OMe-2,6-di-tert-butylphenol, 75.8 kcal/mol in THF)[59,89] to solutions of [$(F_8)Fe^{III}$-$(O_2^{\bullet-})$] (***S***) at –80 °C in THF led to no reaction, as expected. Also, no reaction occurs with similar BDFE substrates for ***HP***, such as 1,4-cyclohexadiene (72.9 kcal/mol in MeCN) and xanthene (72.2 kcal/mol in THF).[89] By contrast, BNAH (1-benzyl-1,4-dihydronicotinamide, 70.7 kcal/mol in DMSO),[97] phenylhydrazine (70.4 kcal/mol in MeCN) and diphenylhydrazine (67.1 kcal/mol in DMSO)[59] do react rapidly with complex ***S***, but we were not able to determine if the initial reaction is actually HAT; based on UV-vis spectroscopic monitoring, the expected hydroperoxide product, [$(F_8)Fe^{III}$-(OOH)] (***HP***), was not observed at the end of the reaction; probably HAT occurs, but side-reactions prevent clean formation of ***HP***. However, the addition of TEMPO–H (66.5 kcal/mol in THF)[89] to a solution of ***S*** in THF at –80 °C led to shifting of the UV-vis spectrum (Figure 4.16A), i.e., yielding an absorption at 418 nm, corresponding to ***HP***, suggesting that substrate hydrogen atom abstraction reaction occurred. Note that this HAT reaction from

TEMPO–H to complex ***S*** is thermodynamically downhill by ca. 7 kcal/mol, thus predicted to be quite favorable.

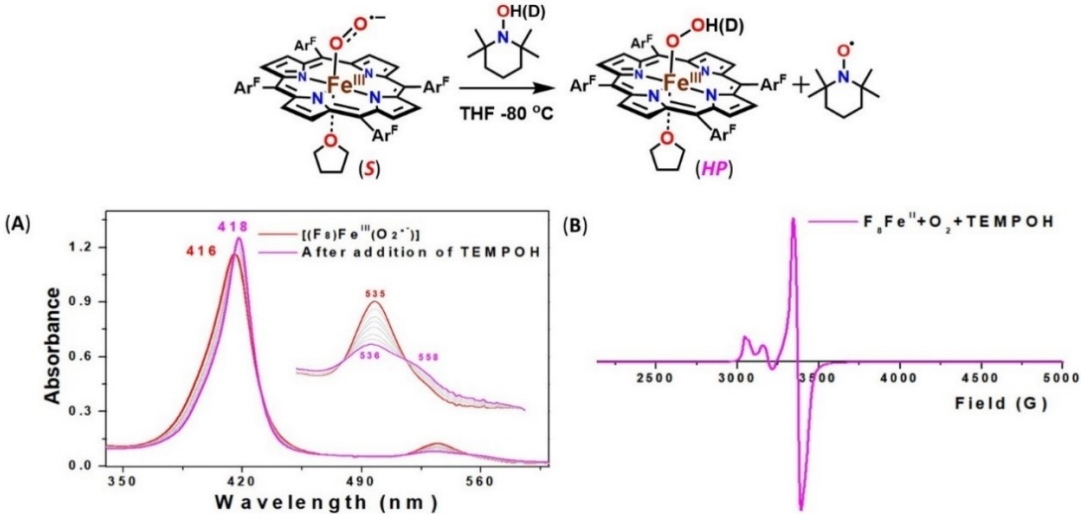

Figure 4.16 (A) UV-vis spectroscopic monitoring the reaction of $[(F_8)Fe^{III}\text{-}(O_2^{\bullet-})]$ (***S***) (red) with TEMPO–H in THF at –80 °C to yield $[(F_8)Fe^{III}\text{-}(OOH)]$ (***HP***) (pink). (B) 10 K EPR spectrum of the final products of TEMPO–H HAT by ***S*** in frozen THF. The yield of hydroperoxide ***HP*** is 94.2 % based on the absorbance and known absorptivity of ***HP*** at 418 nm. Spin quantification finds that the EPR signal corresponds to 92% of TEMPO radical.

Complementary experiments were performed, confirming generation of hydroperoxide species from the reaction between $[(F_8)Fe^{III}\text{-}(O_2^{\bullet-})]$ (***S***) and TEMPO–H. For one thing, addition of $EtP_2(dma)$ base to the product mixture led to the formation of peroxide species ***P*** based on UV-vis spectroscopy (Figure 4.17). Further, frozen solution EPR spectroscopy was also performed and this revealed a signal at $g = 2$ attributed to the TEMPO radical, appearing 'on top of' the signal expected for low-spin ***HP*** (Figure 4.16B), confirming H-atom abstraction by ***S*** from TEMPO–H. In addition, the final product exhibits upfield-shifted pyrrole resonance (δ_{pyrr} –0.63 ppm) in ^2H NMR spectroscopy, indicative of a six-coordinate ferric low-spin (S = 1/2) heme (Figure 4.4).[98,99]

For further insights into the nature of the hydrogen atom abstraction from TEMPO–H by ***S***, kinetic studies were carried out in THF at –80 °C via UV-vis spectroscopy (Figure 4.16). The rate of formation of hydroperoxide ***HP*** obeyed pseudo-first-order kinetics (Figure 4.18) when the reaction was conducted with excess TEMPO–H, and the observed pseudo-first-order constants (k_{obs}) are proportional to concentrations of TEMPO–H as shown in Figure 4.19 with an effectively zero intercept within error. According to this plot of k_{obs} vs [TEMPO–H], the second order rate constant k_2 was obtained to be 0.5 $M^{-1}s^{-1}$ in THF at –80 °C. When deuterated substrate, TEMPO–D, was treated to [$(F_8)Fe^{III}$-$(O_2^{\bullet-})$] (***S***), a significant slowing of the reaction occurred; k_2 = 0.08 $M^{-1}s^{-1}$ in THF at –80 °C (Figure 4.20). The comparison of the rate constants for H vs. D provides for a significant kinetic deuterium isotope effect (KIE) of 6 in THF at –80 °C as shown in Figure 4.19, strongly suggesting that H-atom abstraction by ***S*** is the rate-determining step.

There have been no prior reports of kinetic information to compare the reactivity of [$(F_8)Fe^{III}$-$(O_2^{\bullet-})$] (***S***) with other heme-superoxide complexes reacting with TEMPO–H. {Note: There is a study from Mayer and co-workers,[100] where a heme Fe^{III}-OH complex reacts with TEMPO–H, k_2 = 76 $M^{-1}s^{-1}$ at room temperature in toluene}. However, second order rate constants (k_2) for non-heme metal-superoxide (i.e., M^{n+}-$(O_2^{\bullet-})$) complexes (M = Cu, Mn, Co and Cr) involved in HAT reactions with TEMPO–H have been reported in a number of cases (see Table 4.5).[93,94,101–104]

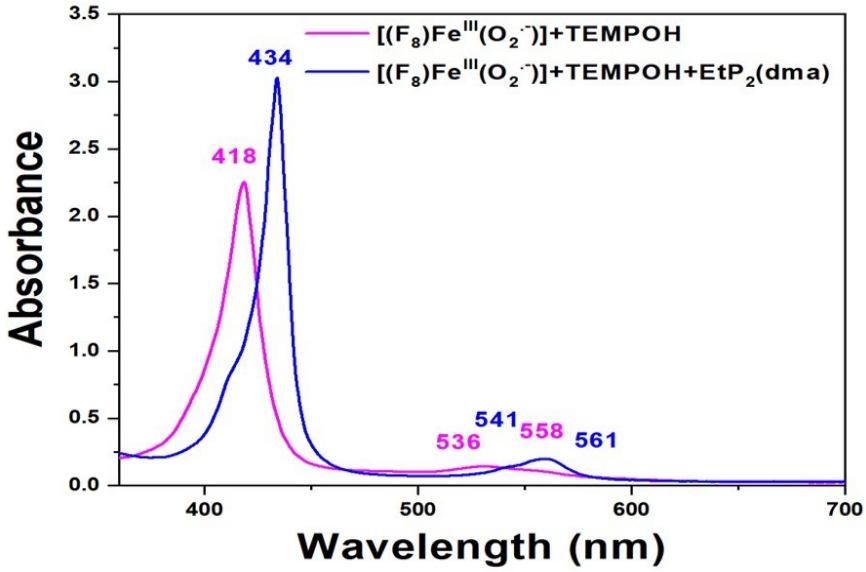

Figure 4.17 Addition of EtP_2(dma) to product mixture of $[(F_8)Fe^{III}\text{-}(O_2^{\bullet-})]$ (***S***) with TEMPO–H reaction (pink spectrum) leads to the formation of peroxide species $[(F_8)Fe^{III}\text{-}(O_2^{2-})]^-$ (***P***) (blue spectrum).

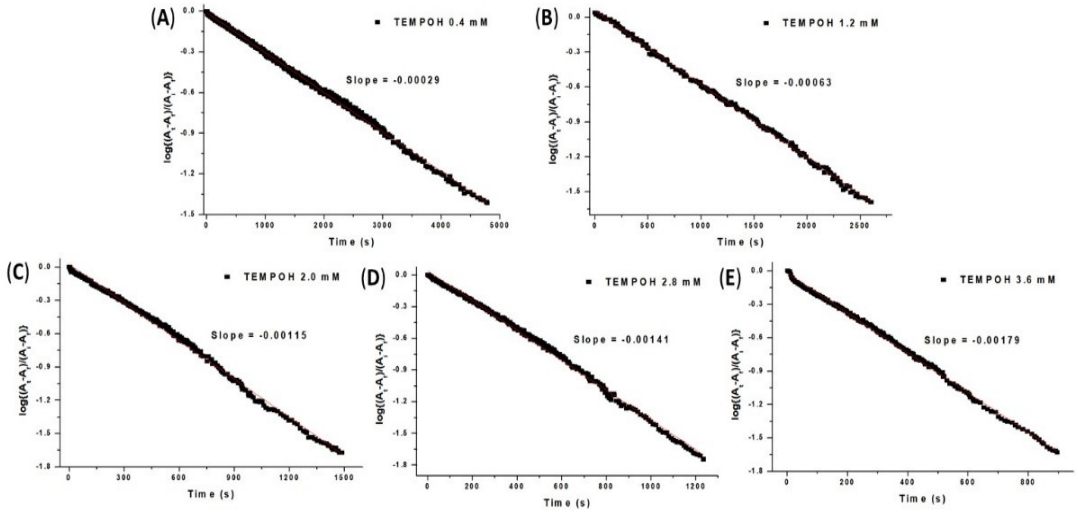

Figure 4.18 Pseudo-first-order plots for the reactions of $[(F_8)Fe^{III}\text{-}(O_2^{\bullet-})]$ (***S***) (0.04 mM) and (A) 0.4 (B) 1.2 (C) 2.0 (D) 2.8 (E) 3.6 mM of TEMPO–H to determine pseudo-first-order rate constants (k_{obs}).

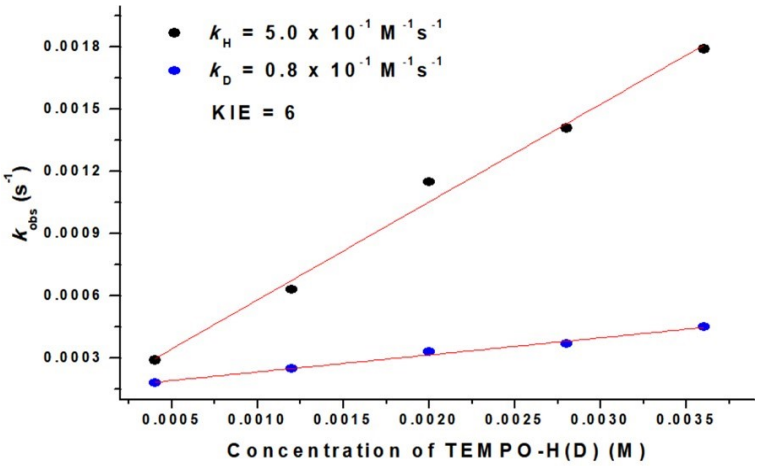

Figure 4.19 Plots of pseudo first order rate constants (k_{obs}) plotted against various concentrations of TEMPO–H(D) to obtain the second order rate constant, k_H = 5.0 x 10^{-1} M^{-1}s^{-1} (black circle) and k_D = 0.8 x 10^{-1} M^{-1}s^{-1} (blue circle) and KIE in THF at –80 °C.

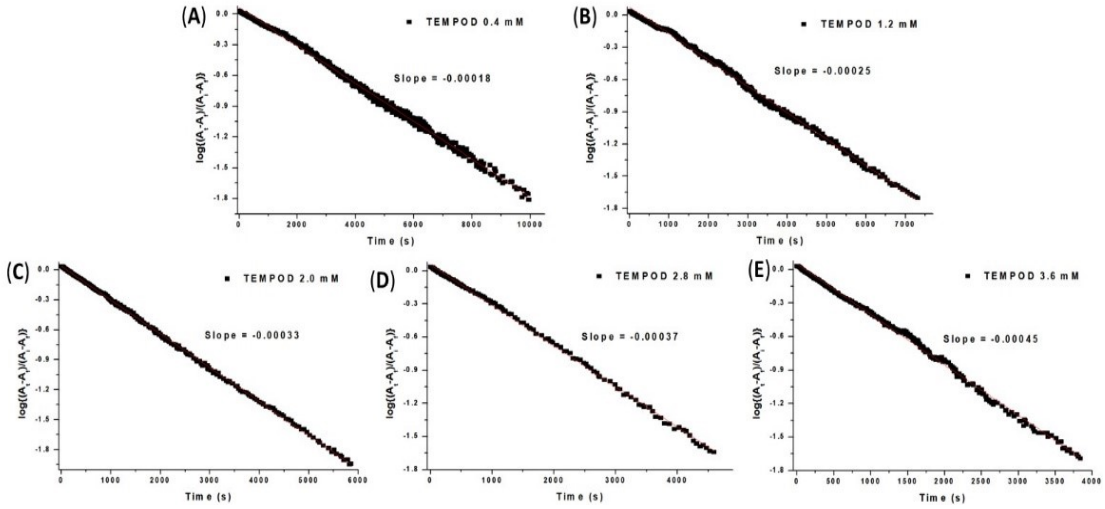

Figure 4.20 Pseudo-first-order plots for the reactions of [(F_8)Fe^{III}-($O_2^{\bullet-}$)] (***S***) (0.04 mM) and (A) 0.4 (B) 1.2 (C) 2.0 (D) 2.8 (E) 3.6 mM of TEMPO–D to determine pseudo-first-order rate constants (k_{obs}).

Table 4.5 Kinetic studies for non-heme metal-superoxide (M^{n+}-($O_2^{\bullet-}$)) complexes (M = Cu, Mn, Co and Cr) with TEMPO–H

complex	k_2 ($M^{-1}s^{-1}$)[h]	temp, solvent	ref
$[L^1Cu^{II}(O_2^{\bullet-})]PF_6$[a]	2.4	−85 °C in acetone	101
$[L^2Cu^{II}(\mu\text{-}1,2\text{-}O_2^{\bullet-})]BPh_4$[b]	0.13	−20 °C in MeCN	94
$[K(Krypt)][L^3Cu(O_2^{\bullet-})]$[c]	34.9	−80 °C in THF/MeCN 10:1	102
$[Mn(BDP^{Br}P)(O_2^{\bullet-})]$[d]	500	−90 °C in THF	103
$[Co(BDPP)(O_2^{\bullet-})]$[e]	0.97	−90 °C in THF	103
$[Co(O_2)(Me_3TACN)(S_2SiMe_2)]$[f]	0.87	−105 °C in MeTHF[i]	93
$[^{iPr}L_2Cr]Li_2O_2(EtCN)_4$[g]	306.6	−80 °C in EtCN	104

[a] L^1 = 1-(2-phenethyl)-5-[2-(2-pyridyl)ethyl]-1,5-diazacyclooctane
[b] L^2 = tacn/pyrazolate hybrid ligand
[c] L^3 = bis(arylcarboxamido)-pyridine ligand
[d] $H_2BDP^{Br}P$ = 2,6-bis((2-(S)-di(4-bromo)phenylhydroxyl-methyl-1-pyrrolidinyl)methyl)-pyridine
[e] H_2BDPP = 2,6-bis((2-(S)-diphenylhydroxylmethyl-1-pyrrolidinyl)methyl)pyridine
[f] reactivity with 4-OMe-TEMPO-H, deuterium-KIE = 8.8
[g] L = ^-O*i*Pr_2SiOSi*i*Pr_2O^-
[h] second order rate constants
[i] 2-methyltetrahydrofuran

As mentioned in the Introduction, recent review articles detail metal-superoxide complexes of the first row transition metals.[56,57] Prior computationally derived generalizations concerning metal superoxide reactivity have been published;[91,105] substrate reactivity depends on factors such as electrophilicity, reaction driving force, and coupling between the metal center and superoxide ligand. A CYP450 ferric superoxide is a weak oxidant for HAT, possessing large activation energy barriers.[18] These results are consistent with our findings where superoxide complex reacts by HAT with an exogenous weak O–H (and perhaps N–H and C–H, vide supra) substrate. Also, a few potentially biologically relevant non-heme iron superoxide complexes are capable of abstracting hydrogen atom from weak X–H substrates such as 2,4-di-tert-butyl phenol,[106] 2-hydroxy-2-azaadamantane

(AZADOL), phenylhydrazine (X–H < 72.6 kcal/mol)[107] and 9,10-dihydroanthracene (DHA; BDE = 76 kcal/mol).[108,109]

4.3 Conclusions

The side-on ferric peroxide species $[(F_8)Fe^{III}\text{-}(O_2^{2-})]^-$ (***P***) generated from $[(F_8)Fe^{III}\text{-}(O_2^{\bullet-})]$ (***S***) by one electron reduction, is protonated by acids such as $[(LutH^+)](OTf)$ to form the end-on ferric hydroperoxide complex $[(F_8)Fe^{III}\text{-}(OOH)]$ (***HP***) which has been characterized by UV-vis, EPR and rR spectroscopies. Thus, the stepwise generation of superoxide (***S***), peroxide (***P***) and hydroperoxide (***HP***) analogs which are involved in catalytic cycle of CYP450 (Scheme 4.1) or many other heme enzymes (see the Introduction) are completed through reduction and protonation processes as outlined in Figure 4.1. More importantly, by direct experimentation, the reduction potential of the superoxide species $[(F_8)Fe^{III}\text{-}(O_2^{\bullet-})]$ (***S***), and the pK_a value for the hydroperoxide analog $[(F_8)Fe^{III}\text{-}(OOH)]$ (***HP***) have been established. With these parameters in hand, the O–H BDFE of ***HP*** could be calculated (73.5 kcal/mol). This work describes the first example of experimentally determined thermodynamics (reduction potential and pK_a) interrelating ***S***, ***P***, and ***HP*** species while also demonstrating the generation of the ferric hydroperoxide complex (***HP***) using an exogenous substrate (TEMPO–H) for HAT by the ferric heme superoxide species (***S***). These results advance the literature concerning the thermodynamics of heme complexes while further showing the utility of synthetic model compounds to provide fundamental insights relevant to reaction cycles of heme enzymes.

As mentioned in Introduction, the peroxide intermediate in catalytic cycle of CYP450 (Scheme 4.1) is thought to have an end-on (η^1) geometry. Davydov, Sligar,

Hoffman, and co-workers[42] detected this end-on bound peroxide intermediate by employing γ-irradiation at cryogenic temperature with P450cam. Thus, one future goal will be research relevant to thermodynamic analysis involving end-on ferric heme peroxide chemistry. We wish to also further assess whether heme or axial ligation modifications may lead to enhancement of the oxidizing capability of a heme-Fe^{II}/O_2 derived adduct.

4.4 Experimental section

4.4.1 Materials and methods

All reagents and solvents purchased and used were of commercially available quality except as noted. Inhibitor-free Tetrahydrofuran (THF) was distilled over Na/benzophenone under argon and deoxygenated with argon before use. Butyronitrile was distilled over sodium carbonate and potassium permanganate and deoxygenated with Ar before use. Cobaltocene was obtained from Sigma Aldrich, sublimed at 75°C, and stored under nitrogen in the glovebox freezer at –30 °C. The 2,6-lutidinium Triflate [(Lu)(H)](OTf) and TEMPO–H(D) were synthesized according to previously published literature procedures.[110–112]

The preparation and handling of air-sensitive compounds were performed under a MBraun Labmaster 130 inert atmosphere (< 1 ppm O_2 and < 1 ppm H_2O) glovebox filled with nitrogen. Dioxygen gas purchased from Airgas and dried through Drierite. $^{18}O_2$ gas was purchased from ICON, Summit, NJ, and $^{16}O_2$ gas was purchased from BOC gases, Murray Hill, NJ.

All UV−vis measurements were carried out using a Hewlett-Packard 8453 diode array spectrophotometer with HP Chemstation software and a Unisoku thermostated cell

holder for low-temperature experiments. A 10 mm path length quartz cell cuvette modified with an extended glass neck with a female 14/19 joint, and stopcock was used to perform all UV–vis experiments, as previously described.[99,113,114] ^{1}H and ^{2}H NMR spectra were measured on a Bruker 300-MHz NMR spectrometer at ambient or low temperatures. Chemical shifts were reported as δ (ppm) values relative to an internal standard (tetramethylsilane) and the residual solvent proton peaks. Electron paramagnetic resonance (EPR) spectra were recorded with a Bruker EMX spectrometer equipped with a Bruker ER 041 × G microwave bridge and a continuous flow liquid helium cryostat (ESR900) coupled to an Oxford Instruments TC503 temperature controller. Spectra were obtained at 10 K under non-saturating microwave power conditions (ν = 9.428 GHz, microwave power = 0.201 mW, modulation amplitude = 10 G, microwave frequency = 100 kHz, and receiver gain = 5.02×10^3).

The compounds $(F_8)Fe^{II}$, and the pyrrole deuterated derivative d_8-$(F_8)Fe^{II}$ were synthesized as previously described.[61,115,116]

4.4.2 UV-vis spectroscopy

4.4.2.1 Generation of [$(F_8)Fe^{III}$-(OOH)] (*HP*)

After generating complex $[(F_8)Fe^{III}\text{-}(O_2^{2-})]^-$ (***P***),[60] 1 equiv [$(LutH^+)$](OTf) or [(H)DMF](OTf) was added to the solution of ***P*** to form [$(F_8)Fe^{III}$-(OOH)] (***HP***) in THF at –80 °C. UV-vis: λ_{max} = 418 (ε = 157048 M^{-1} cm^{-1}), 536 (ε = 9782.5 M^{-1} cm^{-1}) and 558 (ε = 7322.5 M^{-1} cm^{-1}) nm.

4.4.2.2 H_2O_2 quantification by horseradish peroxidase (HRP) test

The spectrophotometric quantification of hydrogen peroxide was carried out by analyzing the intensity of the diammonium 2,2′-azino-bis(3-ethylbenzothiazoline-6-sulfonate)(AzBTS-$(NH_4)_2$) peaks (at different wavelengths to minimize error, Figure 4.5), which was oxidized by horseradish peroxidase (HRP); this was adapted from published procedures.[72,73] Three stock solutions were prepared: 300 mM sodium phosphate buffer pH 7.0 (solution A), 1 mg/mL AzBTS-$(NH_4)_2$ (solution B) and 4 mg of HRP (type II salt free (Sigma)) with 6.5 mg of sodium azide in 50 mL of water (solution C). 3.0 mL of the desired $[(F_8)Fe^{III}\text{-}(O_2^{2-})]^-$ (***P***) or $[(F_8)Fe^{III}\text{-}(OOH)]$ (***HP***) solution were generated in THF at –80 °C, as previously described. The reaction which is before and after being quenched by adding 100μL of triflic acid (HOTf) solution (2.5 equiv) is subject to the H_2O_2 analysis. Subsequently 100 μL of the cold THF sample solution was removed via a syringe and quickly added to a cuvette containing 1.3 mL of water, 500 μL of solution A, 100 μL of solution B, and 50 μL of solution C (all chilled in an ice bath prior to use). After mixing for 15s, the samples were allowed to sit at room temperature for ~2 min until full formation of the 418 nm band was observed (Figure 4.5).

4.4.2.3 Determination of the reduction potential of $[(F_8)Fe^{III}\text{-}(O_2^{\bullet-})]$ (***S***)

$[(F_8)Fe^{III}\text{-}(O_2^{\bullet-})]$ (***S***) generated as previously published[61,62] was titrated with 0.25-2 equiv $Cr(\eta\text{-}C_6H_6)_2$ in THF at –80 °C. For each equilibrium mixture, the concentration of each species in solution was measured using the absorption at 434 nm (Table 4.2). From these equilibrium constants, corresponding reduction potentials were calculated by using the Nernst equation.

4.4.2.4 Reversibility of [(F_8)Fe^{III}-($O_2^{\bullet-}$)] (***S***) and [(F_8)Fe^{III}-(O_2^{2-})]$^-$ (***P***)

In a Schlenk cuvette, the addition of 1 equiv Magic Blue to a solution of [(F_8)Fe^{III}-(O_2^{2-})]$^-$ (***P***) generated from [(F_8)Fe^{III}-($O_2^{\bullet-}$)] (***S***) with 2 equiv Cr(η-C_6H_6)$_2$ in THF at –80 °C leads to the formation of [(F_8)Fe^{III}-($O_2^{\bullet-}$)] (***S***) and again, the addition of 5 equiv Cr(η-C_6H_6)$_2$ gives back [(F_8)Fe^{III}-(O_2^{2-})]$^-$ (***P***) (Figure 4.11).

4.4.2.5 Determination of the pK_a of [(F_8)Fe^{III}-(OOH)] (***HP***)

In a Schlenk cuvette, [(F_8)Fe^{III}-(OOH)] (***HP***) generated as described above, was titrated by 0.75-3 equiv EtP_2(dma) in THF at –80 °C. For each equilibrium mixture, the concentration of each species in solution was measured using the absorption at 434 nm (Table 4.4). From these equilibrium constants, the pK_a was calculated.

4.4.2.6 Reversibility of [(F_8)Fe^{III}-(O_2^{2-})]$^-$ (***P***) and [(F_8)Fe^{III}-(OOH)] (***HP***)

In a Schlenk cuvette, the addition of 3 equiv EtP_2(dma) to solution of [(F_8)Fe^{III}-(OOH)] (***HP***) generated as described above, results in the formation of [(F_8)Fe^{III}-(O_2^{2-})]$^-$ (***P***) in THF at –80 °C and again, the addition of 3 equiv [($LutH^+$)](OTf) gives [(F_8)Fe^{III}-(OOH)] (***HP***) (Figure 4.14).

4.4.2.7 Reactivity study of [(F_8)Fe^{III}-($O_2^{\bullet-}$)] (***S***) with TEMPO–H

Excess amount of TEMPO–H (0.4-3.6 mM) was added to the solution of [(F_8)Fe^{III}-($O_2^{\bullet-}$)] (***S***) in THF at –80 °C in a Schlenk cuvette.

4.4.2.8 Kinetic studies of [$(F_8)Fe^{III}$-$(O_2^{\bullet-})$] (***S***) with TEMPO–H(D)

The substrates TEMPO–H(D) (10, 30, 50, 70, 90 equiv) were added via syringe to a 0.04 mM solution of [$(F_8)Fe^{III}$-$(O_2^{\bullet-})$] (***S***) and the following UV-vis spectra were recorded (Figure 4.16). The hydroperoxide band at 418 nm appeared with time and the pseudo-first-order rate plots were observed. The values of k_{obs} were calculated from plots of $\log[(A_t-A_f)/(A_i-A_f)]$ vs time (s) (Figure 4.18, 4.20). According to this plot of k_{obs} vs [TEMPO–H(D)], the second order rate constant k_2 was obtained in THF at –80 °C (Figure 4.19).

4.4.3 resonance Raman spectroscopy

In the glovebox, 1 mM solutions of $(F_8)Fe^{II}$ in THF were prepared and transferred to rR tube and capped with tightfitting septa. The sample tubes were placed in a cold bath (dry ice/acetone) and oxygenated using $^{16}O_2$ or $^{18}O_2$ gases. The oxygenated samples were set in a cold bath for 10 min and to the cold THF solution of [$(F_8)Fe^{III}$-$(O_2^{\bullet-})$] (***S***) was added 1 equiv $CoCp_2$ for complex [$(F_8)Fe^{III}$-(O_2^{2-})]$^-$ (***P***). Subsequently, 1 equiv [$(LutH^+)$](OTf) was added for complex [$(F_8)Fe^{III}$-(OOH)] (***HP***). Then, the sample tubes were frozen in liquid N_2 and sealed by flame. Resonance Raman samples were excited at 413 nm, using a Coherent I90C-K Kr^+ ion laser while the sample was immersed in a liquid nitrogen cooled (77 K) EPR finger Dewar (Wilmad). Power was ~2 mW at the sample, which was continuously rotated to minimize photodecomposition. The spectra were recorded using a Spex 1877 CP triple monochromator, and detected by an Andor Newton CCD cooled to –80 °C.

4.4.4 EPR spectroscopy

In a glovebox, 1 mM solutions of $(F_8)Fe^{II}$ in THF were prepared and transferred to EPR tube and capped with tightfitting septa. The sample tubes were placed in a cold bath (dry ice/acetone) and oxygenated. The oxygenated samples were set in a cold bath for 10 min and to the cold THF solution of $[(F_8)Fe^{III}\text{-}(O_2^{\bullet-})]$ (***S***) was added 1 equiv $CoCp_2$ for complex $[(F_8)Fe^{III}\text{-}(O_2^{2-})]^-$ (***P***). Subsequently, 1 equiv $[(LutH^+)](OTf)$ was added for complex $[(F_8)Fe^{III}\text{-}(OOH)]$ (***HP***). Then, the sample tubes were frozen in liquid N_2. For EPR data for the reaction of $[(F_8)Fe^{III}\text{-}(O_2^{\bullet-})]$ (***S***) with TEMPO–H, 10 equiv TEMPO–H was added to the 1mM solution of ***S*** generated as described above. The tube was left at –80 °C for 1 hour 30 minutes and then frozen in liquid nitrogen.

4.5 References

(1) *Cytochrome P-450. Structure, Mechanism, and Biochemistry*. Ortiz de Montellano, P. R., Ed., (3rd edition), Kluwer Academic/Plenum Publishers: New York, 2005.

(2) (a) Sono, M.; Roach, M. P.; Coulter, E. D.; Dawon, J. H. Heme Containing Oxygenases. *Chem. Rev*. **1996**, *96*, 2841−2887. (b) Denisov, I. G.; Makris, T. M.; Sligar, S. G.; Schlichting, I. Structure and Chemistry of Cytochrome P450. *Chem. Rev*. **2005**, *105*, 2253−2277.

(3) (a) Meunier, B.; de Visser, S. P.; Shaik, S. Mechanism of Oxidation Reactions Catalyzed by Cytochrome P450 Enzymes. *Chem. Rev*. **2004**, *104*, 3947−3980. (b) Shaik, S.; Kumar, D.; de Visser, S. P.; Altun, A.; Thiel, W. Theoretical Perspective on the Structure and Mechanism of Cytochrome P450 Enzymes. *Chem. Rev*. **2005**, *105*, 2279−2328.

(4) Ortiz De Montellano, P. R. Hydrocarbon Hydroxylation by Cytochrome P450 Enzymes. *Chem. Rev*. **2010**, *110*, 932−948.

(5) Shaik, S.; Cohen, S.; Wang, Y.; Chen, H.; Kumar, D.; Thiel, W. P450 Enzymes: Their Structure, Reactivity, and Selectivity-Modeled by QM/MM Calculations. *Chem. Rev*. **2010**, *110*, 949−1017.

(6) Poulos, T. L. Heme Enzyme Structure and Function. *Chem. Rev*. **2014**, *114*, 3919−3962.

(7) McQuarters, A. B.; Wolf, M. W.; Hunt, A. P.; Lehnert, N. 1958−2014: After 56 Years of Research, Cytochrome P450 Reactivity Is Finally Explained. *Angew. Chem., Int. Ed*. **2014**, *53*, 4750−4752.

(8) Adam, S. M.; Wijeratne, G. B.; Rogler, P. J.; Diaz, D. E.; Quist, D. A.; Liu, J. J.; Karlin, K. D. Synthetic Fe/Cu Complexes: Toward Understanding Heme-Copper Oxidase Structure and Function. *Chem. Rev*. **2018**, *118*, 10840−11022.

(9) Huang, X.; Groves, J. T. Oxygen Activation and Radical Transformations in Heme Proteins and Metalloporphyrins. *Chem. Rev*. **2018**, *118*, 2491−2553.

(10) Dubey, K. D.; Shaik, S. Cytochrome P450-The Wonderful Nanomachine Revealed through Dynamic Simulations of the Catalytic Cycle. *Acc. Chem. Res*. **2019**, *52*, 389−399.

(11) Goto, Y.; Wada, S.; Morishima, I.; Watanabe, Y. Reactivity of Peroxoiron(III) Porphyrin Complexes: Models for Deformylation Reactions Catalyzed by Cytochrome P-450. *J. Inorg. Biochem*. **1998**, *69*, 241−247.

(12) Guengerich, F. P. Cytochrome P450 and Chemical Toxicology. *Chem. Res. Toxicol*. **2008**, *21*, 70−83.

(13) Newcomb, M.; Halgrimson, J. A.; Horner, J. H.; Wasinger, E. C.; Chen, L. X.; Sligar, S. G. X-Ray Absorption Spectroscopic Characterization of a Cytochrome P450 Compound II Derivative. *Proc. Natl. Acad. Sci. U. S. A*. **2008**, *105*, 8179−8184.

(14) Karlin, K. D. Model Offers Intermediate Insight. *Nature* **2010**, *463*, 168−169.

(15) Poulos, T. L.; Finzel, B. C.; Howard, A. J. High-Resolution Crystal Structure of Cytochrome P450cam. *J. Mol. Biol*. **1987**, *195*, 687−700.

(16) Schlichting, I.; Jung, C.; Schulze, H. Crystal Structure of Cytochrome P-450cam Complexed with the (1S)-camphor Enantiomer. *FEBS Lett*. **1997**, *415*, 253−257.

(17) Lai, W.; Chen, H.; Cho, K.-B.; Shaik, S. External Electric Field Can Control the Catalytic Cycle of Cytochrome P450cam: A QM/ MM Study. *J. Phys. Chem. Lett*. **2010**, *1*, 2082−2087.

(18) Lai, W.; Shaik, S. Can Ferric-Superoxide Act as a Potential Oxidant in P450Cam? QM/MM Investigation of Hydroxylation, Epoxidation, and Sulfoxidation. *J. Am. Chem. Soc*. **2011**, *133*, 5444−5452.

(19) Ogliaro, F.; de Visser, S. P.; Cohen, S.; Sharma, P. K.; Shaik, S. Searching for the Second Oxidant in the Catalytic Cycle of Cytochrome P450: A Theoretical Investigation of the Iron(III)-Hydroperoxo Species and Its Epoxidation Pathways. *J. Am. Chem. Soc*. **2002**, *124*, 2806−2817.

(20) de Visser, S. P.; Valentine, J. S.; Nam, W. A Biomimetic Ferric Hydroperoxo Porphyrin Intermediate. *Angew. Chem., Int. Ed*. **2010**, *49*, 2099−2101.

(21) Loew, G. H.; Harris, D. L. Role of the Heme Active Site and Protein Environment in Structure, Spectra, and Function of the Cytochrome P450s. *Chem. Rev*. **2000**, *100*, 407−419.

(22) Davydov, R.; Macdonald, I. D. G.; Makris, T. M.; Sligar, S. G.; Hoffman, B. M. EPR and ENDOR of Catalytic Intermediates in Cryoreduced Native and Mutant Oxy-Cytochromes P450cam: Mutation-Induced Changes in the Proton Delivery System. *J. Am. Chem. Soc*. **1999**, **121**, 10654−10655.

(23) Sono, M.; Roach, M. P.; Coulter, E. D.; Dawson, J. H. Heme-Containing Oxygenases. *Chem. Rev*. **1996**, *96*, 2841−2888.

(24) Huang, X.; Groves, J. T. Beyond Ferryl-Mediated Hydroxylation: 40 Years of the Rebound Mechanism and C-H Activation. *JBIC*, *J. Biol. Inorg. Chem*. **2017**, *22*, 185−207.

(25) Garcia-Serres, R.; Davydov, R. M.; Matsui, T.; Ikeda-Saito, M.; Hoffman, B. M.; Huynh, B. H. Distinct Reaction Pathways Followed upon Reduction of Oxy-Heme Oxygenase and Oxy-Myoglobin as Characterized by Mössbauer Spectroscopy. *J. Am. Chem. Soc*. **2007**, *129*, 1402−1412.

(26) Matsui, T.; Unno, M.; Ikeda-Saito, M. Heme Oxygenase Reveals Its Strategy For Catalyzing Three Successive Oxygenation Reactions. *Acc. Chem. Res*. **2010**, *43*, 240−247.

(27) Matsui, T.; Nambu, S.; Goulding, C. W.; Takahashi, S.; Fujii, H.; Ikeda-Saito, M. Unique Coupling of Mono- and Dioxygenase Chemistries in a Single Active Site Promotes Heme Degradation. *Proc. Natl. Acad. Sci. U. S. A*. **2016**, *113*, 3779−3784.

(28) Zhu, Y.; Silverman, R. B. Revisiting Heme Mechanisms. A Perspective on the Mechanisms of Nitric Oxide Synthase (NOS), Heme Oxygenase (HO), and Cytochrome P450s (CYP450s). *Biochemistry* **2008**, *47*, 2231−2243.

(29) Lehnert, N.; Berto, T. C.; Galinato, M. G. I.; Goodrich, L. E. The Role of Heme-Nitrosyls in the Biosynthesis, Transport, Sensing, and Detoxification of Nitric Oxide (NO) in Biological Systems: Enzymes and Model Complexes. Handbook of Porphyrin Science;

World Scientific Publishing Company: Singapore, 2011; Vol. *14*, Chap. 63, pp 1−247.

(30) Gantt, S. L.; Denisov, I. G.; Grinkova, Y. V.; Sligar, S. G. The Critical Iron-Oxygen Intermediate in Human Aromatase. *Biochem. Biophys. Res. Commun*. **2009**, *387*, 169−173.

(31) Mak, P. J.; Gregory, M. C.; Denisov, I. G.; Sligar, S. G.; Kincaid, J. R. Unveiling the Crucial Intermediates in Androgen Production. *Proc. Natl. Acad. Sci. U. S. A*. **2015**, *112*, 15856−15861.

(32) Mak, P. J.; Duggal, R.; Denisov, I. G.; Gregory, M. C.; Sligar, S. G.; Kincaid, J. R. Human Cytochrome CYP17A1: The Structural Basis for Compromised Lyase Activity with 17-Hydroxyprogesterone. *J. Am. Chem. Soc*. **2018**, *140*, 7324−7331.

(33) Denisov, I. G.; Makris, T. M.; Sligar, S. G. Formation and Decay of Hydroperoxo-Ferric Heme Complex in Horseradish Peroxidase Studied by Cryoradiolysis. *J. Biol. Chem*. **2002**, *277*, 42706−42710.

(34) Veitch, N. C. Horseradish Peroxidase: A Modern View of a Classic Enzyme. *Phytochemistry* **2004**, *65*, 249−259.

(35) Denisov, I. G.; Dawson, J. H.; Hager, L. P.; Sligar, S. G. The Ferric-Hydroperoxo Complex of Chloroperoxidase. *Biochem. Biophys. Res. Commun*. **2007**, *363*, 954−958.

(36) Wang, X.; Ullrich, R.; Hofrichter, M.; Groves, J. T. Heme-Thiolate Ferryl of Aromatic Peroxygenase Is Basic and Reactive. *Proc. Natl. Acad. Sci. U. S. A*. **2015**, *112*, 3686−3691.

(37) Lewis-Ballester, A.; Forouhar, F.; Kim, S. M.; Lew, S.; Wang, Y.; Karkashon, S.; Seetharaman, J.; Batabyal, D.; Chiang, B. Y.; Hussain, M.; Correia, M. A.; Yeh, S. R.; Tong, L. Molecular Basis for Catalysis and Substrate-Mediated Cellular Stabilization of Human Tryptophan 2,3-Dioxygenase. *Sci. Rep*. **2016**, *6*, 35169.

(38) Yan, J. J.; Kroll, T.; Baker, M. L.; Wilson, S. A.; Decréau, R.; Lundberg, M.; Sokaras, D.; Glatzel, P.; Hedman, B.; Hodgson, K. O.; Solomon, E. I. *Proc. Natl. Acad. Sci. U. S. A*. **2019**, *116*, 2854−2859.

(39) Denisov, I. G.; Makris, T. M.; Sligar, S. G. Cryotrapped Reaction Intermediates of Cytochrome P450 Studied by Radiolytic Reduction with Phosphorus-32. *J. Biol. Chem*. **2001**, *276*, 11648−11652.

(40) Davydov, R.; Satterlee, J. D.; Fujii, H.; Sauer-Masarwa, A.; Busch, D. H.; Hoffman, B. M. A Superoxo-Ferrous State in a Reduced Oxy-Ferrous Hemoprotein and Model Compounds. *J. Am. Chem. Soc*. **2003**, *125*, 16340−16346.

(41) Davydov, R.; Perera, R.; Jin, S.; Yang, T. C.; Bryson, T. A.; Sono, M.; Dawson, J. H.; Hoffman, B. M. Substrate Modulation of the Properties and Reactivity of the Oxy-Ferrous and Hydroperoxo-Ferric Intermediates of Cytochrome P450cam as Shown by Cryoreduction-EPR/ENDOR Spectroscopy. *J. Am. Chem. Soc*. **2005**, *127*, 1403−1413.

(42) Davydov, R.; Makris, T. M.; Kofman, V.; Werst, D. E.; Sligar, S. G.; Hoffman, B. M. Hydroxylation of Camphor by Reduced Oxy-CytochromeP450cam: Mechanistic Implications of EPR and ENDOR Studies of Catalytic Intermediates in Native and Mutant Enzymes. *J. Am. Chem. Soc*. **2001**, *123*, 1403−1415.

(43) Collman, J. P.; Gagne, R. R.; Reed, C. A.; Robinson, W. T.; Rodley, G. A. Structure of an Iron (II) Dioxygen Complex; A Model for Oxygen Carrying Hemeproteins. *Proc. Natl. Acad. Sci. U. S. A*. **1974**, *71*, 1326−1329.

(44) Singha, A.; Dey, A. Hydrogen Atom Abstraction by Synthetic Heme Ferric Superoxide and Hydroperoxide Species. *Chem. Commun*. **2019**, *55*, 5591−5594.

(45) Momenteau, M.; Reed, C. A. Synthetic Heme Dioxygen Complexes. *Chem. Rev*. **1994**, *94*, 659−698.

(46) Collman, J. P.; Sunderland, C. J.; Berg, K. E.; Vance, M. A.; Solomon, E. I. Spectroscopic Evidence for a Heme-Superoxide/Cu(I) Intermediate in a Functional Model of Cytochrome c Oxidase. *J. Am. Chem. Soc*. **2003**, *125*, 6648−6649.

(47) Liu, J.-G.; Naruta, Y.; Tani, F. A Functional Model of the Cytochrome *c* Oxidase Active Site: Unique Conversion of a Heme-μ-Peroxo-Cu^{II} Intermediate into Heme-Superoxo/Cu^{I}. *Angew. Chem., Int. Ed*. **2005**, *44*, 1836−1840.

(48) Liu, J.-G.; Ohta, T.; Yamaguchi, S.; Ogura, T.; Sakamoto, S.; Maeda, Y.; Naruta, Y. Spectroscopic Characterization of a Hydroperoxo-Heme Intermediate: Conversion of a Side-on Peroxo to an End-on Hydroperoxo Complex. *Angew. Chem., Int. Ed*. **2009**, *48*, 9262−9267.

(49) Liu, J.-G.; Shimizu, Y.; Ohta, T.; Naruta, Y. Formation of an End-on Ferric Peroxo Intermediate upon One-Electron Reduction of a Ferric Superoxo Heme. *J. Am. Chem. Soc*. **2010**, *132*, 3672−3673.

(50) Li, Y.; Sharma, S. K.; Karlin, K. D. New Heme-Dioxygen and Carbon Monoxide Adducts Using Pyridyl or Imidazolyl Tailed Porphyrins. *Polyhedron* **2013**, *58*, 190−196.

(51) Nagaraju, P.; Ohta, T.; Liu, J.-G.; Ogura, T.; Naruta, Y. The Secondary Coordination Sphere Controlled Reactivity of a Ferric-Superoxo Heme: Unexpected Conversion to a Ferric Hydroperoxo Intermediate by Reaction with a High-Spin Ferrous Heme. *Chem. Commun*. **2016**, *52*, 7213−7216.

(52) Kim, H.; Sharma, S. K.; Schaefer, A. W.; Solomon, E. I.; Karlin, K. D. Heme-Cu Binucleating Ligand Supports Heme/O_2 and $Fe^{II}Cu^{I}/O_2$ Reactivity Providing High- and Low-Spin Fe^{III}-Peroxo-Cu^{II} Complexes. *Inorg. Chem*. **2019**, *58*, 15423−15432.

(53) Vaz, A. D. N.; McGinnity, D. F.; Coon, M. J. Epoxidation of Olefins by Cytochrome P450: Evidence from Site-Specific Mutagenesis for Hydroperoxo-Iron as an Electrophilic Oxidant. *Proc. Natl. Acad. Sci. U. S. A*. **1998**, *95*, 3555−3560.

(54) Newcomb, M.; Shen, R.; Choi, S.-Y.; Toy, P. H.; Hollenberg, P. F.; Vaz, A. D. N.; Coon, M. J. Cytochrome P450-Catalyzed Hydroxylation of Mechanistic Probes That Distinguish between Radicals and Cations. Evidence for Cationic but Not for Radical Intermediates. *J. Am. Chem. Soc*. **2000**, *122*, 2677−2686.

(55) Jin, S.; Makris, T. M.; Bryson, T. A.; Sligar, S. G.; Dawson, J. H. Epoxidation of Olefins by Hydroperoxo-Ferric Cytochrome P450. *J. Am. Chem. Soc*. **2003**, *125*, 3406−3407.

(56) Fukuzumi, S.; Lee, Y.-M.; Nam, W. Structure and Reactivity of the First-Row d-Block Metal-Superoxo Complexes. *Dalt. Trans*. **2019**, *48*, 9469−9489.

(57) Noh, H.; Cho, J. Synthesis, Characterization and Reactivity of Non-Heme 1st Row Transition Metal-Superoxo Intermediates. *Coord. Chem. Rev*. **2019**, *382*, 126−144.

(58) Davydov, R.; Hoffman, B. M. Active Intermediates in Heme Monooxygenase Reactions as Revealed by Cryoreduction/Annealing, EPR/ENDOR Studies. *Arch. Biochem. Biophys*. **2011**, *507*, 36−43.

(59) Warren, J. J.; Tronic, T. A.; Mayer, J. M. Thermochemistry of Proton-Coupled Electron Transfer Reagents and Its Implications. *Chem. Rev*. **2010**, *110*, 6961−7001.

(60) Chufán, E. E.; Karlin, K. D. An Iron-Peroxo Porphyrin Complex: New Synthesis and Reactivity Toward a Cu(II) Complex Giving a Heme-Peroxo-Copper Adduct. *J. Am. Chem. Soc*. **2003**, *125*, 16160−16161.

(61) Ghiladi, R. A.; Kretzer, R. M.; Guzei, I.; Rheingold, A. L.; Neuhold, Y.-M.; Hatwell, K. R.; Zuberbühler, A. D.; Karlin, K. D. $(F_8TPP)Fe^{II}/O_2$ Reactivity Studies {F_8TPP = Tetrakis(2,6-difluorophenyl)porphyrinate(2-)}: Spectroscopic (UV-Visible and NMR) and Kinetic Study of Solvent-Dependent (Fe/O_2 = 1:1 or 2:1) Reversible O_2-Reduction and Ferryl Formation. *Inorg. Chem*. **2001**, *40*, 5754−5767.

(62) Kim, E.; Helton, M. E.; Wasser, I. M.; Karlin, K. D.; Lu, S.; Huang, H.-w.; Moënne-Loccoz, P.; Incarvito, C. D.; Rheingold, A. L.; Honecker, M.; Kaderli, S.; Zuberbühler, A. D. Superoxo, μ-peroxo, and μ-oxo Complexes from $Heme/O_2$ and $Heme\text{-}Cu/O_2$ Reactivity: Copper Ligand Influences in Cytochrome *c* Oxidase Models. *Proc. Natl. Acad. Sci. U. S. A*. **2003**, *100*, 3623−3628.

(63) McCandlish, E.; Miksztal, A. R.; Nappa, M.; Sprenger, A. Q.; Valentine, J. S.; Stong, J. D.; Spiro, T. G. Reactions of Superoxide with Iron Porphyrins in Aprotic Solvents. A High Spin Ferric Porphyrin Peroxo Complex. *J. Am. Chem. Soc*. **1980**, *102*, 4268−4271.

(64) Selke, M.; Sisemore, M. F.; Valentine, J. S. The Diverse Reactivity of Peroxy Ferric Porphyrin Complexes of Electron-Rich and Electron-Poor Porphyrins. *J. Am. Chem. Soc*. **1996**, *118*, 2008−2012.

(65) TPP = meso-tetraphenylporphyrin, OEP = octaethylporphyrin.

(66) VanAtta, R. B.; Strouse, C. E.; Hanson, L. K.; Valentine, J. S. [Peroxotetraphenylporphinato]Manganese(III) and [Chlorotetraphenylporphinato]

Manganese(II) Anions. Syntheses, Crystal Structures, and Electronic Structures. *J. Am. Chem. Soc*. **1987**, *109*, 1425−1434.

(67) There do exist S = 3/2 six-coordinate [(porphyrinate)Fe^{III}-(X)(X')] complexes, where X and X' are weak ligands (e.g., ethanol, H_2O, THF) not involving a side-on bound peroxo ligand. (a) Simonato, J.-P.; Pécaut, J.; Le Pape, L.; Oddou, J.-L.; Jeandey, C.; Shang, M.; Scheidt, W. R.; Wojaczyński, J.; Wo łowiec, S.; Latos-Grażyński, L.; Marchon, J.-C. An Integrated Approach to the Mid-Spin State (S= 3/2) in Six-Coordinate Iron(III) Chiroporphyrins. *Inorg. Chem*. **2000**, *39*, 3978−3987. (b) Ikeue, T.; Ohgo, Y.; Yamaguchi, T.; Takahashi, M.; Takeda, M.; Nakamura, M. Saddle-Shaped Six-Coordinated Iron(III) Porphyrin Complexes Showing a Novel Spin Crossover between S = 1/2 and S = 3/2 Spin States. *Angew. Chem., Int. Ed*. **2001**, *40*, 2617−2620.

(68) Neese, F.; Solomon, E. I. Detailed Spectroscopic and Theoretical Studies on $[Fe(EDTA)(O_2)]^{3-}$: Electronic Structure of the Side-on Ferric-Peroxide Bond and Its Relevance to Reactivity. *J. Am. Chem. Soc*. **1998**, *120*, 12829−12848.

(69) Simaan, A. J.; Döpner, S.; Banse, F.; Bourcier, S.; Bouchoux, G.; Boussac, A.; Hildebrandt, P.; Girerd, J.-J. Fe^{III}-Hydroperoxo and Peroxo Complexes with Aminopyridyl Ligands and the Resonance Raman Spectroscopic Identification of the Fe-O and O-O Stretching Modes. *Eur. J. Inorg. Chem*. **2000**, *2000*, 1627−1633.

(70) Roelfes, G.; Vrajmasu, V.; Chen, K.; Ho, R. Y. N.; Rohde, J.-U.; Zondervan, C.; la Crois, R. M.; Schudde, E. P.; Lutz, M.; Spek, A. L.; Hage, R.; Feringa, B. L.; Münck, E.; Que, L. End-on and Side-on Peroxo Derivatives of Non-Heme Iron Complexes with Pentadentate Ligands: Models for Putative Intermediates in Biological Iron/Dioxygen Chemistry. *Inorg. Chem*. **2003**, *42*, 2639−2653.

(71) Van Wart, H. E.; Zimmer, J. Resonance Raman Evidence for the Activation of Dioxygen in Horseradish Oxyperoxidase. *J. Biol. Chem*. **1985**, *260*, 8372−8377.

(72) Peterson, R. L.; Ginsbach, J. W.; Cowley, R. E.; Qayyum, M. F.; Himes, R. A.; Siegler, M. A.; Moore, C. D.; Hedman, B.; Hodgson, K. O.; Fukuzumi, S.; Solomon, E. I.; Karlin, K. D. Stepwise Protonation and Electron-Transfer Reduction of a Primary Copper-Dioxygen Adduct. *J. Am. Chem. Soc*. **2013**, *135*, 16454−16467.

(73) Adam, S. M.; Garcia-Bosch, I.; Schaefer, A. W.; Sharma, S. K.; Siegler, M. A.; Solomon, E. I.; Karlin, K. D. Critical Aspects of Heme-Peroxo-Cu Complex Structure and Nature of Proton Source Dictate Metal-O_{Peroxo} Breakage versus Reductive O-O Cleavage Chemistry. *J. Am. Chem. Soc*. **2017**, *139*, 472−481.

(74) Carver, C. T.; Matson, B. D.; Mayer, J. M. Electrocatalytic Oxygen Reduction by Iron Tetra-arylporphyrins Bearing Pendant Proton Relays. *J. Am. Chem. Soc*. **2012**, *134*, 5444−5447.

(75) Tajima, K.; Oka, S.; Edo, T.; Miyake, S.; Mano, H.; Mukai, K.; Sakurai, H.; Ishizu, K. Optical Absorption and EPR studies on a Six coordinate Iron(III)-tetramesitylporphyrin-Hydorgen Peroxide complex Having a Nitrogenous Axial Ligand. *J. Chem. Soc., Chem. Commun*. **1995**, *0*, 1507−1508.

(76) Oliveira, R.; Zouari, W.; Herrero, C.; Banse, F.; Schöllhorn, B.; Fave, C.; Anxolabéhère-Mallart, E. Characterization and Subsequent Reactivity of an Fe-Peroxo Porphyrin Generated by Electrochemical Reductive Activation of O_2. *Inorg. Chem*. **2016**, *55*, 12204−12210.

(77) Tajima, K.; Shigematsu, M.; Jinno, J.; Ishizu, K.; Ohya- Nishiguchi, H. Generation of Fe^{III}OEP-Hydrogen Peroxide Complex (OEP = Octaethylporphyrinato) by Reduction of Fe^{II}OEP-O_2 with Ascorbic Acid Sodium Salt. *J. Chem. Soc., Chem. Commun*. **1990**, 144−145.

(78) Davydov, R. M.; Yoshida, T.; Ikeda-Saito, M.; Hoffman, B. M. Hydroperoxy-Heme Oxygenase Generated by Cryoreduction Catalyzes the Formation of α-meso-Hydroxyheme as Detected by EPR and ENDOR. *J. Am. Chem. Soc*. **1999**, *121*, 10656−10657.

(79) Ibrahim, M.; Denisov, I. G.; Makris, T. M.; Kincaid, J. R.; Sligar, S. G. Resonance Raman Spectroscopic Studies of Hydroperoxo-Myoglobin at Cryogenic Temperatures. *J. Am. Chem. Soc*. **2003**, *125*, 13714−13718.

(80) Sengupta, K.; Chatterjee, S.; Samanta, S.; Dey, A. Direct Observation of Intermediates Formed during Steady-State Electrocatalytic O_2 Reduction by Iron Porphyrins. *Proc. Natl. Acad. Sci. U. S. A*. **2013**, *110*, 8431−8436.

(81) Mak, P. J.; Denisov, I. G.; Victoria, D.; Makris, T. M.; Deng, T.; Sligar, S. G.; Kincaid, J. R. Resonance Raman Detection of the Hydroperoxo Intermediate in the Cytochrome P450 Enzymatic Cycle. *J. Am. Chem. Soc*. **2007**, *129*, 6382−6383.

(82) Denisov, I. G.; Mak, P. J.; Makris, T. M.; Sligar, S. G.; Kincaid, J. R. Resonance Raman Characterization of the Peroxo and Hydroperoxo Intermediates in Cytochrome P450. *J. Phys. Chem. A* **2008**, *112*, 13172−13179.

(83) Schaefer, A. W.; Ehudin, M. A.; Quist, D. A.; Tang, J. A.; Karlin, K. D.; Solomon, E. I. Spin Interconversion of Heme-Peroxo-Copper Complexes Facilitated by Intramolecular Hydrogen-Bonding Interactions. *J. Am. Chem. Soc*. **2019**, *141*, 4936−4951.

(84) Tajima, K.; Jinno, J.; Ishizu, K.; Sakurai, H.; Ohya-Nishiguchi, H. Direct Evidence of Heme-tert-Butyl Peroxide Adduct Formation Demonstrated by Simultaneous ESR and Optical Measurements. *Inorg. Chem*. **1989**, *28*, 709−715.

(85) Connelly, N. G.; Geiger, W. E. Chemical Redox Agents for Organometallic Chemistry. *Chem. Rev*. **1996**, *96*, 877−910.

(86) Our statements concerning relative redox potentials for the synthetic heme−superoxide complexes discussed are rough, since experimental or computationally derived redox potentials are from different solvents and approximations are made in converting E°′ values from one reference electrode to another (e.g., $Fc^{+/0}$, SCE, SHE).

(87) Garrido, G.; Koort, E.; Ràfols, C.; Bosch, E.; Rodima, T.; Leito, I.; Rosés, M. Acid-Base Equilibria in Nonpolar Media. Absolute pKa Scale of Bases in Tetrahydrofuran. *J. Org. Chem*. **2006**, *71*, 9062−9067.

(88) Bordwell, F. G.; Cheng, J.-P.; Harrelson, J. A. Homolytic Bond Dissociation Energies in Solution from Equilibrium Acidity and Electrochemical Data. *J. Am. Chem. Soc*. **1988**, *110*, 1229−1231.

(89) Quist, D. A.; Ehudin, M. A.; Schaefer, A. W.; Schneider, G. L.; Solomon, E. I.; Karlin, K. D. Ligand Identity-Induced Generation of Enhanced Oxidative Hydrogen Atom Transfer Reactivity for a $Cu^{II}_2(O_2^{\cdot-})$ Complex Driven by Formation of a $Cu^{II}_2(-OOH)$ Compound with a Strong O-H Bond. *J. Am. Chem. Soc*. **2019**, *141*, 12682−12696.

(90) For Naruta's superstructured ferric heme superoxide, peroxide, and hydroperoxide complexes[51] (with or without a H-bonding moiety to interact with the O_2-derived fragment) (Figure 4.8), theoretical computations were carried out and superoxide-to-peroxide

reduction potentials and hydroperoxide/peroxide pK_a values were provided; however, BDFEs for the ferric heme hydroperoxide complexes were not evaluated.

(91) Chung, L. W.; Li, X.; Hirao, H.; Morokuma, K. Comparative Reactivity of Ferric-Superoxo and Ferryl-Oxo Species in Heme and Non-Heme Complexes. *J. Am. Chem. Soc*. **2011**, *133*, 20076−20079.

(92) Latifi, R.; Tahsini, L.; Nam, W.; de Visser, S. P. Regioselectivity of Aliphatic versus Aromatic Hydroxylation by a Nonheme Iron(II)-Superoxo Complex. *Phys. Chem. Chem. Phys*. **2012**, *14*, 2518−2524.

(93) Gordon, J. B.; Vilbert, A. C.; Siegler, M. A.; Lancaster, K. M.; Moënne-Loccoz, P.; Goldberg, D. P. A Nonheme Thiolate-Ligated Cobalt Superoxo Complex: Synthesis and Spectroscopic Characterization, Computational Studies, and Hydrogen Atom Abstraction Reactivity. *J. Am. Chem. Soc*. **2019**, *141*, 3641−3653.

(94) Kindermann, N.; Günes, C.-J.; Dechert, S.; Meyer, F. Hydrogen Atom Abstraction Thermodynamics of a μ-1,2-Superoxo Dicopper-(II)Complex. *J. Am. Chem. Soc*. **2017**, *139*, 9831−9834.

(95) Dhar and Tolman[95a] determined BDE = 90 kcal/mol for an O−H bond of a Cu^{III}-aqua complex, while Kieber-Emmons and coworkers[95b] determined that a monohydroxo-bridged dicopper(II) complex possesses an O-H BDE of 77 kcal/mol; this species derives from HAT chemistry of the corresponding μ-oxo dicopper(II) complex. Mayer and co-workers[95c−e] reported on several cases of coupled proton−electron transfer (CPET) not involving O−H bond reactions; here, heme or non-heme iron(III) compounds react with a

hydrogen-atom donor substrate such that an electron transfers to the iron while the proton transfers to a basic site on the ligand periphery. (a) Dhar, D.; Tolman, W. B. Hydrogen Atom Abstraction from Hydrocarbons by a Copper(III)-Hydroxide Complex. *J. Am. Chem. Soc*. **2015**, *137*, 1322−1329. (b) Ali, G.; VanNatta, P. E.; Ramirez, D. A.; Light, K. M.; Kieber-Emmons, M. T. Thermodynamics of a a-oxo Dicopper(II) Complex for Hydrogen Atom Abstraction. *J. Am. Chem. Soc*. **2017**, *139*, 18448−18451. (c) Roth, J. P.; Lovell, S.; Mayer, J. M. Intrinsic Barriers for Electron and Hydrogen Atom Transfer Reactions of Biomimetic Iron Complexes. *J. Am. Chem. Soc*. **2000**, *122*, 5486−5498. (d) Mader, E. A.; Davidson, E. R.; Mayer, J. M. Large Gournd-State Entropy Changes for Hydrogen Atom Transfer Reactions of Iron Complexes. *J. Am. Chem. Soc*. **2007**, *129*, 5153−5166. (e) Warren, J. J.; Mayer, J. M. Proton-Coupled Electron Trnasfer Reactions at a Heme-Propionate in an Iron-Protoporphyrin-IX Model Compound. *J. Am. Chem. Soc*. **2011**, *133*, 8544−8551.

(96) Perhaps Naruta and co-workers did not address the issue of BDFEs with their data because they did not explore possible HAT chemistry with their corresponding ferric heme superoxide complexes.

(97) Zhu, X.-Q.; Zhang, M.-T.; Yu, A.; Wang, C.-H.; Cheng, J.-P. Hydride, Hydrogen Atom, Proton, and Electron Transfer Driving Forces of Various Five-Membered Heterocyclic Organic Hydrides and Their Reaction Intermediates in Acetonitrile. *J. Am. Chem. Soc*. **2008**, *130*, 2501−2516.

(98) Corsi, D. M.; Murthy, N. N.; Young, V. G.; Karlin, K. D. Synthesis, Structure, and Solution NMR Studies of Cyanide-Copper(II) and Cyanide-Bridged Iron(III)-Copper(II) Complexes. *Inorg. Chem*. **1999**, *38*, 848−858.

(99) Sharma, S. K.; Schaefer, A. W.; Lim, H.; Matsumura, H.; Moënne-Loccoz, P.; Hedman, B.; Hodgson, K. O.; Solomon, E. I.; Karlin, K. D. A Six- Coordinate Peroxynitrite Low-Spin Iron(III) Porphyrinate Complex The Product of the Reaction of Nitrogen Monoxide (·NO(g)) with a Ferric-Superoxide Species. *J. Am. Chem. Soc*. **2017**, *139*, 17421−17430.

(100) Porter, T. R.; Mayer, J. M. Radical Reactivity of the Fe(III)/(II) Tetramesitylporphyrin Couple: Hydrogen Atom Transfer, Oxyl Radical Dissociation, and Catalytic Disproportionation of a Hydroxylamine. *Chem. Sci*. **2014**, *5*, 372−380.

(101) Tano, T.; Okubo, Y.; Kunishita, A.; Kubo, M.; Sugimoto, H.; Fujieda, N.; Ogura, T.; Itoh, S. Redox Properties of a Mononuclear Copper(II)-Superoxide Complex. *Inorg. Chem*. **2013**, *52*, 10431−10437.

(102) Bailey, W. D.; Dhar, D.; Cramblitt, A. C.; Tolman, W. B. Mechanistic Dichotomy in Proton-Coupled Electron-Transfer Reactions of Phenols with a Copper Superoxide Complex. *J. Am. Chem. Soc*. **2019**, *141*, 5470−5480.

(103) Lin, Y.-H.; Cramer, H. H.; van Gastel, M.; Tsai, Y.-H.; Chu, C.-Y.; Kuo, T.-S.; Lee, I.-R.; Ye, S.; Bill, E.; Lee, W.-Z. Mononuclear Manganese(III) Superoxo Complexes: Synthesis, Characterization, and Reactivity. *Inorg. Chem*. **2019**, *58*, 9756−9765.

(104) Wind, M.-L.; Hoof, S.; Braun-Cula, B.; Herwig, C.; Limberg, C. Switching from a Chromium(IV) Peroxide to a Chromium(III) Superoxide upon Coordination of a Donor in the Trans Position. *J. Am. Chem. Soc*. **2019**, *141*, 14068−14072.

(105) Ansari, A.; Jayapal, P.; Rajaraman, G. C-H Bond Activation by Metal-Superoxo Species: What Drives High Reactivity? *Angew. Chem., Int. Ed*. **2014**, *54*, 564−568.

(106) Hong, S.; Sutherlin, K. D.; Park, J.; Kwon, E.; Siegler, M. A.; Solomon, E. I.; Nam, W. Crystallographic and Spectroscopic Characterization and Reactivities of a Mononuclear Non-Haem Iron(III)-Superoxo Complex. *Nat. Commun*. **2014**, *5*, 5440−5446.

(107) Oddon, F.; Chiba, Y.; Nakazawa, J.; Ohta, T.; Ogura, T.; Hikichi, S. Characterization of Mononuclear Non-Heme Iron(III)- Superoxo Complex with a Five-Azole Ligand Set. *Angew. Chem., Int. Ed*. **2015**, *54*, 7336−7339.

(108) Chiang, C.-W.; Kleespies, S. T.; Stout, H. D.; Meier, K. K.; Li, P.-Y.; Bominaar, E. L.; Que, L.; Münck, E.; Lee, W.-Z. Characterization of a Paramagnetic Mononuclear Nonheme Iron-Superoxo Complex. *J. Am. Chem. Soc*. **2014**, *136*, 10846−10849.

(109) Kovacs and co-workers recently described a nonheme Fe^{III}-superoxide intermediate which abstracts hydrogen atoms from 1,4-cyclohexadiene (CHD) (BDE = 76 kcal/mol) but also THF solvent, that possessing a strong C-H bond (BDE = 92 kcal/ mol); an Fe^{III}-hydroperoxide complex is the product. See, Blakely, M. N.; Dedushko, M. A.; Poon, P. C. Y.; Villar-Acevedo, G.; Kovacs, J. A. Formation of a Reactive, Alkyl Thiolate-Ligated Fe^{III}-Superoxo Intermediate Derived from Dioxygen. *J. Am. Chem. Soc*. **2019**, *141*, 1867−1870.

(110) Curley, J. J.; Bergman, R. G.; Tilley, T. D. Preparation and Physical Properties of Early-Late Heterobimetallic Compounds Featuring Ir-M Bonds (M = Ti, Zr, Hf). *Dalton Trans*. **2012**, *41*, 192−200.

(111) Mader, E. A.; Davidson, E. R.; Mayer, J. M. Large Ground- State Entropy Changes for Hydrogen Atom Transfer Reactions of Iron Complexes. *J. Am. Chem. Soc*. **2007**, *129*, 5153−5166.

(112) Wu, A.; Mader, E. A.; Datta, A.; Hrovat, D. A.; Borden, W. T.; Mayer, J. M. Nitroxyl Radical Plus Hydroxylamine Pseudo Self-Exchange Reactions: Tunneling in Hydrogen Atom Transfer. *J. Am. Chem. Soc*. **2009**, *131*, 11985−11997.

(113) Ghiladi, R. A.; Huang, H.-w.; Moënne-Loccoz, P.; Stasser, J.; Blackburn, N. J.; Woods, A. S.; Cotter, R. J.; Incarvito, C. D.; Rheingold, A. L.; Karlin, K. D. Heme-Copper/dioxygen Adduct Formation Relevant to Cytochrome *c* Oxidase: Spectroscopic Characterization of $[(^{6}L)Fe^{III}\text{-}(O_2^{2-})\text{-}Cu^{II}]^{+}$. *JBIC, J. Biol. Inorg. Chem*. **2005**, *10*, 63−77.

(114) Wasser, I. M.; Huang, H.-w.; Moënne-Loccoz, P.; Karlin, K. D. Heme/Non-Heme Diiron(II) Complexes and O_2, CO, and NO Adducts as Reduced and Substrate-Bound Models for the Active Site of Bacterial Nitric Oxide Reductase. *J. Am. Chem. Soc*. **2005**, *127*, 3310−3320.

(115) Chufán, E. E.; Puiu, S. C.; Karlin, K. D. Heme-Copper/Dioxygen Adduct Formation, Properties, and Reactivity. *Acc. Chem. Res*. **2007**, *40*, 563−572.

(116) Kieber-Emmons, M. T.; Qayyum, M. F.; Li, Y.; Halime, Z.; Hodgson, K. O.; Hedman, B.; Karlin, K. D.; Solomon, E. I. Spectroscopic Elucidation of a New Heme/Copper Dioxygen Structure Type: Implications for O-O Bond Rupture in Cytochrome *c* Oxidase. *Angew. Chem., Int. Ed*. **2012**, *51*, 168−172.

(117) Mak, P. J.; Thammawichai, W.; Wiedenhoeft, D.; Kincaid, J. R. Resonance Raman Spectroscopy Reveals pH-Dependent Active Site Structural Changes of Lactoperoxidase Compound 0 and Its Ferryl Heme O-O Bond Cleavage Products. *J. Am. Chem. Soc.* **2015**, *137*, 349–361.

Chapter 5

Ferric Heme Superoxide Reductive Transformations to Ferric Heme (Hydro)Peroxide Species: Spectroscopic Characterization and Thermodynamic Implications for H-atom Transfer (HAT)

This work was co-authored with the following authors and is published under the following citation:

Hyun Kim,[†] Patrick J. Rogler,[†] Savita K. Sharma,[†] Andrew W. Schaefer,[‡] Edward I. Solomon,*[,‡] and Kenneth D. Karlin*[,†]

[†]Department of Chemistry, Johns Hopkins University, Baltimore, Maryland 21218, USA

[‡]Department of Chemistry, Stanford University, Stanford, California 94305, USA

Angew. Chem. DOI: 10.1002/anie.202013791 and 10.1002/ange.202013791

5.1 Introduction

Heme-containing enzymes show diverse biological functions such as substrate monooxygenation, oxygen reduction in the respiratory chain, nitric oxide synthesis, oxygen storage and delivery, electron transfer, and H_2O_2 activation and dismutation.[1–5] Heme enzyme active sites contain a proximal ligand; cytochrome P450s (CYP450s) as well as NO synthase and chloroperoxidase utilize a cysteinate residue, whereas other peroxidases include a histidyl proximal ligand and catalases possess a tyrosinate ligand. The identity and nature of the axial ligand contributes to or defines spectroscopic properties, coordination, iron reduction potentials and thus the reactivity. These proximal ligand donors contribute the so-called "push effect", due to their electron donation.[1–5] In particular, the "push effect" of the anionic thiolate ligand in CYP450s leads to a much more negative $Fe^{III/II}$ reduction potential[6] and helps effect the heterolytic O–O bond cleavage of a hydroperoxide species, forming Compound I (Cmpd I, $(P^{\bullet+})Fe^{IV}=O$) as the reactive species which hydroxylates substrates.[1–5]

CYP450s act as monooxygenases transferring one atom of molecular oxygen to a substrate, which is either hydroxylated, epoxidized, or sulfoxidized through its catalytic cycle.[1–5] The latter involves formation of heme Fe^{III}–superoxide (i.e., the initial Fe^{II}/O_2 adduct), with subsequent transformation to Fe^{III}–peroxide and Fe^{III}–hydroperoxide intermediates prior to O–O cleavage to give Cmpd I.[1–5,7]

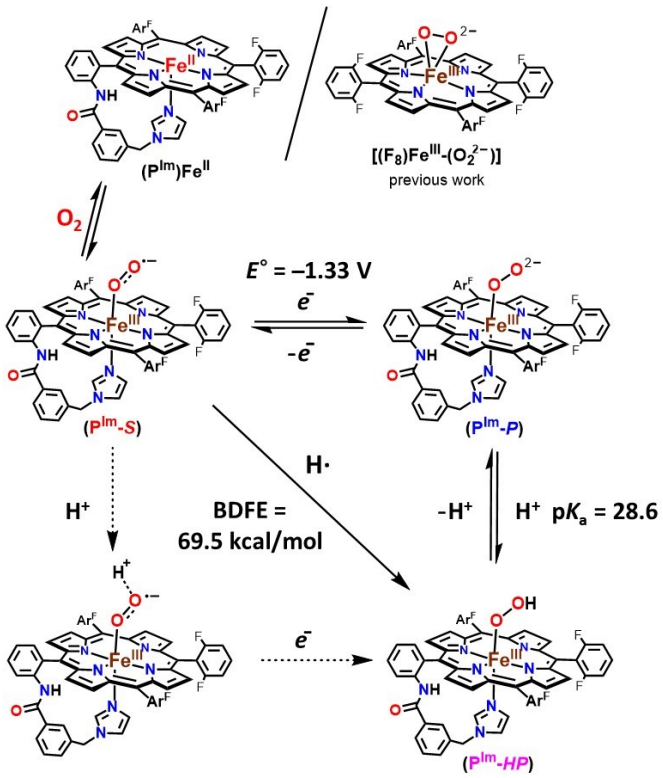

Figure 5.1 Stepwise generation of superoxide, peroxide, and hydroperoxide heme analogues and relevant thermodynamic square scheme ($E°$ as determined vs $Fc^{+/0}$ and pK_a) and OO–H BDFE of ferric heme hydroperoxide. Ar^F = 2,6-difluorophenyl group. Upper right: the previously studied ferric heme peroxide $[(F_8)Fe^{III}–(O_2^{2–})]^–$ with η^2-ligated $O_2^{2–}$ ligand.[8]

For the three initial Fe^{III} CYP450 intermediates, radiolytic cryoreduction/spectroscopic studies and theoretical calculations lead to the conclusion that all of these species have an end-on binding geometry, with Fe^{III}-coordination only to the O_2-derived proximal oxygen atom.[9–13] Synthetic bioinorganic groups have been interested in the generation and characterization of model compounds for the superoxide, peroxide, or hydroperoxide intermediates, as relevant to O_2 or H_2O_2 activating heme enzymes. There are many known end-on ferric heme superoxide[14–24] and hydroperoxide synthetic compounds.[8,21,23–27]

Valentine and co-workers[28–30] originally synthesized and characterized a series of ferric heme peroxides possessing a side-on bound O_2^{2-} ligand (i.e., η^2, with both peroxide O-atoms equivalently bound to Fe^{III}). To date, there has been only one report of an end-on (η^1) bound low-spin peroxide synthetic complex, $[(P)Fe^{III}–(\eta^1:O_2^{2-})]^-$ (P possesses an internal imidazolyl axial ligand), that by Naruta and co-workers.[21] Recently, our group[8,18] reported on an end-on ferric heme superoxide, a corresponding hydroperoxide species, and the related ferric heme peroxide, where the O_2-derived O_2^{2-} ligand is side-on bound (Figure 5.1, upper right); the chemistry was carried out in tetrahydrofuran (THF), which serves as an axial base ligand. In that work, thermodynamic parameters, the $[(F_8)Fe^{III}–(O_2^{\bullet-})]$ (***S***) reduction potential and $[(F_8)Fe^{III}–(OOH)]$ (***HP***) pK_a, led to the determination of the ferric heme hydroperoxide BDFE to be 73.5 kcal/mol.

Herein, the newly generated end-on low-spin peroxide, $[(P^{Im})Fe^{III}–(O_2^{2-})]^-$ (**P^{Im}-*P***), and its subsequent conversion to hydroperoxide species, $[(P^{Im})Fe^{III}–(OOH)]$ (**P^{Im}-*HP***) are described utilizing P^{Im} as the porphyrinate; this possesses an appended axial base strongly donating imidazolyl group (Figure 5.1), which is the same as is suggested to form in CYP450s where the Fe^{III} is bound to only one oxygen atom of the peroxide moiety. Also, a reduction potential for the $[(P^{Im})Fe^{III}–(O_2^{\bullet-})]$ (**P^{Im}-*S***)/ $[(P^{Im})Fe^{III}–(O_2^{2-})]^-$ (**P^{Im}-*P***) couple and a pK_a for the $[(P^{Im})Fe^{III}–(OOH)]$ (**P^{Im}-*HP***) acid-base pair are established. These thermodynamic parameters and use of the Bordwell relationship square scheme (Figure 5.1) allow the determination of OO–H bond dissociation free energy (BDFE) for **P^{Im}-*HP***. We compare and contrast thermodynamic findings (reduction potential and pK_a for P^{Im} and F_8 porphyrinate

complex) and insights obtained for corresponding complexes with hydrogen atom transfer (HAT) reactions.

5.2 Results and Discussion

5.2.1 Generation and characterization of a ferric peroxide, $[(P^{Im})Fe^{III}–(O_2^{2–})]^–$ ($\mathbf{P^{Im}}$-***P***)

The ferric heme superoxide $[(P^{Im})Fe^{III}–(O_2^{\bullet–})]$ ($\mathbf{P^{Im}}$-***S***) generated by bubbling O_2 to a solution of $[(P^{Im})Fe^{II}]$ (Figure 5.1), was previously characterized ($\nu_{O–O}$, 1180 ($\Delta^{18}O_2$, –56) $cm^{–1}$; $\nu_{Fe\text{-}O}$, 575 ($\Delta^{18}O_2$, –23) $cm^{–1}$).[22,31] Addition of cobaltocene ($CoCp_2$) to $\mathbf{P^{Im}}$-***S*** at –80 °C in THF results in the formation of the ferric heme peroxide complex $[(P^{Im})Fe^{III}–(O_2^{2–})]^–$ ($\mathbf{P^{Im}}$-***P***); UV-vis spectral shifts occurring are 423 to 424 nm (Soret) and 532 to 535, 567 nm (Figure 5.2A). These product electronic absorption spectra are very similar to those of Naruta's end-on low-spin ferric heme peroxide, as mentioned the first of its kind.[21] The UV-vis features of $\mathbf{P^{Im}}$-***P*** and Naruta's analog exhibit higher energy Soret λ_{max} values than the side-on bound ferric heme peroxides (also lacking a trans axial base ligand), as in $[(F_8)Fe^{III}–(\eta^2:O_2^{2–})]^–$ (Figure 5.1, upper right).[8,18,20,28–30] The low-spin end-on formulation is confirmed by the EPR spectra which display signals at g = 2.25, 2.14, and 1.95 (Figure 5.2A), matching Naruta's analog,[21] as well as for those end-on ferric peroxide obtained by cryoreduction methods in heme enzymes.[9–13] Such EPR signatures also are distinct from side-on heme peroxide intermediates which are intermediate spin species, g = 4.2 (S = 3/2).[8,18,20,28–30]

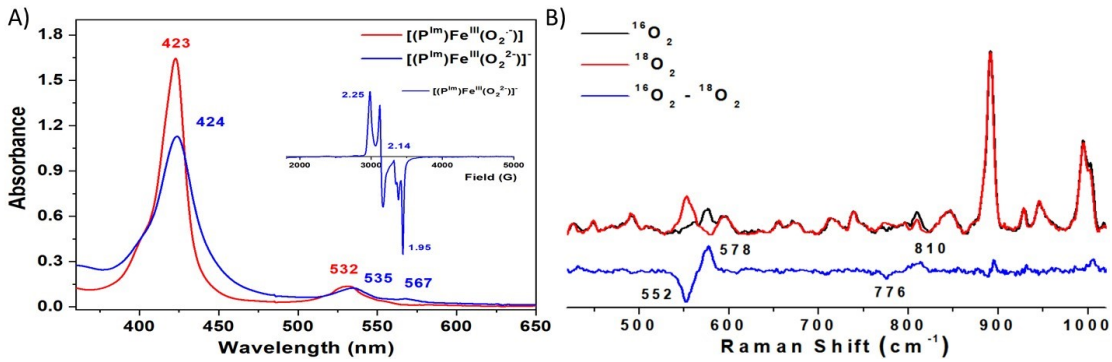

Figure 5.2 (A) Electronic absorption spectra of [(P^{Im})Fe^{III}–($O_2^{\bullet-}$)] (**P^{Im}-*S***) (red) to [(P^{Im})Fe^{III}–(O_2^{2-})]$^-$ (**P^{Im}-*P***) (blue) at –80 °C in THF. Inset: Frozen THF solution EPR (10 K) spectrum of **P^{Im}-*P***. The small feature (g = 1.99) corresponds to an excess of cobaltocene.[18] (B) Resonance Raman spectra of [(P^{Im})Fe^{III}–(O_2^{2-})]$^-$ (**P^{Im}-*P***) in frozen THF obtained at 77 K with 413 nm excitation. The $^{16}O_2$–$^{18}O_2$ difference spectrum is shown in blue. Also, see the text.

Further, [(P^{Im})Fe^{III}–(O_2^{2-})]$^-$ (**P^{Im}-*P***) was characterized using rR spectroscopy. Two $^{16}O_2/^{18}O_2$ isotopic sensitive shifts were observed for this end-on peroxide species **P^{Im}-*P***, at 810 ($\Delta^{18}O_2$ = −34) cm^{-1} and 578 ($\Delta^{18}O_2$ = −26) cm^{-1} corresponding to the ν_{O-O} and ν_{Fe-O} stretches, respectively (Figure 5.2B). This latter stretching frequency value matches the expected value ($\Delta_{Fe\text{-}O,calc}$ ($^{16}O_2/^{18}O_2$) = −26 cm^{-1}) using the harmonic oscillator approximation. The magnitude of the isotope shift for ν_{O-O} is smaller than the calculated value ($\Delta_{O\text{-}O,calc}$ ($^{16}O_2/^{18}O_2$)= −46 cm^{-1}); however, the same trend is found for Naruta's complex [(P)Fe^{III}–(η^1:O_2^{2-})]$^-$ (ν_{O-O}, 808 ($\Delta^{18}O_2$, –37) cm^{-1}; $\nu_{Fe\text{-}O}$, 585 ($\Delta^{18}O_2$, –25) cm^{-1}).[21] It is notable that ν_{Fe-O} in [(P^{Im})Fe^{III}–(η^1:O_2^{2-})]$^-$ (**P^{Im}-*P***), is much larger than that found for the side-on peroxide species which has no internally appended axial base imidazolyl, [(F_8)Fe^{III}–(η^2:O_2^{2-})]$^-$ (Figure 5.1, upper right; ν_{O-O}, 806 ($\Delta^{18}O_2$, −46) cm^{-1}; $\nu_{Fe\text{-}O}$, 466 ($\Delta^{18}O_2$, −19) cm^{-1}).[8] The increased Fe–O stretching frequency is likely a result of both the

monodentate coordination and the σ-symmetry O_2 donation into the fully unoccupied low-spin Fe d_{z2} orbital which is stronger than the π-symmetry donation into the half-occupied Fe d_{xz}/d_{yz} orbital of the side-on peroxide complex. These effects would strengthen the Fe–O bond of **P^{Im}-*P***, and favor the end-on binding mode, giving a low-spin six-coordinate species $[(P^{Im})Fe^{III}–(\eta^1:O_2^{2-})]^-$ (**P^{Im}-*P***).

5.2.2 Generation and characterization of [(P^{Im})Fe^{III}–(OOH)] (P^{Im}-*HP*)

When excess triflic acid (HOTf) is added to $[(P^{Im})Fe^{III}–(O_2^{2-})]^-$ (**P^{Im}-*P***), Fe–O bond cleavage occurs, releasing H_2O_2 (89 % yield; horseradish peroxidase assay, see Figure 5.3), corroborating the complex's peroxide formulation. **P^{Im}-*P*** is singly protonated by adding 1 equiv of 2,6-lutidinium triflate $[(LutH^+)](OTf)$ at –80 °C in THF, giving $[(P^{Im})Fe^{III}–(OOH)]$ (**P^{Im}-*HP***) with absorptions at 423 and 533 nm (Figure 5.4A). EPR spectra of **P^{Im}-*HP*** confirm an end-on low-spin ferric heme hydroperoxide structure (g = 2.25, 2.14, and 1.95) as shown in Figure 5.4B. These values correspond closely to those already known for synthetically derived end-on low-spin hydroperoxide complexes[8,20,21,23–26] as well as for ferric heme hydroperoxides generated within hemoglobin and myoglobin.[32,33] A high yield of H_2O_2 (90.1 %) is also obtained when **P^{Im}-*HP*** is acidified using HOTf (see Figure 5.3). Further, we performed rR spectroscopy; while only noisy spectra could be obtained (Figure 5.5), $\nu_{O–O}$ (808 ($\Delta^{18}O_2$, –48) cm^{-1}) and $\nu_{Fe–O}$ (579 ($\Delta^{18}O_2$, –36) cm^{-1}) resonances could be discerned. These parameters, for **P^{Im}-*HP***, are quite similar to those for the other synthetic or protein low-spin ferric heme hydroperoxide complexes (vide supra).[8,21,27,32–35]

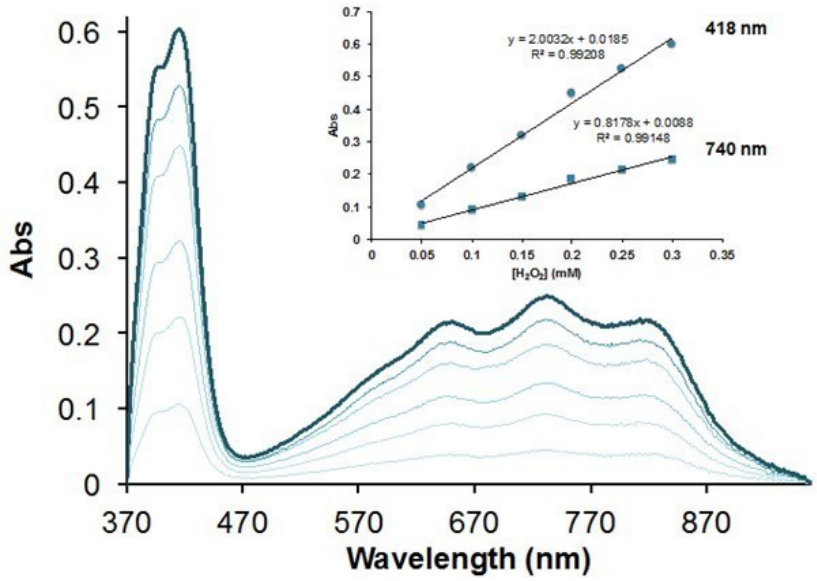

Figure 5.3 Calibration curve (adapted from ref 36) used for H_2O_2 quantification by the horseradish peroxidase (HRP) test. See experimental description (above) for details.

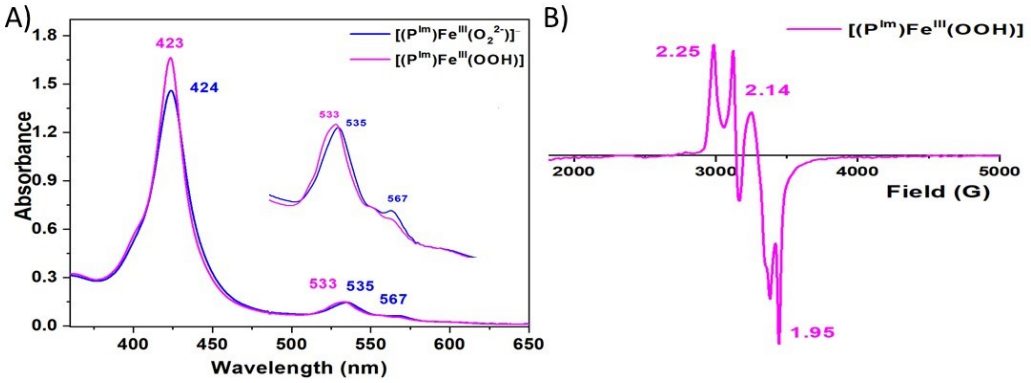

Figure 5.4 (A) UV–vis spectra illustrating the conversion of $[(P^{Im})Fe^{III}–(O_2^{2-})]^-$ (**P^{Im}-*P***) to $[(P^{Im})Fe^{III}–(OOH)]$ (**P^{Im}-*HP***) by addition of $[(LutH^+)](OTf)$ at –80 °C in THF. (B) EPR spectra (10 K) of **P^{Im}-*HP***. Note that there is g = 1.99 signal from excess of cobaltocene used for generation of the peroxide complex.

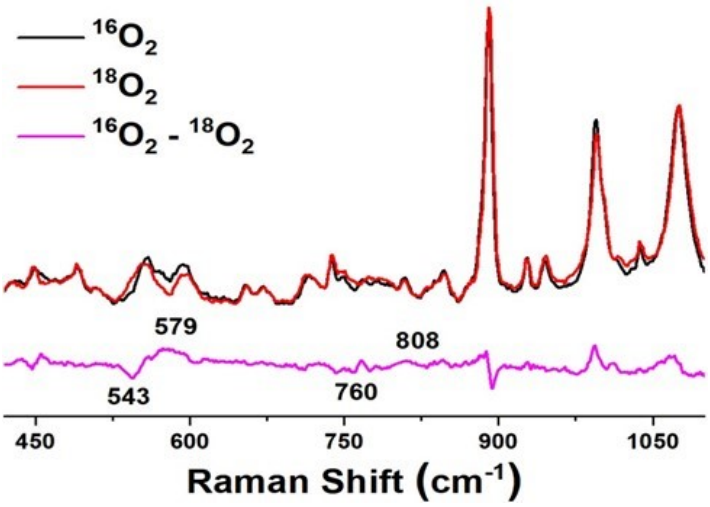

Figure 5.5 Resonance Raman spectra of ferric heme hydroperoxide complex [(P^{Im})Fe^{III}–(OOH)] (**P^{Im}-*HP***) in frozen THF obtained at 77 K with 413 nm excitation.

5.2.3 Reduction potential of the [(P^{Im})Fe^{III}–($O_2^{\bullet-}$)] (**P^{Im}-*S***)/ [(P^{Im})Fe^{III}–(O_2^{2-})]$^-$ (**P^{Im}-*P***)

We find [(P^{Im})Fe^{III}–($O_2^{\bullet-}$)] (**P^{Im}-*S***) and [(P^{Im})Fe^{III}–(O_2^{2-})]$^-$ (**P^{Im}-*P***) are interconvertible (Figure 5.1) using redox reagents. Addition of a ferrocenium reagent (Fc^+; $E_{1/2}$ = 0 V vs $Fc^{+/0}$) to the solution of **P^{Im}-*P*** leads to the reappearance of the optical bands (423 and 532 nm) associated with **P^{Im}-*S*** (Figure 5.6). This oxidation is supported by the EPR silent known diamagnetic behavior of **P^{Im}-*S*** solution generated (10 K, in THF frozen solution). Additionally, the addition of $CoCp_2$ to this resulting solution led to re-reduction giving the peroxide species **P^{Im}-*P*** (Figure 5.7).

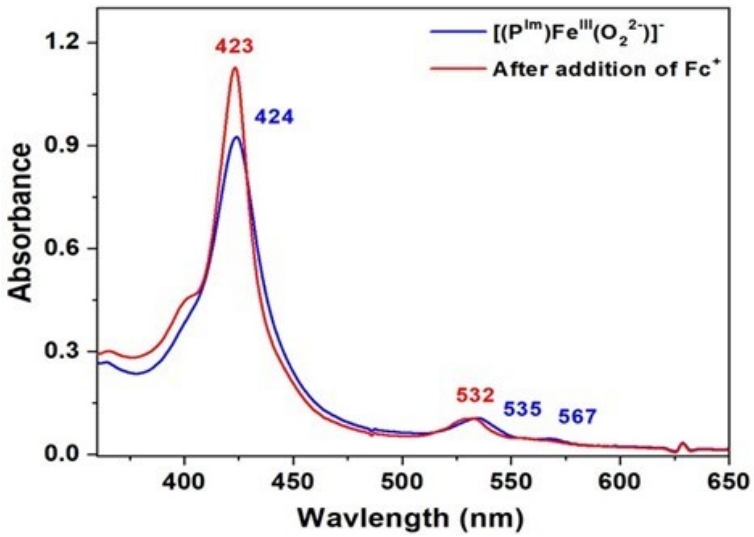

Figure 5.6 UV–vis spectra demonstrating the oxidation of $[(P^{Im})Fe^{III}–(O_2^{2–})]^–$ (**P^{Im}-*P***) to form $[(P^{Im})Fe^{III}–(O_2^{\bullet–})]$ (**P^{Im}-*S***) at –80 °C in THF.

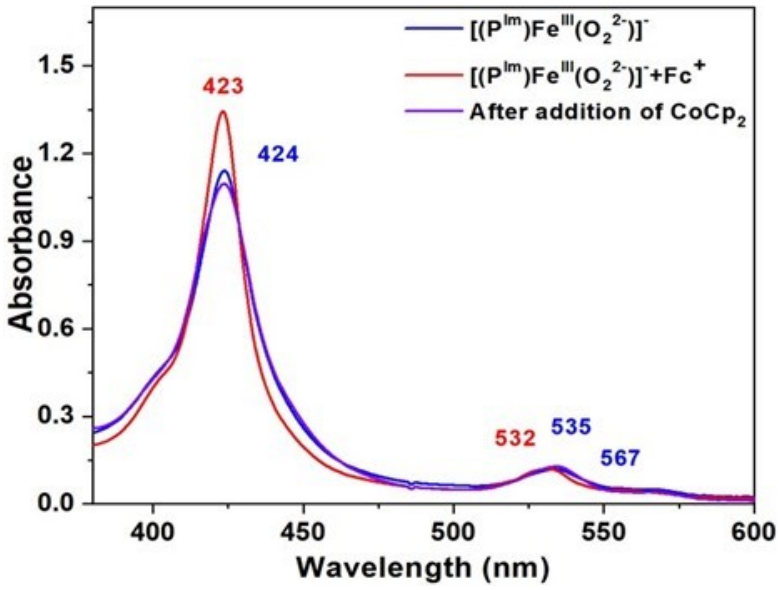

Figure 5.7 Addition of 1 equivalent of ferrocenium to $[(P^{Im})Fe^{III}–(O_2^{2–})]^–$ (**P^{Im}-*P***) (blue) regenerates the formation of $[(P^{Im})Fe^{III}–(O_2^{\bullet–})]$ (**P^{Im}-*S***) (red) and again, upon addition of excess amount of $CoCp_2$, to this resulting solution, $[(P^{Im})Fe^{III}–(O_2^{2–})]^–$ (**P^{Im}-*P***) (purple) is formed.

Interestingly, titration of [(P^{Im})Fe^{III}–($O_2^{\bullet-}$)] (**P^{Im}-*S***) with varying amounts of $CoCp_2$ ($E_{1/2}$ = –1.33 V vs $Fc^{+/0}$ in THF)[37] at –80 °C in THF gives an equilibrium mixture; UV-vis monitoring (at either 423 or 567 nm) (Figure 5.8A, Table 5.1, and Figure 5.9), allowed determination of K_{eq} in each instance. From these results and utilizing the Nernst equation, the reduction potential for the couple, [(P^{Im})Fe^{III}–($O_2^{\bullet-}$)] (**P^{Im}-*S***)/ [(P^{Im})Fe^{III}–(O_2^{2-})]$^-$ (**P^{Im}-*P***) is calculated to be –1.33 V ± 0.01 V vs $Fc^{+/0}$. This value is more negative by ~160 mV than that of previously reported [(F_8)Fe^{III}–($O_2^{\bullet-}$)] (–1.17 V vs $Fc^{+/0}$) (Figure 5.10) which has no internally appended axial base in the porphyrinate complex.[8] Consistent with this finding is the observation that in order to fully reduce [(F_8)Fe^{III}–($O_2^{\bullet-}$)] to its peroxide product, one equivalent of $CoCp_2$ was used, while multiple equivalents of the cobaltocene are required to fully reduce the presently described superoxide complex **P^{Im}-*S***. These findings suggest a "push effect" due to the axial imidazolyl ligand which is covalently appended to the heme of P^{Im} iron-porphyrinate complexes.

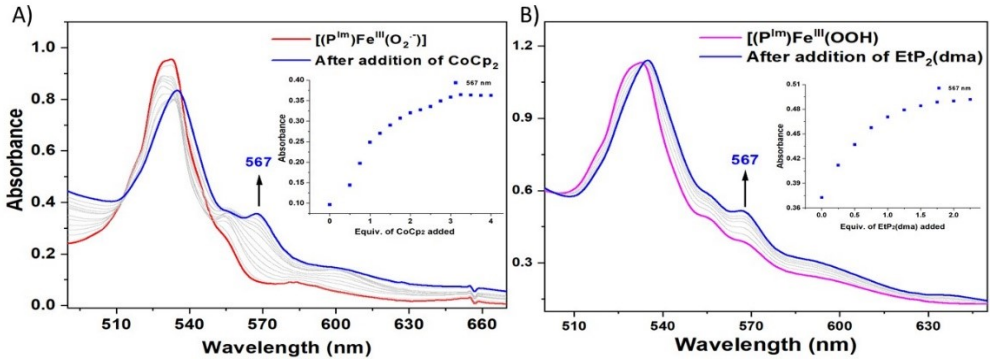

Figure 5.8 UV-vis spectroscopic monitoring of the incremental addition of (A) $CoCp_2$ to a solution of [(P^{Im})Fe^{III}–($O_2^{\bullet-}$)] (**P^{Im}-*S***) (red). Inset: monitoring of the absorbance at 567 nm (blue). (B) EtP_2(dma) addition to a solution of [(P^{Im})Fe^{III}–(OOH)] (**P^{Im}-*HP***) (pink). Inset: monitoring of the absorbance at 567 nm (blue).

Table 5.1 Equilibrium concentrations for the titration of $CoCp_2$ into a solution of [(P^{Im})Fe^{III}–($O_2^{\bullet-}$)] (**P^{Im}-*S***) in THF at –80 °C

At 567 nm

$[CoCp_2]_{added}$	$[CoCp_2]_{eq}$	$[Peroxide]_{eq}$	$[Superoxide]_{eq}$	$[CoCp_2]^+_{eq}$	K_{eq}	Es (mV)
4.98×10^{-5}	3.00×10^{-5}	1.98×10^{-5}	8.02×10^{-5}	1.98×10^{-5}	1.63×10^{-1}	–1.36
9.88×10^{-5}	3.98×10^{-5}	5.90×10^{-5}	4.10×10^{-5}	5.90×10^{-5}	2.13	–1.32
1.47×10^{-4}	7.30×10^{-5}	7.41×10^{-5}	2.59×10^{-5}	7.41×10^{-5}	2.90	–1.31
1.95×10^{-4}	1.09×10^{-4}	8.51×10^{-5}	1.49×10^{-5}	8.51×10^{-5}	4.46	–1.31
2.41×10^{-4}	1.51×10^{-4}	9.07×10^{-5}	9.29×10^{-6}	9.07×10^{-5}	5.88	–1.30

At 423 nm

$[CoCp_2]_{added}$	$[CoCp_2]_{eq}$	$[Peroxide]_{eq}$	$[Superoxide]_{eq}$	$[CoCp_2]^+_{eq}$	K_{eq}	Es (mV)
5.00×10^{-5}	4.04×10^{-5}	9.64×10^{-6}	4.04×10^{-5}	9.64×10^{-5}	5.71×10^{-2}	–1.38
9.95×10^{-5}	8.23×10^{-5}	1.72×10^{-5}	3.28×10^{-5}	1.72×10^{-5}	1.09×10^{-1}	–1.37
1.48×10^{-4}	1.20×10^{-5}	2.87×10^{-5}	2.13×10^{-5}	2.87×10^{-5}	3.24×10^{-1}	–1.35
2.45×10^{-4}	1.57×10^{-4}	3.97×10^{-5}	1.03×10^{-5}	3.97×10^{-5}	9.78×10^{-1}	–1.33
2.92×10^{-4}	1.99×10^{-4}	4.59×10^{-5}	4.07×10^{-6}	4.59×10^{-5}	2.61×10^{-1}	–1.31

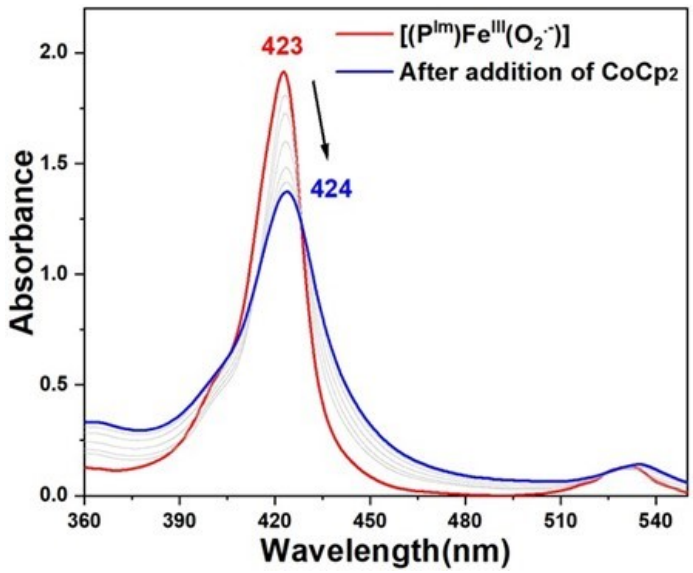

Figure 5.9 UV-vis spectroscopic monitoring of the incremental addition of $CoCp_2$ to a solution of [(P^{Im})Fe^{III}–($O_2^{\bullet-}$)] (**P^{Im}-*S***).

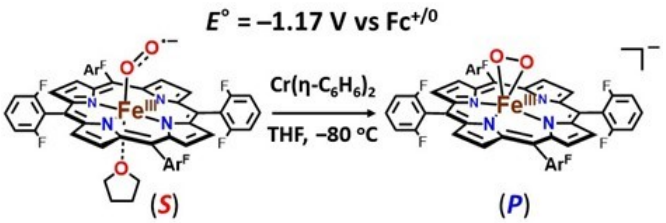

Figure 5.10 The reduction potential of $[(F_8)Fe^{III}–(O_2^{\bullet-})]$ (***S***)/ $[(F_8)Fe^{III}–(O_2^{2-})]^-$ (***P***) couple was calculated to be –1.17 V vs $Fc^{+/0}$ in THF.[8]

Dey and co-workers[6] reported the reduction potentials of iron-porphyrinate complexes ($Fe^{III/II}$) which have thiolate and imidazolyl linkers bound to the iron center of porphyrinate complexes. The thiolate ligated porphyrin complex shows 500 mV more negative $Fe^{III/II}$ reduction potential compared to an imidazolyl ligated porphyrinate analogue; the thiolate is a much better donor than imidazolyl. Thus, in our case, the greater covalent charge donation by an axial imidazolyl ligand in P^{Im} reduces the reduction potential of $[(P^{Im})Fe^{III}–(O_2^{\bullet-})]$ (**P^{Im}-*S***) in comparison with that of $[(F_8)Fe^{III}–(O_2^{\bullet-})]$.

5.2.4 Determination of the pK_a Value of [(P^{Im})Fe^{III}–(OOH)] (P^{Im}-*HP*)

To complete the thermodynamic square scheme analysis (Figure 5.1),[38] the pK_a value of ferric heme hydroperoxide $[(P^{Im})Fe^{III}–(OOH)]$ (**P^{Im}-*HP***) was evaluated at –80 °C in THF. Full deprotonation of **P^{Im}-*HP*** was accomplished by spectral titration using the derivatized phosphazene base $EtP_2(dma)$ (pK_a = 28.1 for the conjugate acid; THF solvent, room temperature).[39] The concentrations of each species (**P^{Im}-*P***, **P^{Im}-*HP***, $EtP_2(dma)$, and $EtP_2(dma)H^+$) were evaluated by examination of the observed absorbance at either 423 or 567 nm in the UV-vis spectra (Figure 5.8B, Table 5.2, and Figure 5.11). Such titration experiments lead to

the establishment of an equilibrium constant for the protonation of $\mathbf{P^{Im}}$-***P*** to give $\mathbf{P^{Im}}$-***HP***, allowing the calculation of the pK_a of the ferric heme hydroperoxide to be 28.6 ± 0.5 (–80 °C, THF). The reversibility of acid-base reaction was further demonstrated by adding [(LutH$^+$)](OTf) to the solution generated in this titration, which gives back to hydroperoxide complex (Figure 5.12).

Table 5.2 Equilibrium concentrations for the titration of EtP_2(dma) into a solution of [(P^{Im})Fe^{III}–(OOH)] ($\mathbf{P^{Im}}$-***HP***) in THF at –80 °C

At 567 nm

$[EtP_2(dma)]_{added}$	$[Peroxide]_{eq}$	$[EtP_2(dma)]_{eq}$	$[Hydroperoxide]_{eq}$	$[EtP_2(dma)H^+]_{eq}$	K_{eq}
2.41 x 10^{-5}	1.05 x 10^{-5}	1.35 x 10^{-5}	8.61 x 10^{-5}	1.05 x 10^{-5}	0.09
4.79 x 10^{-5}	3.81 x 10^{-5}	9.79 x 10^{-6}	5.84 x 10^{-5}	3.81 x 10^{-5}	2.54
7.16 x 10^{-5}	6.08 x 10^{-5}	1.08 x 10^{-5}	3.58 x 10^{-5}	6.07 x 10^{-5}	9.48
9.51 x 10^{-5}	7.52 x 10^{-5}	1.99 x 10^{-5}	2.14 x 10^{-5}	7.52 x 10^{-5}	13.2
1.41 x 10^{-4}	9.02 x 10^{-5}	5.13 x 10^{-4}	6.35 x 10^{-6}	9.02 x 10^{-5}	24.9

pK_{eq}	pK_a
1.02	27.1
–0.40	28.5
–0.97	29.1
–1.12	29.2
–1.39	29.5

At 423 nm

$[EtP_2(dma)]_{added}$	$[Peroxide]_{eq}$	$[EtP_2(dma)]_{eq}$	$[Hydroperoxide]_{eq}$	$[EtP_2(dma)H^+]_{eq}$	K_{eq}
2.5 x 10^{-5}	1.06 x 10^{-5}	1.43 x 10^{-5}	3.74 x 10^{-5}	1.06 x 10^{-5}	0.21
4.95 x 10^{-5}	1.81 x 10^{-5}	3.14 x 10^{-5}	2.99 x 10^{-5}	1.81 x 10^{-5}	0.34
7.35 x 10^{-5}	3.13 x 10^{-5}	4.21 x 10^{-5}	1.67 x 10^{-5}	3.13 x 10^{-5}	1.39
9.71 x 10^{-5}	4.48 x 10^{-5}	5.23 x 10^{-5}	3.25 x 10^{-5}	4.48 x 10^{-5}	11.7

pK_{eq}	pK_a
0.67	27.4
0.45	27.6
–0.14	28.2
–1.07	29.2

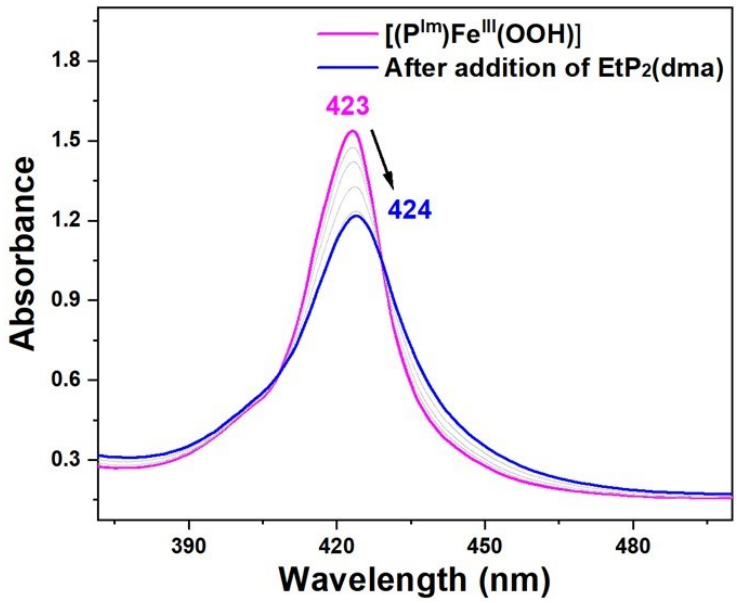

Figure 5.11 Conversion of [(P^{Im})Fe^{III}–(OOH)] (**P^{Im}-*HP***) (pink) to [(P^{Im})Fe^{III}–(O_2^{2-})]$^-$ (**P^{Im}-*P***) (blue) upon addition of EtP_2(dma) at –80 °C in THF, resulting in the generation of equilibrium mixtures which allowed the determination of the pK_a of the **P^{Im}-*HP***.

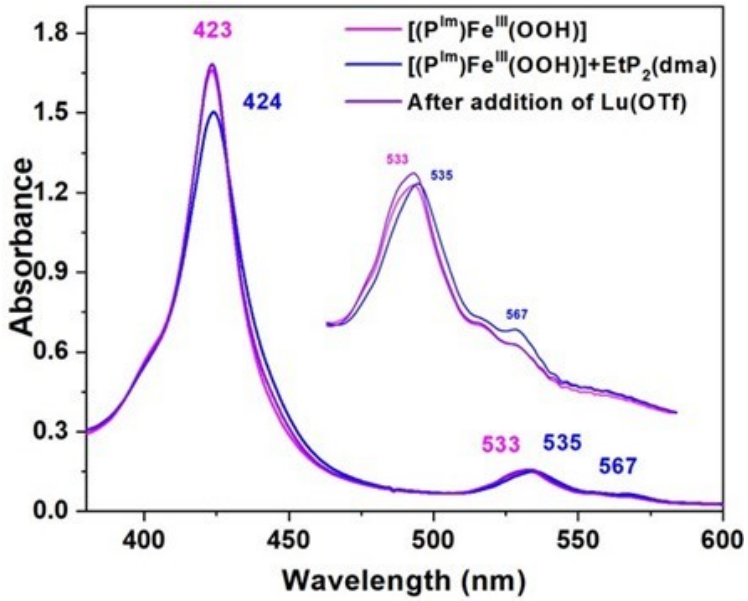

Figure 5.12 Addition of EtP_2(dma) to the solution of [(P^{Im})Fe^{III}–(OOH)] (**P^{Im}-*HP***) (pink) regenerates complex [(P^{Im})Fe^{III}–(O_2^{2-})]$^-$ (**P^{Im}-*P***) (blue). This resulting solution can be protonated again to form complex **P^{Im}-*HP*** (purple) by adding [($LutH^+$)](OTf).

5.2.5 Determination of the OO–H BDFE of [(P^{Im})Fe^{III}–(OOH)] (P^{Im}-*HP*)

This allows the completion of the thermodynamic square scheme for electron and proton transfer reactions (Figure 5.1) using the presently determined thermodynamic parameters, $E°'$ (–1.33 V vs. $Fc^{+/0}$, vide supra) and pK_a (28.6, vide supra), and determination of the BDFE of the OO–H in the ferric heme hydroperoxide complex [(P^{Im})Fe^{III}–(OOH)] (**P^{Im}-*HP***). According to eq. 1 (Bordwell relationship, C_G stands for the $H^+/H^•$ standard reduction potential in a particular solvent),[38] where C_G = 61 kcal/mol in THF, the **P^{Im}-*HP*** BDFE is calculated to be 69.5 kcal/mol (eq. 2).

$$\textbf{BDFE} = 1.37(pK_a) + 23.06E^o + C_{G,solv} \qquad (\textbf{1})$$

$$\textbf{BDFE}_{OO–H} = 1.37(28.6) + 23.06(–1.33) + 61 = \textbf{69.5 kcal/mol} \qquad (\textbf{2})$$

Our own previous report is the only other experimental evaluation of the thermodynamics and use of the square scheme as applied to ferric heme superoxide, peroxide (Figure 5.1, upper right) and hydroperoxide relatives, i.e., for the F_8 heme containing superoxide, (side-on) peroxide and hydroperoxide, [(F_8)Fe^{III}–(OOH)], $BDFE_{OO–H}$ = 73.5 kcal/mol.[8] Our OO–H BDFE value presented here with P^{Im} is shown to be ~ 4 kcal/mol less, and the difference resides primarily in the variation in the superoxide/peroxide redox couple (Figure 5.13). The pK_a values for [(F_8)Fe^{III}–(OOH)] vs [(P^{Im})Fe^{III}–(OOH)] (**P^{Im}-*HP***) are essentially identical, but the $E°'$ reduction potential is measurably more negative for the (**P^{Im}-*S***) / (**P^{Im}-*P***) couple (Figure 5.13). This makes

chemical sense as the P^{Im} system possesses the strong imidazolyl axial base ligand donor, that not present in the F8 heme system. Also, the dissimilarity of BDFE values ([$(P^{Im})Fe^{III}$–(OOH)] $BDFE_{OO–H}$ = 69.5 kcal/mol and [$(F_8)Fe^{III}$–(OOH)] $BDFE_{OO–H}$ = 73.5 kcal/mol) is supported by their hydrogen atom transfer (HAT) reactivities toward H atom donors (vide infra). As we noted previously[8] our BDFE results are also in accord with computationally calculated ferric heme hydroperoxides (those modeling proteins), where a proximal ligand is either an imidazolyl or thiolate group, BDEs (64–66 kcal/mol).[40]

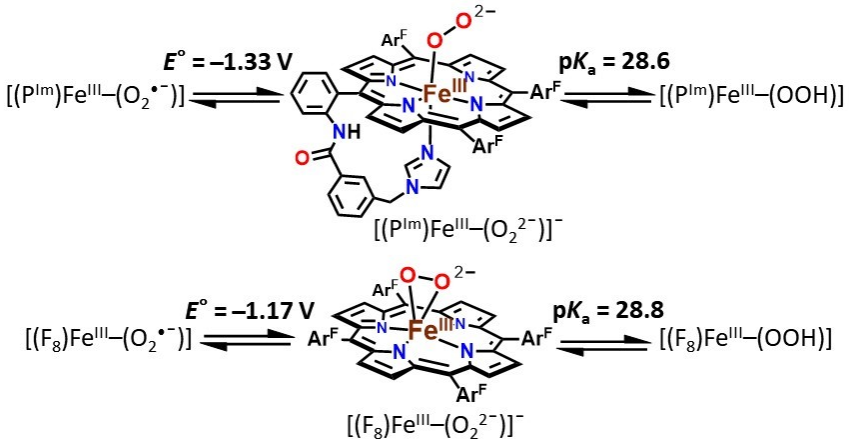

Figure 5.13 Comparison of P^{Im} and F_8 iron-porphyrinate complex for thermodynamic parameters and the geometry of peroxide species.

5.2.6 Reactivity Studies of [$(P^{Im})Fe^{III}$–$(O_2^{\bullet-})$] (P^{Im}-*S*) with O–H and C–H substrates

HAT reactivity (shown in the diagonal of Figure 5.1) studies were performed with [$(P^{Im})Fe^{III}$–$(O_2^{\bullet-})$] (**P^{Im}-*S***) toward external substrates to support our experimentally determined BDFE value. Addition of an excess of substrates such as 9,10-dihydroanthracene (76 kcal/mol in DMSO)[38] and xanthene (72.2 kcal/mol in THF)[39] to the solutions of **P^{Im}-*S*** at –80 °C in THF led to no reaction. These observations are consistent

with our BDFE determination of 69.5 kcal/mol for [(P^{Im})Fe^{III}–(OOH)] **P^{Im}-*HP***. In contrast, TEMPO-H (66.5 kcal/mol in THF, 72.6 kcal/mol in buffered aqueous solution and 69.6 kcal/mol in benzene)[39,41] does react with complex **P^{Im}-*S***. The final spectra (UV-vis and EPR; Scheme 5.1, Figure 5.14 and Figure 5.15) reveal a high yield of TEMPO•, while [(P^{Im})Fe^{III}–(OOH)] (**P^{Im}-*HP***) seems to only form in small amounts (~20% yield), probably due to side-reactions. The results support the conclusion that an initial H-atom abstraction from TEMPO-H to give **P^{Im}-*HP*** occurred. Based on these reactivity studies, the BDFE of [(P^{Im})Fe^{III}–(OOH)] (**P^{Im}-*HP***) can be bracketed to be, 66.5 < $BDFE_{OO-H}$ < 72 kcal/mol, which is consistent with our experimentally determined BDFE value, 69.5 kcal/mol.

Scheme 5.1 Hydrogen atom transfer (HAT) of [(P^{Im})Fe^{III}–($O_2^{\bullet-}$)] (**P^{Im}-*S***) from TEMPO-H at –80 °C in THF

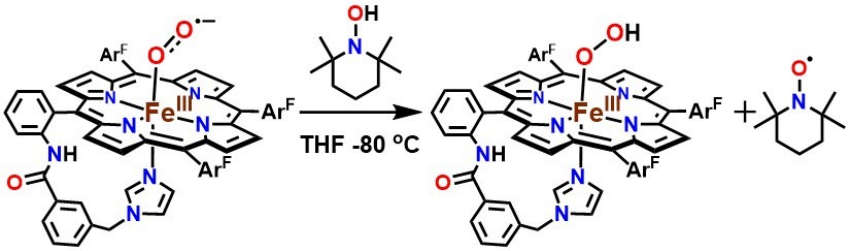

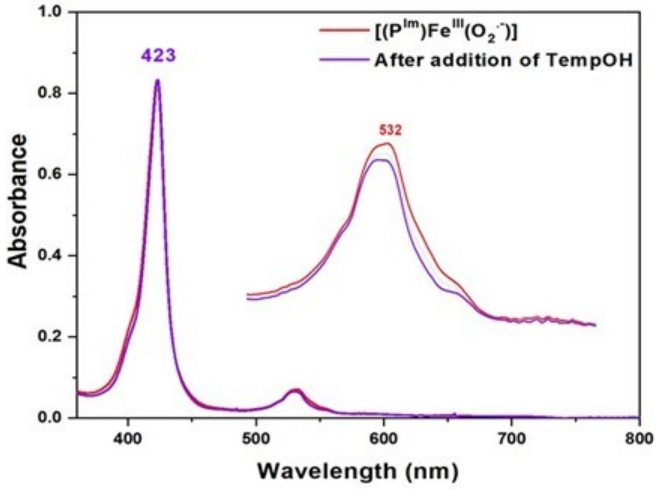

Figure 5.14 UV-vis spectra monitoring the reaction of [(P^{Im})Fe^{III}–($O_2^{\bullet-}$)] (**P^{Im}-*S***) with TEMPO-H at –80 °C in THF.

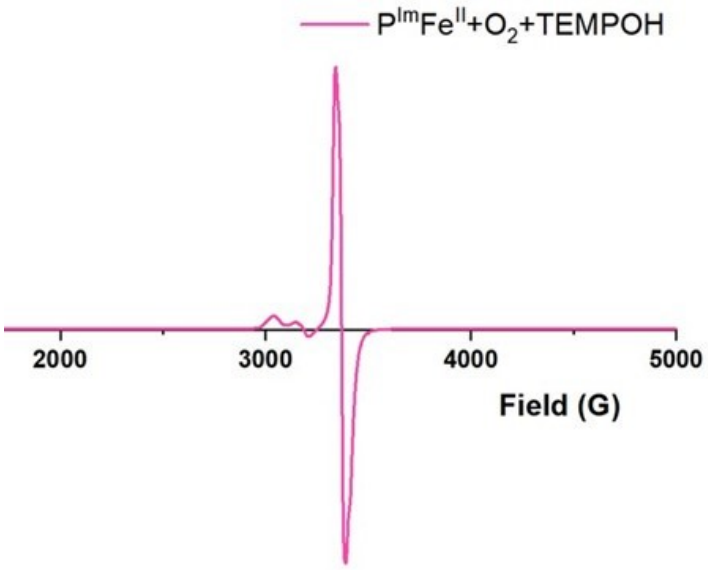

Figure 5.15 EPR spectrum of the reaction of [(P^{Im})Fe^{III}–($O_2^{\bullet-}$)] (**P^{Im}-*S***) with TEMPO-H in frozen THF.

As we previously showed that [(F_8)Fe^{III}–($O_2^{\bullet-}$)] (***S***) reacts with TEMPO-H to cleanly give the TEMPO• and corresponding hydroperoxide complex [(F_8)Fe^{III}–(OOH)] (***HP***), we now see that ***S*** and [(P^{Im})Fe^{III}–($O_2^{\bullet-}$)] (**P^{Im}-*S***) reactions toward TEMPO-H are comparable. Thus, we sought to find a different substrate that might differentiate between the oxidizing capabilities of the two superoxide complexes, which is what we have found here based on our thermodynamic parameter analysis. The superoxide complex ***S*** should be a somewhat stronger oxidant for HAT chemistry as based on our finding of the ~ 4 kcal/mol difference (vide supra).

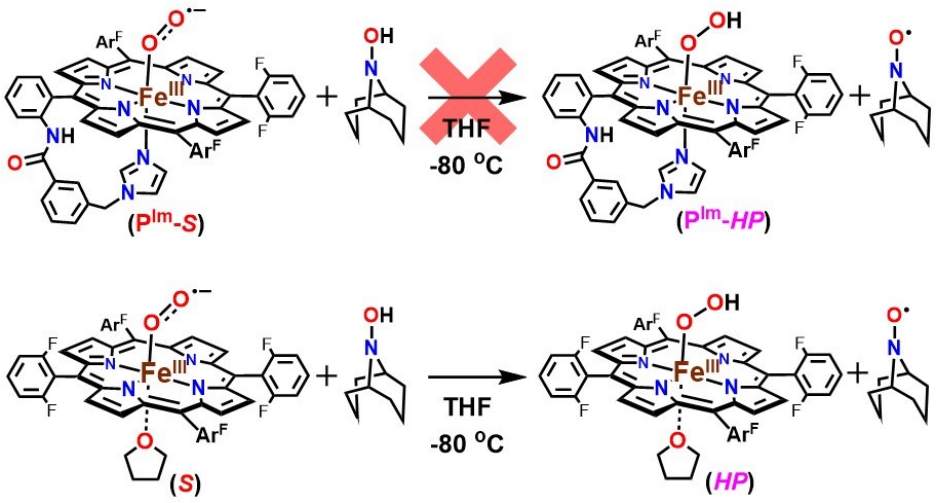

Figure 5.16 Reactivity comparison of P^{Im} and F_8 superoxide complex toward ABNO-H at –80 °C in THF.

Thus, we turned to the use of another hydroxylamine substrate, ABNO-H (9-azabicyclo[3.3.1]nonane-*N*-hydroxide, BDFE = 76.0 kcal/mol in buffered aqueous solution, 76.2 kcal/mol in benzene)[41] whose BDFE value is in the range 3.4-to-6.6 kcal/mol higher than that of TEMPO-H. As summarized in Figure 5.16, there was no reaction between $\mathbf{P^{Im}}$-***S*** and ABNO-H (Figure 5.16 and Figure 5.17), while spectroscopic monitoring (UV-vis and EPR) of the corresponding $[(F_8)Fe^{III}–(O_2^{\bullet-})]$ (***S***) plus ABNO-H reaction (Figure 5.16 and Figure 5.18) revealed both the generation of the organic radical product (ABNO•) along with the formation of the low-spin end-on hydroperoxide species, ***HP*** (See Figure 5.18 for further details). The HAT reaction of ABNO-H with $\mathbf{P^{Im}}$-***S*** is thermodynamically uphill. In contrast, the oxidizing ability of ***S*** via HAT from ABNO-H is thermodynamically downhill, thus favored. ABNO-H is a borderline substrate which enables us to discern the clear difference in the reactivities between $[(P^{Im})Fe^{III}–(O_2^{\bullet-})]$ ($\mathbf{P^{Im}}$-***S***) and $[(F_8)Fe^{III}–(O_2^{\bullet-})]$ (***S***); the results are fully consistent with our findings of heme-hydroperoxide OO–H BDFE's via thermodynamic analyses, here and previously.[8]

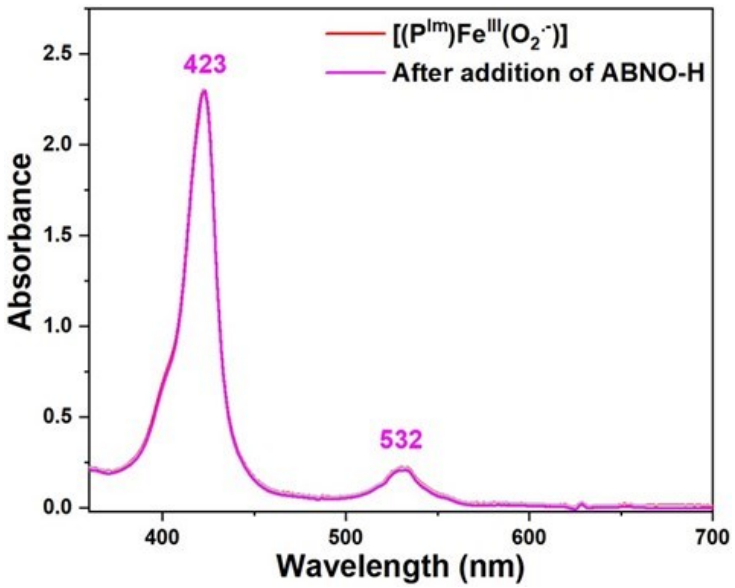

Figure 5.17 UV-vis spectroscopy following the addition of ABNO-H to the solution of [(P^{Im})Fe^{III}–($O_2^{\bullet-}$)] (**P^{Im}-*S***) in THF at −80 °C. No reaction is observed.

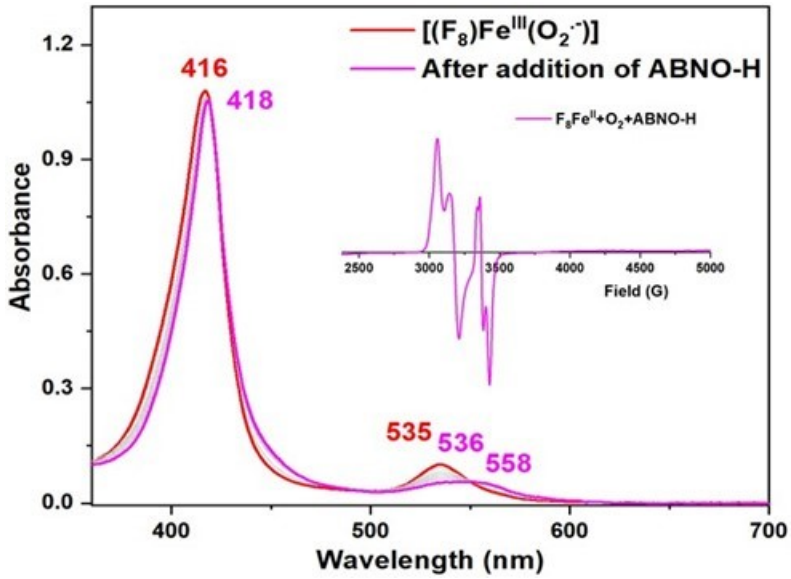

Figure 5.18 UV−vis spectroscopic monitoring the reaction of [(F_8)Fe^{III}–($O_2^{\bullet-}$)] (***S***) (red) with ABNO-H in THF at −80 °C to yield [(F_8)Fe^{III}–(OOH)] (***HP***) (pink). Inset: 10 K EPR spectrum of the final products of ABNO-H HAT by ***S*** in frozen THF. Spin quantification reveals that the EPR signal corresponds to ~68% yield of ***S***, but the yield of ABNO radical is low probably due to side-reactions, yet showing the expected triplet features (at g = 2; Inset). The overall time for the reaction to reach completion is ~5.0 hours.

5.3 Conclusions

In conclusion, using the P^{Im} iron-porphyrinate which includes an imidazolyl moiety appended to the periphery of a fluorinated tetraphenylporphyrin, we here generated a new (only the second one known) end-on low-spin ferric heme peroxide $[(P^{Im})Fe^{III}–(O_2^{2–})]^–$ (**P^{Im}-*P***) and also a hydroperoxide $[(P^{Im})Fe^{III}–(OOH)]$ (**P^{Im}-*HP***) species which are relevant to the catalytic cycle of CYP450s and many other heme enzymes which activate O_2 or H_2O_2. The end-on peroxide binding mode with the P^{Im} heme contrasts with that of the F_8 heme (without the appended axial imidazolyl ligand) which forms a side-on peroxide species. The reversibility of the $[(P^{Im})Fe^{III}–(O_2^{\bullet–})]$ (**P^{Im}-*S***)/ $[(P^{Im})Fe^{III}–(O_2^{2–})]^–$ (**P^{Im}-*P***) redox process and the $[(P^{Im})Fe^{III}–(O_2^{2–})]^–$ (**P^{Im}-*P***)/ $[(P^{Im})Fe^{III}–(OOH)]$ (**P^{Im}-*HP***) acid-base equilibrium allowed for the calculation of reduction potential and pK_a, respectively. With the measured thermodynamic parameters, the ferric heme OO–H BDFE was determined to be 69.5 kcal/mol, contrasting with the value of 73.5 kcal/mol found for $[(F_8)Fe^{III}–(OOH)]$ (***HP***).

This difference is a result of the existence of the appended axial imidazolyl ligand in the P^{Im} system. Its "push effect" appears to contribute significantly to the lower reduction potential found for (**P^{Im}-*S***)/(**P^{Im}-*P***) compared to that measured for the (***S***)/(***P***) couple with F_8-heme. Confirmation of our thermodynamically derived parameters comes from comparison of the $[(P^{Im})Fe^{III}–(O_2^{\bullet–})]$ (**P^{Im}-*S***) versus $[(F_8)Fe^{III}–(O_2^{\bullet–})]$ (***S***) reactivity results employing the hydroxylamine substrates TEMPO-H and/or ABNO-H. Future studies will explore further similar thermodynamic relationships to determine how ligand effects may control such properties and chemical reactivity.

5.4 Experimental section

5.4.1 Materials and methods

All reagents and solvents purchased and used were of commercially available quality except as noted. Inhibitor-free Tetrahydrofuran (THF) was distilled over Na/benzophenone under argon and deoxygenated with argon before use. Butyronitrile was distilled over sodium carbonate and potassium permanganate and deoxygenated with Ar before use. Cobaltocene was obtained from Sigma Aldrich, sublimed at 75°C, and stored under nitrogen in the glovebox freezer at –30 °C. The 2,6-lutidinium Triflate [(Lu)(H)](OTf), TEMPO-H, and ABNO-H were synthesized according to previously published literature procedures.[42–44]

The preparation and handling of air-sensitive compounds were performed under a MBraun Labmaster 130 inert atmosphere (< 1 ppm O_2 and < 1 ppm H_2O) glovebox filled with nitrogen. Dioxygen gas purchased from Airgas and dried through Drierite. $^{18}O_2$ gas was purchased from ICON, Summit, NJ, and $^{16}O_2$ gas was purchased from BOC gases, Murray Hill, NJ.

All UV−vis measurements were carried out as previously described[22,31] using a Hewlett-Packard 8453 diode array spectrophotometer with HP Chemstation software and a Unisoku thermostated cell holder for low-temperature experiments. A 10 mm path length quartz cell cuvette modified with an extended glass neck with a female 14/19 joint, and stopcock was used to perform all UV–vis experiments, as previously described.[31,45,46] ^{1}H NMR spectra were measured on a Bruker 300-MHz NMR spectrometer at ambient or low temperatures. Chemical shifts were reported as δ (ppm) values relative to an internal standard (tetramethylsilane) and the residual solvent proton peaks. Electron paramagnetic

resonance (EPR) spectra were recorded with a Bruker EMX spectrometer equipped with a Bruker ER 041 × G microwave bridge and a continuous flow liquid helium cryostat (ESR900) coupled to an Oxford Instruments TC503 temperature controller. Spectra were obtained at 10 K under non-saturating microwave power conditions (ν = 9.428 GHz, microwave power = 0.201 mW, modulation amplitude = 10 G, microwave frequency = 100 kHz, and receiver gain = 5.02×10^3).

The compound $(P^{Im})Fe^{II}$ was synthesized as previously described.[22]

5.4.2 UV-vis Spectroscopy

5.4.2.1 Generation of $[(P^{Im})Fe^{III}–(O_2^{2–})]$ (P^{Im}-*P*)

In an inert atmosphere glovebox, a 0.05 mM solution of $[(P^{Im})Fe^{II}]$ was prepared in THF in a 2 mm path length quartz Schlenk cuvette capped with a rubber septum. The cuvette was cooled in the cryostat chamber to –80 °C. Dioxygen was bubbled through the solution, and excess O_2 was purged out of the tubes by bubbling with Ar. Then, 15 µL (3 equiv) of a 10 mM solution of $CoCp_2$ dissolved in butyronitrile were added via gastight syringe to the solution of $[(P^{Im})Fe^{III}–(O_2^{\bullet–})]$ (**P^{Im}-*S***) and mixed by bubbling with Ar in THF at –80 °C. UV-vis: λ_{max} = 424, 535, and 567 nm.

5.4.2.2 Generation of $[(P^{Im})Fe^{III}–(OOH)]$ (P^{Im}-*HP*)

After generating complex $[(P^{Im})Fe^{III}–(O_2^{2–})]^–$ (**P^{Im}-*P***) as described above, 10 µL (1 equiv) of a 5 mM solution of $[(LutH^+)](OTf)$ dissolved in THF was added via gastight syringe to the solution of **P^{Im}-*P*** and mixed by bubbling with Ar in THF at –80 °C. UV-vis: λ_{max} = 423 and 533 nm.

5.4.2.3 H_2O_2 Quantification by Horseradish Peroxidase (HRP) Test

The spectrophotometric quantification of hydrogen peroxide was carried out by analyzing the intensity of the diammonium 2,2′-azino-bis(3-ethylbenzothiazoline-6-sulfonate)(AzBTS-$(NH_4)_2$) peaks (at different wavelengths to minimize error, Figure 5.3), which was oxidized by horseradish peroxidase (HRP); this was adapted from published procedures.[36,47] Three stock solutions were prepared: 300 mM sodium phosphate buffer pH 7.0 (solution A), 1 mg/mL AzBTS-$(NH_4)_2$ (solution B) and 4 mg of HRP (type II salt free (Sigma)) with 6.5 mg of sodium azide in 50 mL of water (solution C). 3.0 mL of the desired [$(P^{Im})Fe^{III}$–(O_2^{2-})] (**P^{Im}-*P***) or [$(P^{Im})Fe^{III}$–(OOH)] (**P^{Im}-*HP***) solution were generated in THF at –80 °C, as previously described. The reaction which is before and after being quenched by adding 100μL of triflic acid (HOTf) solution (2.5 equiv) is subject to the H_2O_2 analysis. Subsequently 100 μL of the cold THF sample solution was removed via a syringe and quickly added to a cuvette containing 1.3 mL of water, 500 μL of solution A, 100 μL of solution B, and 50 μL of solution C (all chilled in an ice bath prior to use). After mixing for 15s, the samples were allowed to sit at room temperature for ~2 min until full formation of the 418 nm band was observed (Figure 5.3).

5.4.2.4 Determination of the reduction potential of [$(P^{Im})Fe^{III}$–(O_2^{2-})] (P^{Im}-*P*)

In a 2mm path length quartz Schlenk cuvette, [$(P^{Im})Fe^{III}$–$(O_2^{\bullet-})$] (**P^{Im}-*S***) was generated as previously published.[22] Titrations of 0.25–3 equiv $CoCp_2$ dissolved in butyronitrile were carried out in THF at –80 °C. For each equilibrium mixture, the concentration of each species in solution was measured using the absorption at either 423

or 567 nm (Table 5.1). From these equilibrium constants, corresponding reduction potentials were calculated by using the Nernst equation.

5.4.2.5 Reversibility of [(P^{Im})Fe^{III}–($O_2^{\bullet-}$)] (P^{Im}-*S*) and [(P^{Im})Fe^{III}–(O_2^{2-})] (P^{Im}-*P*)

In a 2 mm path length quartz Schlenk cuvette, 1 equiv ferrocenium prepared in a glovebox was added via gastight syringe to a solution of [(P^{Im})Fe^{III}–(O_2^{2-})] (**P^{Im}-*P***) generated from [(P^{Im})Fe^{III}–($O_2^{\bullet-}$)] (**P^{Im}-*S***) with 3 equiv $CoCp_2$ in THF at –80 °C. Then, excess amount of $CoCp_2$ was added to this resulting solution via gastight syringe (Figure 5.7).

5.4.2.6 Determination of the pK_a of [(P^{Im})Fe^{III}–(OOH)] (P^{Im}-*HP*)

In a 2 mm path length quartz Schlenk cuvette, [(P^{Im})Fe^{III}–(OOH)] (**P^{Im}-*HP***) was generated as described above. Titrations of 0.25–2 equiv EtP_2(dma) prepared in a glovebox were carried out in THF at –80 °C. For each equilibrium mixture, the concentration of each species in solution was measured using the absorption at either 423 or 567 nm (Table 5.2). From these equilibrium constants, the pK_a was calculated.

5.4.2.7 Reversibility of [(P^{Im})Fe^{III}–(O_2^{2-})]$^-$ (P^{Im}-*P*) and [(P^{Im})Fe^{III}–(OOH)] (P^{Im}-*HP*)

In a 2 mm path length quartz Schlenk cuvette, 2 equiv EtP_2(dma) prepared in a glovebox was added via gastight syringe to a solution of [(P^{Im})Fe^{III}–(OOH)] (**P^{Im}-*HP***) generated as described above. Then, 3 equiv [($LutH^+$)](OTf) was added to this resulting solution via gastight syringe (Figure 5.12).

5.4.3 Electron Paramagnetic Resonance (EPR) Spectroscopy

In a glovebox, 1 mM solutions of $(P^{Im})Fe^{II}$ in THF were prepared and transferred to EPR tube and capped with tightfitting septum. The sample tubes were placed in a cold bath (dry ice/acetone) and then O_2 was bubbled through the solution. The excess O_2 was purged out of the tubes by bubbling with Ar, and then the oxygenated samples were set in a cold bath for 10 min. The solution of $CoCp_2$ dissolved in butyronitrile in a glovebox was added via gastight syringe to the solution of $[(P^{Im})Fe^{III}–(O_2^{\bullet-})]$ (**P^{Im}-*S***). Subsequently, 1 equiv $[(LutH^+)](OTf)$ was added via gastight syringe, followed by mixing of the solution by bubbling Ar, for complex $[(P^{Im})Fe^{III}–(OOH)]$ (**P^{Im}-*HP***). Then, the sample tubes were frozen in liquid N_2.

For EPR data for the reaction of $[(P^{Im})Fe^{III}–(O_2^{\bullet-})]$ (**P^{Im}-*S***) with TEMPO–H, 10 equiv TEMPO–H prepared in a glovebox was added via gastight syringe to the 1mM solution of **P^{Im}-*S*** generated as described above. The tube was left at –80 °C for 1 hour 30 minutes and then frozen in liquid nitrogen and sealed by flame.

5.4.4 Resonance Raman Spectroscopy

In the glovebox, 1 mM solutions of $(P^{Im})Fe^{II}$ in THF were prepared and transferred to rR tube and capped with tightfitting septum. The sample tubes were placed in a cold bath (dry ice/acetone) and then either $^{16}O_2$ or $^{18}O_2$ gas was bubbled through the solution. The excess either $^{16}O_2$ or $^{18}O_2$ was purged out of the tubes by bubbling with Ar, and then the oxygenated samples were set in a cold bath for 10 min. The solution of $CoCp_2$ dissolved in butyronitrile in a glovebox was added via gastight syringe to the solution of $[(P^{Im})Fe^{III}–(O_2^{\bullet-})]$ (**P^{Im}-*S***). Subsequently, 1 equiv $[(LutH^+)](OTf)$ was added via gastight syringe,

followed by mixing of the solution by bubbling Ar, for complex [(P^{Im})Fe^{III}–(OOH)] (**P^{Im}-*HP***). Then, the sample tubes were frozen in liquid N_2. Resonance Raman samples were excited at 413 nm, using a Coherent I90C-K Kr^+ ion laser while the sample was immersed in a liquid nitrogen cooled (77 K) EPR finger Dewar (Wilmad). Power was ~2 mW at the sample, which was continuously rotated to minimize photodecomposition. The spectra were recorded using a Spex 1877 CP triple monochromator, and detected by an Andor Newton CCD cooled to –80 °C.

5.5 References

(1) Sono, M.; Roach, M. P.; Coulter, E. D.; Dawson, J. H. Heme-Containing Oxygenases. *Chem. Rev.* **1996**, *96*, 2841–2887.

(2) Denisov, I. G.; Makris, T. M.; Sligar, S. G.; Schlichting, I. Structure and Chemistry of Cytochrome P450. *Chem. Rev.* **2005**, *105*, 2253–2277.

(3) Ortiz de Montellano, P. R. Hydrocarbon Hydroxylation by Cytochrome P450 Enzymes. *Chem. Rev.* **2010**, *110*, 932–948.

(4) Huang, X.; Groves, J. T. Oxygen Activation and Radical Transformations in Heme Proteins and Metalloporphyrins. *Chem. Rev.* **2018**, *118*, 2491–2553.

(5) Adam, S. M.; Wijeratne, G. B.; Rogler, P. J.; Diaz, D. E.; Quist, D. A.; Liu, J. J.; Karlin, K. D. Synthetic Fe/Cu Complexes: Toward Understanding Heme-Copper Oxidase Structure and Function. *Chem. Rev.* **2018**, *118*, 10840–11022.

(6) Das, P. K.; Chatterjee, S.; Samanta, S.; Dey, A. EPR, Resonance Raman, and DFT Calculations on Thiolate- and Imidazole-Bound Iron(III) Porphyrin Complexes: Role of the Axial Ligand in Tuning the Electronic Structure. *Inorg. Chem.* **2012**, *51*, 10704–10714.

(7) Dubey, K. D.; Shaik, S. Cytochrome P450-The Wonderful Nanomachine Revealed through Dynamic Simulations of the Catalytic Cycle. *Acc. Chem. Res.* **2019**, *52*, 389–399.

(8) Kim, H.; Rogler, P. J.; Sharma, S. K.; Schaefer, A. W.; Solomon, E. I.; Karlin, K. D. Superoxide, Peroxide and Hydroperoxide Thermodynamic Relationships: Fe^{III}-$O_2^{\bullet-}$ Complex H-Atom Abstraction Reactivity. *J . Am. Chem. Soc.* **2020**, *142*, 3104–3116.

(9) Davydov, R.; Macdonald, I. D. G.; Makris, T. M.; Sligar, S. G.; Hoffman, B. M. EPR and ENDOR of Catalytic Intermediates in Cryoreduced Native and Mutant Oxy-Cytochromes P450cam: Mutation-Induced Changes in the Proton Delivery System. *J. Am. Chem. Soc.* **1999**, *121*, 10654–10655.

(10) Davydov, R.; Makris, T. M.; Kofman, V.; Werst, D. E.; Sligar, S. G.; Hoffman, B. M. Hydroxylation of Camphor by Reduced Oxy-Cytochrome P450cam : Mechanistic Implications of EPR and ENDOR Studies of Catalytic Intermediates in Native and Mutant Enzymes. *J. Am. Chem. Soc.* **2001**, *123*, 1403–1415.

(11) Davydov, R.; Satterlee, J. D.; Fujii, H.; Sauer-Masarwa, A.; Busch, D. H.; Hoffman, B. M. A Superoxo-Ferrous State in a Reduced Oxy-Ferrous Hemoprotein and Model Compounds. *J. Am. Chem. Soc.* **2003**, *125*, 16340–16346.

(12) Garcia-Serres, R.; Davydov, R. M.; Matsui, T.; Ikeda-Saito, M.; Hoffman, B. M.; Huynh, B. H. Distinct Reaction Pathways Followed upon Reduction of Oxy-Heme Oxygenase and Oxy-Myoglobin as Characterized by Mössbauer Spectroscopy. *J. Am. Chem. Soc.* **2007**, *129*, 1402–1412.

(13) Shaik, S.; Cohen, S.; Wang, Y.; Chen, H.; Kumar, D.; Thiel, W. P450 Enzymes: Their Structure, Reactivity, and Selectivity-Modeled by QM/MM Calculations. *Chem. Rev.* **2010**, *110*, 949–1017.

(14) Collman, J. P.; Gagnet, R. R.; Christopher, A.; Robinson, W. T. Structure of an Iron(II) Dioxygen Complex ; A Model for Oxygen Carrying Hemeproteins. *Proc. Natl. Acad. Sci. U. S. A.* **1974**, *71*, 1326–1329.

(15) Momenteau, M.; Reed, C. A. Synthetic Heme Dioxygen Complexes. *Chem. Rev.* **1994**, *94*, 659–698.

(16) Kim, H.; Sharma, S. K.; Schaefer, A. W.; Solomon, E. I.; Karlin, K. D. Heme−Cu Binucleating Ligand Supports Heme/O_2 and Fe^{II}–Cu^{I}/O_2 Reactivity Providing High- and Low-Spin Fe^{III}–Peroxo–Cu^{II} Complexes. *Inorg. Chem.* **2019**, *58*, 15423–15432.

(17) Collman, J. P.; Sunderland, C. J.; Berg, K. E.; Vance, M. A.; Solomon, E. I. Spectroscopic Evidence for a Heme-Superoxide/Cu(I) Intermediate in a Functional Model of Cytochrome *c* Oxidase. *J. Am. Chem. Soc.* **2003**, *125*, 6648–6649.

(18) Chufan, E. E.; Karlin, K. D. An Iron-Peroxo Porphyrin Complex : New Synthesis and Reactivity Toward a Cu(II) Complex Giving a Heme-Peroxo-Copper Adduct. *J. Am. Chem. Soc.* **2003**, *125*, 16160–16161.

(19) Liu, J. G.; Naruta, Y.; Tani, F. A Functional Model of the Cytochrome *c* Oxidase Active Site: Unique Conversion of a Heme–μ-Peroxo–Cu^{II} Intermediate into Heme–Superoxo/Cu^{I}. *Angew. Chem. Int. Ed.* **2005**, *44*, 1836–1840.

(20) Liu, J.-G.; Ohta, T.; Yamaguchi, S.; Ogura, T.; Sakamoto, S.; Maeda, Y.; Naruta, Y. Spectroscopic Characterization of a Hydroperoxo-Heme Intermediate: Conversion of a Side-on Peroxo to an End-on Hydroperoxo Complex. *Angew. Chem. Int. Ed. Engl.* **2009**, *48*, 9262–9267.

(21) Liu, J. G.; Shimizu, Y.; Ohta, T.; Naruta, Y. Formation of an End-on Ferric Peroxo Intermediate upon One-Electron Reduction of a Ferric Superoxo Heme. *J. Am. Chem. Soc.*

2010, *132*, 3672–3673.

(22) Li, Y.; Sharma, S. K.; Karlin, K. D. New Heme-Dioxygen and Carbon Monoxide Adducts Using Pyridyl or Imidazolyl Tailed Porphyrins. *Polyhedron* **2013**, *58*, 190–196.

(23) Nagaraju, P.; Ohta, T.; Liu, J.-G.; Ogura, T.; Naruta, Y. The Secondary Coordination Sphere Controlled Reactivity of a Ferric-Superoxo Heme: Unexpected Conversion to a Ferric Hydroperoxo Intermediate by Reaction with a High-Spin Ferrous Heme. *Chem. Commun.* **2016**, *52*, 7213–7216.

(24) Singha, A.; Dey, A. Hydrogen Atom Abstraction by Synthetic Heme Ferric Superoxide and Hydroperoxide Species. *Chem. Commun.* **2019**, *55*, 5591–5594.

(25) Tajima, K.; Oka, S.; Edo, T.; Miyake, S.; Mano, H.; Mukai, K.; Sakurai, H.; Ishizu, K. Optical Absorption and EPR Studies on a Six-Coordinate Iron(III)-Tetramesitylporphyrin-Hydrogen Peroxide Complex Having a Nitrogenous Axial Ligand. *J. Chem. Soc., Chem. Commun.,* **1995**, 1507–1508.

(26) Oliveira, R.; Zouari, W.; Herrero, C.; Banse, F.; Schöllhorn, B.; Fave, C.; Anxolabéhère-Mallart, E. Characterization and Subsequent Reactivity of an Fe-Peroxo Porphyrin Generated by Electrochemical Reductive Activation of O_2. *Inorg. Chem.* **2016**, *55*, 12204–12210.

(27) Sengupta, K.; Chatterjee, S.; Samanta, S.; Dey, A. Direct Observation of Intermediates Formed during Steady-State Electrocatalytic O_2 Reduction by Iron Porphyrins. *Proc. Natl. Acad. Sci. U. S. A.* **2013**, *110*, 8431–8436.

(28) Elizabeth McCandlish, A. R. M.; Mario Nappa, Alice Q. Sprenger, J. S. V. Reactions of Superoxide with Iron Porphyrins in Aprotic Solvents. A High Spin Ferric Porphyrin Peroxo Complex. *J. Am. Chem. Soc.* **1980**, *102*, 4268–4271.

(29) Selke, M.; Sisemore, M. F.; Valentine, J. S. The Diverse Reactivity of Peroxy Ferric Porphyrin Complexes of Electron-Rich and Electron-Poor Porphyrins. *J. Am. Chem. Soc.* **1996**, *118*, 2008–2012.

(30) D. L. Wertz, J. S. Valentine, *Struct. Bonding (Berlin)* **2000**, *97*, 37–60.

(31) Sharma, S. K.; Schaefer, A. W.; Lim, H.; Matsumura, H.; Moënne-Loccoz, P.; Hedman, B.; Hodgson, K. O.; Solomon, E. I.; Karlin, K. D. A Six-Coordinate Peroxynitrite Low-Spin Iron(III) Porphyrinate Complex - The Product of the Reaction of Nitrogen Monoxide (·NO(g)) with a Ferric-Superoxide Species. *J. Am. Chem. Soc.* **2017**, *139*, 17421–17430.

(32) Mak, P. J.; Denisov, I. G.; Victoria, D.; Makris, T. M.; Deng, T.; Sligar, S. G.; Kincaid, J. R. Resonance Raman Detection of the Hydroperoxo Intermediate in the Cytochrome P450 Enzymatic Cycle. *J. Am. Chem. Soc.* **2007**, *129*, 6382–6383.

(33) Denisov, I. G.; Mak, P. J.; Makris, T. M.; Sligar, S. G.; Kincaid, J. R. Resonance Raman Characterization of the Peroxo and Hydroperoxo Intermediates in Cytochrome P450. *J. Phys. Chem. A* **2008**, *112*, 13172–13179.

(34) Davydov, R. M.; Yoshida, T.; Ikeda-Saito, M.; Hoffman, B. M. Hydroperoxy-Heme Oxygenase Generated by Cryoreduction Catalyzes the Formation of α-Meso-Hydroxyheme as Detected by EPR and ENDOR. *J. Am. Chem. Soc.* **1999**, *121*, 10656–10657.

(35) Ibrahim, M.; Denisov, I. G.; Makris, T. M.; Kincaid, J. R.; Sligar, S. G. Resonance Raman Spectroscopic Studies of Hydroperoxo-Myoglobin at Cryogenic Temperatures. *J. Am. Chem. Soc.* **2003**, *125*, 13714–13718.

(36) Adam, S. M.; Garcia-Bosch, I.; Schaefer, A. W.; Sharma, S. K.; Siegler, M. A.;

Solomon, E. I.; Karlin, K. D. Critical Aspects of Heme–Peroxo–Cu Complex Structure and Nature of Proton Source Dictate Metal–Operoxo Breakage versus Reductive O–O Cleavage Chemistry. *J . Am. Chem. Soc.* **2017**, *139*, 472–481.

(37) Yandulov, D. V.; Schrock, R. R. Erratum: Studies Relevant to Catalytic Reduction of Dinitrogen to Ammonia by Molybdenum Triamidoamine Complexes. *Inorg. Chem.* **2005**, *44*, 1103–1117.

(38) Warren, J. J.; Tronic, T. A.; Mayer, J. M. Thermochemistry of Proton-Coupled Electron Transfer Reagents and Its Implications. *Chem. Rev.* **2010**, *110*, 6961–7001.

(39) Quist, D. A.; Ehudin, M. A.; Schaefer, A. W.; Schneider, G. L.; Solomon, E. I.; Karlin, K. D. Ligand Identity-Induced Generation of Enhanced Oxidative Hydrogen Atom Transfer Reactivity for a $Cu^{II}_2(O_2^{\bullet-})$ Complex Driven by Formation of a $Cu^{II}_2(-OOH)$ Compound with a Strong O–H Bond. *J. Am. Chem. Soc.* **2019**, *141*, 12682–12696.

(40) Chung, L. W.; Li, X.; Hirao, H.; Morokuma, K. Comparative Reactivity of Ferric-Superoxo and Ferryl-Oxo Species in Heme and Non-Heme Complexes. *J. Am. Chem. Soc.* **2011**, *133*, 20076–20079.

(41) Gerken, J. B.; Pang, Y. Q.; Lauber, M. B.; Stahl, S. S. Structural Effects on the PH-Dependent Redox Properties of Organic Nitroxyls: Pourbaix Diagrams for TEMPO, ABNO, and Three TEMPO Analogs. *J. Org. Chem.* **2018**, *83*, 7323–7330.

(42) Curley, J. J.; Bergman, R. G.; Tilley, T. D. Preparation and Physical Properties of Early-Late Heterobimetallic Compounds Featuring Ir-M Bonds (M = Ti, Zr, Hf). *Dalt. Trans.* **2012**, *41*, 192–200.

(43) Mader, E. A.; Davidson, E. R.; Mayer, J. M. Large Ground-State Entropy Changes for Hydrogen Atom Transfer Reactions of Iron Complexes. *J. Am. Chem. Soc.* **2007**, *129*,

5153–5166.

(44) Porter, T. R.; Capitao, D.; Kaminsky, W.; Qian, Z.; Mayer, J. M. Synthesis, Radical Reactivity, and Thermochemistry of Monomeric Cu(II) Alkoxide Complexes Relevant to Cu/Radical Alcohol Oxidation Catalysis. *Inorg. Chem.* **2016**, *55*, 5467–5475.

(45) Ghiladi, R. a; Huang, H.; Moënne-Loccoz, P.; Stasser, J.; Blackburn, N. J.; Woods, A. S.; Cotter, R. J.; Incarvito, C. D.; Rheingold, A. L.; Karlin, K. D. Heme-Copper/Dioxygen Adduct Formation Relevant to Cytochrome *c* Oxidase: Spectroscopic Characterization of $[(^{6}L)Fe^{III}\text{-}(O_2(^{2-}))\text{-}Cu^{II}]^{+}$. *J. Biol. Inorg. Chem.* **2005**, *10*, 63–77.

(46) Wasser, I. M.; Huang, H. W.; Moe, P.; Karlin, K. D. Heme / Non-Heme Diiron(II) Complexes and O_2, CO, and NO Adducts as Reduced and Substrate-Bound Models for the Active Site of Bacterial Nitric Oxide Reductase. *J. Am. Chem. Soc.* **2005**, *127*, 3310–3320.

(47) Peterson, R. L.; Ginsbach, J. W.; Cowley, R. E.; Qayyum, M. F.; Himes, R. A.; Siegler, M. A.; Moore, C. D.; Hedman, B.; Hodgson, K. O.; Fukuzumi, S.; Solomon, E. I.; Karlin, K. D. Stepwise Protonation and Electron-Transfer Reduction of a Primary Copper-Dioxygen Adduct. *J. Am. Chem. Soc.* **2013**, *135*, 16454–16467.

Hyun Kim

yuneagle@gmail.com • Baltimore, MD 21218, USA

EDUCATION

Johns Hopkins University 05/2018 – 12/2020
Baltimore, MD, USA
Ph.D. in Chemistry
Advisor: Professor Kenneth D. Karlin

Johns Hopkins University 08/2015 – 05/2018
Baltimore, MD, USA
M.A. in Chemistry
Advisor: Professor Kenneth D. Karlin

Seoul National University of Science and Technology 03/2012 – 08/2015
Seoul, Korea
M.S. in Chemistry
Advisor: Professor Cheal Kim

Seoul National University of Science and Technology 03/2008 – 02/2012
Seoul, Korea
B.S. in Chemistry
Advisor: Professor Cheal Kim

RESEARCH EXPERIENCE

Graduate Research Assistant, Johns Hopkins University 08/2015 – 12/2020
Advisor: Professor Kenneth D. Karlin

- Project 1: Synthesis of a new porphyrinate complex as a model for the imidazole-phenol cross-coupling reaction implicated in His 240-Tyr 244 crosslink formation in Cytochrome *c* Oxidase (C*c*O).
  - Synthesized a new porphyrinate iron complex and characterized using ^{1}H-NMR, ^{2}H-NMR, ^{19}F-NMR, UV-vis and Electron Paramagnetic Resonance Spectroscopy (EPR).
  - Collaborative (team player), interpersonal communication skills.
- Project 2: Investigated the coordination chemistry of heme/O_2 and heme/Cu/O_2 adducts with Cytochrome *c* Oxidase-inspired model complex.
  - Developed a strategy for generation of biomimetic small molecule model systems about peroxidic intermediates, characterized these species using variable temperature UV-visible Spectroscopy, variable temperature Nuclear Magnetic Resonance Spectroscopy, EPR and Resonance Raman spectroscopy (rR).
  - Productive independent research with excellent communication and team skills.

- Project 3: Studies on the thermodynamics of biomimetic model complexes relevant to Cytochrome P450s (CYP450).
  - Investigated the optimal redox chemicals for reduction/oxidation of model complexes, calculated the redox potential and pK_a, conducted the reactivity and kinetic studies.
  - Self-directed, innovative, collaborative, able to balance multiple projects.

Graduate Research Assistant 03/2012 – 08/2015

Seoul National University of Science and Technology
Advisor: Professor Cheal Kim

- Thesis: Synthesis, application and analysis of chemosensors based on pyridine and phenol colorimetric and fluorometric sensor for metal ions.
  - Designed, synthesized and characterized novel optical chemosensors for detection of target ions (Al, Zn, Cu, Fe), investigated their unique optical properties using Fourier Transform Infrared Spectroscopy (FT-IR), UV-vis and Fluorescence Spectroscopies.
  - Calculated a detection limit of the target ions using the chemosensors, examined the practicability as a sensor.

Undergraduate Research 03/2011 – 02/2012

Seoul National University of Science and Technology
Advisor: Professor Cheal Kim

- Project: Synthesis and characterization of metal complexes with Saloph ligands.

AWARDS and HONORS

Honor Student Award, Seoul National University of Science and Technology 2012

TEACHING EXPERIENCE

Teaching Assistant – Johns Hopkins University 01/2017 – 05/2017
Class: Chemistry with Problem Solving

Teaching Assistant – Johns Hopkins University 08/2015 – 12/2016
Class: Introductory Chemistry Laboratory

Teaching Assistant – Seoul National University of Science and Technology
Class: Inorganic Chemistry Laboratory 03/2013 – 06/2013
Teaching Assistant – Seoul National University of Science and Technology
Class: Introductory Chemistry Laboratory 03/2012 – 12/2012

TECHNICAL PROFICIENCIES

Synthesis and purification of multi-step organic compounds
Thin layer chromatography, column chromatography

Synthesis of highly air-sensitive compounds

Schlenk/vacuum line techniques, inert atmosphere glovebox (dry-box) maintenance and usage

Crystallization with complexes for X-ray crystallography analysis

Analysis of compounds

Fourier Transform Infrared Spectroscopy, variable temperature UV-visible Spectroscopy, Fluorescence Spectroscopy, variable temperature Nuclear Magnetic Resonance Spectroscopy, Electrospray Ionization Mass Spectrometry, Electron Paramagnetic Resonance Spectroscopy, Gas Chromatography, Gas Chromatography-Mass Spectrometry, Cyclic Voltammetry

Solvent distillation techniques, Nitric Oxide ($NO_{(g)}$) purification

Air-free and low-temperature sample preparation for UV-vis, resonance Raman spectroscopy, Nuclear Magnetic Resonance Spectroscopy, Electron Paramagnetic Resonance Spectroscopy

Expertise in Microsoft Office: Word, Excel, PowerPoint

SCIENTIFIC SOCIETY MEMBERSHIPS

American Chemical Society (Inorganic Chemistry Division) 2017 – present

Korean Chemical Society 2012 – 2013

ORAL PRESENTATIONS

Kim, Hyun; Rogler, Patrick J.; Sharma, Savita K.; Karlin, Kenneth D. *Contributed Lecture to the Division of Inorganic Chemistry: Creative Advances in Synthetic and Biological Coordination Chemistry (invited)*: "Thermochemistry of a ferric heme hydroperoxide complex: hydrogen atom abstraction reactivity of the superoxide partner complex", *259th American Chemical Society National Meeting*, Philadelphia, PA, USA, March 24, **2020**. INOR 549. *Unable to deliver, meeting canceled due to COVID-19 outbreak.*

Kim, Hyun; Sharma, Savita K.; Karlin, Kenneth D. *Contributed Lecture to the Division of Inorganic Chemistry: Many Colors of Copper*: "Binding and activation of small molecules (NO, O_2) by a biomimetic heme-Cu ligand scaffold", *254th American Chemical Society National Meeting*, Washington, DC, USA, August 23, **2017**. INOR 720.

POSTER PRESENTATIONS

Bhadra, Mayukh; **Kim, Hyun**; Herzog, Austin; Karlin, Kenneth D. "Different Projects of the Karlin Lab: A Brief Overview", *Johns Hopkins University Chemistry Department Graduate Student Recruitment Session*, Johns Hopkins University, Baltimore, MD, USA, March 8, **2019**.

Kim, Hyun; Sharma, Savita K.; Karlin, Kenneth D. "Characterization and Reactivity of a New Porphyrinate as a Model for the Imidazole-Phenol Cross-Coupling Reaction Implicated in His-Tyr Crosslink Formation in Cytochrome *c* Oxidase", *Frontiers in*

Metallobiochemistry Symposium, 37th Summer Symposium in Molecular Biology, State College, PA, USA, June 6–8, **2018**.

Kim, Hyun; Sharma, Savita K.; Karlin, Kenneth D. "The Synthesis of a New Porphyrin as a Model System for Cytochrome *c* Oxidase", *Mid-Atlantic Seaboard Inorganic Symposium*, Philadelphia, PA, USA, July 20, **2016**.

PUBLICATIONS

1. **Kim, Hyun**; Rogler, Patrick J.; Sharma, Savita K.; Schaefer, Andrew W.; Solomon, Edward I.; Karlin, Kenneth D "Ferric Heme Superoxide Reductive Transformations to Ferric Heme (Hydro)Peroxide Species: Spectroscopic Characterization and Thermodynamic Implications for H-atom transfer (HAT)", *Angew. Chem*., DOI: 10.1002/anie.202013791 and 10.1002/ange.202013791.

2. **Kim, Hyun**; Rogler, Patrick J.; Sharma, Savita K.; Schaefer, Andrew W.; Solomon, Edward I.; Karlin, Kenneth D. "Heme-Fe^{III} Superoxide, Peroxide and Hydroperoxide Thermodynamic Relationships: Fe^{III}-$O_2^{\bullet-}$ Complex H-Atom Abstraction Reactivity", *J. Am. Chem. Soc*., **2020**, *142*, 3104–3116.

3. **Kim, Hyun**; Sharma, Savita K.; Schaefer, Andrew W.; Solomon, Edward I.; Karlin, Kenneth D. "New Heme–Cu Binucleating Ligand Supports Heme/O_2 and Fe^{II}–Cu^{I}/O_2 Reactivity Providing High- and Low-Spin Fe^{III}–Peroxo–Cu^{II} Complexes", *Inorg. Chem*., **2019**, *58*, 15423–15432.

4. Sharma, Savita K.; **Kim, Hyun**; Rogler, Patrick J.; Karlin, Kenneth D. "Isocyanide or nitrosyl complexation to hemes with varying tethered axial base ligand donors: synthesis and characterization", *J. Biol. Inorg. Chem*., **2016**, *21*, 729–743.

5. Lee, Jae Jun; Lee, Seul Ah; **Kim, Hyun**; Nguyen, LeTuyen; Noh, Insup; Kim, Cheal "A highly selective CHEF-type chemosensor for monitoring Zn^{2+} in aqueous solution and living cells", *RSC Adv.*, **2015**, *5*, 41905–41913.

6. Park, Gyeong Jin; **Kim, Hyun**; Lee, Jae Jun; Kim, Yong Sung; Lee, Sun Young; Lee, Suyeon; Noh, Insup; Kim, Cheal "A highly selective turn-on chemosensor capable of monitoring Zn^{2+} concentrations in living cells and aqueous solution" *Sensors and Actuators B*, **2015**, *215*, 568–576.

7. **Kim, Hyun**; You, Ga Rim; Park, Gyeong Jin; Choi, Ji Young; Noh, Insup; Kim, Youngmee; Kim, Sung-Jin; Kim, Cheal; Harrison, Roger G. "Selective zinc sensor based on pyrazoles and quinoline used to image cells", *dyes and pigments*, **2015**, *113*, 723–729.

8. Song, Eun Joo; **Kim, Hyun**; Hwang, In Hong; Kim, Kyung Beom; Kim, Ah Ram; Noh, Insup; Kim, Cheal "A single fluorescent chemosensor for multiple target ions: Recognition of Zn^{2+} in 100% aqueous solution and F^- in organic solvent", *Sensors and Actuators B*, **2014**, *195*, 36–43.

9. **Kim, Hyun**; Na, Yu Jeong; Park, Gyeong Jin; Lee, Jae Jun; Kim, Yong Sung; Lee, Sun Young; Kim, Cheal "A novel selective colorimetric chemosensor for Cu^{2+} in aqueous solution" *Inorg. Chem. Commun.*, **2014**, *49*, 68–71.

10. Kim, Kyung Beom; Park, Gyeong Jin; **Kim, Hyun**; Song, Eun Joo; Bae, Jeong Mi; Kim, Cheal "A novel colorimetric chemosensor for multiple target ions in aqueous solution: simultaneous detection of Mn(II) and Fe(II)", *Inorg. Chem. Commun.*, **2014**, *46*, 237–240.

11. **Kim, Hyun**; Na, Yu Jeong; Song, Eun Joo; Kim, Kyung Beom; Bae, Jeong Mi; Kim, Cheal "A single colorimetric sensor for multiple target ions: the simultaneous detection of Fe^{2+} and Cu^{2+} in aqueous media", *RSC Adv.*, **2014**, *4*, 22463–22469.

12. Kim, Dong Ha; Im, Ye Seo; **Kim, Hyun**; Kim, Cheal "Solvent-dependent selective fluorescence sensing of Al^{3+} and Zn^{2+} using a single Schiff base", *Inorg. Chem. Commun.*, **2014**, *45*, 15–19.

13. **Kim, Hyun**; Kang, Juhye; Kim, Kyung Beom; Song, Eun Joo; Kim, Cheal "A highly selective quinoline-based fluorescent sensor for Zn(II)", *Spectrochimica Acta Part A: Molecular and Biomolecular Spectroscopy*, **2014**, *118*, 883–887.

14. Park, Gyeong Jin; Hwang, In Hong; Song, Eun Joo; **Kim, Hyun**; Kim, Cheal "A colorimetric and fluorescent sensor for sequential detection of copper ion and cyanide", *Tetrahedron*, **2014**, *70*, 2822–2828.

15. **Kim, Hyun**; Kim, Kyung Beom; Song, Eun Joo; Hwang, In Hong; Noh, Jin Young; Kim, Pan Gi; Jeong, Kwang Duk; Kim, Cheal "Turn–on Selective Fluorescent Probe for Trivalent Cations" *Inorg. Chem. Commun.*, **2013**, *36*, 72–76.

16. Kim, Kyung Beom; **Kim, Hyun**; Song, Eun Joo; Kim, Sumi; Noh, Insup; Kim, Cheal "A Cap-Type Schiff Base Acting as Fluorescence Sensor for Zinc(II) and Colorimetric Sensor for Iron(II), Copper(II), and Zinc(II) in Aqueous Media", *Dalton Trans.*, **2013**, *42*, 16569–16577.

17. Noh, Jin Young; Hwang, In Hong; **Kim, Hyun**; Song, Eun Joo; Kim, Kyung Beom; Kim, Cheal "Salicylimine-Based Colorimetric and Fluorescent Chemosensor for Selective Detection of Cyanide in Aqueous Buffer", *Bull. Korean Chem. Soc.*, **2013**, *34*, 1985–1989.

18. Kang, Juhye; Kang, Hee Kyung, **Kim, Hyun**; Lee, Jungha; Song, Eun Joo; Jeong, Kwang Duk; Kim, Cheal; Kim, Jinheung "Fluorescent chemosensor based on bispicolylamine for selective detection of magnesium ions", *Supramolecular Chemistry*, **2013**, *25*, 65–68.

19. Hwang, In Hong; Jo, Young Dan, **Kim, Hyun**; Kim, Kyeong Beom; Jung, Kwang Deog; Kim, Cheal; Kim, Youngmee; Kim, Sung Jin "Catalytic transesterification reactions of one-dimensional coordination polymers containing paddle-wheel-type units connected by various bridging ligands", *Inorg. Chim. Acta*, **2013**, *402*, 39–45.

20. Hyun, Min Young; Hwang, In Hong; Lee, Myoung Mi; **Kim, Hyun**; Kim, Kyeong Beom; Kim, Cheal; Kim, Ha Yeoung; Kim, Youngmee; Kim, Sung Jin "Zn^{II} coordination polymers constructed with malonate and bipyridyl ligands: Photoluminescence and heterogeneous catalytic reactivity", *Polyhedron*, **2013**, *53*, 166–171.

21. Kang, Jongmin; Song, Eun Joo; **Kim, Hyun**; Kim, Young Hee; Kim, Youngmee; Kim, Sung Jin; Kim, Cheal "Specific naked eye sensing of cyanide by chromogenic host: studies on the effect of solvents", *Tetrahedron Letters*, **2013**, *54*, 1015–1019.

22. Lee, Jungha; **Kim, Hyun**; Kim, Soojin; Noh, Jin Young; Song, Eun Joo; Kim, Cheal; Kim, Jinheung "Fluorescent dye containing phenol-pyridyl for selective detection of aluminum ions", *Dyes and Pigments*, **2013**, *96*, 590–594.

REFERENCES

Kenneth D. Karlin
karlin@jhu.edu
1-410-516-8027

David P. Goldberg
dpg@jhu.edu
1-410-516-6658

Alan T. Stone
astone@jhu.edu
1-410-516-8476